Propriétés électroniques et thermoélectriques des matériaux 2D sur substrat

Salvatore Timpa

UNIVERSITÉ DE PARIS

ÉCOLE DOCTORALE 564 - PHYSIQUE EN ÎLE-DE-FRANCE
LABORATOIRE MATÉRIAUX ET PHÉNOMÈNES QUANTIQUES

THÈSE PRÉSENTÉE PAR

SALVATORE TIMPA

POUR OBTENIR LE GRADE DE
DOCTEUR DE L'UNIVERSITÉ DE PARIS
SPECIALITÉ: PHYSIQUE DE LA MATIÈRE CONDENSÉE

ELECTRIC AND THERMOELECTRIC PROPERTIES OF SUPPORTED 2D MATERIALS

JURY DE THÈSE

Dr. Vincent DERYCKE	Rapporteur	LICSEN - CEA Paris-Saclay
Prof. Philippe LECOEUR	Rapporteur	C2N - Université Paris Saclay
Dr. Sylvie HEBERT	Examinateur	CRISMAT - ENSI Caen
Prof. Matteo COCUZZA	Examinateur	DISAT - Politecnico di Torino
Prof. Jean-Christophe CHARLIER	Examinateur	Université catholique de Louvain
Prof. Maria Luisa DELLA ROCCA	Directrice de thèse	MPQ - Université de Paris

PARIS, 14 OCTOBRE 2021

Résumé

Notre âge a connu une croissance technologique exponentielle jamais enregistrée auparavant. Dans le contexte de ce développement technologique, la disponibilité d'énergies propres et renouvelables est devenue une question stimulante en poussant les efforts de recherche. La conversion thermoélectrique (TE), nommément la capacité d'un matériau à générer de l'énergie électrique à partir d'un gradient de température ou d'un courant thermique à partir d'une tension appliquée, vise à récupérer cette énergie gaspillée et, la recherche de nouveaux matériaux thermoélectriques connaît récemment une nouvelle impulsion d'enthousiasme. Les dispositifs thermoélectriques sont fiables et ne polluent pas l'atmosphère, mais leur faible efficacité de conversion reste la limite d'un développement étendu. Les nouvelles solutions de récupération d'énergie sont actuellement très demandées, en particulier dans le domaine de la micro-électronique et de la nano-électronique.

L'objectif de ce travail de doctorat est de contribuer à la recherche de solutions originales pour concevoir de nouveaux dispositifs basés sur des matériaux 2D améliorant les performances thermoélectriques, en particulier en considérant la configuration sur substrat, plus approprié pour les applications. En particulier, j'ai examiné les propriétés électriques et thermoélectriques des hétérostructures de WSe_2 sur hBN, où la couche d'hBN est utilisée pour découpler le TMD du substrat (SiO_2), et comme diélectrique, pour coupler efficacement le TMD à la grille locale. Le diséléniure de tungstène (WSe_2) a été le matériau de choix puisque seulement quelques travaux se sont concentrés sur ses propriétés thermoélectriques, révélant, jusqu'à présent, des résultats prometteurs. De plus, le WSe_2 possède une conductivité thermique particulièrement basse (1 à 2 W/mK à la température ambiante), ce qui rend ce matériel attrayant pour les applications thermoélectriques. J'ai effectué une analyse détaillée des propriétés électriques et thermoélectriques à température ambiante de tels dispositifs en fonction du métal utilisé pour les contacts électriques. J'ai découvert des valeurs élevées de coefficient de Seebeck, jusqu'à 200 μV/K et facteur de puissance, jusqu'à 4 μW/cm K^2, en fonction du métal utilisé, révélant l'importance des propriétés électroniques à l'interface électrode / matériau 2D pour réaliser des dispositifs avec des performances thermoélectriques améliorées. Ensuite, je me suis intéressé à la complexe question de mesurer correctement les paramètres physiques définissant les performances thermoélectriques dans des dispositifs réels basés sur des matériaux à basse dimensionnalité sur substrat. Le paramètre ZT, qui quantifie l'efficacité de conversion d'énergie d'un dispositif thermoélectrique donné, dépend de la conductivité thermique du matériau choisi, qui, à température ambiante, est dominée par les phonons. Dans une configuration sur substrat, les pertes thermiques au substrat dominent fortement le

transport thermique et, la diffusion des phonons aux interfaces peut modifier fortement la conductivité thermique du matériel. Lors de mon travail de doctorat, j'ai proposé l'utilisation de la méthode de chauffage automatique de Joule, déjà utilisée pour évaluer la conductivité thermique des nano fils métalliques sur substrat, au cas des nano fils de graphène multi-couches. J'ai choisi le graphène comme matériau 2D de base pour la facilité de manipulation dans la fabrication des dispositifs. J'ai découvert que, en utilisant une couche d'oxyde de SiO_2 épaisse et rugueuse, les pertes thermiques au substrat peuvent être considérablement réduites et j'ai dévoilé une forte réduction de la conductivité thermique du graphène, avec des valeurs aussi basses que 40 W/mK. L'idée subissant est de déployer, dans l'avenir, la même approche également aux TMDs pour obtenir une caractérisation thermoélectrique complète des dispositifs étudiés.

Mots clefs : Matériaux 2D, thermoélectricité, transistor à effet de champ, conductivité thermique

Abstract

Our age has seen an exponential technological growth never recorded before. In the context of this technological development, the availability of clean and renewable energy has become a challenging issue pushing research efforts. Thermoelectric (TE) conversion, namely the ability of a material to generate electric power from a temperature gradient or a thermal current from an applied voltage, aims to recover this wasted energy and the research on new thermoelectric materials is recently experiencing a new enthusiastic boost. Thermoelectric devices are reliable and do not pollute the atmosphere, but their low conversion efficiency remains the limit of an extensive development. New energy recovery solutions are currently highly demanded in particular in the domain of micro- and nano-electronics.

The aim of this PhD work is to contribute in finding original solutions to engineer new devices based on 2D materials improving TE performances, particularly considering the on-substrate configuration, actually more appropriate for applications. In particular, I have investigated the electric and thermoelectric properties of hBN/WSe_2 heterostructures, where the hBN layer acts simultaneously as spacer, to decouple the TMD from the SiO_2 substrate, and as dielectric, to efficiently couple the TMD to a local gate. Tungsten diselenide (WSe_2) has been the material of choice since only few works have focused on its thermoelectric properties, revealing, so far, promising results. Moreover, WSe_2 owns a particularly low thermal conductivity (1 - 2 W/mK at room temperature), making this material appealing for TE applications. I have performed a detailed analysis of the electric and thermoelectric properties at room temperature of such devices as a function of the metal used for electrical contacts. I found out high values of Seebeck coefficient, up to 200 μV/K, and power factor, up to 4 μW/cm K^2, depending on the used metal, revealing the importance of the electronic properties at the electrode/2D material interface for enhanced device performances. Furthermore, I got interested into the complex question of correctly measuring the physical parameters defining the TE performances in actual devices based on supported low dimensional materials. The ZT parameter of a given TE device, which quantifies the energy conversion efficiency, depends on the thermal conductivity of the chosen material, which, at room temperature, is dominated by phonons. In a supported configuration, thermal losses to the substrate strongly dominate heat transport and, phonon boundary and interface scattering can strongly modify the material thermal conductivity. During my PhD work, I have proposed the use of the Joule self-heating method, already used to evaluate the thermal conductivity of supported metallic nanowires, to the case of multilayer graphene nanowires. I chose graphene as a test-bed 2D material for the easiness of its manipulation for device fabrication. I found out that, by using a thick and rough SiO_2

oxide layer, thermal losses to the substrate can be considerably reduced and I unveil an effective reduction of the graphene thermal conductivity, with values as low as 40 W/mK. The underlying idea is to extend, in the future, the same approach also to TMDs to achieve a complete in-situ thermoelectric characterization of the studied devices.

Key words: 2D materials, thermoelectricity, field effect transistor, thermal conductivity

Résumé long

Notre âge a connu une croissance technologique exponentielle jamais enregistrée auparavant. Dans le contexte de ce développement technologique, la disponibilité d'énergies propres et renouvelables est devenue une question stimulante en poussant les efforts de recherche. La conversion thermoélectrique (TE), nommément la capacité d'un matériau à générer de l'énergie électrique à partir d'un gradient de température ou d'un courant thermique à partir d'une tension appliquée, vise à récupérer cette énergie gaspillée et, la recherche de nouveaux matériaux thermoélectriques connaît récemment une nouvelle impulsion d'enthousiasme. Les dispositifs thermoélectriques sont fiables et ne polluent pas l'atmosphère, mais leur faible efficacité de conversion reste la limite d'un développement étendu. Les nouvelles solutions de récupération d'énergie sont actuellement très demandées, en particulier dans le domaine de la micro-électronique et de la nano-électronique.

Les matériaux thermoélectriques possèdent la capacité d'effectuer une conversion directe de la chaleur en électricité ou de l'électricité en chaleur grâce à deux mécanismes connexes, l'effet Seebeck et l'effet Peltier. Pour le premier, une différence de température ΔT induit l'accumulation d'une tension thermoélectrique $\Delta V = -S\Delta T$ dans le matériau à travers du coefficient Seebeck S. Inversement, pour le second, un courant électrique I induit un flux de chaleur proportionnel à celui-ci, $\dot{Q} = \Pi I$, où $\Pi = TS$ est le coefficient Peltier. L'efficacité de cette conversion d'énergie est caractérisée par le facteur de mérite ZT. ZT est défini comme $S^2\sigma T/\kappa$, où S est le coefficient de Seebeck, σ est la conductivité électrique, T est la température absolue et κ est la conductivité thermique totale, comprenant les contributions des électrons κ_e et des phonons κ_{ph}. Cependant, la relation colinéaire entre la conductivité thermique et électrique pour les porteurs de charge donnée par la loi de Wiedemann-Franz ($\kappa_e = L\sigma T$, où L est le facteur de Lorentz), est généralement considéré comme une limite pour la conversion d'énergie à haut rendement dans une large gamme de matériaux, en particulier à basse température. A haute température, les phonons dominent le transport de chaleur, limitant les performances TE. De plus, un compromis entre S et σ est nécessaire pour obtenir des valeurs ZT élevées.

En termes de matériaux, le principal défi consiste à surmonter les inconvénients liés à la corrélation entre les propriétés électriques et thermiques de la plupart des matériaux. Le tellurure de bismuth (Bi_2Te_3) et ses alliages sont les matériaux thermoélectriques classiques largement utilisés dans les applications commerciales actuelles nécessitant de grands coefficients Seebeck. Le silicium germanium (SiGe) est également un excellent matériau TE, particulièrement adapté aux applications à haute température et aux modules TE pour les

missions dans l'espace lointain afin de convertir la chaleur des radio-isotopes en électricité. Le tellurure de plomb (PbTe) est un autre exemple de matériau TE populaire souvent étudié. En dehors de ceux-ci, le séléniure d'étain (SnSe) a été étudié en détail ces dernières années, devenant également un matériau TE prometteur. La plupart des matériaux thermoélectriques massifs de pointe ont des valeurs maximales de ZT comprises entre 1 et 2.5. Néanmoins, une telle plage de valeurs n'est souvent atteinte qu'à très haute température et, par conséquent, il n'est pas pratique de réaliser des applications à grande échelle. Pour ces raisons, il est nécessaire de rechercher des propriétés thermoélectriques améliorées des matériaux et une voie intéressante est d'explorer des solutions complètement nouvelles, comme c'est le cas pour les systèmes de faible dimension, et plus particulièrement les matériaux 2D.

Les matériaux bidimensionnels (2D) sont des nano-objets d'une épaisseur allant d'une couche atomique à quelques nanomètres et des dimensions planes de quelques micromètres à des centaines de micromètres. Le graphène, isolé pour la première fois parmi les matériaux 2D en 2004, est l'objet 2D le plus fin présente dans la nature. La structure électronique du graphène était connue depuis les années 40 et des propriétés surprenantes étaient déjà prédites. Son isolement expérimental par la simple méthode de l'exfoliation a représenté le trampoline pour l'émergence d'une grande famille d'autres matériaux 2D. L'étude théorique et expérimentale de ces nouveaux matériaux a révélé des propriétés physiques complètement nouvelles liées au confinement local naturel des porteurs de charge dans les systèmes 2D et à leur structure de bande unique. De plus, les effets de surface, généralement négligeables dans les matériaux massifs, deviennent dominants pour la détermination des propriétés intrinsèques des matériaux. Couvrant une large gamme de tailles de bande interdite énergétique, les matériaux 2D présentent une grande variété de propriétés électroniques, allant de l'isolant au semi-métal, et des applications optiques du spectre visible au proche infrarouge. Les matériaux 2D ont une forte stabilité dans le plan commune donnée par la présence de liaisons covalentes. A l'inverse, l'interaction intercouche est relativement faible, étant de type van der Waals. C'est grâce à cette interaction faible que les matériaux 2D peuvent être exfoliés mécaniquement pour isoler leur homologue monocouche. La facilité de la préparation d'échantillons à base de matériaux 2D a permis d'étudier leurs propriétés physiques avec une multitude d'approches, de la spectroscopie au transport de charges, et le développement des activités de recherche pour les intégrer dans des dispositifs électroniques et photoniques. La structure atomique unique des matériaux en couches permet l'isolation mécanique de fines couches atomiques 2D avec de nombreuses propriétés physiques inattendues. Cependant, si l'obtention de flocons de matériaux 2D de haute qualité peut être extrêmement facile, préserver les propriétés physiques de ces matériaux n'est pas une tâche triviale. Les matériaux 2D ne sont composés que de surfaces et n'ont pas de volume. Pour cette raison, leurs propriétés dépendent fortement de leur état de surface et de l'interaction avec l'environnement. En conséquence, la stabilité thermique et chimique n'est pas la même que celle du matériau massif. Par exemple, la température de fusion diminue en abaissant les dimensions puisque la quantité de liaison en surface est plus faible que dans la masse. Pour la même raison, la réactivité chimique d'un matériau 2D peut augmenter par rapport à la masse et généralement, la couche de passivation qui se forme lorsque le matériau est exposé à l'atmosphère, a un fort impact sur les propriétés du maté-

riau 2D. De plus, même si le matériau est inerte dans l'atmosphère, les molécules adsorbées, comme l'eau ou les hydrocarbures, peuplent généralement la surface du matériau, modifiant fortement les propriétés de structure de bande et la relation de dispersion énergétique.

L'idée de base qui a permis de mieux exploiter les matériaux bidimensionnels, en préservant voire en améliorant leurs propriétés physiques, a été de créer un empilement de couches 2D. Cette conception révolutionnaire permet non seulement une isolation bien contrôlée du "noyau 2D" de l'appareil, évitant la passivation naturelle ou l'interaction avec l'environnement, mais elle permet également de révéler des propriétés physiques qui ne sont présentes dans aucune des couches utilisées. Par exemple, la qualité électronique d'un dispositif en graphène dépend fortement de l'interaction électronique entre la couche de graphène et le substrat (SiO_2 est le plus couramment utilisé). En raison de sa rugosité, de la présence de charges piégées et de phonons de surface, SiO_2 limite la mobilité des porteurs de charge dans le graphène. L'utilisation de nitrure de bore hexagonal (hBN) bidimensionnel comme substrat ou couche d'encapsulation a été développée comme technique d'isolation et de protection pour le graphène, ainsi que pour d'autres 2D. hBN a une surface atomiquement lisse et un faible décalage de réseau (1.8%) avec le graphite. Le hBN massif s'est déjà avéré être un substrat optimal pour le graphène et son homologue 2D est relativement inerte et devrait être libre de liaisons pendantes ou de pièges de charge de surface.

Parmi le vaste paysage de propriétés des matériaux à l'échelle 2D, la thermoélectricité a reçu une attention particulière au cours de la dernière décennie. Selon Hicks-Dresselhaus, l'utilisation du confinement quantique 2D est un moyen simple de concevoir la densité d'états (DOS) afin de découpler le facteur de thermopuissance (défini comme $PF = S^2\sigma$) de la conductivité thermique (κ). Cela peut conduire à une amélioration de la figure de mérite dans les systèmes à dimensionnalité réduite. Par exemple, une conductivité électrique élevée et un coefficient Seebeck relativement élevé conduisent à un très fort pouvoir de refroidissement du graphène. Cependant, la figure de mérite du graphène est généralement extrêmement limitée en raison de la conductivité thermique très élevée résultant de la liaison covalente dans le plan sp^2 qui augmente le libre parcours moyen des phonons (phMFP) jusqu'à environ quelque μm. D'autre part, le libre parcours moyen des phonons dans les systèmes de faible dimension est généralement beaucoup plus grand (au moins un ordre de grandeur à température ambiante) que le libre parcours moyen des électrons (eMFP). Cela signifie que les matériaux peuvent être conçus en augmentant la diffusion des phonons sans affecter la diffusion des électrons afin d'obtenir des conductivités thermiques réduites sans compromettre la conductivité électrique et le coefficient Seebeck. Le nano-pattering et l'ingénierie des substrats dans le graphène sont les moyens les plus simples permettant d'éteindre la conductivité thermique tout en préservant pleinement les performances électroniques de l'appareil.

Dans ce scénario, les dichalcogénures de métaux de transition (TMDs) ont récemment ouvert la possibilité de nouvelles options. Les TMDs sont des matériaux 2D à bande interdite relativement petite qui sont capables d'assurer à la fois la conduction des électrons et des trous, ouvrant ainsi un large éventail d'applications possibles. Ils ont une conductivité électrique relativement élevée, un grand coefficient Seebeck a été mesuré jusqu'à 300 mV/K dans une monocouche de MoS_2, et la conductivité thermique a été théoriquement prédite et mesurée

au moins deux ordres de grandeur inférieure à celle du graphène. De plus, en raison de leur écart énergétique relativement faible, les propriétés électroniques des TMDs peuvent être ajustées en modulant le type et la concentration des porteurs de charge.
L'objectif de ce travail de doctorat est de contribuer à la recherche de solutions originales pour concevoir de nouveaux dispositifs basés sur des matériaux 2D améliorant les performances thermoélectriques, en particulier en considérant la configuration sur substrat, plus approprié pour les applications. En particulier, j'ai examiné les propriétés électriques et thermoélectriques des hétérostructures de WSe_2 sur hBN, où la couche d'hBN est utilisée pour découpler le TMD du substrat (SiO_2), et comme diélectrique, pour coupler efficacement le TMD à la grille locale. Le diséléniure de tungstène (WSe_2) a été le matériau de choix puisque seulement quelques œuvres se sont concentrées sur ses propriétés thermoélectriques, révélant, jusqu'à présent, des résultats prometteurs. De plus, le WSe_2 possède une conductivité thermique particulièrement basse (1 à 2 W/mK à la température ambiante), ce qui rend ce matériel attrayant pour les applications thermoélectriques. J'ai effectué une analyse détaillée des propriétés électriques et thermoélectriques à température ambiante de tels dispositifs en fonction du métal utilisé pour les contacts électriques. J'ai découvert des valeurs élevées de coefficient de Seebeck, jusqu'à 200 μV/K et facteur de puissance, jusqu'à 4 μW/cm K^2, en fonction du métal utilisé, révélant l'importance des propriétés électroniques à l'interface électrode / matériau 2D pour réaliser des dispositifs avec des performances thermoélectriques améliorées.
Ensuite, je me suis intéressé à la complexe question de mesurer correctement les paramètres physiques définissant les performances thermoélectriques dans des dispositifs réels sur substrat basés sur des matériaux à basse dimensionnalité. Le paramètre ZT, qui quantifie l'efficacité de conversion d'énergie d'un dispositif thermoélectrique donné, dépend de la conductivité thermique du matériau choisi, qui, à température ambiante, est dominée par les phonons. Dans une configuration sur substrat, les pertes thermiques au substrat dominent fortement le transport thermique et, la diffusion des phonons aux interfaces peut modifier fortement la conductivité thermique du matériel. Lors de mon travail de doctorat, j'ai proposé l'utilisation de la méthode de chauffage automatique de Joule, déjà utilisée pour évaluer la conductivité thermique des nano fils métalliques sur substrat, au cas des nano fils de graphène multicouches. J'ai choisi le graphène comme matériau 2D de base pour la facilité de manipulation dans la fabrication des dispositifs. J'ai découvert que, en utilisant une couche d'oxyde de SiO_2 épaisse et rugueuse, les pertes thermiques au substrat peuvent être considérablement réduites et j'ai dévoilé une forte réduction de la conductivité thermique du graphène, avec des valeurs aussi basses que 40 W/mK. L'idée subissant est de déployer, dans l'avenir, la même approche également aux TMDs pour obtenir une caractérisation thermoélectrique complète des dispositifs étudiés.

Contents

Introduction

Two-dimensional materials

Two-dimensional (2D) materials are nano-objects with a thickness ranging from one atomic layer up to few nanometers and planar dimensions from few micrometers up to hundreds of micrometers. Graphene, first isolated among the 2D materials in 2004 [1], is the thinnest 2D-object present in nature. The electronic structure of graphene was known since the '40s [2] and surprising properties were already predicted. Its experimental isolation by the simple exfoliation method represented the trampoline for the emergence of a large family of other 2D materials [3, 4]. The theoretical and experimental investigation of these new materials has been revealing completely new physical properties related to the natural local confinement of

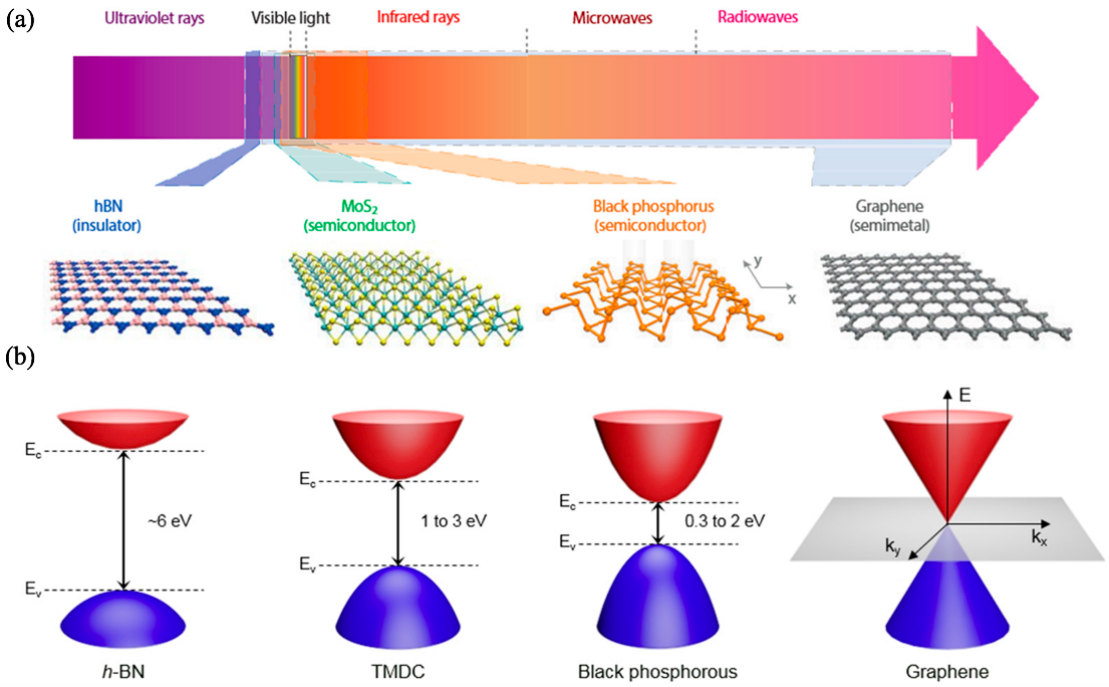

Figure 1 – (a) Energy spectrum of various two-dimensional (2D) materials and their atomic crystal structure. (b) Electronic band structures of hexagonal boron nitride (hBN), transition metal dichalcogenides (TMDs), black phosphorous (BP) and graphene. Extracted from [4].

charge carriers in 2D systems and to their unique band structure. Moreover, surface effects, which are generally negligible in bulk materials, become dominant for the determination of the intrinsic material properties [5]. Covering a wide range of energy bandgap sizes, 2D materials show a large variety of electronic properties, ranging from insulator to semi-metal, and optical applications from visible to near infrared spectrum, as shown in Figure 1.

From the electronic point of view, graphene has shown very high electric conductivity with room temperature mobility on the order of 200 000 $cm^2/V\,s$ originating from the weak electron-phonon interaction [6]. However, its gapless band structure prevents the use of graphene for C-MOS/logic applications. Regarding thermal applications, graphene is an ideal material to make heat-spreading solutions, such as heat sinks. Unlike graphene, which has a semi-metallic behavior, other 2D materials, such as TMDs (transition metal dichalcogenides) or BP (black phosphorous), have been exploited for their semiconducting nature to design high performing electronic devices such as field-effect transistors (FETs). In fact, since these materials are free from dangling bonds, they generally exhibit high mobility depending on the choice of the appropriate substrate and the metal contacts [7]. For example, high effective mobilities have been achieved at room temperature in 10 nm-thick molybdenum disulfide (MoS_2), one of the most studied materials among the TMDs, on the order of 700 $cm^2/V\,s$ using scandium (Sc) contacts [8]. Concerning the large bandgap insulators, hexagonal boron nitride (hBN) is currently the most famous. Layers of hBN consist of hexagonal rings of alternating B and N atoms, with strong covalent sp^2 bonds and a lattice constant nearly identical to that of graphene. hBN is very resistant both to mechanical manipulation and chemical interactions and has a large band gap in the UV range. For these reasons, hBN is the material of choice as encapsulating layer or substrate for other 2D conducting channels, providing an atomically smooth surface free of dangling bonds and charge traps [9].

2D materials have a common strong in-plane stability given by the presence of covalent bonds. On the opposite, the interlayer interaction is relatively weak, being of van der Waals type [10]. It is thanks to this weak interaction that 2D materials can be mechanically exfoliated to isolate their monolayer counterpart. The easiness of 2D material-based sample preparation has allowed for the investigation of their physical properties with a multitude of approaches, from spectroscopy to charge transport, and the growing of research activities to integrate them in electronic and photonic devices.

Transition metal dichalcogenides

Transition metal dichalcogenides (TMDs) are bidimensional compounds with a MX_2 basic unit block as illustrated in Figure 2a. They are composed of an inner layer of transition metal atoms M on a triangular lattice sandwiched between two layers of chalcogen atoms X. Depending on the metal atom, these compounds offer a broad range of electronic properties, from insulating or semiconducting (e.g., Ti, Hf, Zr, Mo, and W) to metallic or semi-metallic (V, Nb, and Ta). The different electronic behavior arises from the progressive electrons filling of the transition metal

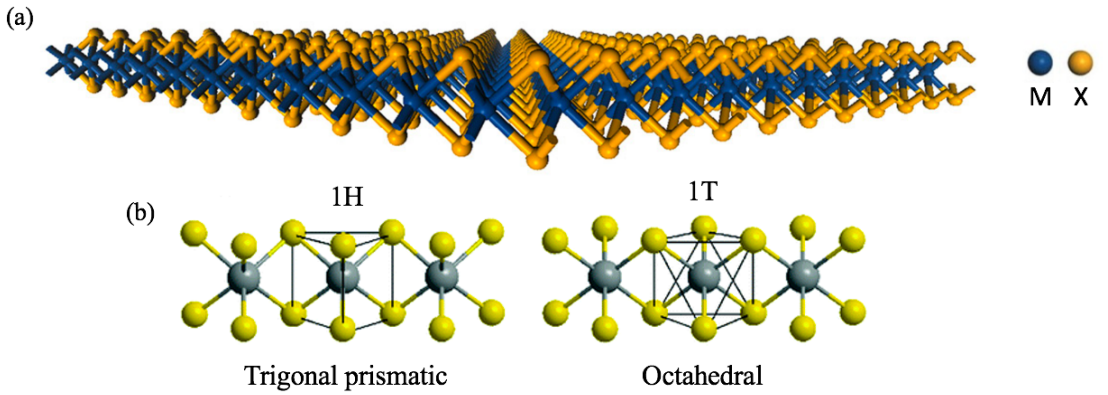

Figure 2 – (a) Atomic model of a typical transition metal dichalcogenides. The inner transition metal atom M (such as Mo or W) is sandwiched between two layers of chalcogen atoms X (such as Se or S). Extracted from [11]. (b) Trigonal prismatic and octahedral transition metal coordination in TMDs. Extracted from [12].

d bands. The main interest in semiconducting TMDs monolayers has been primarily with Mo and W metals, and Se, S and Te chalcogenides. The most commonly encountered polymorphs of TMDs are 1H and 1T, where the letters represent different crystal symmetry of the system (hexagonal or trigonal), and the digits stand for number of X-M-X layers, respectively. As illustrated in Figure 2b, in the 1H form, the metal is in trigonal prismatic coordination, while, in the 1T form, the metal is in octahedral coordination [12]. The 1H structure is the most commonly found and the most thermodynamically stable configuration at room temperature, and for that it is the most studied for possible applications [13].

Due to the van der Waals interaction between adjacent layers, electronic properties of TMDs multilayers are highly sensitive to the number of layers and their relative orientation. In particular, in bilayer and thicker multilayers, interlayer interaction, geometrical confinement and crystal symmetry play a collective role in defining their electronic structure [14, 15, 16]. Referring to density functional theory (DFT) calculations [17, 18], we can look at the electronic properties of MX_2 compounds (with M = Mo, W and X = S, Se). The main outcome of interlayer interaction is the indirect-to-direct band gap crossover which results from local shift of valence band hills and conduction band valley in the Brillouin zone and which is a basic ingredient for electronic, photonic and optoelectronic applications. Figure 3 shows the band structure evolution of tungsten diselenide (WSe_2) with the number of layers. In the single layer, the conduction band minimum (CBM) and valence band maximum (VBM) coincide at the K point, making this TMD a direct gap semiconductor. By increasing the number of layers, the valence band hill at the Γ point is raised above the hill at the K point. The conduction band valley at the Q point (midpoint between K and Γ) shifts downwards with increasing interlayer interaction. As a consequence, the material changes to an indirect bandgap semiconductor. In contrast, the states near the K point are comparatively less sensible to the number of layers. This is due to the fact that K valleys/hills are defined by the *d* orbital wave functions localized around the transition metal atoms [18, 19] which are significantly less affected by interlayer spacing.

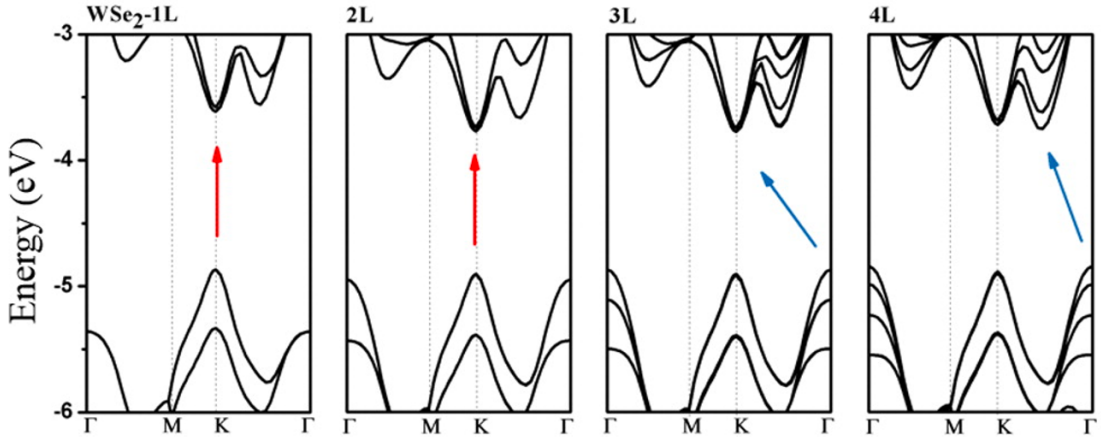

Figure 3 – Band structure evolution of WSe_2 as a function of the number of layers obtained with DFT calculations, including spin-orbit coupling (SOC). Extracted from [20].

A more accurate analysis shows that the interlayer coupling is not the only parameter determining the indirect-to-direct band gap crossover. Due to the presence of heavy elements, the spin-orbit coupling (SOC) needs to be included to fully understand the physical properties of few-layers TMDs. As illustrated in Figure 4 for the case of WSe_2, spin-orbit coupling leads to an appreciable splitting of the valence band at the K point, which is almost independent of the layer thickness. When reducing the number of layers, Sun et al. [20] have predicted that the indirect-to-direct band gap transition takes place in the bilayer WSe_2 and the tetralayer WTe_2, both of which having heavy elements and a strong SOC effect. In the case of MoS_2, $MoSe_2$, and WS_2, the SOC is not strong enough to compete with the interlayer coupling, and the indirect-to-direct band gap transition only occurs in the monolayer form when coupling between layers completely vanishes. By comparing the band structure of WSe_2 with and without the inclusion of the SOC effect, as shown in Figure 4 for the monolayer and bilayer cases, it is possible to observe an appreciable splitting ($\sim$ 467 meV) at the K point of valence band due to the SOC effect [21]. This energy splitting is independent of the layer thickness and plays a significant role in the indirect-to-direct band gap crossover in WSe_2. In fact, according to calculations which do not include SOC, the energy splitting at the K point in bilayer WSe_2 is negligible and the valence band maximum is located at the Γ point. Only if the SOC effect is taken into account, WSe_2 bilayer turns into a direct band gap semiconductor.

The versatility of band structure engineering, which determines the electronic and optical properties of 2D materials, makes transition metal dichalcogenides appealing for a plethora of applications. The first theoretical and experimental works on TMDs have addressed their optical and optoelectronic properties [22, 23, 24, 25] by studying the indirect-to-direct bandgap transition when reducing the thickness from few-layers to monolayer [25], by investigating spin-valley locking [26], valleytronic [27], and piezoelectricity [28] related to the lack of inversion symmetry in TMDs monolayers. Moreover, plenty of interesting electronic behaviors have been demonstrated as well, such as metal-insulator transitions [29], electronic correlations [30] and energy bandgap tuning [31].

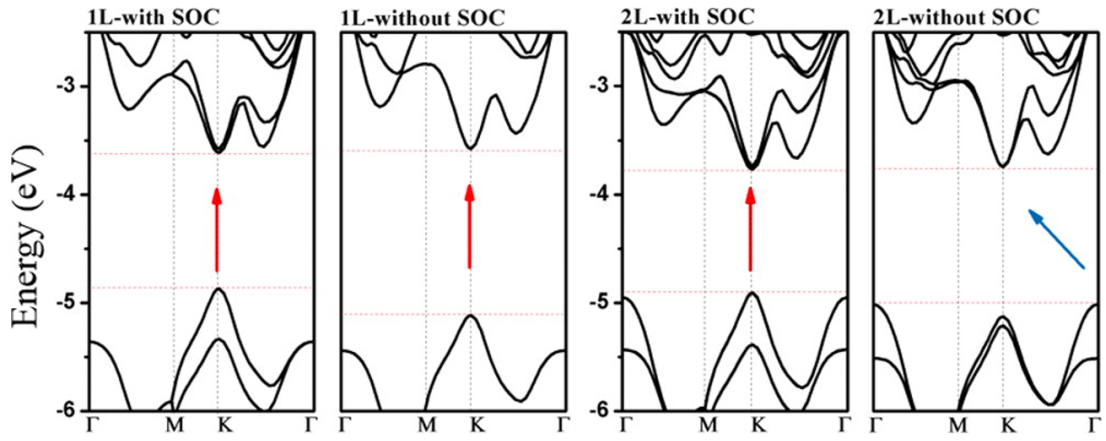

Figure 4 – Band structure of monolayer and bilayer WSe_2 with and without SOC. Extracted from [20].

Combining 2D materials: van der Waals heterostructures

The unique atomic structure of layered materials allows for the mechanical isolation of atomic thin 2D layers with plenty of unexpected physical properties. However, if obtaining high quality 2D material flakes could be extremely easy, preserving those materials physical properties is not a trivial task. 2D materials are only composed by surfaces and do not have a bulk. For this reason, their properties strongly depend on their surface state and on the interaction with the environment. As a result, thermal and chemical stability are not the same as in the bulk material counterpart [10]. For example, the melting temperature decreases by lowering dimensions since the amount of bonding at the surface is lower than in the bulk. For the same reason, the chemical reactivity of a 2D material might increase with respect to the bulk and usually, the passivation layer that is formed when the material is exposed to atmosphere, strongly impacts on the 2D material properties. Moreover, even if the material is inert in atmosphere, adsorbed molecules, like water or hydrocarbons, usually populate the material surface strongly modifying the band structure properties and the energy dispersion relation. Oxidation is another source of extrinsic disorder in many air-sensitive 2D materials [10]. A representative example is given by the semiconducting black phosphorus (BP): it has been shown that small amounts of adsorbed water are seen by atomic force microscopy (AFM) immediately after exfoliation in ambient conditions, and TEM imaging shows that few-layer BP completely collapses after 20 seconds of exposure to air [32].

The basic idea that has allowed to better exploit two-dimensional materials, preserving or even improving their physical properties, has been to create stacking of 2D layers [10] as illustrated in Figure 5. This revolutionary design not only allows for a well-controlled isolation of the "2D core" of the device, avoiding natural passivation or interaction with the environment, but it also permits to reveal physical properties that are not present in none of the employed layers. For example, the electronic quality of a graphene device strongly depends on the electronic interaction between the graphene layer and the substrate (SiO_2 is the most commonly used). Due to its roughness [33], presence of trapped charges [34], and surface phonons [35], SiO_2

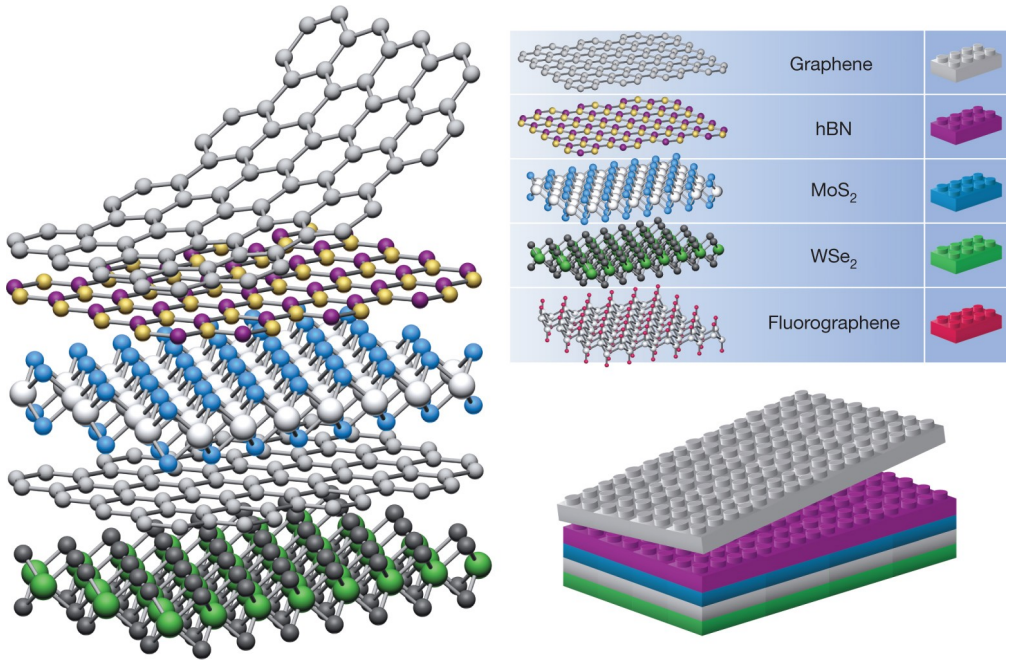

Figure 5 – Lego-style assembly of different two-dimensional materials to create a van der Waals heterostructure. Extracted from [10].

limits the mobility of charge carriers in graphene. Graphene obtained by mechanical cleavage on top of an oxidized silicon (Si) wafer exhibits a mobility $\mu \approx 10\,000$ cm^2/V s for electron concentrations up to $n_{2D} = 10^{13}$ cm^{-2} [1]. By suspending single layer graphene, it is possible to achieve mobilities exceeding 200 000 cm^2/V s at electron densities of $\sim 2 \times 10^{11}$ cm^{-2} [36]. However, due to mechanical instability under large applied gate voltages, it is not possible to induce high charge carrier densities in suspended devices [37]. In addition, the fabrication of electrical gated suspended devices is more challenging and time consuming, not actually practicable for applications. The use of 2D hexagonal boron nitride (hBN) as a substrate or encapsulation layer has been developed as an insulation and protection technique for graphene, as well as for other 2D materials [38, 39, 40]. hBN has an atomically smooth surface and a small (1.8%) lattice mismatch with graphite [41]. Bulk hBN was already proved to be an optimal substrate for graphene and its 2D counterpart is relatively inert and is expected to be free of dangling bonds or surface charge traps [9]. As a result, encapsulated graphene has shown room temperature ballistic transport over micrometric distances and mobility higher than 100 000 cm^2/V s for low charge carrier densities, $n_{2D} \approx 10^{11}$ cm^{-2}, even at room temperature [42].

The effect of encapsulation has shown very promising results also in the case of TMDs. Very recently, the mobility of heterostructures formed by stacking layers of hBN, graphene and WSe_2 has been measured as high as 350 000 cm^2/V s with resistivities as low as 15 Ω at room temperature. These results, explained as originating from a modified acoustic phonon band at the graphene-WSe_2 interface, outperform the room temperature mobility of today's best

graphene/hBN devices [43]. A second example worthy to be cited concerns the optical response of encapsulated 2D material. As direct-bandgap semiconductors, monolayer TMDs show efficient photoluminescence (PL), with spectra dominated by strong excitonic resonances with the underlying substrate. As shown for monolayer TMDs in Figure 6, when extrinsic disorder is reduced in monolayer TMDs through hBN encapsulation and sufficient screening of charge disorder in the underlying SiO_2 substrate, a substantial narrowing of the linewidth is observed [44].

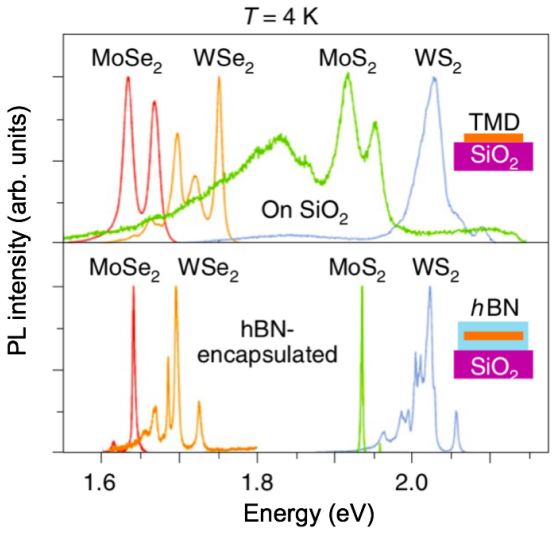

Figure 6 – Typical PL spectra for different single layer TMDCs at $T = 4$ K when deposited directly onto SiO_2 (top) and when capped with hBN (bottom). The excitation density is 1 $\mu W/\mu m^2$. Extracted from [44].

The control of the crystallographic alignment of van der Waals heterostructures is another key point having very relevant consequences. It has been achieved with an accuracy of less than 1° [45]. Although the interaction between stacked 2D layers is relatively weak, electron orbitals extending out of the plane affect the charge carrier density of an adjacent 2D layer. As a consequence, the relative layer orientation induces Moiré patterns that depend on the rotation angle between adjacent layers and their lattice mismatch. In the case of graphene on hBN, it has been demonstrated that a periodic potential created by the hBN substrate results in secondary Dirac cones at high electron and hole densities [46, 47] and a gap opening in the electron spectrum can be recorded [48, 49]. This can be explained by considering that, in order to match the interatomic spacing of hBN, stretching of graphene occurs to achieve the most favorable energetic configuration. However, due to its high Young modulus, a perfect stretching cannot be achieved across the whole interface and it can only be local. Thus, periodic stretched regions generate periodic potentials in graphene on hBN. In the landscape of 2D superlattices and proximity effects, stacking of two graphene sheets has also been studied at small twist angle. For angles near 1.1°, known as the first "magic" angle, twisted bilayer graphene (TBG) exhibits ultra-flat bands near charge neutrality and superconductivity phases with a tunable zero-resistance states with a critical temperature T_C up to 1.7 K [50]. Twisted bilayer graphene has also shown insulating states exhibiting ferromagnetism [51]. Materials with transition metals in their chemical composition are particularly prone to many-body instabilities such as superconductivity, charge density waves (CDWs), and spin density

waves (SDWs). Such effects can also be induced by proximity if these materials are sandwiched with other 2D materials. As an example, spin-orbit interaction can be enhanced in graphene by neighboring transition metal dichalcogenides [52, 53].

Thermoelectricity and 2D materials

Our age has seen an exponential technological growth never recorded before. In the context of this technological development, the availability of clean and renewable energy has become a challenging issue pushing research efforts. No matter the type of energy we can think about (e.g., mechanical, electrical, chemical, solar, etc.), all dissipative processes are accompanied by the release of thermal energy which is wasted in the environment of the system under consideration. Thermoelectric (TE) conversion, namely the ability of a material to generate electric power from a temperature gradient or a thermal current from an applied voltage, aims to recover this wasted energy and the research on new thermoelectric materials is recently experiencing a new enthusiastic boost. In fact, thermoelectricity offers the important advantage of clean approaches for energy recovery. Thermoelectric materials have extensive potential applications, mostly related to power generation. This includes waste heat recovery, use of solar energy, and power supplying for wearable electronics [54, 55, 56, 57]. Thermoelectric materials also offer refrigeration technology applications which are widely applied in many areas of electric refrigeration due to their solid-state nature, absence of vibrations, simplicity and environmental friendliness [58]. Thermoelectric devices are reliable and do not pollute the atmosphere, but their low conversion efficiency remains the limit of an extensive development. For this reason, they have been typically relegated to niche applications where other energy sources are not readily available (e.g., deep space, submarines, etc.). New energy recovery solutions are currently highly demanded in particular in the domain of micro- and nano-electronics.

Thermoelectric materials own the ability to perform a direct conversion of heat into electricity or electricity into heat through two related mechanisms, the Seebeck effect and the Peltier effect. For the first, a temperature difference ΔT will induce the build-up of a thermoelectric voltage $\Delta V = -S\Delta T$ across a material with Seebeck coefficient S. Vice versa, for the second, an electrical current I induces a heat flow proportional to it, $\dot{Q} = \Pi I$, where $\Pi = TS$ is the Peltier coefficient. The efficiency of this energy conversion is characterized by the figure of merit, ZT. ZT is defined as $S^2\sigma T/\kappa$, where S is the Seebeck coefficient, σ is the electric conductivity, T is the absolute temperature and κ is the total thermal conductivity, including the electron κ_e and phonon κ_{ph} contributions. However, the co-linear relation between the thermal and electrical conductivity for charge carriers given by the Wiedemann-Franz law ($\kappa_e = L\sigma T$, where L is the Lorentz factor), is usually considered a limit for high efficiency energy conversion in a wide range of materials, particularly at low temperature. At high temperature, phonons dominate heat transport, limiting TE performances. Moreover, a trade-off between S and σ is necessary to achieve high ZT values.

In terms of materials requirements, the main challenge relies in overcoming the disadvantages related to the correlation between electric and thermal properties of most materials. Bismuth telluride (Bi_2Te_3) and its alloys are the classical thermoelectric materials widely used in current commercial applications requiring large Seebeck coefficients [59, 60, 61]. Silicon germanium (SiGe) is an excellent TE material too, particularly suited for high temperature applications and TE modules for deep-space missions to convert radio-isotope heat into electricity [62, 63]. Lead telluride (PbTe) is another example of popular TE material often studied [64]. Other than these, tin selenide (SnSe) was studied in detail in recent years [65, 66, 67], becoming a promising TE material as well. Most state-of-the-art TE bulk materials have maximum ZT values between 1 and 2.5 [68]. Nevertheless, such a range of values is often achieved only at very high temperature and, thus, it is not practical to achieve large-scale application [69]. For these reasons, it is necessary to search for improved thermoelectric properties of materials and one intriguing way is to explore completely new solutions, as it is the case for low-dimensional systems, and more in particular 2D materials.

Among the vast landscape of properties in the 2D scale, thermoelectricity has received particular attention in the last decade. According to Hicks-Dresselhaus [70, 71], the use of 2D quantum confinement is an easy way to engineer the density of states (DOS) in order to decouple the thermopower factor (defined as $PF = S^2\sigma$) from the thermal conductivity (κ). This can lead to an enhancement of the figure of merit in systems with reduced dimensionality. For example, high electrical conductivity and relatively large Seebeck coefficient lead to a very strong cooling power in graphene [38]. However, the figure of merit in graphene is generally extremely limited due to the very high thermal conductivity arising from the in-plane sp^2 covalent bond which increases the phonon mean free path (phMFP) up to some μm. On the other hand, the phonon mean free path in low dimensional systems is typically much larger (at least one order of magnitude at room temperature) than the electron mean free path (eMFP). This means that materials can be engineered by increasing phonon scattering without affecting electron diffusion in order to achieve reduced thermal conductivities without compromising the electrical conductivity and the Seebeck coefficient. Nano-pattering [72] and substrate engineering [73] in graphene are the easiest ways allowing to quench the thermal conductivity while fully preserving the electronic performances of the device.

In this scenario, transition metal dichalcogenides (TMDs) have recently opened the possibility for new options. TMDs are relatively small-bandgap 2D materials which are able to ensure both electron and hole conduction, opening a broad range of possible applications. They have relatively high electrical conductivity [74], large Seebeck coefficient have been measured to be as high as 300 mV/K in MoS_2 monolayer [75], and the thermal conductivity has been theoretically predicted and measured at least two orders of magnitude lower than that of graphene [76, 77, 78]. Moreover, due to their relatively small energy gap, TMDs electronic properties can be tuned by modulating the charger carrier type and concentration.

Scope and structure of the thesis

The aim of this PhD work is to contribute in finding original solutions to engineer new devices based on 2D materials improving TE performances, particularly considering the on-substrate (or supported) configuration, actually more appropriate for applications. In particular, I have investigated the electric and thermoelectric properties of hBN/WSe_2 heterostructures, where the hBN layer acts simultaneously as spacer, to decouple the TMD from the SiO_2 substrate, and as dielectric, to efficiently couple the TMD to a local gate. Tungsten diselenide (WSe_2) has been the material of choice since only few works [79, 80] have focused on its thermoelectric properties, revealing, so far, promising results. Moreover, WSe_2 owns a particularly low thermal conductivity (~ 1 - 2 W/mK at room temperature) [81, 82], making this material appealing for TE applications. I have performed a detailed analysis of the electric and thermoelectric properties at room temperature of such devices as a function of the metal used for electrical contacts. I found out high values of Seebeck coefficient, up to ~ 200 μV/K, and power factor, up to ~ 4 μW/cm K^2, depending on the used metal, revealing the importance of the electronic properties at the electrode/2D material interface for enhanced device performances.

Furthermore, I got interested into the complex question of correctly measuring the physical parameters defining the TE performances in actual devices based on supported low dimensional materials. As explained previously, the ZT parameter of a given TE device depends on the thermal conductivity of the chosen material, which, at room temperature, is dominated by phonon heat transport. In a supported configuration, thermal losses to the substrate strongly dominate heat transport and, phonon boundary and interface scattering can strongly modify the material thermal conductivity. During my PhD work, I have proposed the use of the Joule self-heating method, already used to evaluate the thermal conductivity of supported metallic nanowires [83], to the case of multilayer graphene nanowires. I chose graphene as a test-bed 2D material for the easiness of its manipulation for device fabrication. I found out that, by using a thick and rough SiO_2 oxide layer, thermal losses to the substrate can be considerably reduced and I unveil an effective reduction of the graphene thermal conductivity, with values as low as 40 W/mK. The underlying idea is to extend, in the future, the same approach also to TMDs.

The manuscript is organized as follows:

In the **first chapter**, I will discuss the state-of-the-art of the main parameters necessary to boost the efficiency of thermoelectric materials, i.e., Seebeck coefficient and thermal conductivity. In particular, I will highlight the main results reported in literature regarding graphene, black phosphorous, and most commune TMDs.

In the **second chapter**, I will introduce the fabrication techniques employed to design van der Waals heterostructures with electrical connection in a field effect transistor (FET) fashion. I will also talk about the interlayer impurities, which are a very common problem in staked layers.

In the **third chapter**, I will deal with the charge injection in hBN-supported WSe_2 transistors with a different choice of metals for the electrical connections. I will evaluate the Schottky barriers at the metal-semiconductor interface and I will discuss about the Fermi level pinning and the modified transport gap.

In the **fourth chapter**, I will talk about the Seebeck coefficient measurements performed in hBN-supported WSe_2 devices, again with a different choice of metals for the electrical connections. The influence of orbital hybridization at the metal-semiconductor interface, already evident from the charge transport measurements, is highlight by the Seebeck coefficient investigation.

In the **fifth chapter**, I will move the discussion to the measurement of the thermal conductivity of SiO_2-supported multilayer graphene nanowires. This part of work can be considered as a preliminary work aiming to evaluate the thermal conductivity in supported 2D materials to achieve a fully in-situ electric and thermoelectric characterization.

1 Thermoelectric and thermal properties of 2D materials: a state of art

Two-dimensional (2D) materials, well studied in the field of nanoelectronics and optoelectronics, have revealed intriguing properties also for thermoelectric applications [84, 85, 86]. As already defined in the introduction, the efficiency of a thermoelectric device is commonly expressed by the figure of merit, defined as $ZT = S^2\sigma T/\kappa$, with S the Seebeck coefficient (also known as thermoelectric power, TEP), σ the electrical conductivity, κ the total thermal conductivity and T the absolute temperature. High ZT values are necessary to increase the energy conversion efficiency, which is a requirement generally difficult to satisfy. Enhancement of ZT, achievable by size confinement and quantum effects at the nanoscale, has been proposed in literature [87, 88, 89, 90] and experimentally proved [91, 92]. Figure 1.1 shows the progress in thermoelectric material development over time across three classes of bulk materials, i.e., inorganic semiconductors, conducting polymers and organic-inorganic hybrids, which highlight the variety and diversity of materials systems that have been identified for thermoelectricity [93]. It is worthy to notice that the highest values of ZT (shown in Figure 1.1a) are achieved in particular systems conditions, e.g., SnSe attains a ZT of 2.6 only at 923 K, while at room temperature $ZT = 0.12$ [65]. Highest room temperature ZT values (Figure 1.1b) are all below the unity and they belong to hybrid organic-inorganic compounds based on poly(3,4-ethylenedioxythiophene) or PEDOT [94].

One of the main ideas that had an enormous impact on the latest boost of thermoelectricity was the prediction that in a significant fraction of materials, phonon mean free paths tends to be an order of magnitude larger than electron mean free paths [95]. Thus, by creating devices with sizes intermediate between these two transport regimes, one could achieve some reduction in thermal conductivity without detracting too much from the electrical conductivity or Seebeck coefficient, delivering a net boost to ZT. In general, low dimensionality allows for a decoupled modification of the parameters defining ZT, opening to an increased interest in 2D layered systems for thermoelectric material science.

In this chapter, I will present a state of the art as exhaustive as possible about thermoelectric power and the thermal conductivity of the most common 2D materials, such as graphene, black phosphorus (BP), molybdenum disulfide (MoS_2) and tungsten diselenide (WSe_2). The

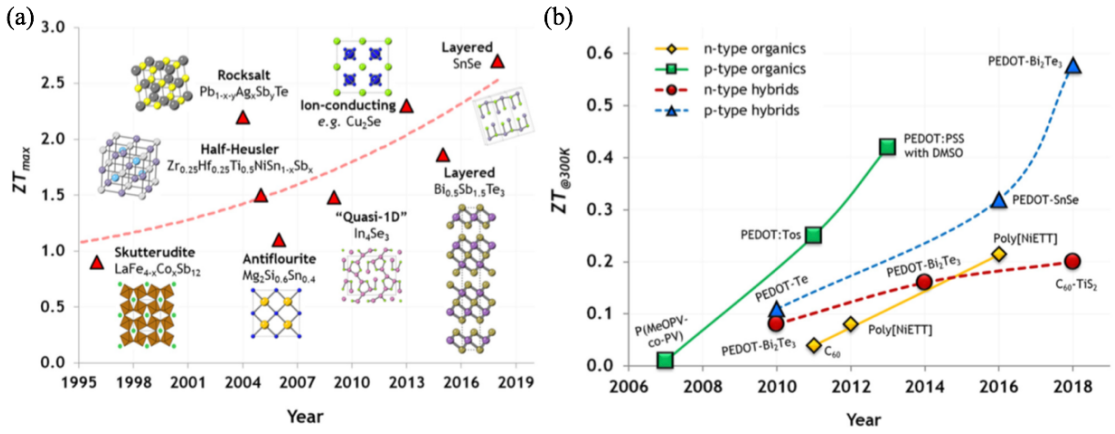

Figure 1.1 – (a) Progress of maximum figure of merit (ZT) in bulk inorganic systems achieved over time, highlighting the diversity of chemical systems and mechanisms that have shown high thermoelectric performance. (b) Progress of ZT at 300 K in p- and n-type organic materials and organic–inorganic hybrid systems over time. Figures extracted from [93].

optimization of these two parameters is the key point in which most research efforts are currently focus on. For both quantities, I will give a short insight of their theoretical derivation in the Landauer formalism, I will present the most used techniques employed in literature to measure them, and finally, I will summarize the most remarkable results.

1.1 Seebeck coefficient or thermoelectric power (TEP)

Thermoelectricity is the direct conversion between a temperature gradient and an electrical potential. When a material is subjected to a temperature gradient, as illustrated in Figure 1.2, charge carriers diffuse from the hot side to the cold side. Charge diffusion creates an electric field which in turn sustains a voltage potential across the material.

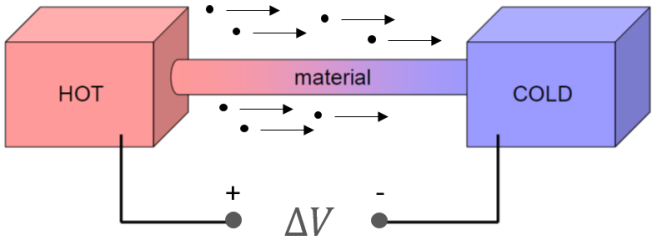

Figure 1.2 – Schematic representation of the Seebeck effect: under an applied temperature gradient charge carriers move from the hot side to the cold side generating an electrical potential.

The ratio between the developed potential ΔV and the applied temperature gradient ΔT defines the Seebeck coefficient S (also known as thermoelectric power, TEP):

$$S = -\frac{\Delta V}{\Delta T} \tag{1.1}$$

The sign of S is proportional to the sign of the charge majority carriers, i.e., positive for holes and negative for electrons. The general expression for the Seebeck coefficient, as well as the other transport coefficients, can be derived equivalently following the Landauer approach or by solving the Boltzmann transport equation (BTE). Here, I will briefly recall the derivation of the Seebeck coefficient by following the Landauer approach, which has the merit to be more intuitive and gives a clear physical insight of charge and heat transfer in nano-devices.

Let us consider a conducting object of length L through which we impose a voltage and temperature gradient, ∇V and ∇T, respectively. Charge and heat density currents, J and Q, respectively, can be written as a function of the driving fields via the response function matrix:

$$\begin{pmatrix} J \\ Q \end{pmatrix} = \begin{pmatrix} \sigma & S\sigma \\ \Pi\sigma & \kappa + \Pi S\sigma \end{pmatrix} \begin{pmatrix} -\nabla V \\ -\nabla T \end{pmatrix} \tag{1.2}$$

where σ is the electrical conductivity, S is the Seebeck coefficient, Π is the Peltier coefficient and κ is the open circuit electron component of the thermal conductivity. The derivation of the Seebeck coefficient can be easily approached by considering its relation with the Peltier coefficient given by the Kelvin relation, $\Pi = ST$. The Peltier coefficient can be extracted from Eq. 1.2 in the case of $\nabla T = 0$. In this condition, $Q = -\Pi\sigma\nabla V = \Pi J$ and thus:

$$S = \frac{\Pi}{T} = \frac{1}{T}\frac{Q}{J} \tag{1.3}$$

To evaluate the Seebeck coefficient form Eq. 1.3, we need to compute the heat density current and the charge density current. In the Landauer description, the general expression of charge current is given by:

$$I = \frac{2q}{h}\int T(E)M(E)[f_L(E) - f_R(E)]dE \tag{1.4}$$

where $T(E)$ is the transmission coefficient of an electron with energy E and $M(E)$ is the number of conduction channels. The functions $f_L(E)$ and $f_R(E)$ are the Fermi functions at the left and right electrodes, respectively, $f_{L/R}(E) = 1/[\exp((E - E_{F_{L/R}})/k_B T) + 1]$. Near equilibrium, at $\Delta T = 0$ and for a small voltage difference ΔV, $f_L(E) - f_R(E)$, which defines the window of electronic states around the chemical potential contributing to charge and heat transport, can be approximated as $-q\Delta V(df_0/dE)$, being f_0 the Fermi-Dirac distribution function at equilibrium. Thus, the charge current can be written as:

$$I = -G\Delta V \qquad G = \frac{2q^2}{h}\int T(E)M(E)\left(-\frac{df_0}{dE}\right)dE \tag{1.5}$$

where $2q^2/h$ is the quantum of charge conduction and G is the electric conductance. In the diffusive limit ($\lambda(E) \ll L$), the electron transmission is given by $T(E) = \lambda(E)/L$, where $\lambda(E)$ is

the electron mean free path (eMFP) and L is the conductor length. By considering $G = \sigma A/L$, with A the section of the conductor and σ the electrical conductivity, we can write:

$$\sigma = \int \sigma'(E)dE = \frac{2q^2}{h} \int \frac{\lambda(E)}{A} M(E) \left(-\frac{df_0}{dE}\right) dE \tag{1.6}$$

The energy dependent electrical conductivity, $\sigma'(E)$, is the fundamental quantity allowing to express all the transport coefficients, and it contains all the microscopic ingredients (eMFP, number of conduction channels) related to the electronic structure and transport properties. Given σ, we can write the charge density current as:

$$J = -\sigma \Delta V = -\left(\int \sigma'(E)dE\right) \Delta V = \int J'(E)dE \tag{1.7}$$

where $J'(E)$ is the charge carrier density at a given energy.

The heat density current can be evaluated following a similar approach. Let us consider that at a given energy E, the flux of transferred heat can be written as the amount of energy $(E - E_F)$ carried by one electron with electrical charge $-q$, multiplied by the number of flowing electrons $(J'(E)/(-q))$ and integrating over the energy. We obtain:

$$Q = \frac{1}{q}\left(\int (E - E_F)\sigma'(E)dE\right) \Delta V \tag{1.8}$$

Finally, the ratio between Eqs 1.8 and 1.7 allows to obtain the expression for the Seebeck coefficient:

$$S = \frac{1}{T}\frac{Q}{J} = -\frac{1}{qT}\frac{\int (E - E_F)\sigma'(E)dE}{\int \sigma'(E)dE} \tag{1.9}$$

Eq. 1.9 gives the expression of the Seebeck coefficient in terms of the energy dependent electrical conductivity $\sigma'(E)$. The latter can be theoretically computed by band structure calculations and by considering the main scattering mechanisms affecting charge transport. By assuming that the energy dependent conductivity is a smooth function of E around the Fermi energy E_F, the expression of $\sigma'(E)$ can be expanded and in the degenerate limit $(\frac{E_F}{k_B T} \to \infty)$ further simplified to:

$$S = -\frac{\pi^2 k_B^2 T}{3q}\left(\frac{d\ln(\sigma'(E))}{dE}\right)_{E=E_F} \tag{1.10}$$

This is the well-known Mott formula [96], widely used in literature [97]. It is worthwhile to note that the thermopower is linearly proportional to temperature and to the derivative of the

conductivity evaluated at the Fermi energy. This means that the thermopower is much more sensitive to variations of the electronic structure than the conductivity itself. This relation also illustrates that the sign of the thermopower is proportional to the sign of the charge majority carrier. In fact, experimentally the thermopower is often used to determine the carrier type in semiconducting materials with unknown doping.

When dealing with thermoelectric energy conversion processes, what actually matters for applications is the conversion efficiency, meaning the ratio between the injected heating power and the developed useful electrical power. Ideally, for a fully reversible thermodynamic cycle, the efficiency of a system working between a hot and a cold reservoir, at temperature T_h and T_c, respectively, is given by the Carnot limit:

$$\eta_{\text{Carnot}} = 1 - \frac{T_c}{T_h} \tag{1.11}$$

In practice, irreversible losses, such as Joule heating, limit the actual efficiency that can be written as

$$\eta = \eta_{\text{Carnot}} \times \frac{\sqrt{1+ZT}-1}{\sqrt{1+ZT}+T_c/T_h} \tag{1.12}$$

where ZT describes the performances of the thermoelectric system:

$$ZT = \frac{S^2 \sigma T}{\kappa} \tag{1.13}$$

From equation Eq. 1.12, it is clear that, in order to maximize the efficiency, the figure of merit needs to be maximized. However, in bulk materials, the factors entering in the definition of ZT (Eq. 1.13) are mutually coupled and it is not possible to control them individually. Figure 1.3 illustrates a semi-schematic diagram of the thermoelectric quantities entering in the figure of merit and how they evolve with the carrier concentration spanning from the semiconducting to the metallic regime. According to the Wiedemann-Franz law, increasing σ leads to an increase in the electronic contribution to κ. Moreover, the Mott formula shows that an increase of σ implies a reduction of S [98]. For these reasons, the figure of merit is reduced in a metallic material or when a semiconductor overcomes its insulating-to-metallic transition. A large Seebeck coefficient is usually found in low carrier concentration semiconductors. In this regime, the thermal conductivity is reduced and it saturates to the value given by the phonon contribution only. On the other hand, a large electrical conductivity is found in high carrier concentration metals. For this reason, the best compromise to obtain good thermoelectric materials is to use heavily doped narrow-bandgap semiconductors. In fact, in a finite bandgap semiconductor, electrons and holes can be separated to avoid the opposite contribution to the Seebeck coefficient, maintaining relatively high electrical conductivities. Doping can be

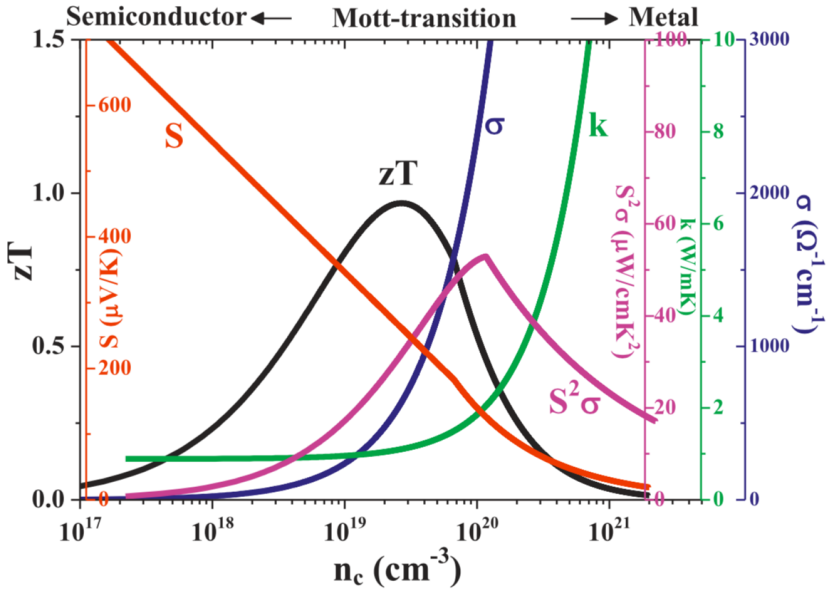

Figure 1.3 – A semi-schematic diagram of thermoelectric properties ($S, \sigma, \kappa, S^2\sigma$, and ZT) vs. carrier concentration (n_c) for semiconducting and metallic regions. The values indicated in the figure are representative of the order of magnitude of typical thermoelectric materials. Extracted from [100].

employed to produce a high density of single carrier type. Moreover, materials composed by heavy elements offer low thermal conductivities. Today, the most affirmed bulk materials for room temperature thermoelectric applications are materials such as Bi_2Te_3, SiGe and PbTe which were introduced in the 1950–1970s thanks to the advancement of semiconductor technology. These materials own figures of merit smaller than 1 [99, 100].

In the '90s, the interest for thermoelectric materials was renovated thanks to the works of Hicks and Dresselhaus [70, 71] who suggested that nanostructuring materials into lower dimensional systems should provide a much higher ZT. This enhancement in low-dimensional systems is mainly related to the enhancement of the Seebeck coefficient due to size-quantization and to the reduction of phonon thermal conductivity due to interface effects. To understand the size-quantization effect we can look at the Mott relation for the Seebeck coefficient (Eq. 1.10). By expressing the energy-dependent conductivity as $\sigma'(E) = q\,n(E)\,\mu(E)$, we obtain:

$$S = -\frac{\pi^2 k_B^2 T}{3q}\left(\frac{1}{n}\frac{dn(E)}{dE} + \frac{1}{\mu}\frac{d\mu(E)}{dE}\right)_{E=E_F} \tag{1.14}$$

where $n(E) = g(E)f(E)$ is the carrier density and $\mu(E)$ is the electron mobility. A local enhancement of the density of state $g(E)$ corresponds to an enhanced energy dependence of the charge density $n(E)$. Being $S \propto \frac{1}{n}\frac{dn(E)}{dE}$, a steeper variation in the density of states boosts the Seebeck coefficient more than the electrical conductivity even for low charge density values. Compared with three-dimensional system, in which the density of states follows a square root trend, lower dimensional systems can provide a much higher $dn(E)/dE$ dependency.

Many theoretical works have been published calculating electrical, thermal and thermoelectric properties of 2D materials [101]. As an example, ZT value at room temperature for large MoS_2 is expected on the order of 0.5 [102]. When the size of a nanomaterial is comparable or smaller than the mean free path of electrons, the transport becomes ballistic rather than diffusive. In this case, thermoelectric properties of TMDs have been investigated using ballistic transport approaches based on the electronic band structures and phonon dispersion obtained from first-principles calculations [103]. As a result, large ZT has been predicted for bidimensional TMDs with values exceeding 1 at room temperature in both n-type and p-type doping regimes, and increasing at higher temperatures, as illustrated in Figure 1.4. The highest predicted values are 2.4 for bi-layer $MoSe_2$, 2 for tri-layer WS_2 and 1.9 for bi-layer WSe_2 [104].

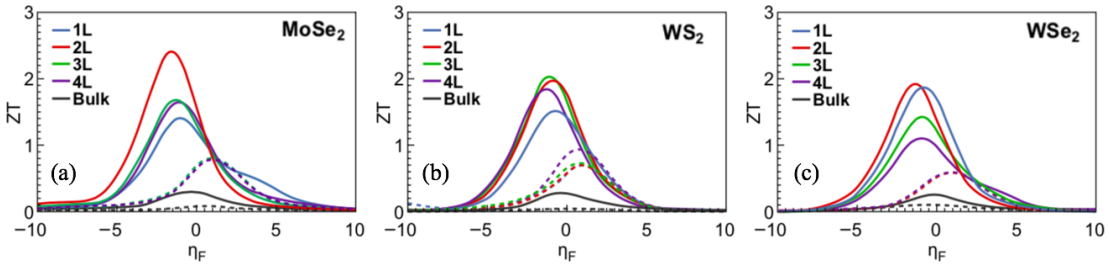

Figure 1.4 – ZT at 300 K for (a) $MoSe_2$, (b) WS_2, and (c) WSe_2 for a different number of layers as a function of the reduced Fermi energy $\eta_F (= (E - E_F)/k_B T)$. The n-type ZT is plotted with a solid line and p-type ZT with a dotted line. Extracted from [104].

1.2 Experimental methods for TEP investigation

To perform a Seebeck coefficient measurement of a given material, one needs to be able to generate and accurately measure a temperature difference along the material. Simultaneously, it is also necessary to measure the generated thermoelectric voltage, typically in the range of μV. To generate a controlled temperature gradient, several approaches are used in literature for low dimensional materials. In this paragraph, I will shortly recall the most used methods.

1.2.1 DC and AC joule heating methods

In low dimensional systems, such as nanowires, carbon nanotubes and 2D materials, one of the most used configurations is to heat the desired material through the substrate by a local micro-heater close to the material of interest but electrically disconnected from it. Figure 1.5a shows a schematic example of this approach. Due to Joule effect, a DC current I_{heater} flowing into the micro-heater generates a local temperature rise across the sample, which follows a quadratic dependence on the heating current. Being this method the chosen one for this work, a more detailed description will be given in Chapter 4. Another method often applied is the so-called 2ω method or AC method. The device configuration is exactly the same as in the previous case. However, an AC current with frequency ω is applied to the micro-heater. The temperature difference generated across the sample will be proportional to a 2ω signal, being

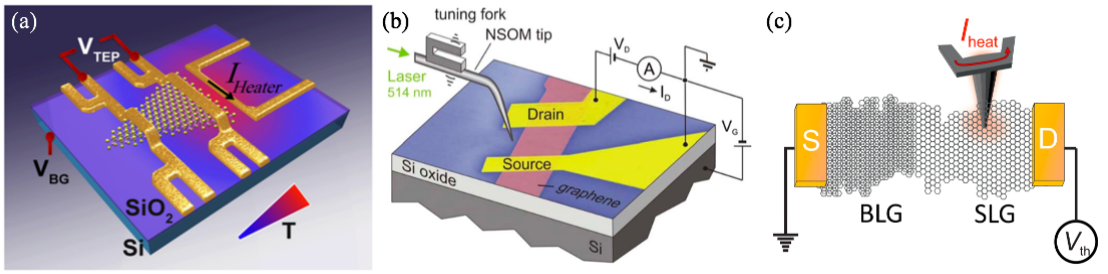

Figure 1.5 – (a) Schematics of the DC/AC method: two electrodes are used as 4-probe thermometers to determine the temperature gradient generated by the heating current flowing in a local heater and to measure the thermoelectric voltage drop. Extracted from [106]. (b) Schematics of the set-up used for SPCM: a laser light source locally illuminates the sample surface and the induced photocurrent is recorded with a lock-in amplifier as the probe tip is scanned across the sample. Extracted from [107]. (c) Schematics of the set-up used for SThM A micro-fabricated resistor incorporated to an AFM tip is used as a local heat source which is scanned over the sample with nanometer precision to record the position dependent open-circuit voltage drop on the device. Extracted from [105].

$\Delta T \propto I^2_{\text{heater}} = I^2 \sin^2(\omega t)$. A lock-in amplifier is employed to measure the ΔV signal at 2ω which is induced by the temperature difference [86].

1.2.2 Scanning photocurrent microscopy and Scanning thermal microscopy

DC and AC measurements approaches can be quite precise, but they provide the average properties of the entire device. Local measurements of thermoelectric effects are possible by scanning probe approaches such as Scanning Photocurrent Microscopy (SPCM) [75] or Scanning Thermal Microscopy (SThM) [105]. In the first case, a laser beam is focused on the sample as illustrated in Figure 1.5b and the local temperature rise is calibrated following some Raman peaks shifting as a function of the temperature and the laser power. However, this approach presents the difficulty of correctly evaluate the temperature rise in the sample if the material absorption is not known, particularly if the material is not suspended due to the dominant thermal interaction with the substrate. The temperature increase caused by the laser can only be simulated with finite element analysis and the technique is intrinsically measuring a mix of photo-thermoelectric and photovoltaic effects. On the other hand, SThM uses the typical experimental set up of an AFM where a micro-fabricated resistor is incorporated on the cantilever of the AFM probe close to the tip as shown in Figure 1.5c. When applying a high DC or AC voltage to the resistor, the tip can be heated up and used as a local heat source. This approach is compatible with the electrical gating to modulate the doping of the material and it measures the local thermoelectric properties with a very high space resolution.

1.3 Seebeck coefficient in 2D materials

In this section, I will report the most recent and remarkable results concerning measurements of the Seebeck coefficient in the most studied 2D materials such as graphene, black phosphorus (BP), molybdenum disulfide (MoS_2) and tungsten diselenide (WSe_2).

1.3.1 Graphene

Being in absolute the most studied bi-dimensional material, graphene has received large attention also for its thermoelectric properties. However, even though graphene owns excellent transport properties both in suspended or in supported configurations, its gapless band structure and its extremely high thermal conductivity make graphene a very bad candidate for thermoelectric applications. On one side, due to its strong in-plane covalent bonds [1, 108], graphene phonon mean free path can attain values of the order of hundreds of nm, resulting in extremely high values of thermal conductivity of the order of 4000 - 5000 W/mK in suspended configurations [109] or 600 W/mK in the SiO_2-supported case [110]. The large phonon mean free path results in ballistic phonons transport easily attained in particularly small samples [111], resulting in very efficient in plane heat transport and making it difficult to maintain an in-plane temperature gradient. However, big efforts are done to reduce the thermal conductivity by device or surface engineering [73, 112, 113]. More details will be given in Chapter 5. On the other hand, due to the gapless nature of graphene band structure, it is difficult to isolate the opposite contributions of electrons and holes in the Seebeck coefficient. However, the strong energy-dependence of the electrical conductivity $\sigma(E)$ close to the charge neutrality point (CNP) allows to obtain a finite S value.

The first measurement of Seebeck coefficient in graphene was published in 2009 by Zuev et al. [114]. Single layer graphene was exfoliated on a 300 nm-thick SiO_2 substrate with a heavily doped Si back gate for the carrier density modulation. The SEM image of the discussed sample is reported in the upper inset of Figure 1.6a, where the electrical connections are visible. Mainly, a local heater is used to create a temperature gradient and two thermometers are employed

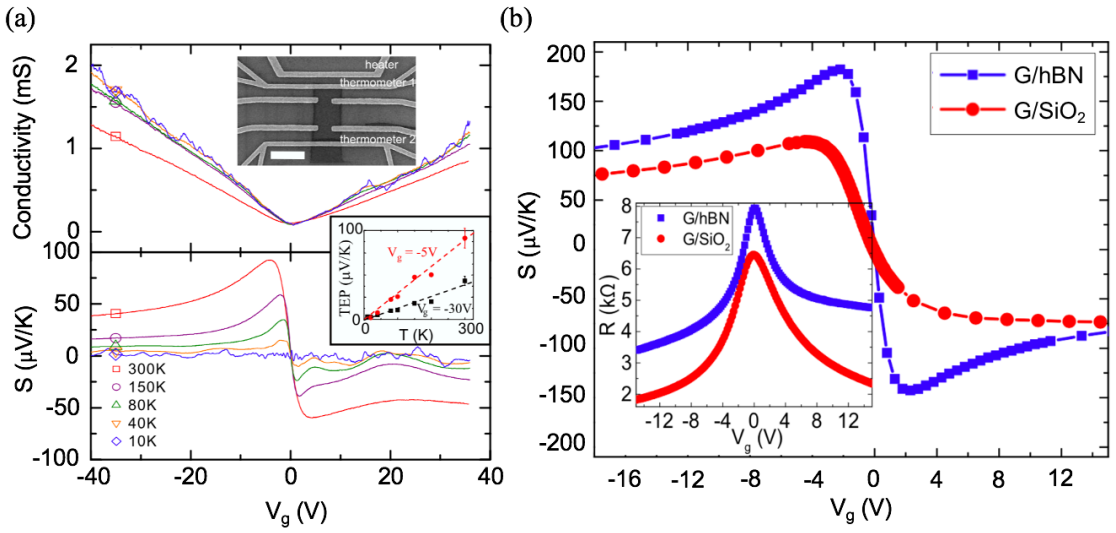

Figure 1.6 – (a) Conductivity and TEP of a graphene sample as a function of V_G for different temperatures. (Upper Inset) SEM image of a typical device, the scale bar is 2 μm. (Lower Inset) TEP values taken at V_G = -30 V (circle) and -5 V (square). Dashed lines are linear fits to the data. Extracted from [114]. (b) Measured Seebeck coefficient in graphene/hBN (blue) and graphene/SiO_2 (red) devices as function of back gate at 290 K. Extracted from [38].

to measure the in-plane temperature difference along the sample. The Seebeck coefficient is plotted as a function of the gate voltage and it shows a room temperature peak reaching a value of ~ 80 μV/K before it vanishes in correspondence of the charge neutrality point (CNP). As expected from the conductivity measurement, the sign of the Seebeck coefficient changes as the gate voltage crosses the CNP, indicating the change of sign of the majority charge carriers.

Thermoelectric performances of graphene can be significantly improved by using hexagonal boron nitride (hBN) substrate instead of SiO_2. In fact, it has been demonstrated that SiO_2 substrates have surface charge states and impurities that cause Coulomb scattering limiting the mobility and introducing relevant potential fluctuations in graphene/SiO_2 devices [33, 115, 116]. Being atomically flat, hBN reduces the potential fluctuations and increases the graphene mobility. Figure 1.6b shows the comparison between the Seebeck coefficient measured in a graphene/hBN and a graphene/SiO_2 device performed more recently by Duan et al. [38]. The thermoelectric power follows the same trend for both devices and the change of sign at the charge neutrality point. However, in the case of hBN-supported graphene, the Seebeck coefficient shows a sharper peak and almost a double absolute value, reaching the highest value of 182 μV/K.

Surface charge states and potential fluctuations have been proved to strongly reduce the graphene Seebeck coefficient by using Scanning Thermal Gate Microscopy (STGM) allowing to analyze the spatial variation of the thermoelectric power. Figure 1.7a illustrates the Seebeck coefficient topography measured by Harzheim et al. [105] in a rectangular single layer graphene sample around the charge neutrality point. The high local variation with changing polarity is caused by charge puddles. Maximum values of ~ ± 500 μV/K are recorded in some points of the channel. However, these values are local fluctuations rather than a representation of the global Seebeck coefficient. The latest is measured on the order of ~ ± 40 μV/K.

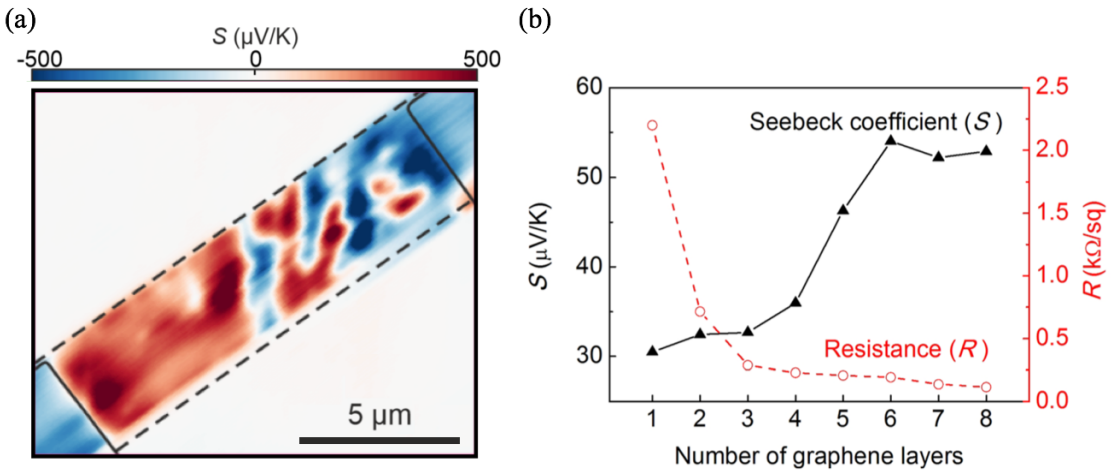

Figure 1.7 – (a) Seebeck coefficient topography in a rectangular single layer graphene sample recorded by Scanning Thermal Gate Microscopy. Extracted from [105]. (b) Layer-dependent Seebeck coefficient (black triangles, solid curve) and resistance (red circles, dotted curve) in graphene. Extracted from [117].

In the attempt to maximize the power factor ($PF = S^2\sigma$), some studies have been carried out to

investigate the dependence of the Seebeck coefficient in graphene as function of the number of layers. It is known, in fact, that the electrical conductivity increases with the number of layers. In the work of Li et al. [117], a strong layer-dependence of the Seebeck coefficient of CVD grown graphene is demonstrated. As illustrated in Figure 1.7b, the thermoelectric power increases with increasing thickness to reach a peak value at six layers that is ~ 80% higher than monolayer and ~ 300% higher than graphite, unlike the monotonic decrease in electric resistance. The measurements are performed without the application of any gate voltage and the positive sign of the Seebeck coefficient is related to ambient environment p-type doping due to the adsorption of oxygen and water molecules which is common in graphene [118, 119].

1.3.2 Black Phosphorus

Black phosphorus (BP) is a layered elemental semiconducting material with a direct band gap of ~ 0.3 eV. A BP single layer possesses a honeycomb structure, where each phosphorus atom is covalently bonded with other three adjacent phosphorus atoms [120, 121]. The structure of BP is anisotropic with zigzag and armchair directions, which results in anisotropic transport properties [122]. As graphene, the relatively weak van der Waals force between its layers allows to obtain nanometer-thick BP layers via mechanical exfoliation. Due to its high field effect mobility [123, 124, 125] as well as its photonic [126] and ambipolar transport properties [127], black phosphorus has lately received renewed attention. Moreover, BP thin films or its monolayer, phosphorene, have been theoretically predicted to be promising thermoelectric materials [128, 129, 130]. However, BP is also well known for being unstable in ambient environment.

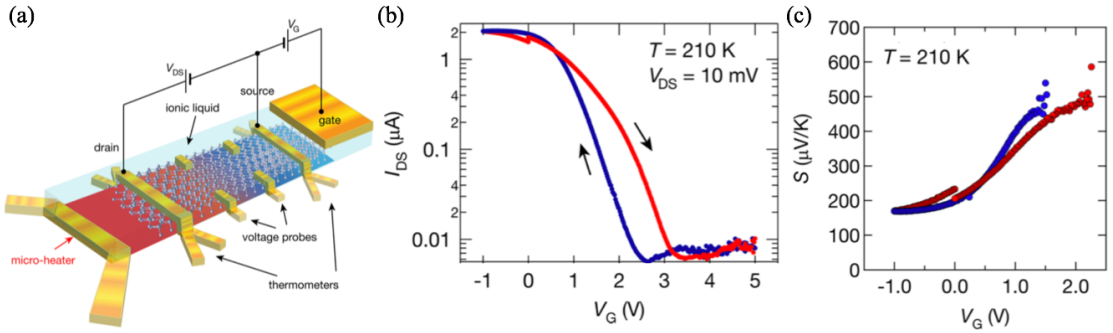

Figure 1.8 – (a) Conceptual image of a BP-EDLT for thermoelectric measurements. (b) Source-drain current as a function of gate voltage at T = 210 K and V_{DS} = 10 mV. (c) Tunable thermoelectric power as a function of gate voltage at T = 210 K. Extracted from [131].

Saito et al. [131] have reported the gate-tuning of thermoelectric power in a 40 nm-thick black phosphorus crystal flake. The use of an electric-double-layer transistor (EDLT) configuration [132], which is schematically represented in Figure 1.8a, allows the authors to apply a large electric field of over 10 MV/cm at a liquid/solid interface, resulting in sharp band bending. A droplet of ionic liquid (DEME-TFSI) is employed to cover both the channel area of the BP thin flake and the gate electrode. A temperature gradient is generated, via Joule effect, by the

current flowing in a local micro-heater. The thermoelectric power was measured with two extra voltage probes. In this measurement set-up, all the electrodes (Cr/Au) including the heater and the thermometers are covered by 20 nm-thick SiO_2 films in order to be electrically disconnected from the ionic liquid. The BP-EDLT exhibits a reversible p-type transistor behavior, as illustrated in Figure 1.8b. The arrows indicate the direction of gate voltage V_G scan. At V_G = 0 V, the BP-EDLT is in the ON-state configuration, which is due to the large amount of hole carriers unintentionally doping the BP crystal. While a negative V_G further accumulates hole carriers, a positive V_G causes a depletion of bulk hole carriers to the opposite direction from the surface, leading to an insulating state (OFF-state). As shown in Figure 1.8c, the ion-gated BP reached values of thermoelectric power S of ~ 500 μV/K at 210 K in the hole depleted state, which are higher than the reported bulk crystal value of 340 μV/K at 300 K [133].

One of the first studies of Seebeck coefficient in Black Phosphorus as function of temperature was carried out by Choi et al. [134]. In order to characterize the BP, they exfoliated thin flakes on 300 nm-thick SiO_2 substrate, with a back Si gate control. The electrically contacted device was coated with a PMMA layer to protect the BP and to minimize contamination from moisture absorption under ambient conditions. The experimental results reported in Figure 1.9 refer to a 30 nm-thick black phosphorus. The authors also investigated thinner samples of 10 and 8 nm, since in relatively thick flakes the applied gate could affect only the bottom layers, resulting in a lower boundary estimation for S. However, thinner samples are more sensitive to defects and charge impurities at the interface, leading to a suppression of the thermopower. Figure 1.9a shows the two-probes electrical conductance G measurement as a function of back-gate voltage at different temperatures. The device shows a clear p-type character. The detailed analysis of the T-dependent conductance of the BP device reveals that the charge-transport mechanism changes from the thermally activated transport process (for T > 150 K) to a 2D Mott's variable range hopping (VRH) process with lowering temperature.

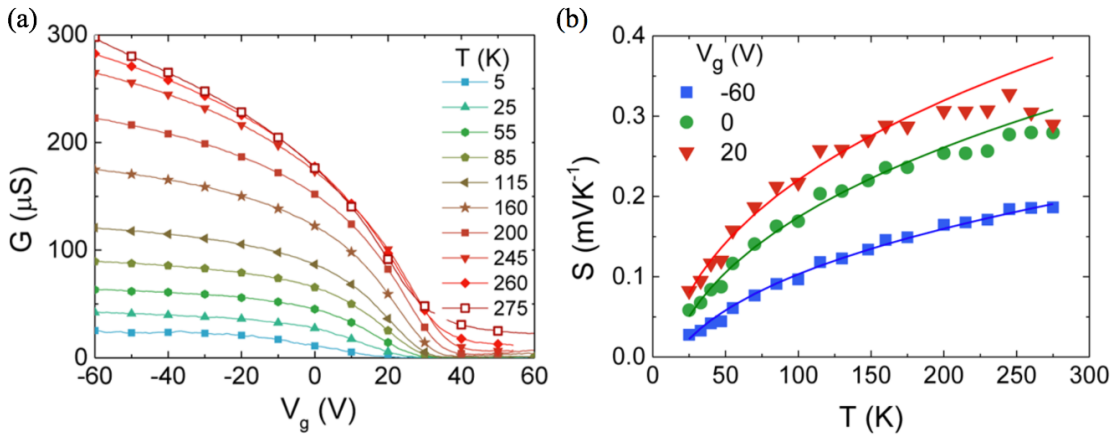

Figure 1.9 – (a) Conductance as a function of the gate voltage for different temperatures. G was obtained by the two-probe measurement. (b) Seebeck coefficient (scattered points) as a function of T for various V_G. The solid curves are fit-results with a relation of $S \propto T^{1/3}$ based on the 2D Mott's VRH model. Extracted from [134].

This indicates that, for $T > 150$ K, the contribution to the electrical current is dominated by charge transport in the BP channel through localized charge states rather than the Schottky or tunnel barriers forming at the metal contact regions. On the other hand, the transport mechanism in the BP channel appears to deviate from the thermally activated process for $T < 150$ K. In this case, the BP channel acts as multiple localized quantum dots. This behavior is explained by the authors as originating from local trap sites at the SiO_2-BP interface. In agreement with the proposed 2D Mott's VRH transport model [135], the Seebeck coefficient is expected to follow a $T^{1/3}$ dependence. Figure 1.9b shows the experimental values of S (points) at different gate voltages. The solid lines in the plot represent the $T^{1/3}$ fit based on the Mott's VRH model. The deviation from the $T^{1/3}$ dependence for $T > 200$ K may be related to thermionic hopping process over the Schottky barriers to the channel. Independently on the detailed transport mechanism playing a role, the reported values of Seebeck coefficient are particularly high, with the highest values of the order of 0.3 mV/K.

1.3.3 Transition metal dichalcogenides

Transition metal dichalcogenides are a large family of 2D semiconducting materials generally characterized by a heavy transition metal atom (Mo, W, etc.) and two chalcogen atoms (S, Se, or Te). The experimental research on the thermoelectric properties of this family of materials has been focused mostly on molybdenum disulfide (MoS_2) as n-type semiconducting material. Some work has been carried out also on tungsten diselenide (WSe_2) as p-type semiconductor. TMD materials show great potential for thermal management and thermoelectric energy conversion due to their advantageous combination of electrical and thermal transport properties. Significantly large values of figure of merit are expected in TMD-based devices.

Molybdenum disulfide

The first measurement of thermoelectric effect on exfoliated MoS_2 monolayer was performed by Buscema et al. [75]. By means of scanning photocurrent measurements with a continuous wave green laser excitation ($\lambda = 532$ nm $h\nu = 2.33$ eV), they were able to record the spatially resolved generated photocurrent. Their device and measurement technique are illustrated in Figure 1.10a. The central and larger electrode is connected to a current-to-voltage amplifier while all the other electrodes are grounded. The intensity of the reflected laser light and the photocurrent generated in the device are simultaneously recorded at every position during the scanning of the laser spot. The superposition of the two data sets allows to accurately determine where the photocurrent is generated. A current is recorded flowing through the device at zero bias, even when the laser spot is placed inside the area of the electrodes. To exclude the generation of electron-hole pairs that would simply imply a photo-generated current, the same experiment has been carried out with red light illumination ($\lambda = 750$ nm $h\nu = 1.65$ eV). The observed current cannot be generated with photon energies lower than the MoS_2 energy gap (1.8 eV) and the phenomenon was explained as a photo-thermoelectric effect. As a result of the light absorption, a temperature gradient is generated across the MoS_2-metal

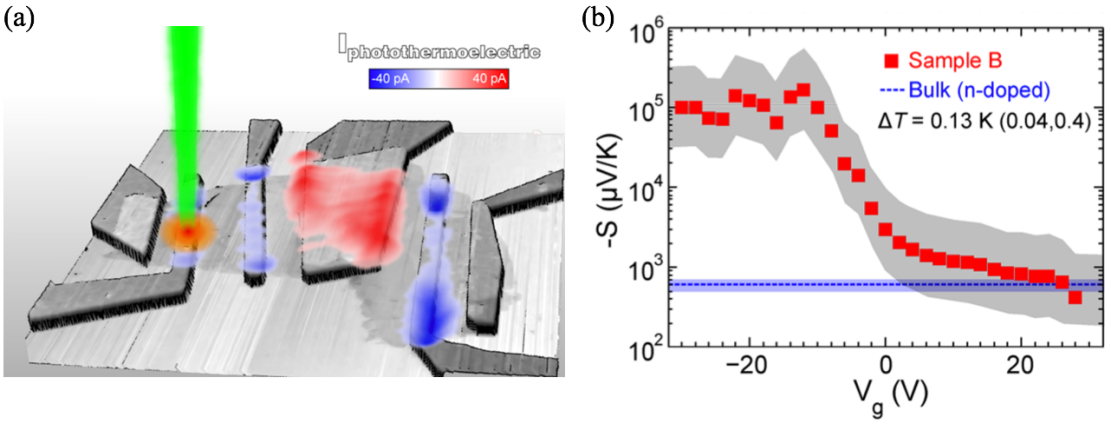

Figure 1.10 – (a) Illustration of photocurrent generation due to thermoelectric effect in MoS_2 monolayer. (b) Estimated Seebeck coefficient versus gate voltage. The gray shaded area is the uncertainty due to the incertitude on the estimation of the temperature gradient. The dashed light blue line corresponds to the Seebeck coefficient value of bulk MoS_2 with experimental uncertainty (shaded light blue area). The saturation effect at negative gate values is due to the high resistance of the device, leading to a current value below the noise level of the current-to-voltage amplifier. Extracted from [75].

junction, that translates into a thermoelectric voltage. The thermoelectric voltage can be expressed as a function of the thermopower of the MoS_2 and of the Ti/Au metallic contacts:

$$\Delta V = (S_{MoS_2} - S_{Ti/Au})\Delta T \tag{1.15}$$

The Seebeck coefficient of Ti/Au is negligible with respect to that of MoS_2 and no gate dependence is expected. Figure 1.10b shows the evaluated thermoelectric power of single layer MoS_2 as a function of the applied gate voltage, in comparison with a bulk sample. To evaluate the temperature gradient, the authors have performed a finite element modeling (FEM) analysis taking into account absorption and reflection of the laser illumination. They found a large Seebeck coefficient ranging between -200 and -1500 μV/K in the conducting state and between -30 and -300 mV/K in the OFF-state. This large Seebeck coefficient estimation could be the result of the generation of hot electrons which are not taken into account in the FEM simulation. If this is the case, the temperature gradient could have been underestimated. In fact, the presence of hot electrons, which are carriers not in thermal equilibrium with phonons, implies that the extracted ΔT would be a lower boundary estimation, leading to an over estimation of the Seebeck coefficient. Buscema's work has surely the merit of being among the first works revealing high thermoelectric power values in TMDs, and it has also revealed the wide tunability of the Seebeck coefficient which is a unique property related to 2D materials.

Wu et al. [106] have also measured a large and tunable Seebeck coefficient in MoS_2. Their research is focused on the electric and thermoelectric measurements of CVD-grown single layer MoS_2 on SiO_2 substrates over a wide temperature range (20 K - 300 K) by employing micro-fabricated heaters and thermometers. They have observed large TEP of ~ 30 mV/K

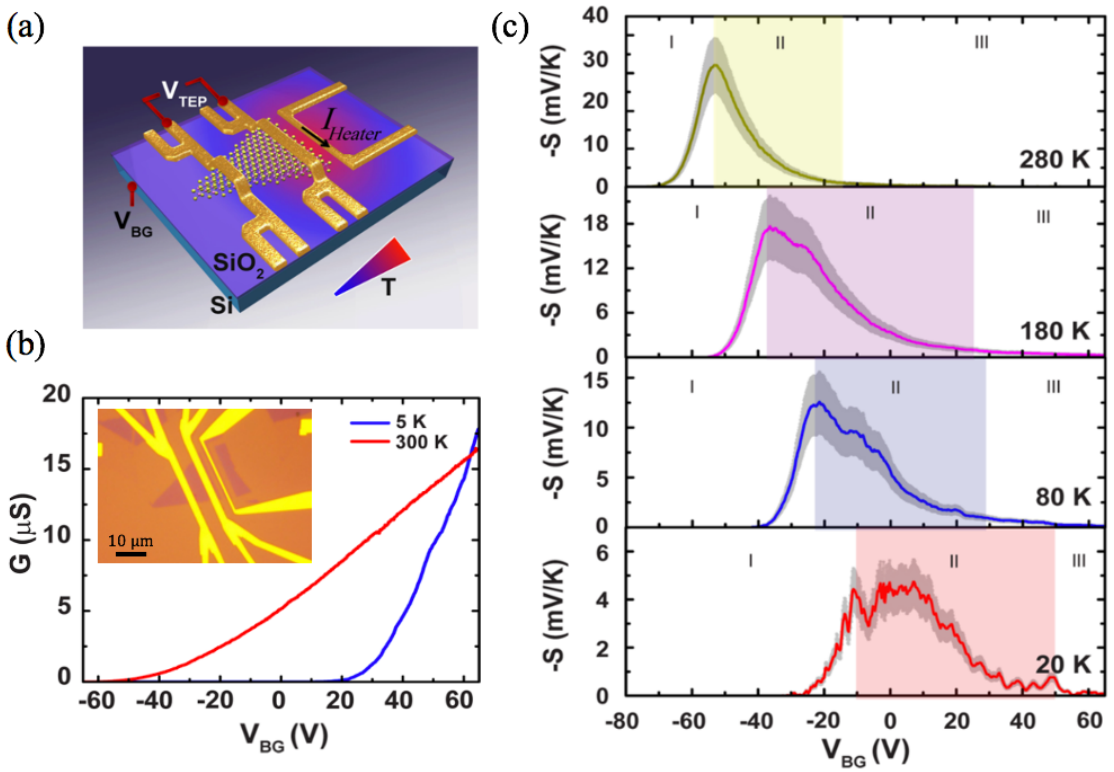

Figure 1.11 – (a) Schematic of the device with electrical connections for electric and thermoelectric measurements. (b) Electrical transport characteristics of the single layer CVD MoS_2 measured at 5 and 300 K. The inset shows an optical image of the contacted device. (c) Thermopower as a function of back gate voltage at different temperatures. The gray shaded region indicates the measurement uncertainty. Three distinct regimes (I, II, III) are identified, shifting with temperature. Extracted from [106].

with a gate-modulation which is greatly enhanced in the low carrier density region. The measurements have been performed after a vacuum annealing that has been proved to change the doping of the MoS_2 by shifting the Fermi level toward the conduction band and also to reduce the contact resistance significantly. A schematic layout of the device is shown in Figure 1.11a. Two electrodes contacting the single layer CVD MoS_2 flake are used as 4-probe thermometers to determine the heat gradient applied by the heating current I_{heater} and also to measure the thermoelectric voltage drop. A back-gate voltage V_{BG} is applied to tune the carrier density of the device. The electrical transport characteristics of the sample, measured at 5 K and 300 K, are reported in Figure 1.11b, showing the electrical conductance G of the system measured as function of the gate voltage. The inset shows an optical image of the contacted device. Figure 1.11c displays the gate dependence of the Seebeck coefficient at different temperatures. The maximum value for the TEP is obtained at 280 K and it reaches the high value of 30 mV/K. In the range of back gate voltages studied, Wu et al. identify three distinct regimes (I, II, III). When the back-gate voltage is at high positive values (III), the Seebeck coefficient shows very small values in the range of 1-10 μV/K, which is comparable to what can be typically measured in metals. In fact, if compared with the conductance measurement in Figure 1.11b, this indicates that the system approaches the metallic regime. As the back-gate

voltage is reduced, the Fermi level is shifted into the bandgap and MoS_2 undergoes a transition from a metallic to an insulating behavior (region II). The carrier density and the conductance decrease as expected for a semiconductor. At the same time, the TEP starts to increase as expected from Eq. 1.14 and finally reaches the maximum value. This is followed by a sharp decrease in TEP as the back-gate voltage is swept to higher negative values (region I). This sharp decrease coincides with the OFF-state in MoS_2.

Even if those results are quite promising, further investigations are required to prove the real origin of the enhanced Seebeck in MoS_2. In fact, CVD-grown MoS_2 has been known to have a higher density of sulfur vacancies compared to mechanical exfoliated flakes, resulting in lower mobility. The reported metallic values of S of some μV/K in the MoS_2 ON-state would indicate that the Fermi level is well inside the conduction band, which is unlikely even for degenerately doped semiconductors.

Recent and more accurate measures on MoS_2 have revealed a Seebeck coefficient on the order of hundreds of μV/K [136, 137]. In particular, Kayyalha et al. [136] studied the correlation between the number of layers and the electric and thermoelectric properties in MoS_2 (schematic of the device shown in Figure 1.12a). As illustrated in Figure 1.12b, they proved that the electrical conductivity increases when reducing the MoS_2 thickness down to two layers. On the other hand, they measured a much weaker dependence of S on the channel thickness. In fact, even if the single-layer flake gives notably smaller Seebeck coefficient ($\sim$ 200 μV/K) compared to thicker flakes ($\sim$ 400 - 500 μV/K), S remains almost constant for samples thicker than the monolayer, showing a slight peak at four layers (Figure 1.12c). The significant drop in Seebeck coefficient in the single-layer MoS_2 compared to double-layer MoS_2 is explained as arising from different energy dependencies of the electron mean-free-path for backscattering (constant for the single layer and linear for the double layer).

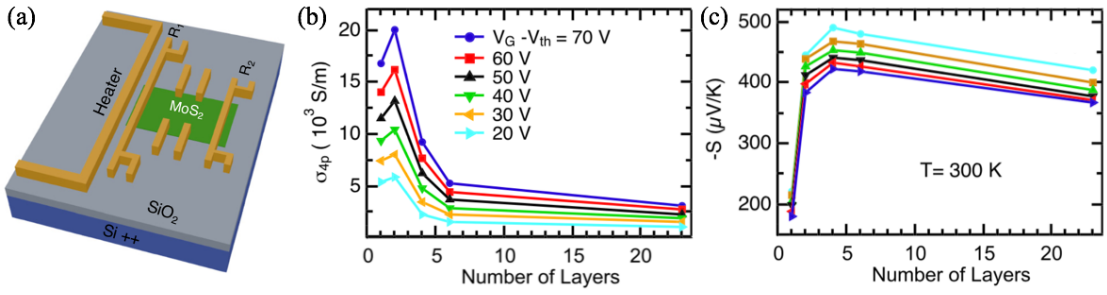

Figure 1.12 – (a) Schematic of the device with electrical connections for electric and thermoelectric measurements. (b) Four-probe electrical conductivity σ_{4p} and (c) Seebeck coefficient $-S$ of MoS_2 as functions of the thickness (number of layers) measured at different $V_G - V_{th}$ values. The electrical conductivity shows a maximum at two layers, while the Seebeck coefficient shows a slight peak at four layers. Extracted from [136].

Tungsten diselenide

Tungsten diselenide (WSe_2) is one of the more studied 2D material among the TMDs because of its pronounced p-type transport properties. However, if one can find in literature plenty of

works about transport and optical properties in WSe_2, very little has been done concerning the thermoelectric properties of this material, although it is a very promising material for TE applications. In fact, WSe_2 has a very low in-plane thermal conductivity (~ 1-2 W/mK) that has been theoretically and experimentally proved [81, 82]. This is one of the reasons why this material has been chosen as the main material of investigation for this PhD work.

Yoshida et al. [79] have studied a mechanically exfoliated three-layer WSe_2 flake using an organic ionic liquid (DEME-TFSI) as gate dielectric, which has already been introduced before for the Black Phosphorus [131, 132]. This very efficient gating approach has allowed to access both electrons and holes conducting regimes. In their device, as illustrated in Figure 1.13a, the temperature gradient is established by Joule heating by applying a DC voltage (V_{Heat}) on the heater electrode, electrically disconnected from the 2D material. Two 4-probe (Ti/Au) metallic nanowires, Th_1 and Th_2, are used as local thermometers to measure the ΔT across the three-layer WSe_2 flake and they are also employed to determine the ΔV. Figure 1.13b summarizes the gate dependence of the sheet conductance and Seebeck coefficient measured at T = 300 K. The arrows indicate the direction of V_G scan. In agreement with the ambipolar gate dependence, the positive and negative values of S indicate that holes and electrons are the majority charge carriers, respectively. The maximum value of Seebeck coefficient reached both in the hole and electron transport regimes is on the order of 300 μV/K.

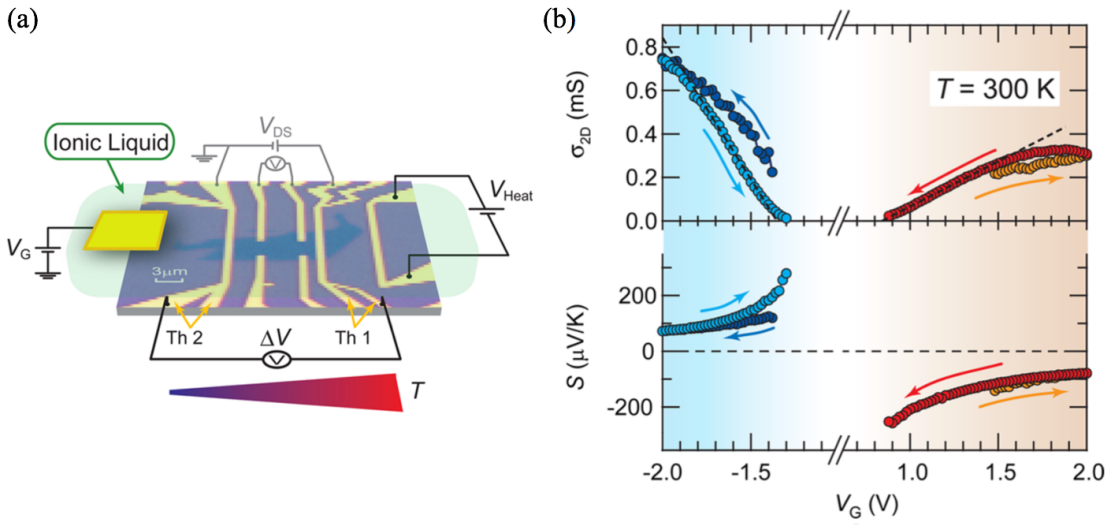

Figure 1.13 – (a) Schematic of the EDLT-based three layer WSe_2 sample with electrical connections for electric and thermoelectric measurements. (b) Gate voltage dependence of sheet conductance and Seebeck coefficient at T = 300 K. The arrows indicate the direction of V_G scan. Extracted from [79].

The same value is confirmed by the work of Pu et al. [80] which studied the thermoelectric response of large-area CVD-grown WSe_2 monolayers. As in the previous case, they use an electric double-layer transistors (EDLTs) configuration to achieve a high doping control. The schematic representation of their device is illustrated in Figure 1.14a. In order to extract the Seebeck coefficient of their monolayers, the fabricated EDLTs were placed between two Peltier modules, one used for heating and the other for cooling. Two thermocouples (K type) were

placed on both edges of the channel to monitor the temperature difference (ΔT). A reference electrode was employed to estimate the voltage drop on the WSe_2 interface. Figure 1.14b shows the measured Seebeck coefficient as a function of $V_R - V_{th}$ for three WSe_2 samples. V_R is the voltage applied to the reference electrode and V_{th} is the threshold voltage. The obtained maximum $|S|$ value reached 380 μV/K for the p-type and 250 μV/K for the n-type WSe_2. The different shape of S among the three devices the authors have measured is attributed to a different filling of the conduction and valence band.

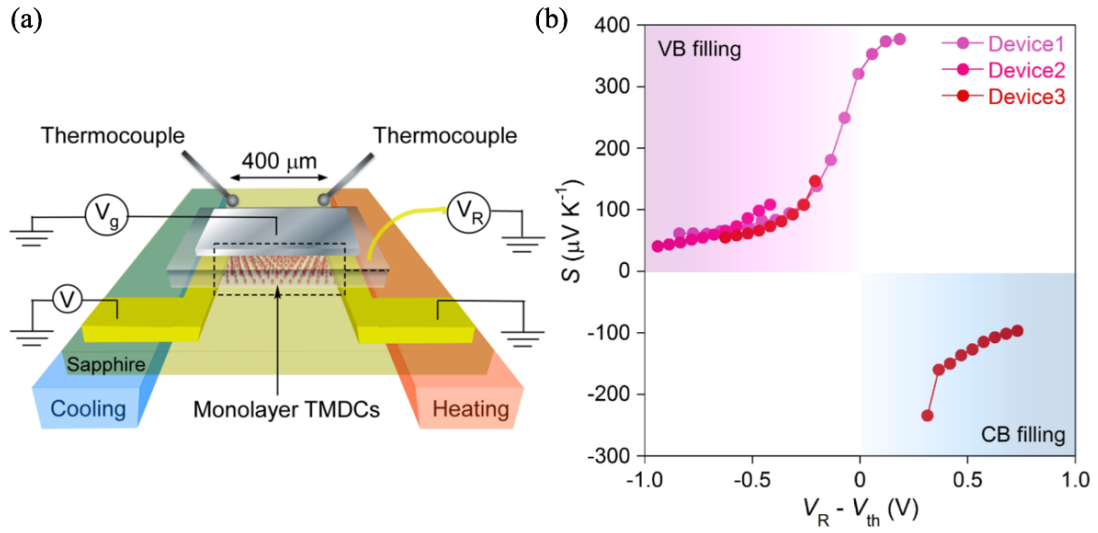

Figure 1.14 – (a) Schematic representation of the large-area CVD-grown EDLT-based WSe_2 monolayer for thermopower measurements. (b) Seebeck coefficient as a function of $V_R - V_{th}$ for three WSe_2 devices. V_R is the voltage applied to a reference-electrode and V_{th} is the threshold voltage. Extracted from [80].

The thermoelectric properties of WSe_2 have been also investigated in polycrystalline WSe_2 synthesized on a large scale by thermally assisted conversion (TAC) [138]. This approach allows to produce continuous films of controlled thickness with a polycrystalline morphology. Moreover, the growth of the films takes place at a temperature of 600°C, which is very low compared to that required for CVD synthesis. As illustrated in Figure 1.15a, a thin W film is deposited on pre-patterned geometry on a SiO_2 substrate and it is subsequently converted to WSe_2 in selenium vapor at 600°C. Raman spectroscopy has been employed to confirm that the W film was successfully converted to WSe_2. However, due to the fabrication procedure, the material has an incomplete crystal structure compared to the bulk single crystal and it presents a high defect density. Due to the polycrystalline morphology, the charge transport properties show a low ON/OFF ratio and a weak gate modulation, as visible in Figure 1.15b. These experimental evidences are attributed to the defects that acts as dopants. To characterize the thermoelectric properties of the sample, a temperature gradient is generated by local Joule heating. As illustrated in Figure 1.15b, the maximum value of reported Seebeck coefficient is ~ 60 μV/K which is about five times lower than the previously reported Seebeck coefficient values for WSe_2.

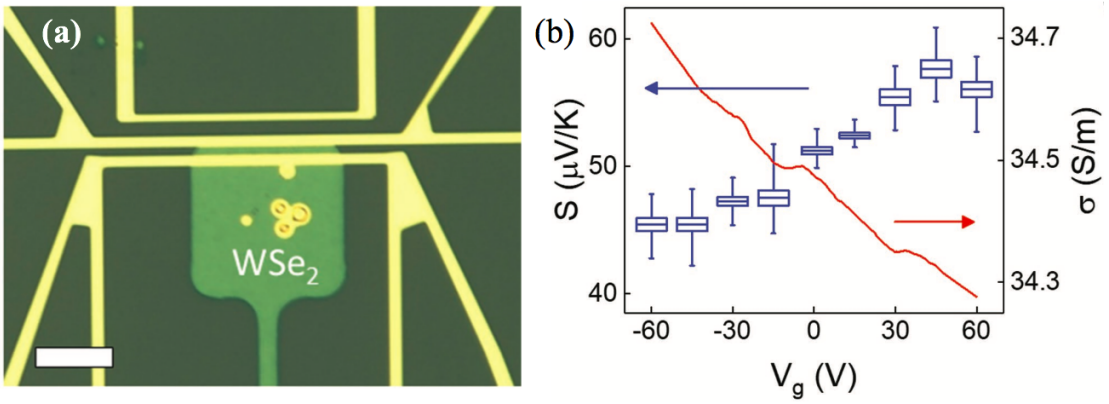

Figure 1.15 – (a) Optical microscope image of the device (the scale bar is 20 μm). (b) Gate-voltage-dependent Seebeck coefficient (S, left y-axis) and electrical conductivity (σ, right y-axis). Extracted from [138].

1.4 Heat transport in 2D materials

Thermal properties of 2D materials can be understood by studying the lattice vibrational modes of the material. In fact, while in metals electrons carry most of the heat, in semiconductors and insulators, lattice vibrations (or phonons) are mostly responsible for heat transfer. The description of phonons in solids can be done in an equivalent way to that of electrons. Inspired by the Landauer approach for the electron transport description, a general mathematical model for phonon transport can be developed. Let us consider phonon heat transfer in a conductor. The Landauer formula for the heat current can be written by replacing in Eq. 1.4 the electron charge by the phonon energy $\hbar\omega$ and the Fermi-Dirac distribution by the Bose-Einstein distribution function $n(E) = 1/[\exp(\hbar\omega/k_BT) - 1]$ as follows:

$$I_Q = \frac{1}{h}\int \hbar\omega T_{ph}(\hbar\omega) M_{ph}(\hbar\omega)[n_L(\hbar\omega) - n_R(\hbar\omega)]d(\hbar\omega) \tag{1.16}$$

where $T_{ph}(\hbar\omega)$ is the transmission coefficient of phonons with energy $\hbar\omega$ and $M_{ph}(\hbar\omega)$ is the number of phonons conduction channels. Near equilibrium, for a small temperature difference ΔT, $n_L(\hbar\omega) - n_R(\hbar\omega)$, which defines the energy window over which the thermal current flows, can be approximated by $-\hbar\omega/T(-dn_0/d(\hbar\omega))\Delta T$, where $n_0(\hbar\omega)$ is the Bose-Einstein distribution function at equilibrium. Thus, the heat current becomes:

$$I_Q = -K_L\Delta T \qquad K_L = \frac{\pi^2 k_B^2 T}{3h}\int T_{ph}(\hbar\omega) M_{ph}(\hbar\omega)\left[\frac{3}{\pi^2}\left(\frac{\hbar\omega}{k_BT}\right)^2\left(\frac{-dn_0}{d(\hbar\omega)}\right)\right]d(\hbar\omega) \tag{1.17}$$

where $\pi^2 k_B^2 T/3h$ is the quantum of heat conduction and K_L is the phonon thermal conductance. In the diffusive limit ($\lambda_{ph}(\hbar\omega) \ll L$), $T_{ph}(\hbar\omega) = \lambda_{ph}(\hbar\omega)/L$, where $\lambda_{ph}(\hbar\omega)$ is the phonon mean free path (phMFP) and L is the conductor length. By considering $K_L = \kappa_L A/L$, with A the section of the conductor and κ_L the thermal conductivity, we can write:

$$\kappa_L = \frac{\pi^2 k_B^2 T}{3h} \int \frac{\lambda_{ph}(\hbar\omega)}{A} M_{ph}(\hbar\omega) \left[\frac{3}{\pi^2} \left(\frac{\hbar\omega}{k_B T} \right)^2 \left(\frac{-dn_0}{d(\hbar\omega)} \right) \right] d(\hbar\omega) \tag{1.18}$$

Eq. 1.18 recalls Eq. 1.6 for the electrical conductivity, emphasizing the one-to-one correspondence between phonon and charge transport. One important difference is related to the band-width (BW) of the dispersion relations. While for electrons the BW $\gg k_B T$, allowing to consider only electronic states close to the band edges, for phonons the BW $\sim k_B T$ and all phononic states contribute to thermal transport. Simplified approximations, such as the linear dispersion in the Debye model, are only valid for small wave number at low temperature.

As shown in Eq. 1.18, the phonon mean free path is a relevant parameter determining phonon thermal transport. The phMFP is defined as

$$\lambda(\hbar\omega) = v(\hbar\omega)\tau(\hbar\omega) \tag{1.19}$$

where $v(\hbar\omega)$ is the phonon velocity determined by the dispersion relation and $\tau(\hbar\omega)$ is the average phonon scattering time. As electrons, phonons are scattered by defects, other phonons, surface and lateral boundaries, and by electrons. The total phonon scattering time can be expressed, in accordance to the Matthiessen's rule, as:

$$\frac{1}{\tau(\hbar\omega)} = \frac{1}{\tau_D(\hbar\omega)} + \frac{1}{\tau_B(\hbar\omega)} + \frac{1}{\tau_U(\hbar\omega)} \tag{1.20}$$

where $1/\tau_D(\hbar\omega)$ is the rate of impurity scattering ($\propto \omega^4$), $1/\tau_B(\hbar\omega)$ is the rate of boundary scattering ($\propto v(\hbar\omega)/L$), and $1/\tau_U(\hbar\omega)$ is the rate of Umklapp scattering ($\propto T^3$). Among all the scattering processes, the Umklapp, which is the phonon-phonon scattering without momentum conservation, is the one mainly affecting the thermal conductivity, and it reduces κ_L as the temperature rises. At low temperature, the major phonon scattering mechanism is scattering by defects, which is temperature independent. In this case, the temperature dependence of thermal conductivity is given by the number of populated phonon modes.

The phonon velocity can be determined from the phonon dispersion relation. Figures 1.16a and 1.16b show the phonon band diagram for two of the mainly studied 2D materials, graphene and MoS_2, respectively. For both materials, the phonon dispersion relation, $E = E(q)$ (with q the phonon wave vector), displays typical longitudinal (L) modes corresponding to atomic displacements along the wave propagation direction (compressive waves), and transverse (T) modes corresponding to in-plane displacements perpendicular to the propagation direction (shear waves). The uniqueness of 2D materials lies in the presence of out-of-plane atomic displacements, also known as flexural (Z) phonons, that play a fundamental role. The contribution from different phonon modes to the thermal conductivity of MoS_2 is quite different from that in graphene and it results from the sandwiched X-M-X structure of monolayer MoS_2 and the much weaker Mo-S bonds with respect to the strong C-C bonds.

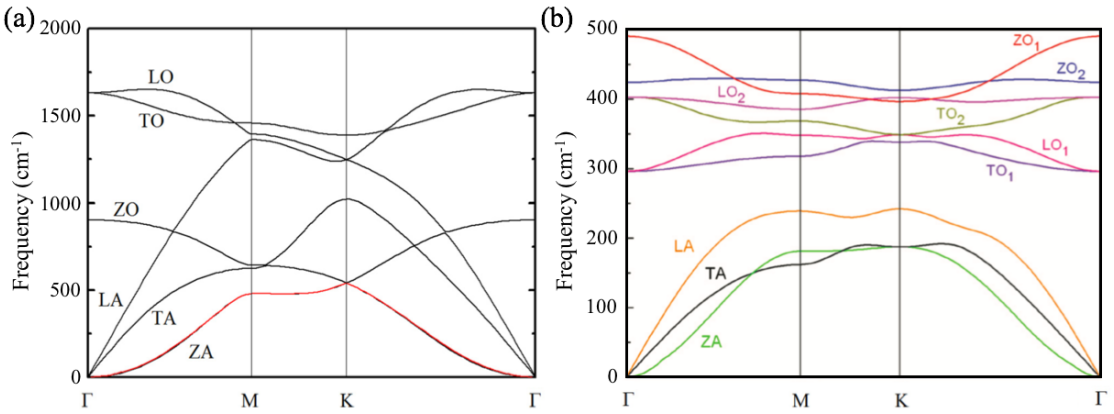

Figure 1.16 – (a) Phonon dispersion diagram for graphene. Extracted from [139]. (b) Phonon dispersion diagram for monolayer MoS_2. There are three acoustic branches: transverse acoustic (TA), longitudinal acoustic (LA), and out-of-plane acoustic (ZA) branches, which are separated by a gap of ~ 50 cm^{-1} below the non-polar transverse optical (TO) and longitudinal optical (LO) modes, labeled as TO_1 and LO_1, respectively. Extracted from [140].

In the case of graphene, at low q near the center of the Brillouin zone, the frequencies of the transverse acoustic (TA) and longitudinal acoustic (LA) modes have linear dispersions ($\omega \sim vq$) with group velocity of 10-20 km/s, four to six times higher than those in silicon or germanium because of the strong in-plane sp^2 bonds of graphene and the small mass of carbon atoms. In contrast, the flexural ZA modes have an approximately quadratic dispersion, responsible for many of the unusual thermal properties of graphene. Large group velocities in suspended graphene results in large phMFP of the order of 775 nm [141]. In MoS_2, the dominating acoustic mode near the center of the Brillouin zone is found to be the LA mode with a value of around 18 nm, which is much larger than that of the TA mode (5 nm) [140]. Since the sizes of most reported MoS_2 flakes are around 1 μm, the thermal conduction in these samples is more likely to be in the diffusive regime. Theoretical calculations have recently shown that the room temperature thermal conductivity in TMDs can be quite low. This aspect is highly promising for applications. As an example, in the case of monolayer MoS_2, κ is found to be 23.2 W/mK, remarkably lower than that of graphene [140]. On the other hand, the in-plane thermal conductivity of graphene at room temperature is among the highest of any known material, up to 5000 W/mK for freely suspended samples [142]. However, those values are strongly reduced when the 2D material is laying on a substrate due to a strong suppression of the ZA phonon branch [110].

The thermal conductivity κ of a finite-sized sample is related to the thermal conductance K and it satisfies the Fourier's scaling law $\kappa = K(L/A)$, where L is the length of the sample and A is its cross section. In the diffusive phonon limit ($L \gg \lambda_{ph}$), κ is less sensitive to the length variation and it is generally considered independent of the system size. On the other hand, in the ballistic limit ($L \ll \lambda_{ph}$), the scaling law does not apply and boundary becomes important, considerably reducing phonon transport. In this case, the thermal conductance at a given temperature approaches a constant value, $K_{\text{ball}}(T)$. As a consequence, the thermal conductivity becomes proportional to L as imposed from the relation $\kappa_{\text{ball}} = K_{\text{ball}}(L/A)$. Its

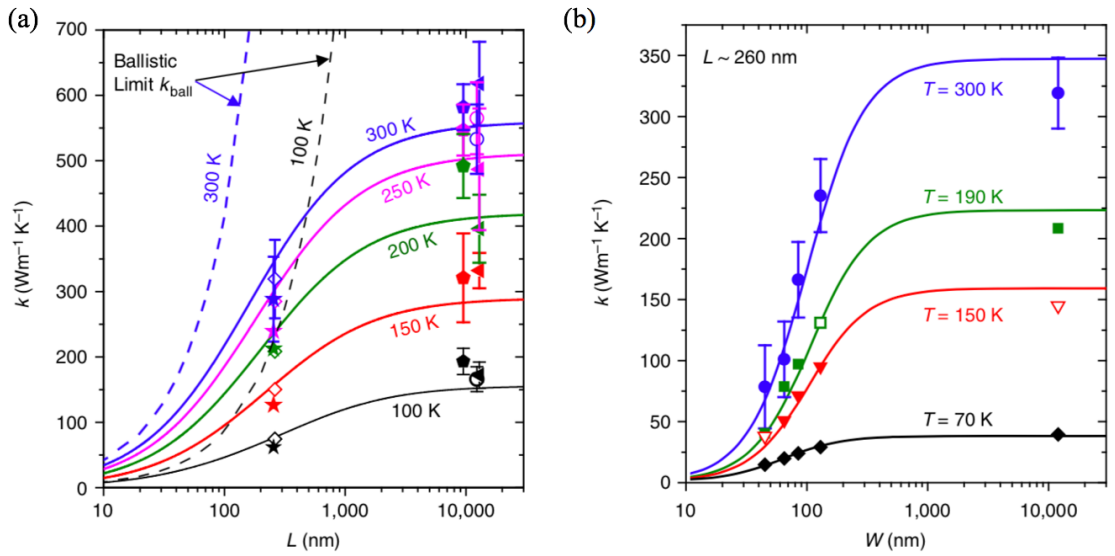

Figure 1.17 – (a) Thermal conductivity reduction with length for "wide" samples ($W \gg \lambda$), compared to the ballistic limit (κ_{ball}) at several temperatures. Symbols are data for our "short" unpatterned graphene samples. Solid lines are model from Eq. 1.22. (b) Thermal conductivity reduction with width for GNRs, all with $L \sim 260$ nm. Solid symbols are experimental data, open symbols are interpolations for the listed temperature; lines are fitted model from Eq. 1.21. Extracted from [143].

value gets saturated in the diffusive limit, and typically grows gradually with increasing L in the intermediate region as illustrated in Figure 1.17a in the case of a single layer graphene sample. Note that, the typical sample length below which the Fourier scaling is no more valid is of the order of few μm, comparable to typical device dimensions. For this reason, in nanostructures, boundary effects cannot be neglected. Moreover, edges of 2D material samples are not atomically regular but rather rough. The edge roughness causes phonon scattering and further decreases the thermal conductivity. Figure 1.17b illustrates the width (W) dependence of the thermal conductivity of graphene nano-ribbons (GNRs). The experimental values are fitted with an empirical model introduced by Bae et al. [143], in agreement with previews experimental works [144, 145]:

$$\kappa_{\text{eff}}(L,W,T) = \left[\frac{1}{c}\left(\frac{\Delta}{W}\right)^{n} + \frac{1}{\kappa(L,T)}\right]^{-1} \tag{1.21}$$

The first term inside the square brackets takes into account the sample size effects: Δ is the rms edge roughness, $c = 0.04$ W/mK and $n = 1.8 \pm 0.3$ are best-fit parameters given by literature [143]. $\kappa(L,T)$ is the length-dependent thermal conductivity and it is given by

$$\kappa(L,T) = \sum_{s}\left(\frac{A}{LK_{s,\text{ball}}} + \frac{1}{\kappa_{s,\text{diff}}}\right)^{-1} \tag{1.22}$$

with s the phonon mode (longitudinal, transverse or flexural). κ_{diff} takes into account for the

flexural modes suppression due to the substrate interaction and it is estimated for a wide sample. Thus, the influence of the interfaces, which scatter phonons more efficiently than charge carriers or impurities, is another important effect related to low dimensionality. This results in a strong reduction of thermal conductivity which generally does not affect the reduction of the electrical conductivity. While in bulk materials, thermal conductivity can be considered as an intrinsic material property, independent of the system size, boundary effect and ballistic thermal transport breaks down this assumption in nanoscaled systems. All these aspects prove that the investigation of thermal and thermoelectric properties of low dimensional materials can provide new insights to answer fundamental questions and new solutions for a more efficient thermoelectric energy conversion.

1.5 Experimental techniques for thermal conductivity measurements

The knowledge of the effective thermal conductivity of supported materials is a required quantity to properly evaluate the figure of merit in thermoelectric devices. While measuring the Seebeck coefficient and the electrical conductivity in 2D materials does not require any complex device engineering or sophisticated experimental set-ups, the measurement of the effective thermal conductivity of supported materials can be a difficult task to achieve. Many different techniques are employed nowadays to investigate thermal conductivity in low dimensional materials, which are typically implemented in suspended configurations. Raman opthotermal spectroscopy [146, 147], micro-resistance thermometry [112, 110], 3ω method [148], thermoreflectance [149] and electrical self-heating [73, 83, 150, 151] are the most used. Each of them presents different limitations such as poor resolution, complex nanofabrication or limited sample dimensions. Furthermore, when using supported configurations, thermal losses through the substrate increase the difficulty of modeling heat diffusion. The ability to measure all the relevant parameters defining the thermoelectric efficiency on the same device represents a major goal to unveil thermal and thermoelectric properties of unexplored new materials in realistic configurations. Being the measurement of the thermal conductivity of low-dimensional systems a difficult task, it is worth trying to give a short description of the different methods developed in literature, each presenting its own advantages and disadvantages.

1.5.1 3ω method

The 3ω method is widely used to measure thermal properties of both bulk materials and thin films after it was first introduced in 1990 by Cahill et al. [152]. Figure 1.18a shows a typical schematic of the 3ω measurement. The thin film of interest is grown or deposited on a substrate and a metallic strip is deposited on top of it, acting as a transducer. The metallic strip serves both as electrical heater and temperature sensor. An AC current at frequency ω, $I(t) = I_0 \cos(\omega t)$, passes through the heater/sensor. This results in Joule heating of the resistive metallic strip which is subjected to a temperature change at a frequency 2ω,

$\Delta T(t) = \Delta T_0 \cos(2\omega t + \phi)$. The temperature change perturbs the heater/sensor's electrical resistance, express as $R(T) = R_0[1 + \alpha \Delta T_0 \cos(2\omega t + \phi)]$, where α is the temperature coefficient of resistance of the heater/sensor, and R_0 is the electrical resistance in absence of heating. When multiplied by the driving current, a small voltage signal across the heater/sensor can be detected at a frequency 3ω. This change in voltage at frequency 3ω contains the information about thermal transport within the sample. This method can be applied for both cross-plane and in-plane measurements. For cross-plane thermal conductivity measurement, as illustrated in Figure 1.18b, the heater width should be relatively large compared to thin film thickness in order to satisfy the assumption that heat conduction is uniform across the thin film. For the in-plane thermal conductivity measurement (Figure 1.18c), a narrower-width heater is used so that the in-plane thermal conductivity can be deduced through heat spreading in the thin film. The 3ω method can be used for measuring dielectric, semiconducting, and electrically conducting thin films. For electrically conducting and semiconducting materials, samples need to be electrically isolated from the metallic heater/sensor with an additional insulating layer, which introduces an extra thermal resistance and inevitably reduces both sensitivity and measurement accuracy [153]. Another limitation of this method is that it involves the microfabrication of a metallic heater/sensor transducer which modifies the device and thus the intrinsic properties of the material under investigation.

1.5.2 Time-domain thermoreflectance

The time-domain thermoreflectance (TDTR) technique is extensively implemented to study the thermal transport mechanisms across interfaces, including bulk-to-bulk interfaces, interface between low-dimensional materials and bulk substrates, interfacial thermal conductance between metals and dielectrics, etc. [154, 155]. This method measures the thermoreflectance response as a function of the delay time between the arrival of a pump pulse and a probe pulse on the sample surface. The pump beam generates a heat flux on the sample surface and the probe beam detects the corresponding temperature change through the reflectance change [156]. To apply the TDTR method to the study of thermal conductivity in 2D materials, the penetration depth of the laser-generated thermal wave needs to be smaller than the 2D layer. In fact, as illustrated in Figure 1.18d, if a large beam spot modulated at high frequency is used to measure the thermal properties, the cross-plane heat transfer dominates. In this case, the thermal response is controlled by the substrate. At high frequency limit, the penetration depth would be so small that the temperature gradient only penetrates into a limited depth of the layer (Figure 1.18e). On the other hand, if the beam is tightly focused to the thin film sample at low modulation frequency, the heat transfer is dominated in the in-plane radial direction (Figure 1.18f). In this case, the in-plane thermal conductivity dominates the thermal response of the material [153].

Owing to the fact that both 3ω and TDTR methods are mainly suited for cross-plane thermal transport measurements and they require a metallic transducer, they have not been widely used for the investigation of the in-plane thermal properties of atomically thin 2D materials.

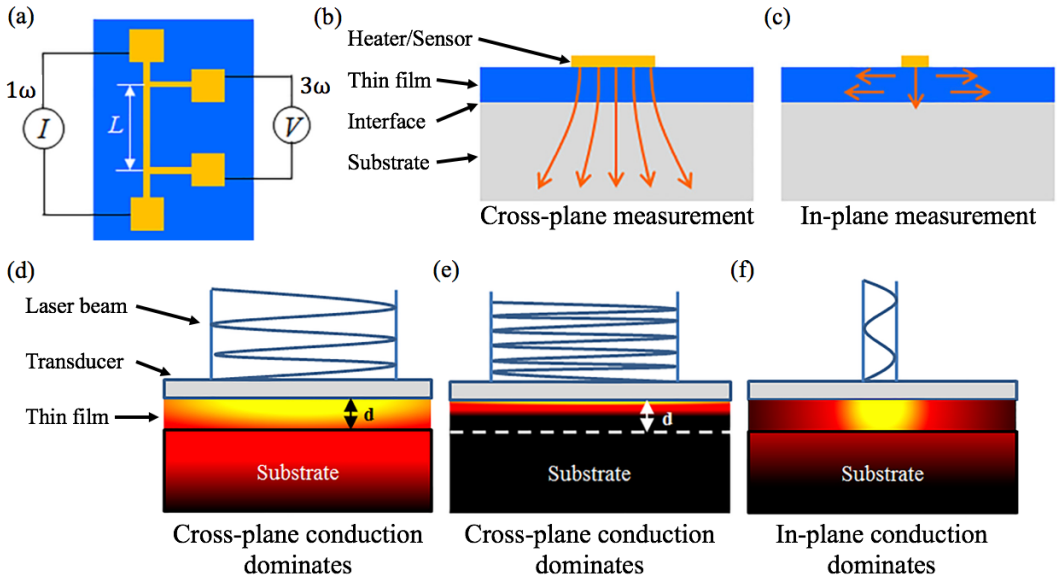

Figure 1.18 – (a) Top view of a typical 3ω method set-up for thermal characterization of thin films. (b, c) Schematic of metallic transducer configuration for the cross-plane and the in-plane thermal conductivity measurement using the 3ω method. (d, e, f) Schematic of a temperature profile in a thin film in the case where the cross-plane penetration depth is much larger than thickness of the film, the thermal excitation only penetrates into a limited depth into the thin film, and in-plane heat transfer dominates. Figures extracted from [153].

1.5.3 Micro-Raman spectroscopy

The first measurement of thermal conductivity in a 2D material was performed by Balandin et al. in 2008 [146], employing one of the currently most used techniques for thermal conductivity measurements in 2D materials: the micro-Raman optothermal technique. A focused laser creates a local hot spot on a suspended micrometer-scale 2D material (Balandin et al. studied a single layer graphene at room temperature), and generates a heat wave propagating toward heat sinks as illustrated in Figure 1.19a. Raman spectroscopy exploits the temperature sensitivity of Raman peaks at frequency ω (2D and G in the case of graphene) to monitor the local temperature change produced by the variation of the laser excitation power P ($\Delta\omega = \chi\Delta P$). The heat conduction is analyzed by solving the heat transport equation in cylindrical coordinates:

$$\kappa \frac{1}{r}\frac{d}{dr}\left[r\frac{dT(r)}{dr}\right] + q(r) = 0 \tag{1.23}$$

where κ is the thermal conductivity of the suspended layer and r is the radial position. Here, $q(r) = (I\alpha/t)\exp(-2r^2/r_0^2)$ is the heat inflow per unit volume due to laser excitation, $I = P/(\pi r_0^2)$ is the laser power per unit area at the center of beam spot, α is the light absorption, t is the layer thickness and r_0 is the half of the Gaussian beam width [77]. However, Raman spectroscopy has several limitations. The laser resolution is generally ~ 1 μm and this prevents the possibility to study nanostructured devices having dimension lower than that since the

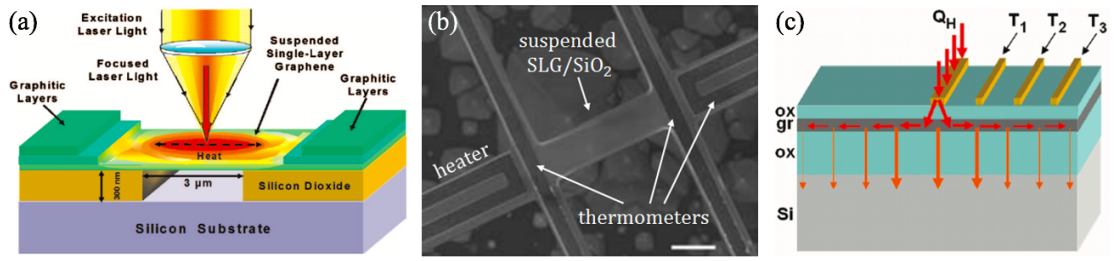

Figure 1.19 – (a) Schematic of the Raman spectroscopy experiment showing the excitation laser light focused on a graphene layer suspended across a trench. Extracted from [146]. (b) Scanning electron microscopy (SEM) image of micro-resistance thermometry device with SLG supported on a suspended SiO_2 membrane between thermometers. Scale bar is 3 μm. Extracted from [110]. (c) Schematic of SiO_2/Si-supported micro-resistance thermometry device to measure encased few-layer graphene (FLG). Extracted from [112].

laser would interact with the environment at the edges of the material under investigation. Moreover, Raman spectroscopy is preferentially applied only for suspended sample to avoid the substrate influence. Finally, it is difficult to precisely determine the laser power absorbed by the 2D material since the 2D material absorption coefficient can strongly vary from sample to sample, furthermore strain and impurities in the sample affect the Raman peaks position and their temperature dependence, leading to a limited temperature resolution.

1.5.4 Micro-resistance thermometry

Micro-resistance thermometry is another frequently used technique which can be applied to measure both suspended and supported 2D materials. It is based on the use of electrical resistances, acting as thermometers and heating elements, with no limitations on the sample size and temperature range. 2D materials can be fully suspended between two thermometers [157], supported by a suspended SiO_2/SiN_x membrane [110], as in Figure 1.19b, or fully substrate supported [112, 143], as in Figure 1.19c. With this approach, a local heater is used to generate a temperature gradient across the sample. Several thermometers monitor the temperature changes in terms of their electrical resistance changes. The thermal conductivity is extracted by solving the equivalent thermal resistance circuit for the suspended material or supported on membrane. In the latter configuration, the knowledge of the membrane heat flow is necessary. This is done by repeating the measurement after the complete etching of the 2D material in order to record the substrate contribution which can be subtracted from the total thermal conductivity. In the case of fully supported device the evaluation of the thermal conductivity requires complicate 3D finite element modeling (FEM) simulations to take into account the significant heat leakage into the substrate.

1.5.5 Joule self-heating

Another way to measure the thermal conductivity is by the Joule self-heating method. This method has been successfully used in the case of metallic nanowires, but it is scarcely applied

in the case of low dimensional materials. An electrical heating current flowing through a quasi-1D sample generates a temperature profile along the sample, inducing a change in its electrical resistance which can be precisely measured in a 4-probes configuration [83]. In an equivalent way, the temperature profile generated by the applied electrical power p can be recorded by mid-infrared thermal emission spectroscopy, as illustrated in Figure 1.20, where an electrical current is injected in a fully hBN-encapsulated graphene layer and the resulting temperature profile is recorded in a thermal emission map [150]. The temperature profile will depend on the thermal losses to the substrate g for supported materials, and on the thermal conductivity κ of the material itself. The configuration of fully suspended device corresponds to $g = 0$. The method requires the resolution of the heat transport equation in the one-dimensional heat transport approximation:

$$\kappa A \frac{d^2 T(x)}{dx^2} + p\,[1 + \alpha(T(x) - T_0)] - g(T(x) - T_0) = 0 \tag{1.24}$$

where A is the cross-sectional area of the nanowire, α (or TCR) is the temperature coefficient of resistance and T_0 is the temperature of the environment. Typically, thermal losses through the substrate dominate, preventing the correct determination of κ. This represents the most important limitation of the Joule self-heating method. However, a careful device engineering can produce quite accurate results [83]. Joule self-heating does not have any limitation on the device geometry and nanostructuring, but it can be applied only for conductive materials. It allows to evaluate other than the thermal conductivity, also the thermal losses through the substrate. In optimized conditions, it turns out to be an alternative and easy method to measure the effective thermal conductivity of supported low dimensional materials with the clear advantage to be implementable in device architectures compatible with thermopower and electrical conductivity investigations, for a complete thermoelectric characterization. Moreover, this method is able to highlight the variations of thermal conductivity due to the different device configurations (namely, different substrates, nanostructuring, functionalization, etc.). This approach will be further discussed and applied in Chapter 5.

1.5.6 Breakdown voltage method

In an analogous setup as for the Joule self-heating method, the resolution of the heat transport equation can be achieved also by the knowledge of the breakdown temperature T_{BD} and the required electrical power P_{BD} for it to occur. In this case we talk about breakdown method. Solving for $T(x)$ the heat transport equation in vacuum conditions and considering the breakdown occurs at the center of the sample, one obtains:

$$T_{BD} = T_0 + \frac{P_{BD} L}{8 \kappa W t} \tag{1.25}$$

where T_0 is the environment temperature, κ is the thermal conductivity, L, W and t are related

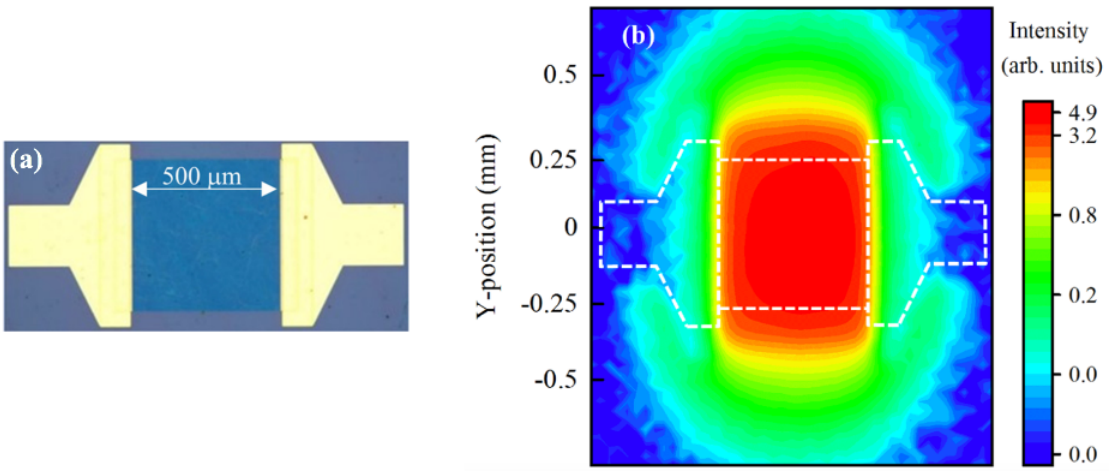

Figure 1.20 – (a) Optical image of a hBN/graphene/hBN heterostructure with electrical interconnections to inject a heating current in the graphene layer. (b) Thermal emission map on a logarithmic vertical scale. The white dotted lines indicate the position of the metal contacts and multilayer graphene. Extracted from [150].

to the sample geometry. This method allows to study suspended or supported devices in high field and high temperature regimes and is mainly used to study the thermal conductivity of carbon nanotubes [151], but few examples are available also for suspended graphene [158].

1.6 Thermal conductivity in 2D materials

For the sake of completeness, I will report in this section the main results concerning thermal conductivity measurements in 2D materials. Experimentally, thermal properties of 2D materials are generally difficult to investigate and, typically, this is done by suspending the material. However, measurements on suspended 2D materials are not very relevant for actual applications. Moreover, the experimental production of thermoelectric suspended devices is impracticable for its complexity, fragility and costs. On the other hand, the direct measurement of κ in supported 2D materials suffers the limit of dominant heat diffusion through the substrate, that drastically change the system response. Besides, the interaction with the environment becomes a dominant factor for phononic thermal transport [159] and typically reduces κ. This is a fundamental aspect to take into account for practical applications.

1.6.1 Graphene

The intrinsic thermal conductivity of graphene is limited only by phonon-phonon scattering and electron-phonon scattering. Moreover, the electron contribution to the thermal conductivity is expected to be lower than 1% and, for this reason, it is generally neglected [160]. Due to the very strong bonding of light atoms, carbon allotropes own the highest thermal conductivity values thanks to the large phonon mean free path which can reach several hundreds of nm. In particular, suspended graphene reaches values of thermal conductivity as high as 5000

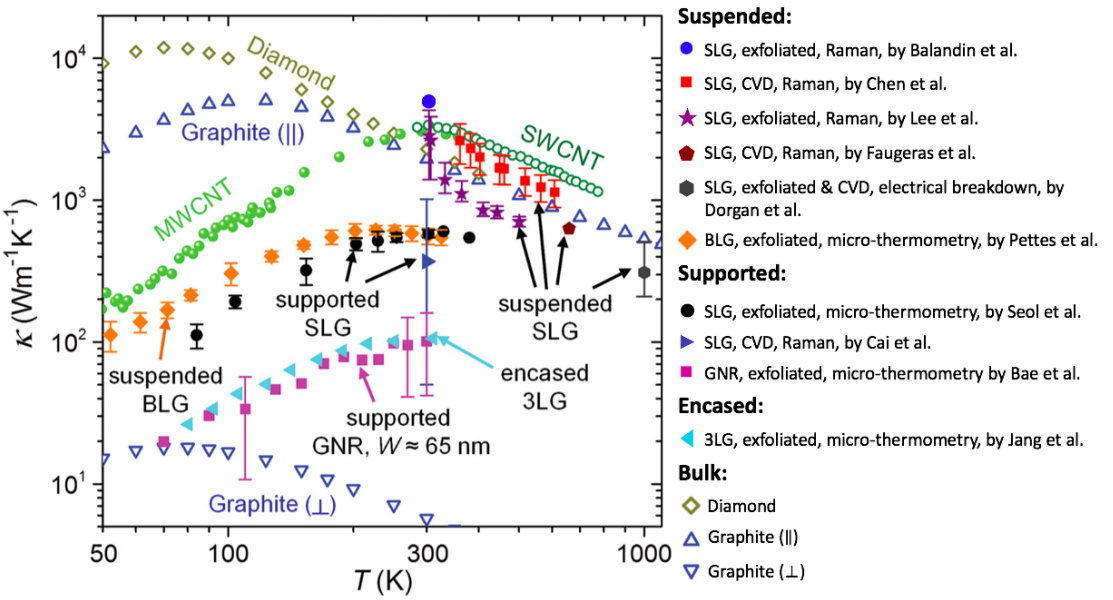

Figure 1.21 – (a) Experimental thermal conductivity values as a function of temperature: (solid blue circle) suspended exfoliated SLG by Balandin [146], (solid red square) suspended CVD SLG by Chen et al. [161], (solid purple asterisk) suspended exfoliated SLG by Lee et al. [162], (solid brown pentagon) suspended CVD SLG by Faugeras et al. [163] , (solid grey hexagon) suspended SLG by Dorgan et al. [158], (solid orange diamond) suspended exfoliated BLG by Pettes et al. [164], (solid black circle) supported exfoliated SLG by Seol et al. [110], (solid blue right-triangle) supported CVD SLG by Cai et al. [147], (solid magenta square) supported exfoliated GNR by Bae et al. [143] , (solid cyan left-triangle) encased exfoliated 3-layer graphene by Jang et al. [112], (open gold diamond) diamond [165], (open blue up-triangle) in-plane graphite [165], (open blue down-triangle) cross-plane graphite, (open dark-green circle) SWCNT by Pop et al. [166] and (solid light-green circle) MWCNT by Kim et al. [167]. Extracted from [84].

W/mK [146]. However, when graphene is laying on a substrate, a strong interface scattering of flexural phonon modes leads to an important quenching of thermal conductivity. Figure 1.21 shows the most significant data available up to date for suspended and supported graphene.

Data of suspended SLG thermal conductivity based on Raman opthothermal method available up to now only cover the temperature range 300 K - 700 K. Starting from values in the range 2000 - 4000 W/mK at room temperature, the thermal conductivity decreases to values in the range of 700 - 1500 W/mK at 500 K [161, 162] and reaches ~ 600 W/mK at ~ 660 K [163]. The variation of obtained values could be attributed to different choices of graphene optical absorbance, thermal contact resistance, different sample quality. For higher temperature, Dorgan et al. [158] used the electrical breakdown method, founding $\kappa \sim 310$ W/mK at 1000 K for suspended SLG. This behavior is attributed to stronger second-order three-phonon scattering enabled by flexural (ZA) phonons of suspended graphene. For temperature below 300 K, the micro-resistance thermometry needs to be employed. However, there are not reliable data for single-layer suspended graphene but only for few-layers graphene (FLG) or for supported samples (see Figure 1.21).

At room temperature, the thermal conductivity of single layer graphene supported by sus-

pended SiO_2 was measured for the first time by Seol et al. [110] and it was estimated to be ~ 600 W/mK with the micro-resistance thermometry approach. The thermal conductivity reduction in supported graphene was attributed to substrate scattering which strongly affects the out-of-plane flexural (ZA) mode of graphene. This effect becomes stronger in encased graphene, where graphene is sandwiched between a bottom and a top SiO_2. The thermal conductivity in this case was measured to be 160 W/mK, as reported by Jang et al. [112], using the micro-resistance thermometry in a fully supported and SiO_2-encased graphene samples. For encased graphene, beside the phonon scattering by bottom and top oxides, the evaporation of top oxide could cause defects in graphene, which can further lower the thermal conductivity. Figure 1.22a shows the reduction of thermal conductivity of 3 and 4 layers graphene flakes due to the deposition of 30 nm-thick upper oxide. At 310 K the reduction is 64% and 38%, respectively. Figure 1.22b shows the thermal conductivity of several encased graphene samples as a function of temperature. In the range 60 K < T < 150 K, the thermal conductivity follows a power law trend between $T^{1.5}$ and T^2. At higher T, the data trend moves to a much weaker power law. A peak in $\kappa(T)$ near or just above room temperature is expected, indicating the onset of significant Umklapp phonon scattering, although, because of the limited temperature range measured, the peak is only clearly evident for the 19 layers flake. When compared to bulk graphite, the thermal conductivity is weaker and the suppression is more evident at low temperature.

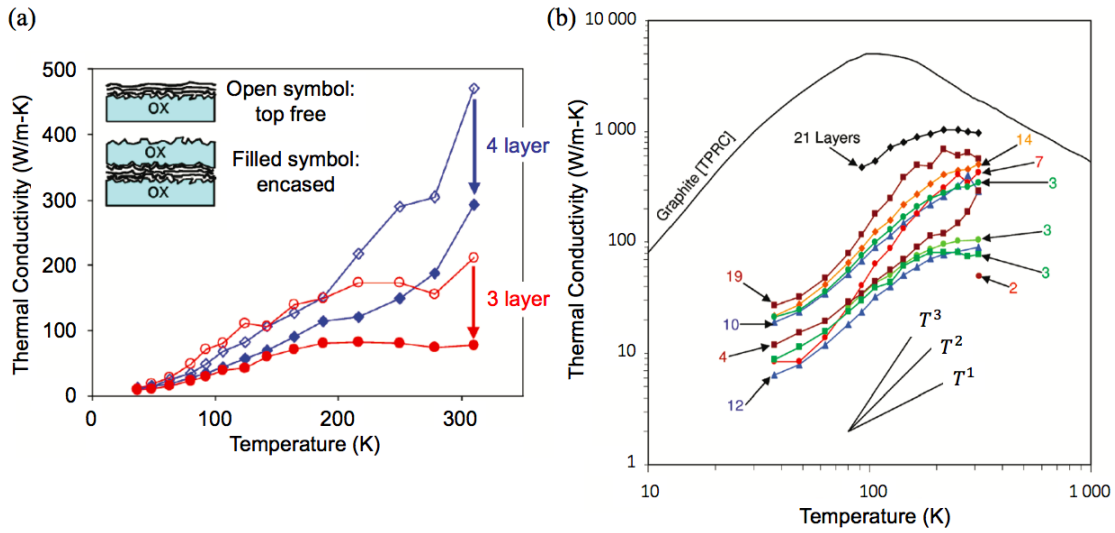

Figure 1.22 – (a) Thermal conductivity of 3 and 4 layers supported graphene before (open symbols) and after (filled symbols) top oxide deposition as a function of temperature. (b) Temperature dependence of thermal conductivity for encased graphene flakes with different number of layers, up to ultra-thin graphite. Extracted from [112].

As already pointed out, the thermal conductivity is not only influenced by the interaction with the substrate, but it also depends on the sample geometry. In particular, size reduction or nano-patterning could have a strong impact on the thermal conductivity due to enhanced phonon scattering. As a representative example, Figure 1.23a shows a parallel array of ~ 65 nm-wide single layer graphene nanorribons (GNRs) that have been studied by Bae et al. [143]

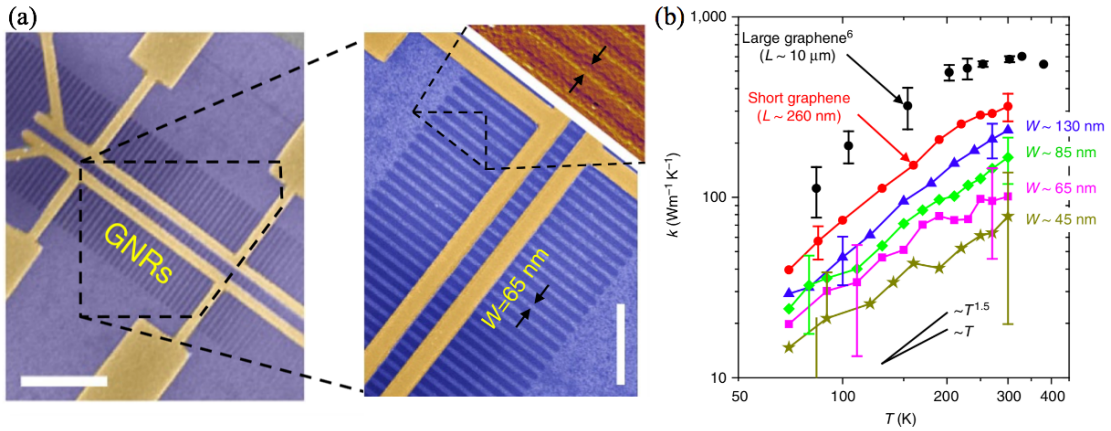

Figure 1.23 – (a) False-colored SEM image of a GNR array on SiO_2/Si with micro-resistance thermometers. The top right inset is a zoom-in atomic force microscopy (AFM) image of the GNRs. (b) Thermal conductivity versus temperature for GNR samples ($L \sim 260$ nm and W as listed in the plot). The red data set refers to short and wide (unpatterned) samples. The black data set represent a comparison to a long and wide sample (data from Seol et al. [110]). Extracted from [143].

using the micro-resistance thermometry to extract their thermal conductivity. They have found that for short devices, in which the length is comparable to the mean free path, the thermal conductance is much higher than micrometer size samples and it reaches the 30% of the ballistic limit at room temperature. However, when the width is reduced $W \approx \lambda$, the phonon scattering with the edge disorder leads to an important reduction of the thermal conductivity (Figure 1.23b). For the ~ 65 nm-wide and ~ 260 nm-long graphene nanoribons, the room temperature thermal conductivity was estimated to be on the order of ~ 100 W/mK and it keeps reducing when reducing the GNR width.

No data are available for supported graphene at high temperature. This is a weakly investigated regime. However, high temperature operation devices are more appealing for actual applications and thus, they are worthy to be studied.

1.6.2 Hexagonal boron nitride

Hexagonal boron nitride (hBN) is a one-atomic layer two-dimensional (2D) material with a honeycomb structure analogous to the graphene one, in which an equal number of Boron and Nitrogen atoms are linked by sp^2 bonds. Due to the strong covalent bond between B-N, hBN and graphene hold similar structural and physical properties such as high mechanical strength, high thermal stability and superior thermal conductivity. However, compared to graphene, there are much less experimental data for the thermal conductivity of few-layers hBN. Some of the most relevant results present in literature are illustrated in Figure 1.24a.

Theoretical computations based on the numerical solution of the phonon Boltzmann transport equation by Lindsay et al. [168] have predicted values of κ exceeding 1200 W/mK for isotopically pure single layer hBN and 800 W/mK for naturally occurring single layer hBN. In

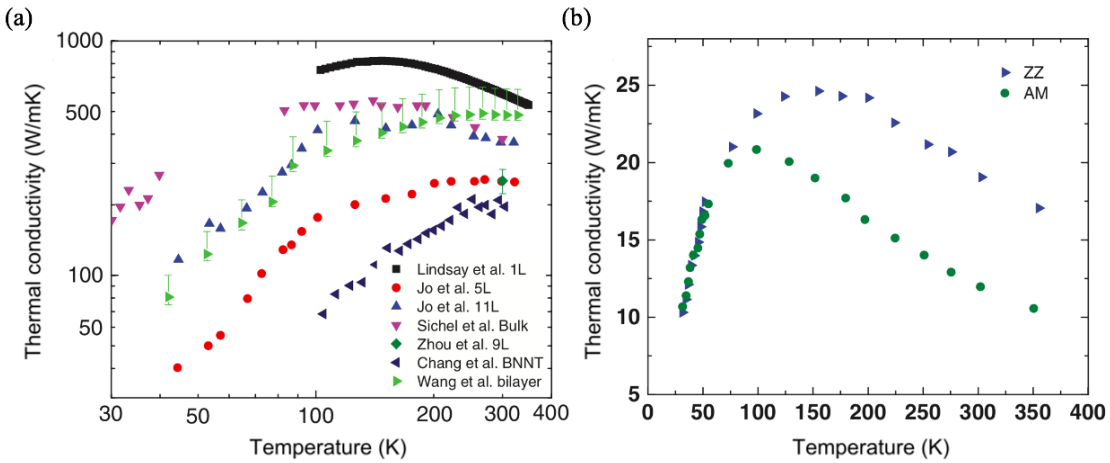

Figure 1.24 – (a) Temperature-dependent thermal conductivity of few layer hBN reported by Lindsay et al. [168], Jo et al. [170], Sichel et al. [172], Chang et al. [173], Zhou et al. [171], and Wang et al. [169] (b) Temperature-dependent thermal conductivity of BP flake in the armchair (AM) and zigzag (ZZ) directions [174]. Extracted from [175].

both cases, the peak of thermal conductivity is reached in the range of temperature between 100 and 150 K. The subsequent decrease of κ with increasing T indicates that three-phonon scattering becomes dominant, leading to values of thermal conductivity smaller than 500 W/mK at room temperature [168]. Prediction also show a reduction of κ when increasing number of layers. The thermal conductivity of atomically thin hBN has also been experimentally explored. It can reach up to 484 W/mK in bilayer hBN as measured by suspended prepatterned microstructures [169], and around 360 W/mK in 11 layers hBN measured with the micro-resistance approach with built-in thermometers [170] at room temperature. Zhou et al. [171] reported in 2014 an experimental measurement of room-temperature thermal conductivity of few-layers suspended hBN sheets by using a non-contact micro-Raman spectroscopy method. They found values ranging from 227 to 280 W/mK, which are comparable to those of bulk hBN, indicating their potential use as important components to solve heat dissipation problems in thermal management configurations.

1.6.3 Black phosphorus

Black phosphorus (BP) has been revisited recently as a new two-dimensional material showing potential applications in electronics and optoelectronics. Unlike the well-explored electrical properties, there are only few experimental studies of thermal transport in BP. Luo et al. [130] reported the anisotropic in-plane thermal conductivity of suspended few-layers BP measured by micro-Raman spectroscopy. To make a quasi-one-dimensional heat transfer along certain direction, a thin aperture was used to yield ultra-thin focal laser line perpendicular to the suspended BP on a narrow trench. The measured armchair (AM) and zigzag (ZZ) thermal conductivities were ~ 20 and ~ 40 W/mK, respectively, for BP films thicker than 15 nm, showing a significant anisotropy. Those values decrease to ~ 10 and ~ 20 W/mK if the film thickness is reduced. Lee et al. [174] reported similar results for a 170 nm-thick BP, which are shown

in Figure 1.24b, using the micro-resistance thermometry method. As in the previous case, they also reported a decrease in thermal conductivity as the sample thickness is reduced, but the anisotropy ratio stays around two within the thickness range. Theoretical modelling reveals that the observed anisotropy is primarily related to the anisotropic phonon dispersion, whereas the intrinsic phonon scattering rates are found to be similar along the armchair and zigzag directions. Surface scattering in the black phosphorus films is shown to strongly suppress the contribution of long mean-free-path acoustic phonons.

1.6.4 Transition metal dichalcogenides

Several theoretical investigations on thermal conductivity of TMDs are available in literature focusing on the phonon transport properties, anisotropic properties, and effect of defects and strains. However, the experimental results are still few, and they are mostly related to the most "popular" TMDs, such as MoS_2 and WSe_2.

Molybdenum disulfide

Among the TMDs family, MoS_2 is doubtless the most studied. Interestingly, as shown in Figure 1.25a, the experimental values of thermal conductivity of monolayer and few-layers MoS_2 are lower than that of bulk MoS_2, which is reported on the order of 100 W/mK by Liu et al. [176] for (001)-oriented MoS_2 crystals at room temperature. The experimental study of thermal transport in few-layers MoS_2 prepared by chemical vapor deposition method has been reported by Sahoo et al. [76] by investigating the temperature dependence of in-plane and out-of-plane Raman modes. The thermal conductivity of a suspended 11 layers sample was measured to be about 52 W/mK at room temperature. Yan et al. [77] proposed a more detailed study of temperature- and laser-power-dependent Raman characterization on monolayer MoS_2 exfoliated from naturally occurring bulk materials. They also compare Raman measurements from both suspended and supported monolayer MoS_2 flakes in order to isolate the substrate effects. Starting from the assumption that the supported (κ') and suspended (κ) MoS_2 have the same thermal conductivity ($\kappa' = \kappa$) and taking $G = 50$ MW/m^{2}K as a typical value for van der Waals interface thermal conductance between MoS_2 and the Si_3N_4 employed substrate, the extracted thermal conductivity value was 34.5 W/mK. They found that for a value of G ranging from 10 to 300 MW/m^{2}K, the extracted thermal conductivity slightly changes by only 0.4 W/mK, suggesting that the interface is not the dominant factor in the thermal transport. Similar values are confirmed by Jo et al. [78] which used the micro-resistance method to measure the in-plane thermal conductivity of suspended MoS_2 across a wide temperature range. The obtained room-temperature thermal conductivity values are in the ranges 44 – 50 and 48 – 52 W/mK for two samples that are 4 and 7 layers thick, respectively. For both samples, the peak thermal conductivity occurs at a temperature close to 120 K. This peak is justified by the dominant intrinsic phonon-phonon scattering at high temperature and phonon scattering by surface disorders at low temperature.

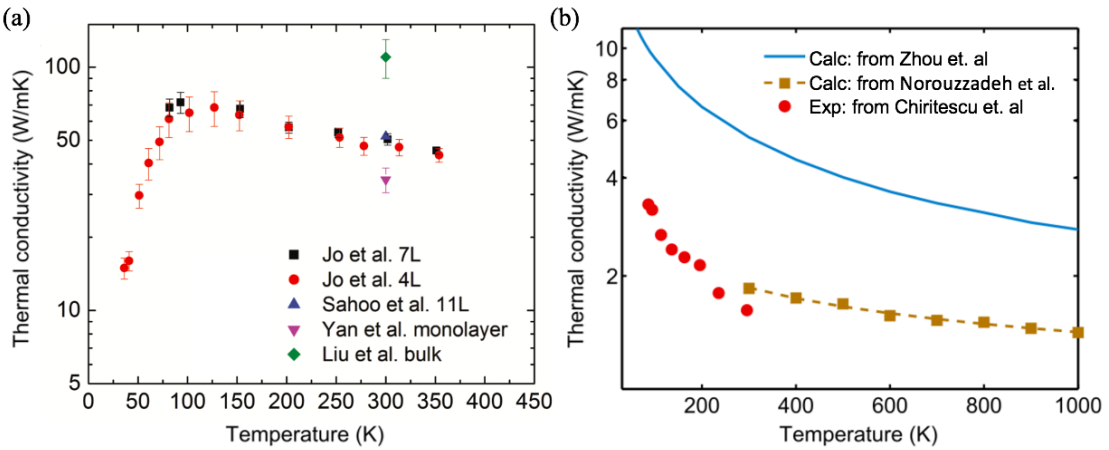

Figure 1.25 – (a) In-plane thermal conductivity of MoS_2 vs. temperature reported by Jo et al. [78], Sahoo et al. [76], Yan et al. [77] and Liu et al. [176]. Extracted from [175]. (b) In-plane thermal conductivity of single-layer WSe_2 vs. temperature reported by Zhou et al. [178], Chiritescu et al. [81] and Norouzzadeh et al. [82]. Extracted from [82].

Tungsten diselenide

Very few are the available measurements of thermal conductivity on other TMDs. Among the first experiments concerning WSe_2, Chiritescu et al. [81] studied the thermal conductivity of CVD grown single-crystal WSe_2 at low temperature, finding low values on the order of few units of W/mK with a behavior approximately proportional to $1/T$, as illustrated in Figure 1.25b. Consistent results where proposed by Mavrokefalos et al. [177], which employed the micro-resistance technique to measure the in-plane thermal conductivity of patterned and suspended WSe_2. The obtained in-plane κ at room temperature are in the range of 1.2-1.6 W/mK. Those values were recently confirmed by the simulations of Norouzzadeh et al. [82]. They studied the in-plane thermal conductivity of single-layer WSe_2 using non-equilibrium molecular dynamics simulation. The obtained value of κ is $\sim$ 1.83 W/mK. Such a low value is due to the remarkably small phonon mean free path evaluated to be 42 Å. Slightly larger values were computed from first-principles calculations by Zhou et al. [178]. However, they predicted a trend consistent with other works. The room temperature thermal conductivity of monolayer WSe_2 for a typical sample size of 1 μm was found $\sim$ 4 W/mK and a reduction of 95% was predicted in the same conditions for a 10 nm-sized sample. Such an ultra-low thermal conductivity was justified due to the ultra-low Debye frequency and heavy atom mass.

Other TMDs

Other TMDs, which are less recurrent in literature, show values of thermal conductivity in the same order of magnitude as MoS_2 or WSe_2. A value of 32 W/mK has been measured with the optothermal Raman technique for a monolayer WS_2 [179], which is comparable to the monolayer MoS_2 in Yan's work [77]. With the same method, the thermal conductivity of a 45 nm-thick mechanically exfoliated $TaSe_2$ sample was measured as 9 W/mK [180].

1.7 Thermal losses to the substrate

When a 2D material is in contact with a substrate, heat propagation is very often dominated by the heat flux to the underlying substrate itself. In the most general case, the heat flux to the substrate can be represented by the equivalent thermal resistance model in Figure 1.26a. Flowing from the temperature T to the equilibrium/environment temperature T_0, the heat faces a series of thermal resistances R_{th}. The first contribution is given by the interface between the 2D material and the SiO_2. In the majority of the cases, this resistance is the dominant one and it is strongly sample dependent because it depends on the fabrication of each sample and on the different van der Waals interaction between the 2D material and the substrate. It follows the thermal resistance given by the silicon dioxide, the SiO_2/Si interface and finally the Si. This thermal network is generally described by the effective substrate thermal conductance G as:

$$G = \frac{1}{R_{th}} \approx \left(\frac{1}{G_{2D/SiO_2} A} + \frac{t_{SiO_2}}{\kappa_{SiO_2} A} + \frac{1}{2\kappa_{Si} A^{1/2}} \right)^{-1} \tag{1.26}$$

where G_{2D/SiO_2} is the thermal conductance at the 2D material/substrate interface, A is the device area, t_{SiO_2} is the oxide thickness, κ_{SiO_2} ($\sim$ 1.4 W/mK) [152] is the oxide thermal conductivity and κ_{Si} ($\sim$ 140 W/mK) [181, 182] is the silicon substrate thermal conductivity. The thermal conductance at the SiO_2/Si interface ($>$ 600 MW/m^{2}K) [183] is generally neglected.

1.7.1 Experimental results for the thermal losses to the substrate

Seol et al. [110] have studied the thermal losses at the graphene/SiO_2 interface, evaluated in their equivalent thermal resistance circuit as the difference in thermal conductance to the substrate before and after the etching of a SLG by the micro-resistance thermometry technique, revealing a value of 10^8 W/m^{2}K. In accord with their work, the thermal boundary conductivity has been evaluated on the same order of magnitude for SLG and few layers graphene [184] at 300 K decreasing down to 2×10^6 W/m^{2}K at 50 K (for exfoliated non transferred and encased graphene). The same value ($\sim$ 0.5 - 1 $\times$ 10^8 W/m^{2}K) has been also found for SWCNTs by the breakdown technique [151]. Room temperature Raman measures on thermal boundary conductance for transferred large CVD-grown 2D materials flakes report values of 27, 22 and 15 MW/m^{2}K for SLG/SiO_2, MoS_2/SiO_2 and WSe_2/SiO_2 interface, respectively [185], revealing a reduction of two order of magnitude due to the different measurement approach. The recorded reduction could also be related to the employed transfer technique for the 2D material. More recent results have put in evidence how weaker interaction with the substrate can occur. Tang et al. [186] have shown a strong reduction of the interfacial thermal conductance due to the weak van der Waals interaction between graphene and its substrate. The analysis they have carried out relays on a Raman-based dual thermal probe that allows for the direct measurement of the temperature drop across a few nm gap interface induced by a second laser beam. The values they reported are 183 and 266 W/m^{2}K for graphene/Si and graphene/SiO_2, respec-

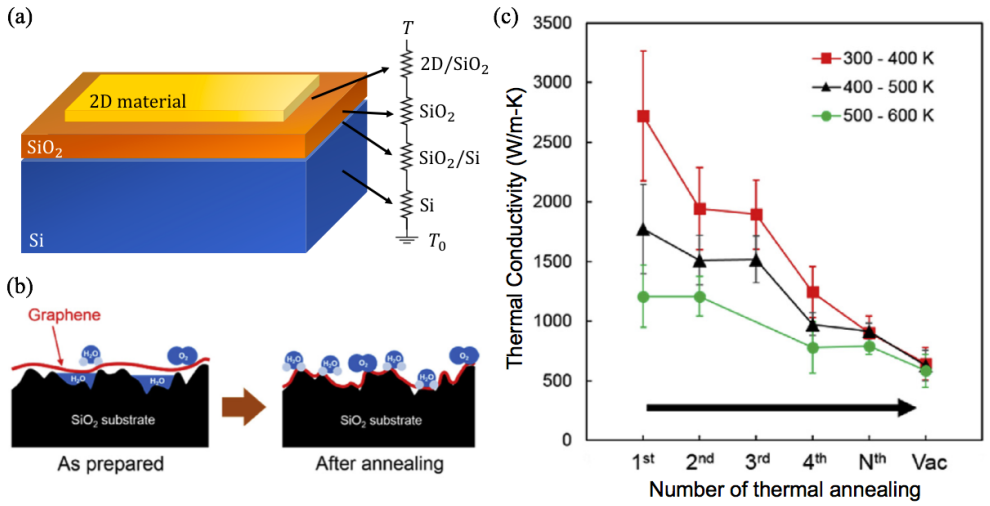

Figure 1.26 – (a) Schematic of the thermal resistance for a $Si/SiO_2/2D$ device in which the 2D material is at the temperature T and the environment is at the temperature T_0. (b) Annealing effect for supported graphene on a SiO_2 substrate with nanoscale surface roughness. Before the thermal annealing, the graphene is loosely contacting the substrate with possible intercalation of a H_2O layer. After the annealing, the graphene-substrate conformity is increased while the intercalated H_2O layer is likely dehydrated. (c) Progressive decrease of thermal conductivity with repeated thermal annealing for three different temperature ranges. Fig. (b) and (c) are extracted from [188].

tively. Those results are explained by an intrinsic and extrinsic corrugation of graphene and by a partial bound with the substrate leading to semi-suspended graphene as schematically illustrated in Figure 1.26b. Scanning probe microscopy measurements have found that SLG exfoliated on SiO_2 is partially conformal to the surface [33] and partially suspended between hills on the surface [187]. This weak interface conformity impacts on both thermal losses and thermal conductivity. As it has been proved by Kim et al. [188] and illustrated in Figure 1.26c, graphene-substrate conformity is progressively increased with repeated thermal annealing cycles. As a consequence, the thermal conductivity decreases from approximately 3000 W/mK, which is as high as that of suspended graphene due to "roughness suspension", to less than 1000 W/mK. This is believed to be primarily due to the increased interfacial scattering related to thermally enhanced graphene-substrate conformity. It is known that heating of supported graphene on a SiO_2 substrate enhances the degree of interface conformity, which implies a notable increase in the contact surface area of graphene to the substrate. According to Huang et al. [189], the annealing of a graphene flake promotes the removal of gas molecules between graphene and SiO_2 surface via the edges. The flake edges act as a one-way valve: the pressure built up below the graphene during annealing is released by the transfer of gas away from the interface. Once a more uniform contact is established between the flake and the substrate, the increased van der Waals interaction prevents gas from re-entering during cooling.

1.7.2 Interlayer thermal conductivity and substrate dependency

It has been also demonstrated that the interfacial thermal conductivity to the substrate is generally independent of the number of layers. For example, the interfacial thermal conduc-

tance of MoS_2 shows a negligible dependence on the number of layers and is maintained at around 16 - 17 MW/m^{2}K [190]. This result allows to affirm that all the layers of a van der Waals material are in thermal equilibrium between each other because the interlayer thermal conductance is much larger than the interfacial one between MoS_2 and underlying substrate. In fact, the interlayer thermal conductivity has been estimated on the order of 2 W/mK [176], which correspond to 3.33 GW/m^{2}K if considering 0.3 nm as interlayer distance. However, these values are quite low and they are the result of the weak van der Waals interlayer interaction. Even for graphene, which is the 2D material with the highest in-plane thermal conductivity, heat flow in the cross-plane direction is strongly limited. The thermal conductivity along the *c*-axis of pyrolytic graphite is ~ 6 W/mK at room temperature, which corresponds to an interlayer thermal conductance of ~ 18 GW/m^{2}K [85]. Chiritescu et al. [81] found (by TDTR) that the cross-plane thermal conductivity of disordered WSe_2 thin films is as low as 0.05 W/mK. Even though the interfacial thermal conductivity does not show any dependence on the number of layers, a difference can be highlight between transferred flakes and grown ones. In fact, the firsts have a 40% - 50% lower interfacial thermal conductivity than that of the grown counterparts [190]. This is directly related to the weaker interaction with the substrate of the transferred samples. Moreover, the interfacial thermal conductivity changes depending on the employed substrate. As an example, the values recorded by Yu et al. [190] are: 6.1 ± 1.0 MW/m^{2}K for MoS_2 on GaN, 8.0 ± 1.2 MW/m^{2}K for MoS_2 on Au, 7.1 ± 1.1 MW/m^{2}K for MoS_2 on Cu, 2.3 ± 0.5 MW/m^{2}K for MoS_2 on Ni, and 13 ± 2.0 MW/m^{2}K for MoS_2 on highly oriented pyrolytic graphite (HOPG).

Finally, TMDs have been shown to own the lowest values of thermal conductivity among all solid-state materials. The results presented in this chapter show the tremendous opportunities given by 2D materials for thermoelectric applications. Stacking or combining 2D layered materials can represent an original way to optimize electrical and phononic properties.

2 Van der Waals materials and devices fabrication

Van der Waals (vdW) materials, such as graphite, hexagonal boron nitride (hBN), transition metals dichalcogenides (TMDs), are characterized by a very robust in-plane honeycomb lattice structure where atoms are connected by covalent bonds. The out-of-plane interaction is weak and is of van der Waals type. Thanks to this conformation, it is easy to scale form bulk crystal to 2D material flakes by using simple mechanical exfoliation [3]. Moreover, layers of different 2D materials can be organized in staking, hold together by van der Waals forces [10]. From here the name van der Waals heterostructures (vdWHs).

In this chapter, I will start discussing about the techniques allowing to precisely manipulate 2D material flakes and stack them one over the other. The fabrication and exfoliation of 2D materials are well consolidate in literature and they rely on both top-down (e.g., mechanical or chemical exfoliation from bulk samples) and bottom-up (e.g., molecular beam epitaxy (MBE), chemical vapor deposition (CVD)) approaches [189, 191, 192, 193, 194]. In this chapter, I will explain in detail the stacking of 2D materials, starting from the mechanical exfoliation of bulk crystals to the fabrication of van der Waals heterostructures. I will also present the main steps for device engineering for electric and thermoelectric measurements.

2.1 2D materials exfoliation

For the first time in 2004, Geim and Novoselov prepared "thin carbon films" by repeated peeling of small masses of highly oriented pyrolytic graphite [1]. With this approach they were able to prepare single layer graphene (SLG) and few layers graphene (FLG) films up to 10 μm in size. Even though their films were few atoms thick, they were stable under ambient conditions and they presented remarkably high quality. From this incredible discover, mechanical exfoliation remains the primary method to rapidly access to high quality flakes for research aims. Extensive investigations by transmission electron microscopy (TEM) and scanning tunneling microscopy (STM) have shown that graphene flakes obtained by mechanical exfoliation from bulk graphite crystals are remarkably free of defects [195]. In the last two decades, plenty of 2D materials have been isolated with this top-down technique. The so-called Scotch tape

technique consists in the use of an adhesive tape which is placed on the bulk material and subsequently removed several times. Tiny flakes are peeled off from the bulk material and are brought down onto a substrate. By removing the adhesive tape from the substrate, monolayer and multilayer flakes are deposited. This technique produces small samples, typically about 5-30 μm in diameter, with a statistical distribution in the number of layers. The substrate that is generally used for the deposition of exfoliated flakes is a 280 nm SiO_2/Si wafer. This particular oxide thickness maximizes the optical reflection contrast in order to easily identify flakes with different thickness down to monolayers [196].

The Scotch tape technique is a top-down approach to obtain 2D materials flakes. Top-down approaches generally rely on various chemical/physical driving forces which can be employed to break the weak van der Waals interactions between the stacked layers of a bulk crystal to isolate single layers [197]. These approaches are of particular interest because they are easy to perform under ambient conditions and they produce high quality samples [189]. On the other hand, bottom-up approaches rely on the direct build-up of 2D materials with precursor atoms. Bottom-up synthetic strategies include CVD, physical vapor deposition, molecular beam epitaxy, atomic layer epitaxy, and wet chemical syntheses. These methods generally require harsh reaction conditions (e.g., high temperature, high vacuum) and complicated post-treatment steps (e.g., substrate transfer and purification) [197]. Moreover, it has been proved that 2D materials fabricated with bottom-up techniques exhibit lower mobility and greater impurity doping if compared to exfoliated samples. These differences are indicative of disorder and scattering processes that are not present in exfoliated samples and they are related to lattice defects and grain boundaries resulting from the growth process as well as structural defects and chemical contamination [198].

2.2 2D materials transfer techniques

The investigation of the physical properties of two-dimensional materials and their assembly in the so-called van der Waals heterostructures is nowadays one of the main goals in solid state physics. Mechanical exfoliation, applied for the first time in 2004 [1], is still the most employed technique to fabricate high quality flakes of 2D materials. The ability to pick-up and drop-down a reduced number of layers of different 2D materials is the key to build up functionalized heterostructures with well-known sequence and well-controlled properties. The hot pick-up technique, which is the method of choice employed during my PhD thesis, is a very innovative approach which allows to build layered materials with clean interfaces and well controlled electro-optical properties, by using simple fabrication steps at near room temperature [199]. The hot pick-up is a very versatile procedure, deterministic and fairly simple to perform. Moreover, it has been demonstrated that this technique is able to produce clean interfaces between 2D materials which result in the best device performance [200] since any contaminant presents between interfaces leads to deterioration of transport properties [201] as well as compromising the perfect interlayer adhesion [202].

2.2.1 Sacrificial polymer layers and wet chemistry transfer techniques

Up to 2014, the most common transfer methods relied on the use of sacrificial polymer layers and wet chemistry [203]. As an example, Schneider et al. have proposed the wedging method where water is used as active component for the transfer [204]. A hydrophobic polymer layer is spin-coated onto a hydrophilic substrate containing the material that one wants to transfer, which is required to be a hydrophobic nanostructure (as graphene flakes). When the substrate is dip in water, the polymer film is released entrapping the nanostructure and it floats at the air-water interface. The nanostructure can subsequently be deposited onto a target substrate by the removal of the water and the dissolution of the polymeric film. Similarly, Dean et al. have proposed a transfer method based on a water soluble PVA polymer layer [9]. The main steps of the technique are shown in Figure 2.1a. The flakes are transferred onto a substrate covered with PVA and a polymer sacrificial layer. The substrate is floating on the surface of a deionized water bath and once the water-soluble polymer has dissolved, the substrate sinks to the bottom of the bath. The polymer layer is then mounted in a micromanipulator to transfer the flakes to an arbitrary substrate. After the transfer, the polymer sacrificial layer is dissolved with solvents. More similar to the hot pick-up is the technique implemented by Zomer et al. [37], where the flakes are transferred onto a glass slide which has been spin-coated with a low glass temperature polymer (Evalcite). The glass slide is mounted in a micromanipulator and the acceptor substrate is heated up to 75°C - 100°C. When the polymer touches the substrate, it melts and adheres strongly to the surface, facilitating the transfer from the glass slide to the surface. After the transfer, the polymer layer has to be removed with solvents as in the previous methods. These methods turn out to be very time-consuming. They suffer from the presence of process residues related to the employed polymers during the fabrication steps and capillary forces which can create surface stress.

2.2.2 Dry transfer techniques

More recent dry transfer techniques are enabling the possibility of very fast and easy fabrication of van der Waals heterostructures. The hot pick-up technique [199] is one of the most famous among those. The central feature of this technique, of which process flow is depicted in Figure 2.1b, is related to the glass transition temperature of a polypropylene carbonate (PPC) polymer used to capture and release the desired flakes. The PPC polymer, with a glass transition temperature around 40°C [205], is spin-coated over a square-shaped polydimethylsiloxane (PDMS) polymer used as a support. The two polymers are mounted on a glass slide which is controlled by a x, y, z micro-manipulator (Figure 2.1b i). Once the PPC is in contact with the 2D flake, previously exfoliated on a SiO_2 substrate, by overcoming its glass transition temperature a strong and uniform interaction between the polymer and the 2D crystal can be obtained. As a consequence, the 2D material can be lifted from the original substrate. By tuning the temperature, it is possible to modulate the van der Waals adhesion between different materials. For example, a temperature of 40°C is sufficient to lift hBN from the SiO_2 substrate (Figure 2.1b i). The graphene adhesion to a plasma treated SiO_2 surface is stronger

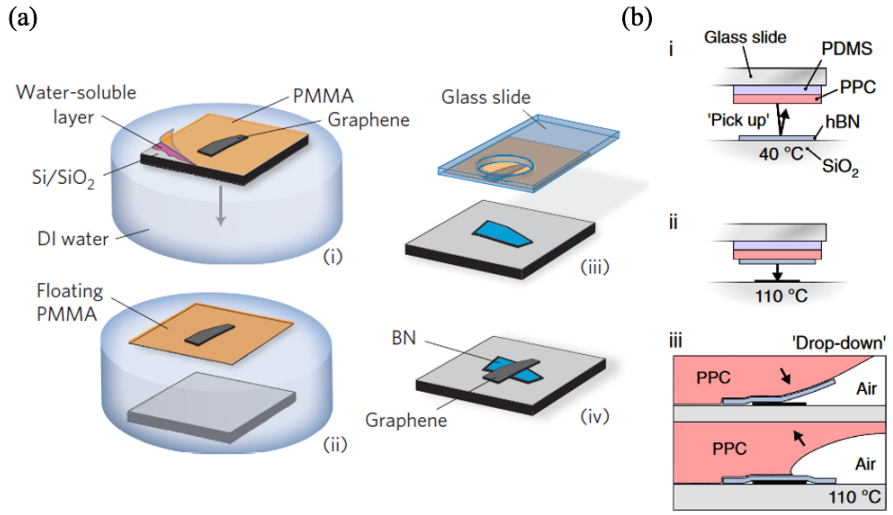

Figure 2.1 – (a) Schematic illustration of the transfer process used to fabricate graphene-on-hBN devices employing a water soluble polymer. Extracted from [9]. (b) Schematic process flow for assembly of 2D heterostructures by hot pick-up technique. Extracted from [199].

than hBN and a temperature of 110°C is required to pick-up graphene using a hBN crystal on PPC (Figure 2.1b ii). The drop-down is also performed at high temperature (Figure 2.1b iii).

The hot pick-up technique is not the only dry method used nowadays. For example, the transfer technique implemented by Castellanos-Gomez et al. [203] is another dry approach based, in this case, on the viscoelasticity principle. Instead of using a modulation of the temperature, this method exploits the speed of the polymer deposition/removal on the 2D flake. The employed polymer stamp is a thin layer of commercially available viscoelastic material (Gelfilm from Gelpak). It has been demonstrated that the stamp behaves as an elastic solid at short timescales while it can slowly flow at long timescales. The viscoelastic material gets a strong contact with the flakes which can be slowly peeled off and released from the polymer to the acceptor surface.

2.3 Fabrication of 2D van der Waals heterostructures

2.3.1 Exfoliation of graphene, hBN and WSe_2

The 2D materials employed in this work are initially isolated by classical mechanical exfoliation. Highly-pure single crystal bulk materials, illustrated in Figures 2.2a, 2.2b and 2.2c, are purchased from HQ graphene industry. A small piece of crystal is placed on an adhesive tape (F07-6.0 from MICROWORLD) to start the peeling procedure. After few peeling iterations, the tape is put on the SiO_2 substrate and gently removed. Some flakes of the 2D material are left on the substrate and can be used to build the heterostructure. As shown in Figures 2.2d and 2.2e, this approach works well for hBN and graphene, allowing to obtain a high enough density of exfoliated flakes with diameters of ~ 25 - 30 μm. Generally, the density of exfoliated flakes

is much higher for graphene than for hBN. The thickness of the flakes has a wider statistical distribution for graphene as well, going from the monolayer up to bulky flakes. The reported hBN flakes are more dispersed on the SiO_2 substrate and their thickness is generally around 40 nm. Concerning WSe_2 (Figure 2.2f), this approach produces a very high density of bulky flakes with quite small diameters of the order of few μm. This may be easily explained by the fact that graphene and hBN own a honeycomb lattice structure with strong in-plane sp-hybridized covalent bonds, while WSe_2 has a relatively weaker in-plane bond strength due to the trigonal prismatic coordination [206, 207].

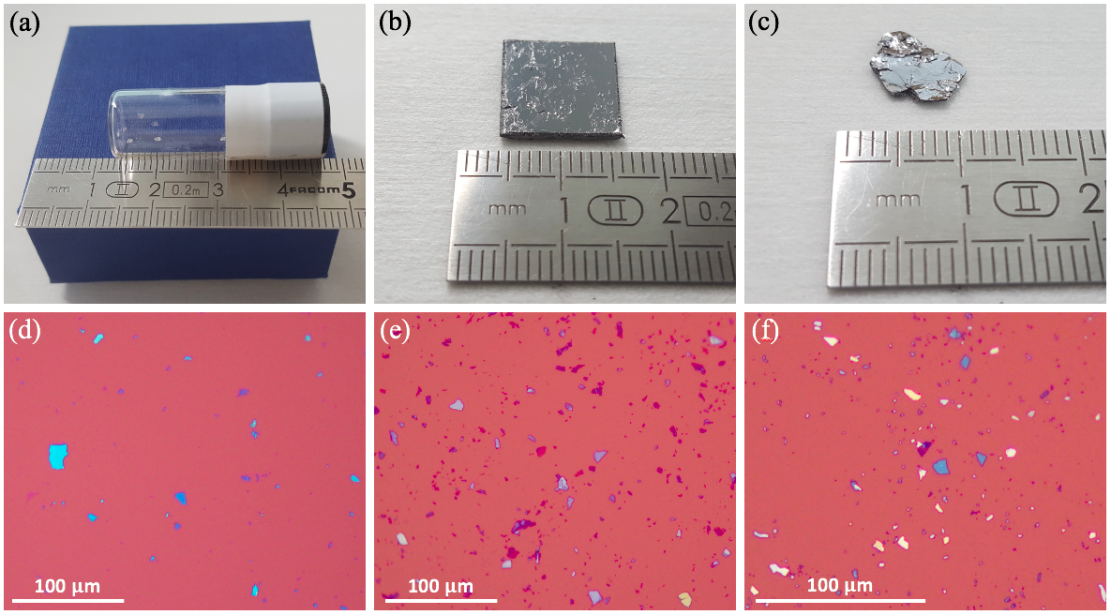

Figure 2.2 – Bulk crystal materials of (a) hBN, (b) graphene and (c) WSe_2. (d,e,f) Optical images of exfoliated materials on 280 nm SiO_2/Si wafer.

In order to achieve larger surface and thinner WSe_2 flakes, I have used for this material a different mechanical exfoliation approach. WSe_2 bulk crystal is exfoliated with PDMS Gel Film (DGL-30/17-X4), as shown in Figure 2.3a. Once the PDMS containing the exfoliated WSe_2 is in contact with the SiO_2 substrate, its removal is not performed by peeling it away from the substrate but with a shear stress. With this approach, it is possible to obtain single layers (SL) and few layers (FL) WSe_2 with lateral sizes up to 20 μm, as illustrated in Figure 2.3b.

To improve the transfer yield of exfoliated 2D materials from the scotch tape to the substrate, it is possible to proceed with an O_2 plasma treatment of the SiO_2 substrate before the flakes transfer. Such a treatment ensures a good adhesion with the substrate and increases both the density and the size of the transferred flakes. However, this procedure can also be detrimental since excessively increases the adhesion between the substrate and the flakes complicating the following steps of the fabrication, namely the hot pick-up transfer. Moreover, O_2 plasma-treated substrates could induce an undesired doping to the 2D flakes. For these reasons, this procedure is not employed in this work.

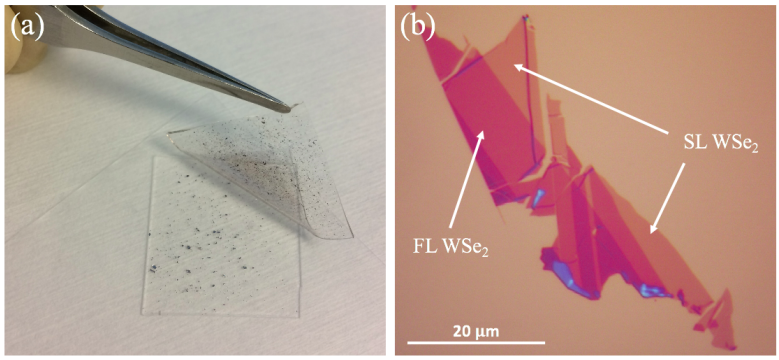

Figure 2.3 – (a) Exfoliation of WSe_2 with PDMS Gel Film. (b) Optical image of exfoliated WSe_2 on 280 nm SiO_2/Si substrate.

2.3.2 Glass slide support for dry transfer

The exfoliated 2D materials are subsequently transferred by the hot pick-up transfer technique to fabricate the desired stacking. In order to perform the pick-up and the drop-down of the 2D materials, a polypropylene carbonate (PPC) coated polydimethylsiloxane (PDMS) block is mounted on a glass slide. Differently from the configuration mostly used in literature, a drop-like shaped PDMS/PPC, as Figure 2.4a illustrates, is employed to have a higher control on the contact location with the flakes and to facilitate the stacking procedure. The PDMS is prepared from SYLGARD 184, by mixing 10 parts of base and 1 part of curing agent at room temperature. The solution is let to dry for almost 8 hours at room temperature to make it more viscous and after it is deposited on the extremity of the glass. The glass is positioned upside-down to obtain the drop structure and it is left overnight to solidify. The PPC polymer is spin-coated (2500 rpm for 40 s) on the solidified PDMS drop. Each drop can be re-used several times for pick-up/drop-down as long as the PPC is still uniform and free of defects on the top of the PDMS. In case of delamination of the PPC from the PDMS, some residues of polymer can remain on the sample. A rapid cleaning in acetone and isopropanol is effective to completely remove the PPC.

2.3.3 Staking of 2D materials in a van der Waals heterostructure

The stacking of the different 2D layers is performed in a clean-room environment by using two micro-manipulators to achieve micrometric alignment accuracy. The SiO_2 substrate containing the exfoliated flakes is hold with a double side tape on a hot plate moved by the first micro-manipulator. The glass slide containing the polymer drop is hold upside-down by a second independent micro-manipulator. The pick-up, the alignment and the drop-down are performed by using an optical microscope ($\times 10 - \times 50$) in reflection mode. The employed set-up is shown in Figure 2.4b. By tuning the temperature of the SiO_2 substrate, it is possible to modulate the interaction strength between the 2D layers and the substrate itself. Moreover, overcoming the glass transition temperature of the polymer in contact with the 2D flake allows to have a higher and more uniform adhesion at the interface. This will favor the flake to leave

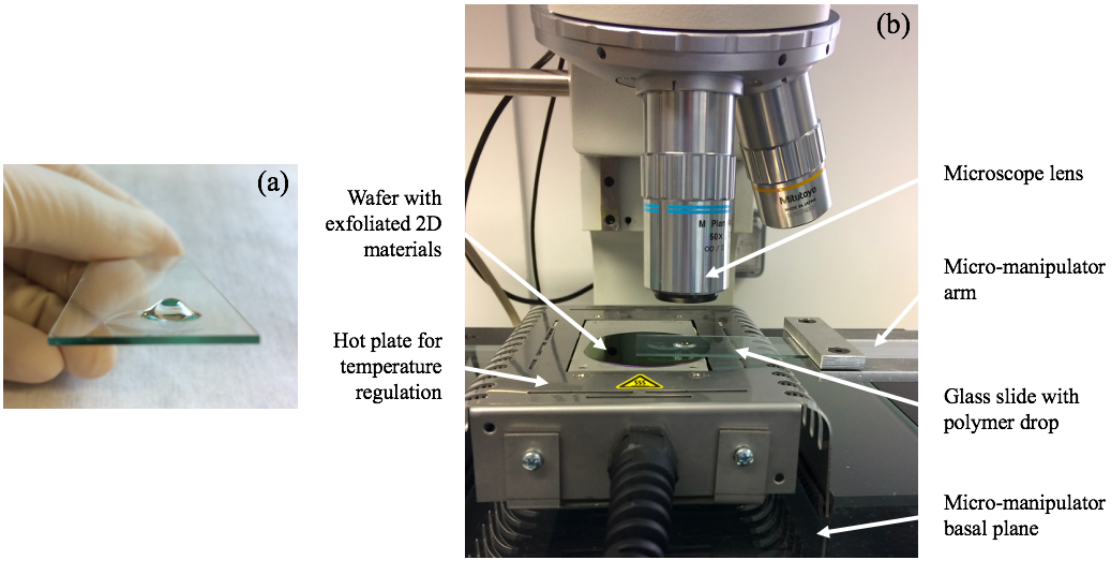

Figure 2.4 – (a) Drop-like shape of the PDMS/PPC on a glass slide support. (b) Set-up for hot pick-up transfer: a hot plate is used to modulate the temperature; the wafer substrate containing the exfoliated 2D samples is fixed on the hot plate and an optical microscope is used to locate the flakes by optical contrast; a second mico-manipulator moves the glass-supported PDMS/PPC drop.

its original substrate during the pick-up. The temperature of the hot plate is kept between 65°C and 75°C. It is important to ensure that the drop slides on the substrate with enough fluency without being too liquid. For lower temperatures the drop will remain glued on the substrate, while for higher temperatures the PPC will delaminate from the PDMS.

The first step to build the heterostructure is to find the desired flake among the exfoliated ones. The 280 nm thick SiO_2 allows to distinguish the number of layers by optical contrast. Once the flake is selected, we align the drop above it with the help of the two micro-manipulators. The drop is first approached roughly. At a distance lower than few mm, it is possible to focus with the microscope objective on the tip of the drop. Typically, only the central part of the drop is transparent while the rest of the drop appears gray and opaque. More the drop is pronounced, smaller will be the diameter of the transparent part and easier will be the alignment over the flake. By moving the focal plane into an intermediate location between the end of the drop and the substrate, we can follow the landing of the drop that will reach the focal plane during its descent, and gently approach it to the substrate (Figure 2.5 (a-d)). When the drop and the substrate are simultaneously on-focus, we locate the flake in the center of the drop and establish the contact. After waiting few second to ensure the thermalization of the drop with the substrate, we pull-up the drop gently at the beginning, but fast when the drop is covering an area comparable to the flake size. We realize that the flake has been removed from the substrate because it has become transparent but more opaque with respect to the drop and its profile is on-focus in the drop focus plane. We can now pull-up the drop and change the substrate. Again, we approach the drop to the new substrate following the same procedure to achieve the contact. In this second step, the important difference is that the pulling-up of

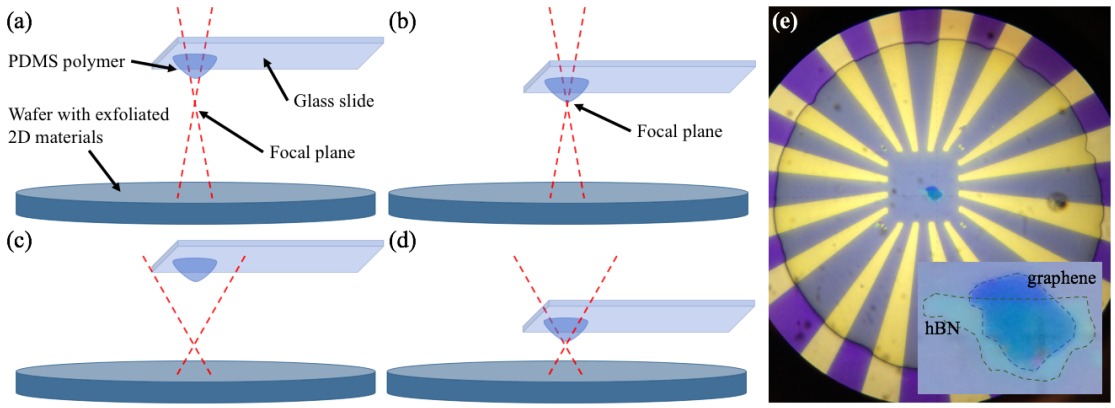

Figure 2.5 – (a-d) Schematic cartoon illustrating how the polymer drop gently approach the substrate containing the 2D flake by step-approaching the focal plane to the wafer substrate. (e) Optical microscope image of a two-layers heterostructure made of graphene/hBN deposited on a pre-patterned substrate. Inset: zoom on the graphene/hBN heterostructure.

the drop has to be as slow as possible. In this way, the interaction between the flake and the substrate dominates and the flake will leave the polymer drop. Finally, an acetone/isopropanol cleaning is recommended to eliminate eventual polymer residues. The entire procedure can be repeated several times to pick-up and drop down the desired 2D material flakes in the desired locations. Figure 2.5e shows an optical microscope image during the drop-down of a hBN flake (light blue) over a graphene flake (dark blue) as illustrated in the inset. The drop is still in contact with the substrate. Another possible procedure is to pick-up one flake above the other and then drop-down the entire structure at once. This approach allows to avoid the contact between the lower layers of the heterostructure and the polymer, since only the top layer will touch the polymer. However, due to the transparency of the layers, this procedure makes harder the alignment of the different flakes during the stacking.

2.4 Interlayer contaminants within van der Waals heterostructures

When dealing with van der Waals heterostructures, interfacial contamination is an important issue to address. In fact, when 2D crystals are stacked together, surface contaminants become trapped between the layers, creating small blisters that are not always visible with the optical microscope. Even though dry transfer techniques offer time-saving fabrication alternatives and cleaner devices, they still remain affected by polymer residues from the transfer and lithographic processes. These residues can hinder the assembly of multilayer structures by aggregating into "bubbles" between layers [10, 199]. Figure 2.6a illustrates the AFM image of a hBN/graphene/hBN stack in which it is evident the presence of trapped blisters of different size. The line profile highlights how the bigger blisters can reach diameters as wide as 5 μm and heights exceeding 100 nm (Figure 2.6b). Recent studies have investigated the nature of these contaminants down to a few attomoles with nanoscale resolution employing photothermal induced resonance (PTIR) technique [208]. Analyzing heterostructures based on WSe_2, WS_2,

and hBN, Schwartz et al. [208] found that the interlayer blisters contain significant amounts of poly(dimethylsiloxane) (PDMS) and polycarbonate, corresponding to the stamp materials generally used in dry transfer techniques. They also demonstrate that cleaning PDMS stamps with isopropyl alcohol or toluene before the vdWH fabrication reduces PDMS contamination within the structures. On the other hand, acetone or hexane turn out to be ineffective at reducing or preventing contamination.

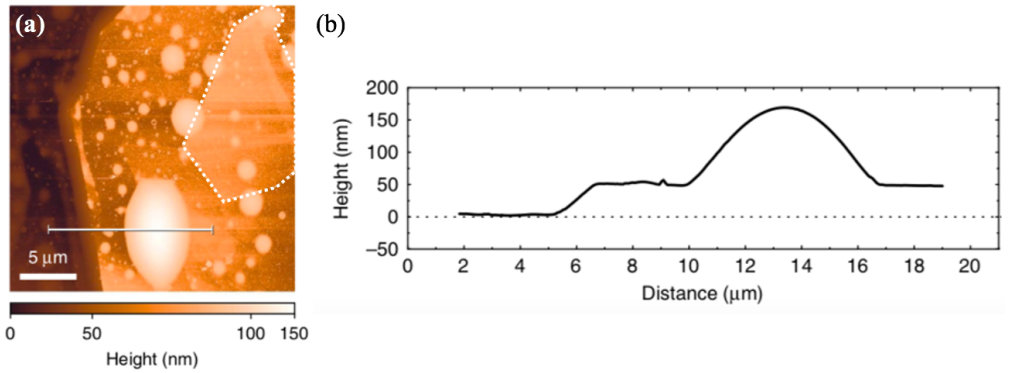

Figure 2.6 – (a) AFM image of hBN/Graphene/hBN stack. Encapsulated graphene flake is indicated by dotted line. Many hemispherical blisters are visible over the stack surface. (b) Topography line profile of blister from indicated region in (a). Extracted from [199].

Improved performances have been seen upon the removal of these residues, which can be also achieved by annealing in oxygen [209, 210], by "sweeping" with an AFM tip [211, 212] or thanks to fully micrometer-scale hBN-encapsulated sample fabrications [213]. As an example, Figure 2.7 illustrates schematically how it is possible to push the interlayer blisters at the edges of a vdW heterostructure by applying a normal force on the flakes while scanning with an AFM tip. With this technique it is possible to collect the contaminants into a pocket, leaving behind a region free of bubbles.

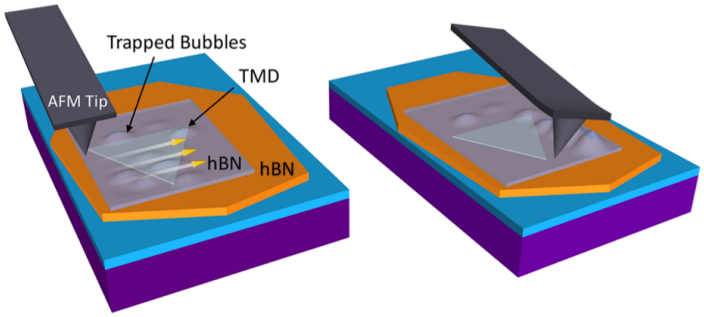

Figure 2.7 – Cartoon illustrating the general concept of AFM flattening by applying a normal load with the AFM tip during the scanning. Contaminants are collected in lateral pockets, leaving behind a region without bubbles. Extracted from [212].

To achieve even cleaner interfaces, a hBN flake can be used to prevent the 2D material of interest to come in contact with the polymers employed in the transfer. Large-area hBN-

encapsulated devices are assembled by using the top layer in the heterostructure to pick-up subsequent layers, using only van der Waals forces, so that the interior flakes are never in contact with the polymers [214]. For example, the graphene-hBN interfaces produced by this van der Waals assembly technique has been proved to show no evidence of contamination in cross-sectional imaging by scanning transmission electron microscopy (STEM), and bubble-free areas in the size of tens of micrometers can be achieved. However, electrical contact to the fully-encapsulated core layer needs to be performed by metallization of the 2D material edge exposed after etching [214], which is a challenging step.

2.4.1 Thermal treatment to reduce the inter-layer contamination

During my PhD, I have tried to address the issue of interfacial contamination reduction during the staking of 2D materials. To do so, I have characterized the fabricated van der Waals heterostructures by (tapping mode) AFM. AFM analysis is useful to measure the thickness of the stacked layers and the surface roughness, but also to reveal details that cannot be observed by optical microscopy. In particular, it emerges that the adhesion between the layers is non uniform and some bubbles with different size are present in the overlapping regions. To make an example, Figure 2.8a shows a graphene/hBN/WSe_2 heterostructure optical image and Figure 2.8b shows the corresponding AFM image taken at room temperature and atmospheric pressure. The presence of interlayer bubbles appears evident in the AFM image. The bubbles located between graphene and hBN appear different in dimension and density from the ones located between hBN and WSe_2. A small density of large bubbles underneath the hBN is in opposition to a higher density of small bubbles below the WSe_2. Figure 2.9 shows a typical AFM profile analysis of these asperities. In Figure 2.9a is illustrated the profile of a bubble between graphene and hBN, while in Figure 2.9b the profile of bubbles between hBN and WSe_2. In the first case, the diameter is generally larger, and it ranges from 0.5 μm to 2 μm. The maximum height reached is around 25 nm. In the second case, the bubbles are smaller and their diameter ranges from 100 nm to 0.6 μm. The approximate height is around 16 nm.

The evidence of a different bubble nature related to the location in the heterostructure cannot be simply explained by the possible residues of the transfer process or lithography resists [10, 199, 208]. For instance, these bubbles could be caused by a sudden release of the strain generated by the applied pressure of the viscoelastic stamp during the transfer [203]. Goler et al. [215] have proved that "blistered" graphene surface is due to strain induced by the transfer process itself and it is not related to the presence of underlying nanoparticles. They have also shown that heating the sample at a temperature of 150°C for 20 minutes yielded a decrease of both blister density and height of around 20% on average.

In order to reduce the presence of bubbles, I have performed thermal annealing tests on some samples, both in vacuum and at atmospheric pressure. As a representative example, the graphene/hBN/WSe_2 heterostructure shown in Figure 2.8 has been annealed in vacuum ($\sim 10^{-6}$ mbar) at 350°C for 1 hour. Afterword, a second AFM image has been acquired as

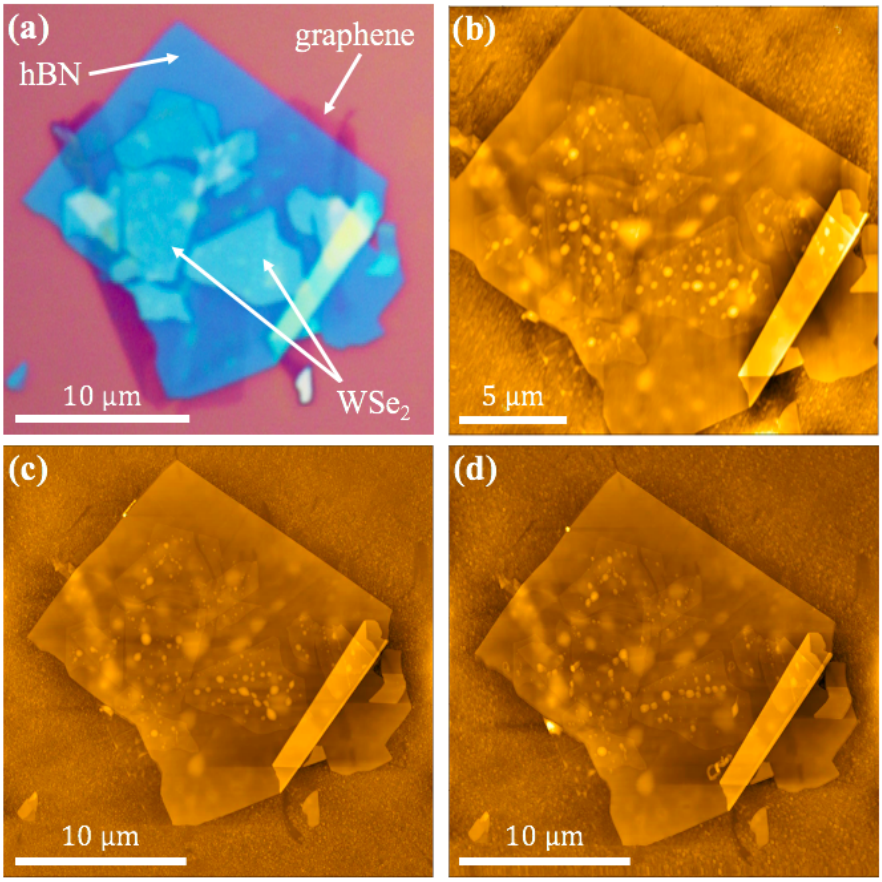

Figure 2.8 – (a) Optical image of a graphene/hBN/WSe_2 heterostructure and (b) corresponding AFM image. AFM images (c) after a vacuum thermal annealing followed by (d) a atmospheric pressure thermal annealing in flowing H_2/Ar gas. Both annealing have been performed at 350°C for 1 hour.

shown in Figure 2.8c. Compared to Figure 2.8b, an important reduction in the number of bubbles between hBN and WSe_2 is visible. However, no relevant changes can be noticed on the blisters between graphene and hBN. After the annealing in high vacuum atmosphere, an annealing in flowing H_2/Ar gas at 350°C for 1 hour has been performed at atmospheric pressure (Figure 2.8d). In this case, the density of the small blisters between hBN and WSe_2 is almost unchanged but important displacements can be remarked. Again, no changes occur in the underling layers.

These experimental observations seem to indicate that bubbles between hBN and WSe_2 have a higher mobility when compared with bubbles between graphene and hBN. This can be explained by a weak interface affinity between hBN and WSe_2, which explains the smaller blisters, present in a larger number between these two materials. On the other hand, contaminants between graphene and hBN agglomerate in bigger and less numerous blisters in order to maximize the contact surface of the two 2D materials. This is in agreement with the fact that graphene and hBN have a very small lattice mismatch. Supposing that the affinity between the two 2D crystals is larger than the affinity between the crystals and the contaminants, then

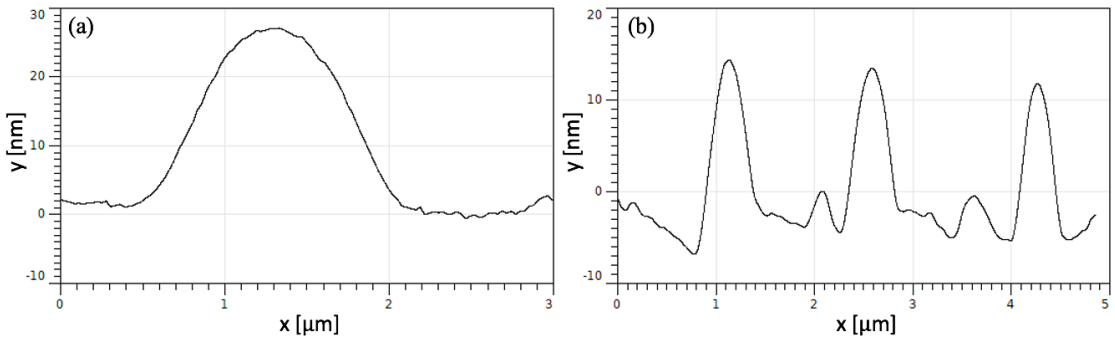

Figure 2.9 – Typical bubble profiles (a) between graphene and hBN and (b) between hBN and WSe_2. These profiles are extracted from the AFM image in Figure 2.8.

the energetically favorable situation is when the two 2D crystal flakes have the largest possible common interface [201]. To achieve this condition, the contaminants are pushed away, allowing the rest of the interface to become atomically clean. This explains the observation of bubbles under transferred 2D crystals and the fact that the pockets of contaminants merge together when the heterostructure is annealed. This phenomenon is defined as "self-cleaning" mechanism of van der Waals heterostructures [10, 201]. Figure 2.10 shows schematically how the "self-cleaning" mechanism takes place when a 2D materials undergoes to a temperature annealing. Increasing the temperature promotes the removal of gas molecules between the 2D material and its substrate surface via the edges, driven by an increase in pressure at the interface. When the sample is cooled to room temperature, the flake edges act as a one-way valve: they allow pressure built up during annealing to be released by the transfer of gas away from the interface, however, once a tighter and more uniform contact is established between the 2D layer and the support, the increased van der Waals force prevents gas from re-entering during the cooling down. As a result, trapped species are eliminated from the interface and a tighter and more uniform contact is established [189].

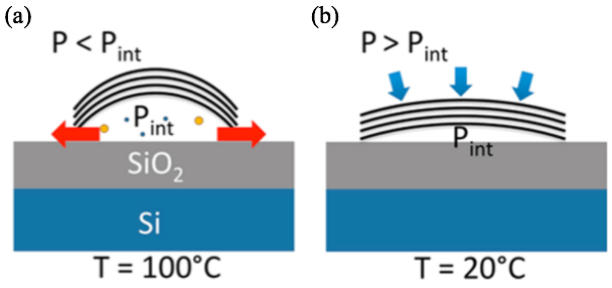

Figure 2.10 – (a) Annealing of the substrate in contact with a 2D material. The increase in temperature builds the pressure at the interface between the 2D material and the underlying substrate, which is released by the escape of gas. (b) Cooling the temperature results in a reduction of the pressure at the interface. This leads to a tightened substrate/2D material interface. Extracted from [189].

To have a closer look at the graphene/hBN interface, I have performed some thermal annealing treatments to a graphene/hBN heterostructure (illustrated in Figure 2.11a). Some blisters are visible already from the optical image in the hBN region as clear spots. Figure 2.11b shows the

correspondent AFM image before any treatment. The sample is annealed at 350°C for 1 hour in flowing H_2/Ar. The resulting AFM image is reported in Figure 2.11c. The blisters are slightly larger both in diameter and height, and some of them start to merge. After another hour of annealing in the same conditions (AFM in Figure 2.11d), the small bubbles start to disappear while the bigger ones are more increased. Other two annealing steps (Figures 2.11e and 2.11f) have been performed for 2 and 4 hours, respectively. In this case, no major changes have been detected.

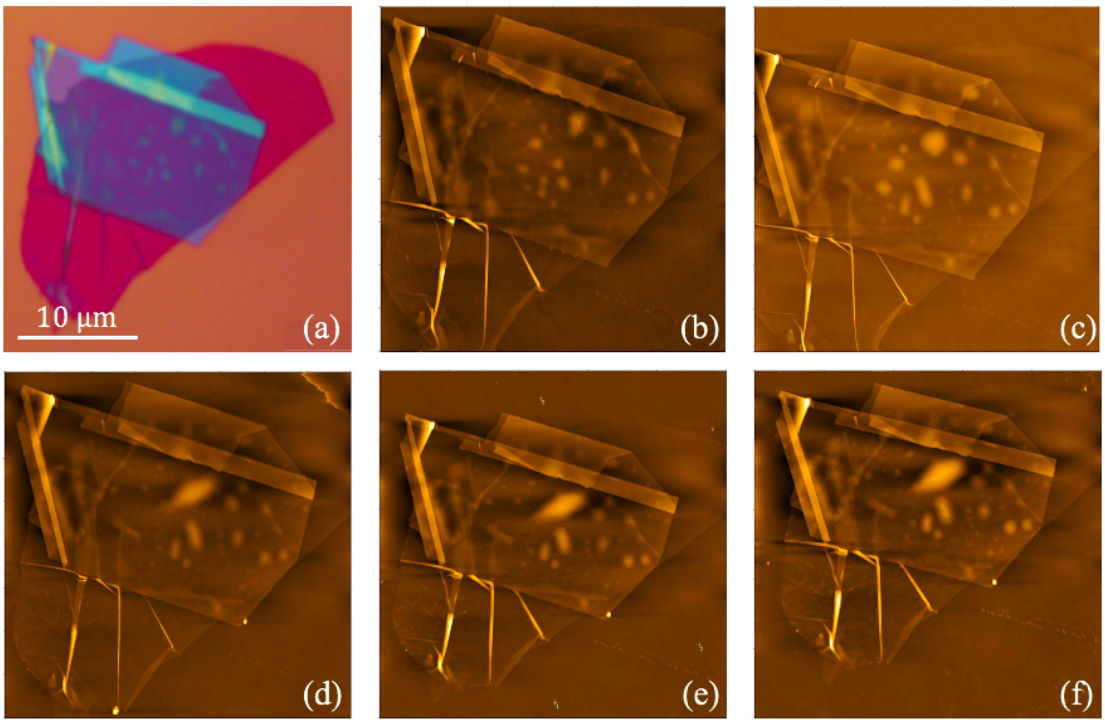

Figure 2.11 – (a) Optical image of a graphene/hBN heterostructure and (b) corresponding AFM image before any thermal treatment (t=0). AFM image of the sample after a thermal annealing at 350°C in flowing H_2/Ar at atmospheric pressure at (c) t+1h, (d) t+2h, (e) t+4h, (f) t+8h.

During the annealing steps, a reduction in the surface roughness (RMS) has been recorded. This is probably related to the fact that the high temperature reduces the amount of stress present on the surface, as suggested by Jain et al. [216]. This hypothesis is consolidated by the fact that even if the amount of bubbles does not decrease, the RMS surface roughness is reduced. In conclusion, given the results of this brief analysis, we can suppose that the interlayer impurities present in the fabricated heterostructures are related to several factors mainly including residues of polymers and stress generated during the transfer procedure. Since moving pockets of defects could influence the electric and thermoelectric measurements which will be discussed in the following (Chapters 3 and 4), an in-situ temperature annealing at 400°C is performed on every device at high vacuum ($\sim 10^{-7}$ mbar). Subsequently, the measurements are performed without breaking the vacuum.

2.5 Example of device fabrication

During my PhD work, I have fabricated 2D material-based devices using the hot pick-up transfer technique. In particular, I have designed field effect transistors (FET) based on WSe_2 semiconducting channel, coupled to a local gate by a hBN flake acting as dielectric. The local gate has been made by a metallic pad or a graphene flake. The use of hBN as dielectric results in a more efficient gate coupling and control. Moreover, the atomically flat and free-of-charge-traps surface of the hBN prevents Coulomb scattering and enhances the performances of the device. hBN can also be employed to fully encapsulate the core material of the heterostructure in order to prevent its interaction with the environment and a possible degradation due to the atmosphere or the adsorption of gas molecules. The WSe_2-based FETs have been electrically and thermoelectrically investigated.

In a second experiment done during my PhD, I have fabricated multilayer graphene nanowires by reshaping (by reactive-ion etching (RIE)) graphene flakes directly deposited on a thick SiO_2 substrate by hot pick-up transfer. In this case, I studied the thermal transport through such a 2D material-based device. The thick oxide layer, fabricated by PECVD, was designed to thermally decouple the nanowire from the environment.

To illustrate a complete fabrication process, I will present here, as an example, the fabrication of a hBN/WSe_2-based FET-like device with a metallic local gate. The use of graphene as local gate has been widely adopted during my PhD. However, local defects in graphene (such as wrinkles, charges puddles, etc.) can generate a non-uniform electric field which creates instability in the electrical gating. Indeed, preliminary tests performed with local graphene gate have shown unstable and non-reproducible electric measurements. Moreover, due to the non-uniform electric field, electric leakages through the hBN dielectric layer were likely to open. For these reasons, I decided to use as local gate a metallic pad underneath the hBN.

Optical lithography step

As a first step, before the transfer of the 2D materials, 16 electrodes defining the perimeter of a square working area of 100 × 100 μm^2 are obtained by optical lithography and metal evaporation. Optical lithography allows for the exposure of very large areas in order to create several 100 × 100 μm^2 working areas, but the maximum resolution of the geometries is quite coarse ($\sim$ 1 μm). To proceed with the optical lithography, a clean 280 nm-thick SiO_2 wafer is spin-coated (500 rpm for 3 s followed by 4000 rpm for 30 s) with an adhesion promoter resist (Ti-prime) and annealed for 2 minutes at 120°C. A reversible resist (AZ 5214 E) is then spin-coated (same spinning parameters) and subsequently annealed at 110°C for 60 s to ensure the solvent evaporation. The sample is installed in the mask aligner (MJB4 Suss Microtec) and it is put in contact with the lithographic mask. Figure 2.12a shows the digital image used to design the quartz mask, in which the illustrated pattern is repeated over a large area. Vacuum contact mode is used to improve the resolution by reducing the space between the mask and the resist. The sample is selectively illuminated for 1.8 s by UV radiation. At this stage, the illuminated

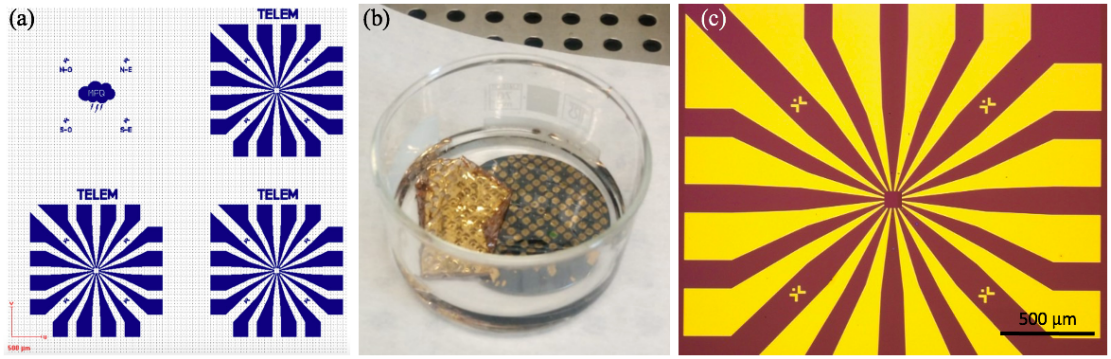

Figure 2.12 – (a) Digital image used to design the quartz mask for optical lithography. (b) Complete lift-off in acetone of a metallic layer after photolithography and contacts evaporation. (c) Pre-patterned substrate with metal electrodes defining a working area of 100 × 100 μm^2.

areas become soluble. Then, the sample is baked for 2 minutes at 120°C and exposed to a flood illumination for 60 s. These last two steps allow for an inversion of the solubility. Finally, the wafer is dip in the developer (AZ 326 MIF) for 18 s and rinsed in deionized water. Before the metallic evaporation, the wafer is treated in O_2 plasma for 1.5 minutes to eliminate resist residues and improve the adhesion of the metal. A Ti/Au (5/100 nm) metallic layer is deposited by e-gun evaporation. To remove the resist and lift-off the undesired metallic layer, the wafer is immersed in acetone for few hours, as illustrated in Figure 2.12b. An optical image of the patterned substrate with micrometric-sized electrodes is reported in Figure 2.12c. The large-ending side of the 16 electrodes will be used to connect the device in a micro-probe station by clamps or for micro-bonding. On the other hand, the tiny-ending pads in the central area will be connected to the heterostructure with extra electrodes fabricated by e-beam lithography and metal deposition.

Electron-beam lithography step

Once the 100 × 100 μm^2 working area is defined, a first e-beam lithography step, allowing to attain high resolution down to some tens of nanometers, can be performed to design a local gate and a local micro-heater as schematically represented in Figure 2.13a. An electron-sensitive resist (PMMA A6 dilute 2:1 in anisole) is spin-coated on the sample (500 rpm for 5 s followed by 4000 rpm for 40 s) and then annealed at 180°C for 60s to evaporate the solvent. The resist is exposed by an electron beam (dose = 200 $\mu C/cm^2$; gun = 10 kV; aperture = 20 μm) on the surface of the sample in a customized pattern designed by means of a computer design software (Raith). PMMA is a positive resist and the e-beam exposed windows become soluble in the developer (MIBK 1:3 in IPA for 18 s then rinsed in pure IPA). Figure 2.13b shows the optical image of a representative sample after the metallic deposition (Ti/Au 5/35 nm) and lift-off. The 2D material flakes, hBN and WSe_2, can be finally transferred on the top of prefabricated gate by the previously described dry transfer technique (Figures 2.13c and 2.13d). Finally, a second e-beam lithographic step is performed to electrically connect the semiconducting material with 80 nm-thick metallic electrodes (Figures 2.13e and 2.13f).

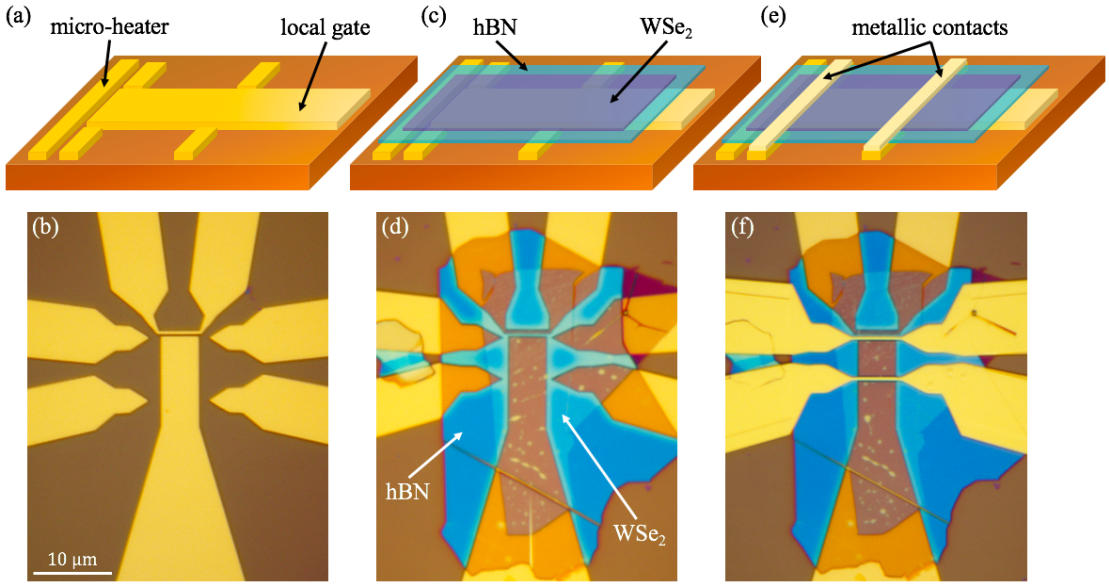

Figure 2.13 – Device fabrication steps: (a,b) local gate and micro-heater for gate modulation and thermoelectric measurements; (c,d) transfer of hBN and WSe_2; (e,f) metal contacts for electric transport and V_{TE} measurements.

Since the WSe_2 is electrically isolated from the local heater by the hBN, as required for the thermoelectric measurements, no etching/patterning is required. Concerning the electric measurements, the charge transport channel can be fairly approximated as the WSe_2 area in which the charge density can be modulated by the gate electrode. This allows to avoid further lithographic processes and interaction with etching gases which could deteriorate the properties of the semiconducting material. In fact, etching processes generally require resists which are too adhesive to remove and the interaction with gasses which could modify the properties of the resist and the 2D material itself. Moreover, etching processes are not able to control the lateral-edge roughness. This introduces scattering processes which are difficult to master and discern [138].

Metallic deposition

Each lithography step is followed by a metallic deposition. The samples are loaded in the e-beam evaporator (Plassys) and they are systematically degassed before the metal evaporation of the electrodes over the heterostructure. To this purpose, the sample holder is heated at 120°C for 2 hours under vacuum ($\sim 10^{-6}$ mbar), then it is naturally cooled down while the chamber is let to pump all night long, reaching a typical pressure of $\sim$ 1-2 $\times$ 10^{-7} mbar. A titanium pre-cleaning of the chamber is performed right before the metal evaporation to further decrease the pressure ($\sim 5 \times 10^{-8}$ mbar). The evaporation takes place with a rate of 0.04 nm/s. The metal lift-off removes the unwanted metal.

The choice of the metal contact is crucial to optimize charge injection, in particular for 2D materials, since interface properties could dominate the whole device response. This topic

will be developed with more details in Chapters 3 and 4. To study the influence of the metal contact, I have fabricated several devices with silver (Ag), palladium (Pd), cobalt (Co) and titanium (Ti) electrodes with a thickness of 20 nm, all cupped with 60 nm-thick gold (Au) layer to prevent metal oxidation and give electrical stability to the metallic lines.

2.6 2D materials reshaping

For research purposes, good quality 2D materials are derived from mechanically exfoliated bulk crystals and thus, they typically have random shapes, defined by the interactions between the atoms. However, in many cases, a well-defined sample geometry is necessary when preparing devices to explore electronic [42, 53] or optical [217] properties. Graphene is usually etched by defining a resist mask and using oxygen plasma. However, oxygen is not suited to etch other 2D materials since it reacts efficiently only with organic compounds. For this reason, mastering a selective etching technique for 2D materials is a prime necessity when constructing heterostructures. Although all the materials are sensible to the physical sputtering aspect of the etching process, the selectivity holds in the difference of their response to the physio-chemical plasma.

During my PhD, I have optimized a recipe to etch van der Waals heterostructures based on WSe_2 and I have used this procedure to reshape the WSe_2-based devices fabricated with a graphene flake acting as local gate. Even if these graphene-gated devices are not shown in this manuscript, I still decided to show the etching procedure that I developed. In fact, even though in the presented devices the need to reshape the 2D materials was bypassed by the use of a pre-patterned metallic gate and micro-heater, the developed etching recipe could be of essential use for future device designs. Finally, I will show the procedure implemented to reshape graphene flakes to fabricate graphene nanowires to study their thermal conductivity as it will be discussed in Chapter 5.

2.6.1 hBN and WSe_2 etching

Sulfur hexafluoride (SF_6) is the reactive gas that I employed to selectively etch both hBN and WSe_2 in van der Waals heterostructures without affecting graphene. When used with WSe_2, fluorine radicals form volatile compounds with selenium (Se) and tungsten (W). These volatile species remain on the substrate for a residence time before desorbing from the surface. Ion bombardment can reduce the residence time [218]. An identical behavior occurs when fluorine reacts with boron atoms of hBN flakes forming highly volatile BF_3 molecules [219]. To investigate the etching rate, I have selected and transferred uniform 2D material flakes on a SiO_2 substrate. A layer of PMMA is spin-coated over the samples and an etching window is defined by e-beam lithography. The sample is placed in a reactive-ion etching (RIE) chamber filled with 25 sccm of SF_6 at a pressure of 40 mTorr. An oscillating electric field in the radio frequency range (RF bias of 5.0 V $\pm$ 0.3 V amplitude) applied at 8 W ionizes the gas, creating a plasma. The plasma is kept ON for a time t with an uncertainty of $\sim$ 3 s which are required

to turn ON and OFF the electric field. The positively charged ions collide with the exposed surface of the sample and chemically react with it. At the same time, they also sputter some material atoms by kinetic energy transfer. The part of the sample uncovered by the resist is etched faster than the resist itself because of chemical selectivity. Afterwards, the resist is weakened with an oxygen plasma cleaning (525 mTorr, 160 W and 10 sccm of O_2) for 5 minutes and washed away in acetone/isopropanol. The procedure is repeated to open a second etching window which is etched with a different time t.

The etching procedure has been performed on 8 hBN samples starting from a minimum etching time of 3 s and increasing in steps of 3 s up to 21 s. Figure 2.14a shows a flake of hBN before and after 7 etching steps performed in adjacent etching windows with different exposition time. During the procedure the flake is only partially etched away, while the last etching window shows the complete absence of the material. This is particularly evident in Figure 2.14b which shows a scanning electron microscopy (SEM) image of the same sample. The etching is not uniform and some residues, caused by the interaction between the SF_6 plasma with the 2D material, remain in the etching window. Since no etching residues remain on the SiO_2, as clearly evidenced in the AFM image shown in Figure 2.14c, we can conclude that these residues are not related to the resist.

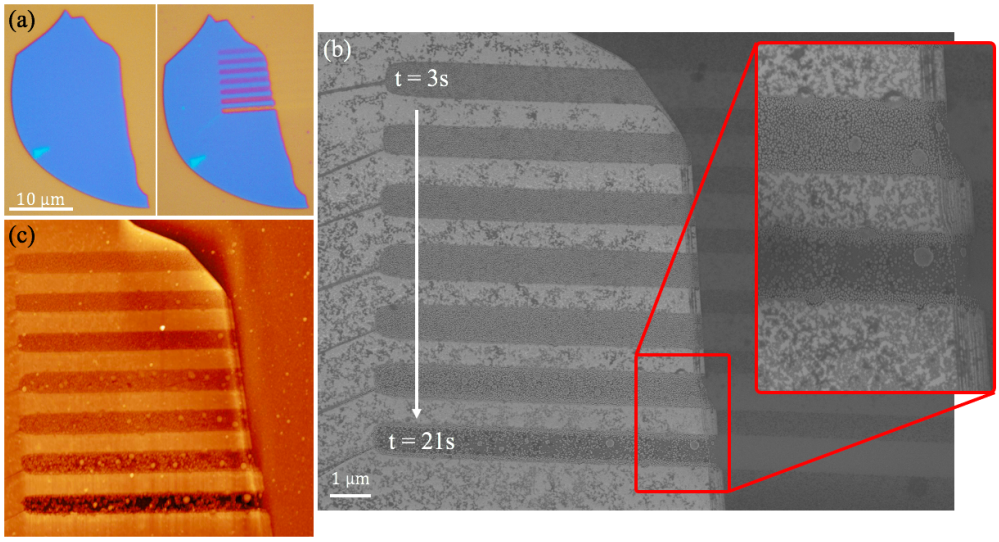

Figure 2.14 – (a) Optical image of a hBN flake before and the etching process. (b) SEM image of the etched windows for different etching time. The zoom illustrate the etching for t = 18 s and t = 21 s. (c) AFM image of the etched windows in that same sample.

After all the etching steps, the samples have been characterized by AFM to evaluate the etched thickness. Figure 2.15a illustrates the thickness of 2D material removed as a function of the exposure time in SF_6 plasma. The error bar is given by the statistical dispersion among the samples, incremented by the AFM uncertainty related to the surface roughness. The etching rate for hBN is evaluated to be 0.49 ± 0.06 nm/s which results to be particularly low, and thus controllable to a few nanometers. However, given the hBN single layer thickness (~ 0.33 nm) and the minimum amount of time needed to turn the plasma ON and OFF, this

etching procedure has a limiting etching sensibility of 1.5 nm corresponding roughly to 5 hBN layers. Moreover, due to the non-uniform etching, this protocol does not allow to master a layer-by-layer removal.

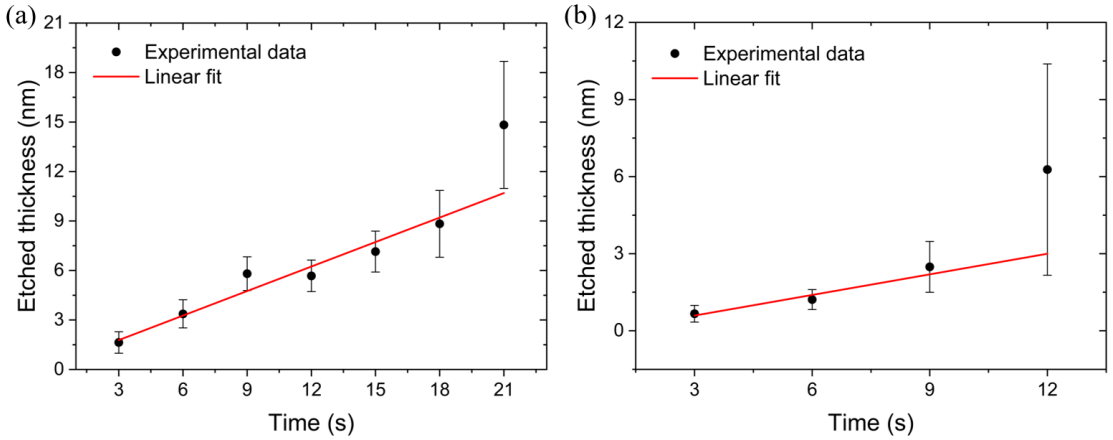

Figure 2.15 – Etched thickness of (a) hBN and (b) WSe_2 as a function of etching time. For a given etching time t, the reported thickness of the removed 2D material is the average of the experimentally measured etched thickness of the studied samples (8 for hBN and 10 for WSe_2) and the error bars are given by the statistical dispersion among the samples. The red line is a linear fit to the data.

The same procedure has been applied on 10 WSe_2 samples. Since the WSe_2 flakes employed in this work are less then 10 layers-thick, I explored the etching time in the range between 3 and 12 s. Figure 2.15b illustrates the thickness of WSe_2 removed as a function of the etching time. The etching rate has been evaluated to 0.27 ± 0.09 nm/s. Also in this case, a layer-by-layer removal is not possible.

Heterostructure reshaping for thermoelectric measurements

To correctly perform a Seebeck coefficient measurement, one needs to design a local heater as close as possible (~ 100 nm) to the heterostructure, without any electrical connection to it. Given the random shape of the flakes composing the heterostructure, one way to fulfill this requirement is to completely etch the heterostructure between the heater and the first electrode of the heterostructure after the metal deposition. Figure 2.16a shows an equivalent heterostructure as the one illustrated in Figure 2.13f with a graphene flake used as gate electrode, just after the fabrication of the metal interconnections. A rectangular masque (red dashed contour in Figure 2.16a) is created by using a negative resist (MaN-2401) covering the heterostructure. Country to the previously-used positive resist, the negative resist will remain in the exposed regions to protect the sample from the etching. The sample is first dehydrated at 120°C for 4 minutes. An adhesion promoter resist layer (Ti-Prime) is spin-coated (500 rpm for 3 s followed by 4000 rpm for 30 s) and annealed at 120°C. The negative electron sensitive resist (MaN-2401) is spin-coated (same spin parameters) and baked at 95°C for 60 s. The MaN-2401 has a thickness of 100 nm. If longer etching is needed, it is possible to use the MaN-2403 which results in a 300 nm-thick layer. The region of the sample that we want to

protect is exposed to the electron beam (dose = 270 μC/cm^2; gun = 20 kV; aperture = 20 μm). The development is done in a double cycle of MIF 726: first for 10 s and rinsed in water for 20 s, then for 40 s and again rinsed in water for 50 s. After development, the sample is introduced in the RIE and it is etched in SF_6 for 80 s (or 240 s if one uses the MaN-2403) to make sure that all the WSe_2 and the hBN has been removed. This step does not remove the graphene at the bottom of the heterostructure and a second etching step it is necessary. The chamber is fill with oxygen reaching a pressure of 100 mTorr with 100 sccm O_2 flow. The plasma is activated with a power of 70 W and a RF bias of 290 V for 90 s. The sample is finally cleaned in acetone and isopropanol to remove the residual resist.

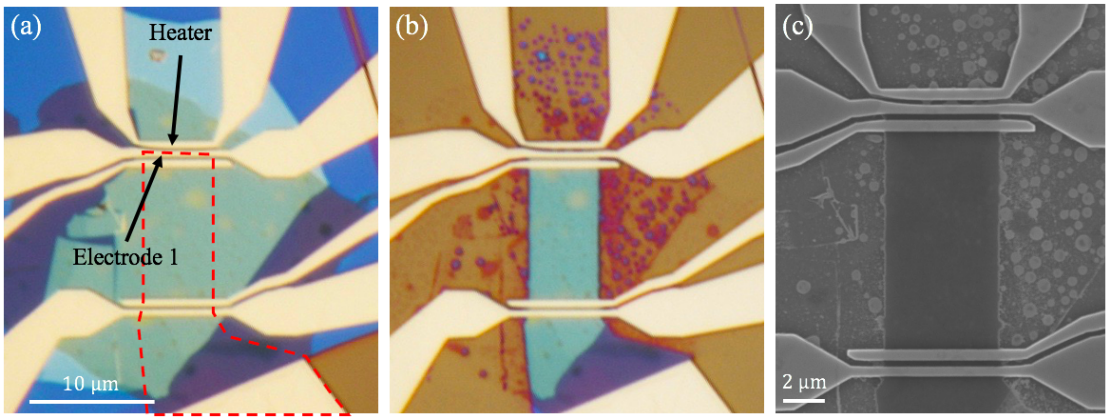

Figure 2.16 – Example of geometrical reshaping of a graphene/hBN/WSe_2 heterostructure with reactive ion etching. Optical image of the heterostructure (a) before and (b) after the etching. (c) SEM image of the heterostructure after the etching.

Figure 2.16b shows the result of the entire procedure. Some residues are visible around the reshaped heterostructure. The blue ones are likely to be originated from the hBN flake, while the red ones from graphene. Figure 2.16c shows the SEM image of the same sample, where some residues are also visible between the heater and the first electrode, meaning that the heater could be not fully isolated from the heterostructure. However, electrical measurements do not detect leakage currents between these two metal contacts, nor between any of the electrodes and the local gate.

The developed etching technique is a powerful tool to reshape van der Waals heterostructures and to give them a quite precise geometry. During my PhD, I have used this approach to reshape all the samples with a graphene local gate (which compose the 80% of all the fabricated samples). However, since I realized that local gates made by graphene do not provide a stable gating effect, I decided to introduce a metallic gate instead, which is fabricated, together with the local heater, before the hBN/WSe_2 transfer. Thus, since in this case the heater is already electrically isolated from the semiconducting channel, no etching is required. All the WSe_2-based transistors presented in the next two chapters of my manuscript have been fabricated without any reshaping of the 2D materials and they present a typical optical image as the one shown in Figure 2.13f. In this way, once the WSe_2 flake is transferred, it undergoes only to one e-beam lithography step to define the electrode mask and no other micro-fabrication process

involving high contamination risk. This choice aims to reduces the probability to deteriorate the WSe_2 channel physical properties affecting the device performances.

2.6.2 Graphene etching

To study thermal transport in graphene nanowires, subject that will be treated in Chapter 5, the design of 2D flakes with well-defined geometry is compulsory and an etching step cannot be avoided. Graphene etching is fairly easy to perform. A rectangular masque (as illustrated by the dotted contour in Figure 2.17a) is created following the same procedure as in the case of heterostructures etching. The samples were etched in O_2 RIE plasma. Figure 2.17b shows an optical image of the sample after the etching. The complete removal of graphene is even more evident from the SEM image of the sample, shown in Figure 2.17c, where no residues are visible around the etched sample.

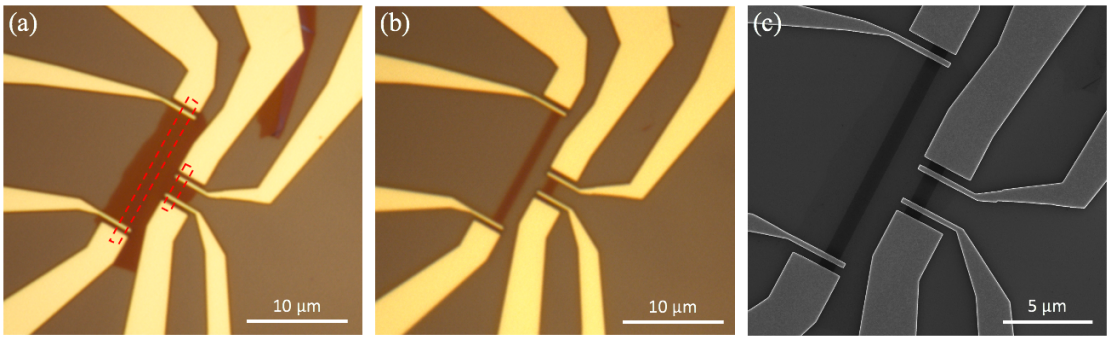

Figure 2.17 – Example of geometrical reshaping of a graphene flake with reactive ion etching. Optical image of the sample (a) before and (b) after the etching. (c) SEM image of the sample after the etching.

2.7 Conclusion

In this chapter, I have presented the main fabrication techniques that I have used to fabricate the devices studied during my PhD. In particular, I have focused the attention on van der Waals heterostructures based on graphene, hBN and WSe_2, starting from the mechanical exfoliation of bulk layered materials to the dry hot pick-up transfer technique used to stack the 2D flakes one over the other. I have illustrated the lithographic steps to design the metallic contacts necessary for electrical and thermoelectrical analysis. When 2D materials are combined in a van der Waals heterostructure, some contamination can be trapped between the flakes, creating some interlayer bubbles. By means of thermal treatments, I have investigated the nature of these blisters. Their different shape and mobility are symptomatic of a different interlayer affinity. Moreover, thermal annealing turns out to be effective to reduce the amount of interlayer impurities. Finally, I have turned my interest on the reshaping of 2D materials by reactive ion etching to give a defined geometry to the fabricated devices. In the chapters dedicated to the experimental work, I will recall the device geometry and characteristics by referring to the presented chapter for details.

3 Charge injection in hBN-supported WSe_2 field effect transistors

Transition metal dichalcogenides (TMDs) have recently attracted a big interest for electronic applications because of their tunable bandgap [220, 221] and high predicted room temperature mobilities (up to thousands of cm^2/Vs) [222]. In general, the mobility μ of a material is related to its electronic band structure and, in particular, it is proportional to the scattering time, τ, and to the inverse of the effective mass, m^*, for electrons and holes ($\mu = e\tau/m^*$). The main mechanism that limits the intrinsic transport properties is the carrier interaction with the lattice vibrations. Due to their structural similarities, all transition metal dichalcogenides exhibit qualitatively comparable phonon scattering characteristics. Even though TMDs show small effective masses, theoretical studies based on density functional theory (DFT) [223, 224] have predicted that the intrinsic carrier mobility in TMDs is limited by the longitudinal optical (LO) phonon scattering, except for MoS_2 and WS_2 in which the mobility is limited by the longitudinal acoustic (LA) phonon scattering [224]. This sets the upper limit for free-standing and defects-free 2D semiconductors.

Experimentally, besides charge-phonon scattering, the mobility in TMDs is often limited by scattering of charge carriers with impurities and defects, as well as charge trapping. Moreover, in actual applications, metal contacts and interfaces properties highly affect the conduction properties in semiconducting materials. In fact, when metal and semiconductor are put together, the bands alignment generates a Schottky barrier at the interface. The shape of this barrier is mainly imposed by the metal work function (ϕ_m) [8]. Depending on the work function, different types of barriers can be created with the conduction or valence band. This allows one to promote electron or hole injection according to the choice of the metal. For example, Figure 3.1a shows on the left part a schematic plot of WSe_2 band diagram compared to the work function of different metals (Ti, Co and Pt) before band alignment. When the metal-semiconductor contact occurs, as depicted in the right side, different Schottky barriers for electrons (ϕ_{Bn}) and holes (ϕ_{Bp}) are generated with WSe_2 [225]. According to the Schottky-Mott rule, the Schottky barrier height (SBH) for electrons and holes can be evaluated as:

$$\phi_{SBn} = \phi_m - \chi \tag{3.1}$$

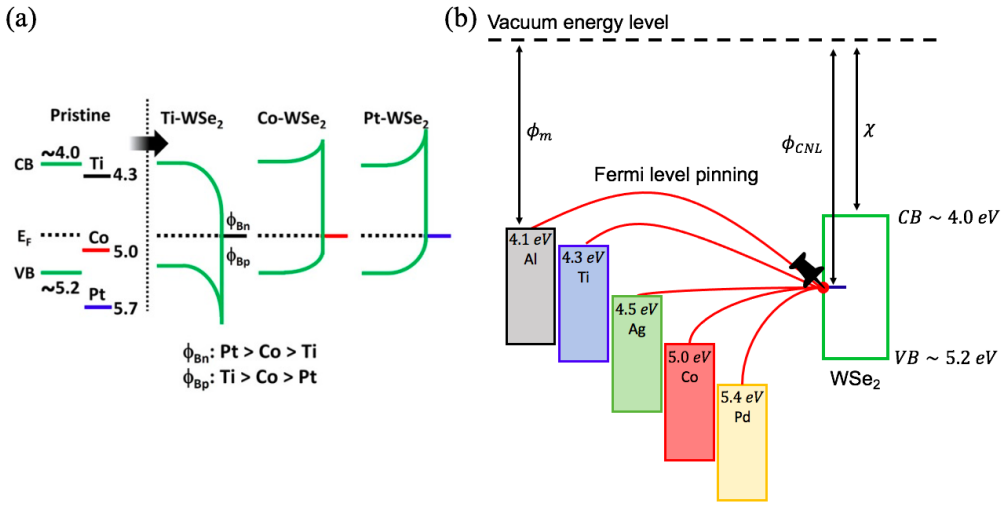

Figure 3.1 – (a) Schematic band diagram for Ti–, Co–, and Pt–WSe_2 FETs before and after band alignment. The unit of CB, VB, and E_F is eV. Extracted from [225]. (b) Interface states, such as tunnel barrier (van der Waals gap), metal-semiconductor orbital overlap and defect states can modify the bands alignment and induce Fermi level pinning.

$$\phi_{SBp} = \chi + E_g - \phi_m \tag{3.2}$$

where χ is the electron affinity of the semiconductor and E_g is its energy gap.

In reality, orbital overlap between the metal and the semiconductor, as well as defects states, often modify the interface properties leading to a weak dependence of the Schottky barrier height on the metal work function [226]. This results in the so-called Fermi level pinning. In this case, one can characterize the SBH by introducing the pinning factor, s, and the charge neutrality level (CNL), ϕ_{CNL}.

$$\phi_{SBn} = s(\phi_m - \phi_{CNL}) + (\phi_{CNL} - \chi) \tag{3.3}$$

$$\phi_{SBp} = s(\phi_{CNL} - \phi_m) + (\chi + E_g - \phi_{CNL}) \tag{3.4}$$

The pinning factor for electron injection is given by the slope of the linear fit of the Schottky barrier height plot versus the metal work function as $s = d\phi_{SBn}/d\phi_m$ (or $s = -d\phi_{SBp}/d\phi_m$ for hole injection). When $s = 1$ the interface is unpinned and Eqs 3.3 and 3.4 restore to Eqs 3.1 and 3.2. Instead, when $s = 0$ the interface is strongly pinned, meaning that the Fermi level of the metal is pinned to the charge neutrality level. This phenomenon is conceptually represented in Figure 3.1b. Generally, a strong Fermi level pinning induces high contact resistances and it hinders the formation of ohmic contacts.

In my PhD, I have studied the electrical properties of hBN-supported WSe_2-based transistors, with a particular attention to the influence related to the use of different metal contacts. In

this chapter, I will first briefly discuss how theoretically evaluate the Schottky barrier height of a metal-semiconductor interface. Subsequently, I will present the electrical characterization of WSe_2-based field effect transistors fabricated as described in Chapter 2, which show an efficient gate modulation and ambipolar behavior. Finally, I will present my results about the investigation of contact barriers with different metal contacts.

3.1 TMDs-based field effect transistor

Understanding charge transport in semiconducting TMDs is a fundamental issue to address if we want to carry out an exhaustive thermoelectric analysis of 2D materials-based devices. Conduction mechanisms in 2D MX_2 are strongly dependent on the doping level or, equivalently, on the Fermi energy (E_F) position as schematically illustrated in Figure 3.2. When the Fermi energy lies inside the energy gap, the material is in its insulating state. A positive gate voltage shifts E_F to the conduction band edge where electrons start to become mobile. In this limit, thermal activated transport dominates. A further increase in gate bias leads to the shift of E_F above the conduction band edge and band transport takes place. A similar picture is valid for hole transport at negative gate biases. The transition from the insulating state to the conducting state is often gradual, involving progressive filling of localized states or band edge disorder states arising from impurities and structural defects as illustrated in the density of states diagram [74]. At intermediate doping levels, electrical conduction occurs via localized states, often described by the variable range hopping (VRH) model [106, 227]. In this regime, the resistivity of a 2D TMD typically varies widely from 10^5 to 10^{12} Ω, decreasing with increasing temperatures. Band transport through extended states is indicated by a positive temperature dependence of the resistivity and low device resistance on the order of 10^2 to 10^4 Ω. In this regime, transport is limited by phonons, and short- and long-range scattering such as defects and charged impurities scattering. Band transport can be achieved at sufficiently large doping concentrations, typically $n_{2D} > 10^{13}$ cm^{-2} [74].

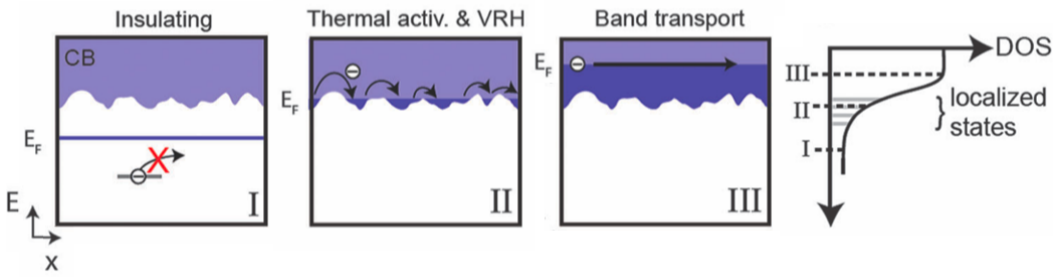

Figure 3.2 – Schematic energy diagram representing different charge transport regimes: (I) insulating (II) conducting by thermal activated hopping and (III) band transport. The density of states diagram shows the disorder-derived band tail states. Extracted from [74].

The study of the transfer characteristic I_{DS} vs. V_G of a TMD-based transistor, with I_{DS} being the source-drain current and V_G the gate voltage, is a powerful tool to investigate charge transport. WSe_2 is an important member of the TMDs family due to its smaller effective

electron and hole masses if compared to most of other TMDs [223] and more importantly due to the ambipolar nature of its electrical characteristics, that is, its ability to support the injection and transport of both electrons and holes [228]. These are, in fact, among the reasons why WSe_2 has been the TMD material of choice for this work.

3.1.1 Electron transport in the subthreshold regime

To understand charges injection and transport in 2D material, let us start focusing on electron injection and conduction only. The TMD conduction band represents in this case the transistor channel, whose position is settled by the gate voltage V_G. The transmission from source to drain is mainly determined by the Schottky barrier (SB) at the contact interfaces. Let us assume that the source-drain voltage V_{DS} is high enough to move the barrier at the drain contact out of the electron path and let us ignore scattering inside the channel. In this case, the Schottky barrier at the source contact is the only limitation to charge injection and so to the final current passing through the device. The total current across the metal-semiconductor interface can be described by the diode current model which, in the case of a 2D material, is modified with a reduction of temperature power low as follow:

$$I = W A^*_{2D} T^{3/2} \exp\left(-\frac{E_b}{k_B T}\right)\left[\exp\left(\frac{qV_{DS}}{k_B T}\right) - 1\right] \tag{3.5}$$

where W is the 2D material channel width, $A^*_{2D} = q\sqrt{8\pi m^* k_B^3}/h^2$ is the 2D equivalent Richardson constant, T is the absolute temperature and $E_b = q\phi_B$ is the interface energy barrier, being ϕ_B the Schottky barrier which can be modulate by the gate voltage V_G, as illustrated in Figure 3.3a and 3.3c.

Let us consider the device in its OFF-state, meaning V_G = 0 V. The yellow line and star in Figures 3.3a and 3.3b, respectively, capture the situation in this case. Carriers are injected by thermionic emission from source over the barrier fixed by the highest conduction band edge position inside the channel (Figure 3.3a). The injection depends on the actual temperature which defines the "tail" of the Fermi distribution at the source. When a more positive gate voltage is applied, the current increases since the conduction band moves downwards allowing for more carriers to be injected into the channel (brown line and star). The change in band position is ideally linearly dependent on the change in gate voltage. This implies (from Eq. 3.5) that the current changes exponentially with gate voltage and the so-called subthreshold swing (or inverse subthreshold slope) is given by

$$SS = \left(\frac{d[\ln(I_D)]}{dV_G}\right)^{-1} = \ln(10) \cdot \frac{k_B T}{q} \cdot \left(1 + \frac{C_d}{C_{ox}}\right) \tag{3.6}$$

where C_d is the depletion layer capacitance at the metal-semiconductor interface, C_{ox} is the gate-oxide capacitance and $k_B T/q$ is the thermal voltage. This quantity represents the gate

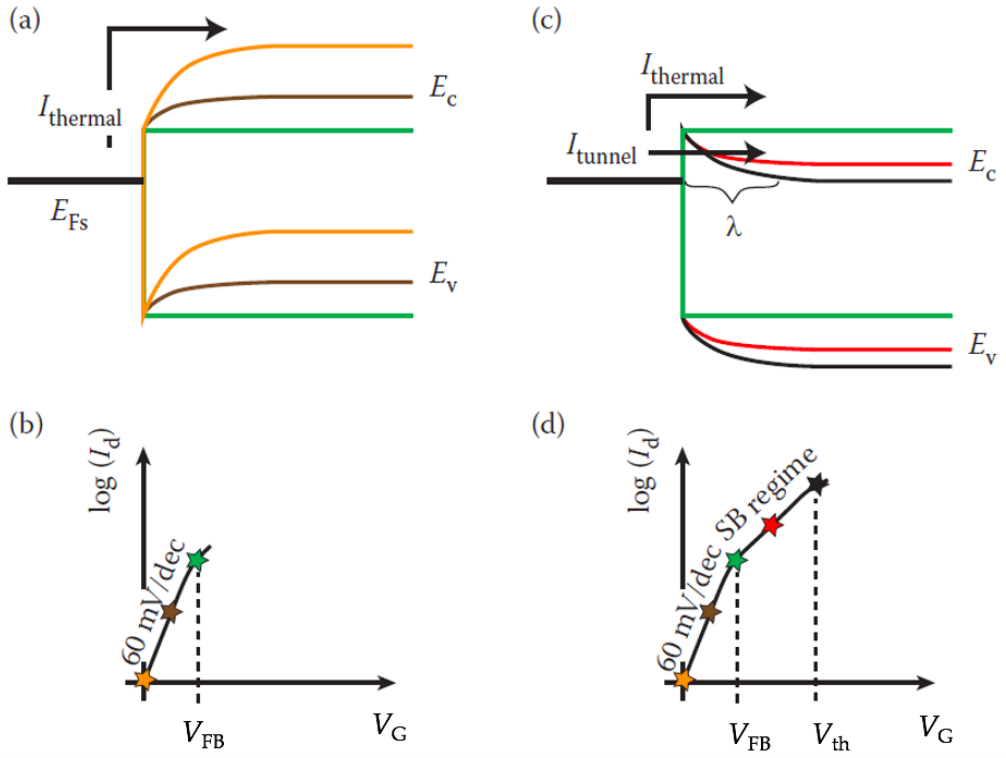

Figure 3.3 – (a,c) Band alignment at the source contact of a TMD-based FET for various gate voltages. (b,d) Corresponding trans-characteristics in a semi-log scale. The star colors are correlated to the bands alignment representation. Extracted from [231].

voltage required to change the drain current by one order of magnitude in the subthreshold regime. The minimum value for the subthreshold swing of a conventional transistor can be found by letting $C_d \to 0$ and/or $C_{ox} \to \infty$, which yields to $SS \sim 60$ mV/dec at room temperature [229]. This trend continues until the flat band condition is reached at $V_G = V_{FB}$ (green line and star in Figure 3.3). Up to this point, the gate voltage response was not different from what could have been found in a conventional device. However, for gate voltages beyond flat band, the situation in an ultrathin body SB-FET becomes drastically different from its conventional bulk counterpart. The key to understand this difference lies in the characteristic length scale λ (see Figure 3.3c) that determines the decay of the potential at the source contact interface of the semiconducting nano-channel. As discussed by Frank et al. [230], the doping-dependent screening length in a bulk device is given by

$$\lambda_{\text{bulk}} = \sqrt{\frac{\varepsilon_{body-x}}{\varepsilon_{ox}} W_{DM} t_{ox}} \tag{3.7}$$

where t_{ox} and ε_{ox} are the thickness and the dielectric constant of the dielectric layer, respectively, ε_{body-x} is the dielectric constant of the channel material in the transport direction. W_{DM} is the maximum depletion width that needs to be replaced by the channel thickness (also called body, t_{body}) if the channel material is thinner than the maximum depletion width,

as it is the case for 2D materials. Equation 3.7 becomes

$$\lambda = \sqrt{\frac{\varepsilon_{body-x}}{\varepsilon_{ox}} t_{body} t_{ox}} \tag{3.8}$$

It is the evident difference between λ_{bulk} and λ for thin body devices in particular at low doping levels that make the reevaluation of the transport across the Schottky barrier for a nano SB-FET necessary. For example, for a doping level of $n_{3D} \sim 10^{18}$ cm^{-3}, $\lambda_{\text{bulk}} \sim 20$ nm and, tunneling through the Schottky barrier can be neglected. On the contrary, for a single layer of TMD, λ reduces to ~ 3 nm. In this case, it is crucially important to take into account the gate voltage dependent tunneling through the thin SB in order to understand the performance of nano SB-FETs. In fact, thermal assisted tunneling plays an important role even when the doping level is very low. Figures 3.3c and 3.3d graphically illustrate how the "below-threshold" region of a SB-FETs is impacted by SB-tunneling. Once the gate voltage is high enough to move the conduction band edge below the flat band position, in addition to the thermal excitation of electrons "over" the Schottky barrier (I_{thermal}), thermal assisted tunneling "through" the barrier needs to be considered, (I_{tunnel}). In fact, if I_{tunnel} would not exist because of a too large λ, the current beyond V_{FB} would not increase. In case of sufficiently small body thicknesses (such as few layers TMDs), λ-values are of the order of nanometers and a gate voltage-dependent tunneling component adds to I_{thermal}. If we first assume a λ-value close to zero, the transmission probability for tunneling becomes close to unity. In this case, the conduction band edge determines the amount of carriers injected into the channel. In this condition, the room temperature inverse subthreshold slope remains 60 mV/dec even above V_{FB}. An increasing λ-value decreases the tunneling probability and the inverse subthreshold slope exhibits values larger than 60 mV/dec. The general trend of the transfer characteristics when changing λ is captured by Figure 3.4a.

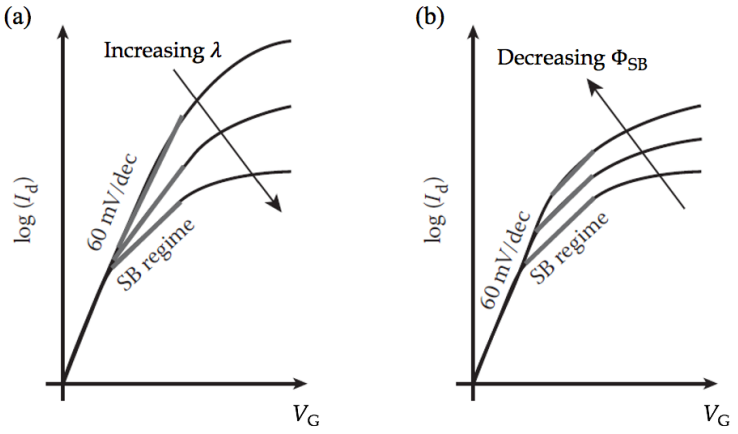

Figure 3.4 – (a) Impact of increasing λ on the nano SB-FET transfer characteristics below threshold. (b) Impact of a change in SB height for a given λ-value. Extracted from [231].

The SB height (ϕ_{SB}) also impacts the tunneling current evolution in the gate voltage range between V_{FB} and V_{th}, where V_{th} is the gate voltage determining the transition between the FET OFF- and ON-state. The threshold voltage is reached when the conduction band edge coincides with the source Fermi energy (black line and star in Figures 3.3c and 3.3d) and it is

almost unaffected by the actual SB height. As illustrated in Figure 3.4b, a smaller ϕ_{SB} implies that the flat band voltage occurs closer to V_{th} (green line and star in Figures 3.3c and 3.3d).

3.1.2 Ambipolar FET

So far, the discussion has been focused on electron injection and the electron branch of the subthreshold characteristics. If the contact Fermi energy lines-up close to the conduction band of the semiconductor, the electron injection becomes predominant while a line-up close to the valence band of the semiconductor translates into efficient hole injection [229]. In this context, transition metal dichalcogenides are receiving great attention because their Fermi level can be effectively shifted between the valence band and the conduction band under application of an external electric field [228, 232, 233, 234, 235], resulting in the so-called ambipolar behavior, graphically illustrated in Figure 3.5. The figure summarizes the electron and hole contributions to the total current as a function of the gate voltage. When no source-drain bias is applied, the flat band condition occurs at the same gate voltage V_{FB} for electrons and holes and its value depends on the Schottky barriers height. The threshold voltage for the electrons (V_{th-n}) and holes (V_{th-p}) are determined, respectively, by the line-up of the conduction and valence band with the source Fermi energy, independently of the actual V_{DS} value [232].

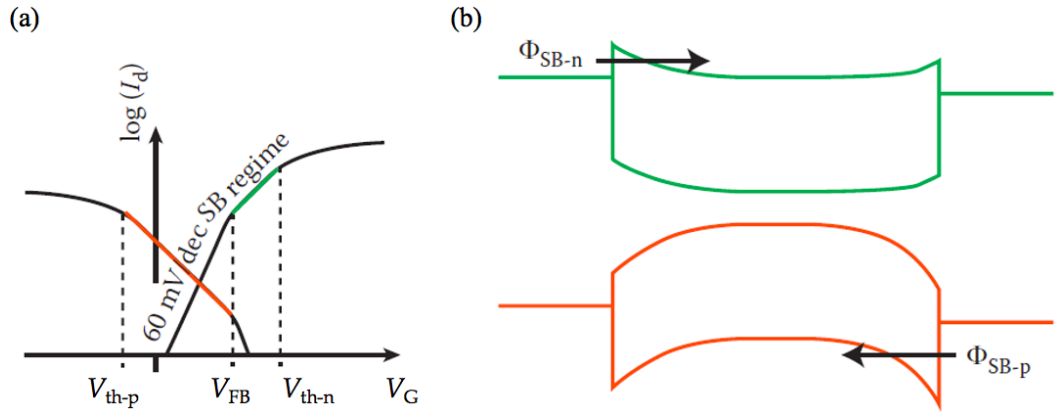

Figure 3.5 – (a) Qualitative illustration of the contributions of electrons (positive slope curve) and holes (negative slope curve) for an ambipolar SB-FET. (b) Electron injection through the source SB and hole injection through the drain SB for positive V_{DS}. Extracted from [231].

As a proof of concept, Das et al. [228] designed a WSe_2-based FET using nickel as source contact electrode and palladium as drain contact electrode, to show how ambipolar device characteristics with similar ON-state performance for both the electron and the hole branches can be achieved. Figure 3.6a shows the experimental transfer characteristics of the transistor. Under zero bias conditions ($V_{DS} = 0$ and $V_{DRIVE} = 0$, being $V_{DRIVE} = V_G - V_{min}$ with V_{min} the gate bias corresponding to minimum current) the source (Ni) Fermi level is aligned closer to the conduction band of WSe_2, and the drain (Pd) Fermi level is aligned closer to the valence band of WSe_2, as illustrate in the red band diagram in Figure 3.6b. For positive V_{DS}, electrons

are injected from the source contact ($V_{DRIVE} > 0$, green square), and holes are injected from the drain contact ($V_{DRIVE} < 0$, blue square) through relatively small Schottky barriers which translate into high current levels for both the electron and the hole branches. On the other hand, for negative V_{DS}, electrons are injected from the drain contact ($V_{DRIVE} > 0$, brown square), and holes are injected from the source contact ($V_{DRIVE} < 0$, purple square) through relatively large Schottky barriers which translate into reduced current levels for both the electron and the hole branches.

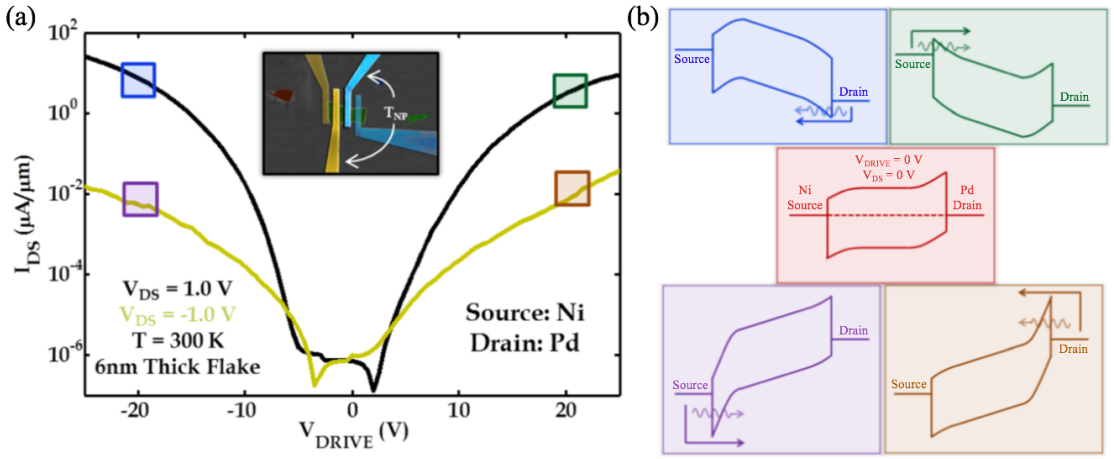

Figure 3.6 – (a) Transfer characteristics of a WSe_2-channel transistor with Nickel as source and Palladium as drain contact electrode, for V_{DS} = 1 V (black curve) and V_{DS} = -1 V (yellow curve) at 300 K. The current level is equal for both positive and negative V_{DRIVE}, indicating efficient ambipolar transport. (b) Associated energy band diagrams for electron and hole injection corresponding to different bias conditions. Extracted from [228]

3.2 Schottky barrier height modeling

The analysis of the subthreshold characteristic of an ultra-thin SB-FET clearly shows that determining the flat band voltage V_{FB} allows to identify the Schottky barrier (for electrons or holes) of a metal-contacted FET, which is an important parameter affecting the transport properties. In this paragraph, I will present two experimental approaches that can be followed to determine the source and drain Schottky barrier heights.

3.2.1 Temperature-dependent thermionic injection model

The technique generally proposed in literature to extract the Schottky barrier height relays on a temperature-dependent measurement of the transfer characteristics [236, 237]. As illustrated schematically in Figure 3.7a, the thermionic component of the current is strongly dependent on the temperature, while the tunneling component is not. By making the approximation of a sufficiently high enough applied source-drain bias, it is possible to neglect the barrier at the channel-drain interface. Eq. 3.5 becomes:

$$I = WA^*_{2D}T^{3/2}\exp\left(\frac{q}{k_BT}(V_{DS}-\phi_B)\right) \tag{3.9}$$

and it can be rewritten as :

$$\ln\left(\frac{I}{WA^*_{2D}T^{3/2}}\right) = \left[\frac{q}{k_BT}(V_{DS}-\phi_B)\right]\frac{1}{T} \tag{3.10}$$

We can rephrase Eq. 3.10 as $y = m \cdot x$, where

$$y = \ln\left(\frac{I}{WA^*_{2D}T^{3/2}}\right) \qquad x = \frac{1}{T} \qquad m = \frac{q}{k_BT}(V_{DS}-\phi_B)$$

The plot of Eq. 3.10 is known as Arrhenius plot and it is schematically shown in Figure 3.7b. For a given value of gate voltage, we can evaluate the "apparent" Schottky barrier (ϕ_B) from the Arrhenius plot slope. Finally, we can plot the "apparent" barrier height as a function of the gate potential, as illustrated in Figure 3.7c, and extract the real Schottky barrier (ϕ_{SB}) which is defined at the flat band condition.

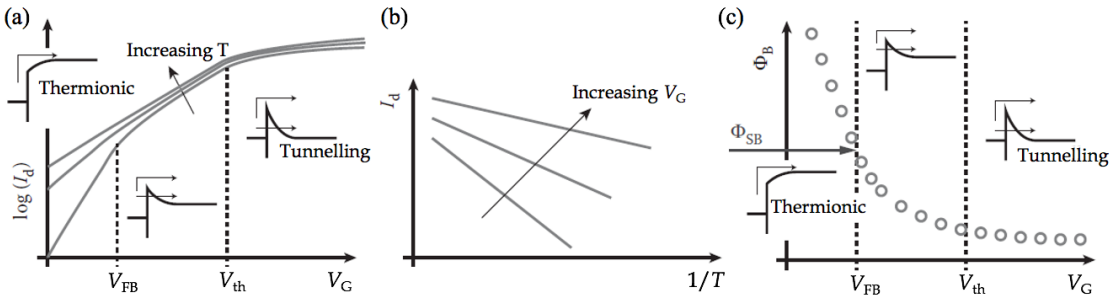

Figure 3.7 – (a) Qualitative temperature dependence of $\log(I)$ versus V_G. (b) Arrhenius plots at various gate voltages. (c) Trend of "apparent" barrier height ϕ_B as a function of V_G, different transport regimes and extraction of the "real" SB height ϕ_{SB}. Extracted from [231].

For gate voltage values below V_{FB}, ϕ_B decreases linearly with V_G since the conduction band edge is pushed downwards. Once the tunneling regime is reached for $V_G > V_{FB}$, the linear dependence between ϕ_B and V_G no longer prevails. As indicated in Figure 3.7c, the actual SB height is defined at the flat band voltage, that can be individuate as the deviation from linearity in the "apparent" $\phi_B(V_G)$.

This model hides some limitations that are difficult to overcome. First, the method is not accurate at high temperature. In fact, when the sample is heated above room temperature, the device can undergo important modifications which might modify its transfer characteristic permanently. Second, the model does not take into account both the barriers at the source and at the drain. Applying a "large-enough" source-drain bias does not fully justify the possibility of neglecting one barrier to study the other one.

3.2.2 Back-to-back Schottky diode model

In actual FET-like devices, such as the one illustrated in Figure 3.8a, the semiconducting channel is always connected to two metal electrodes which create two Schottky barriers. In this Metal-Semiconductor-Metal configuration, the two interfaces can be represented by a back-to-back Schottky diode (BBSD) model as illustrated in Figure 3.8b [238]. Here, D_1 and D_2 are the two diodes connected in back-to-back configuration, representing the source and drain contacts, and R_S is the total series resistance of the device, including the semiconducting channel resistance and the contact resistances.

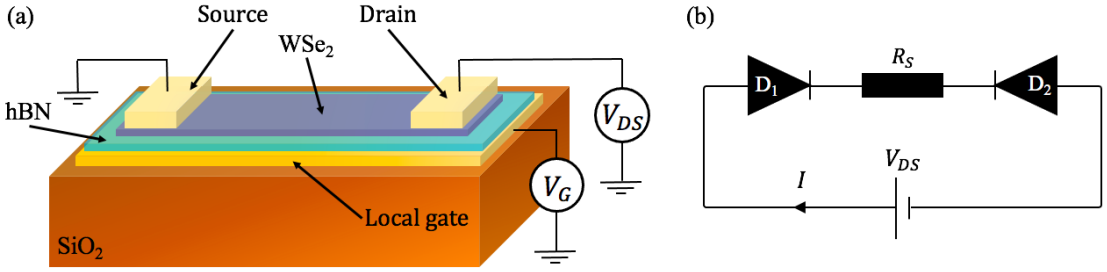

Figure 3.8 – (a) Schematic illustration of the fabricated device. (b) Equivalent circuit of the device.

For a given value of V_G, R_S can be evaluated from the linear region of the $I_{DS} - V_{DS}$ at high bias. When a source-drain bias V_{DS} is applied, one of the diodes is reversed-biased, while the other one is forward-biased. The overall current will be limited by the smaller current in the reverse biased diode. If the carrier transport across the junctions is assumed to follow the thermionic transport theory, the BBSD current of the equivalent circuit in Figure 3.8 can be expressed by the Eq. 3.5. We recall that E_b is the interface energy barrier and it can be defined as:

$$E_b = q\phi_B + qV_{DS}\left(1 - \frac{1}{n}\right) \tag{3.11}$$

where ϕ_B is the "apparent" Schottky barrier of the junction and n is the ideality factor which takes into account for the voltage dependence of the Schottky barrier. Including the voltage drop at R_S, Equation 3.5 becomes

$$I = I_S \exp\left(\frac{q(V_{DS} - IR_S)}{nk_BT}\right)\left[1 - \exp\left(-\frac{q(V_{DS} - IR_S)}{k_BT}\right)\right] \tag{3.12}$$

where I_S is the reverse saturation current, independent of V_{DS}:

$$I_S = WA^*_{2D}T^{3/2}\exp\left(-\frac{q\phi_B}{k_BT}\right) \tag{3.13}$$

Since the current flowing into the device is given by the reverse current, Eq. 3.12 has to be

considered only for values of V_{DS} exploring the reverse bias regime, meaning $V_{DS} < 0$. More in general, according to the model [238], we can write:

$$\begin{cases} I = I_{S1} \exp\left(\frac{q(V_{DS}-IR_S)}{n_1 k_B T}\right)\left[1-\exp\left(-\frac{q(V_{DS}-IR_S)}{k_B T}\right)\right] & \text{for} \quad V_{DS} < 0 \\ I = I_{S2} \exp\left(-\frac{q(V_{DS}-IR_S)}{n_2 k_B T}\right)\left[\exp\left(\frac{q(V_{DS}-IR_S)}{k_B T}\right)-1\right] & \text{for} \quad V_{DS} > 0 \end{cases} \tag{3.14}$$

Thus, we can rewrite Eq. 3.14 as:

$$\begin{cases} \ln\left\{\frac{I}{\left[1-\exp\left(-\frac{q(V_{DS}-IR_S)}{k_B T}\right)\right]}\right\} = \ln(I_{S1}) + \frac{q(V_{DS}-IR_S)}{n_1 k_B T} & \text{for} \quad V_{DS} < 0 \\ \ln\left\{\frac{I}{\left[\exp\left(\frac{q(V_{DS}-IR_S)}{k_B T}\right)-1\right]}\right\} = \ln(I_{S2}) - \frac{q(V_{DS}-IR_S)}{n_2 k_B T} & \text{for} \quad V_{DS} > 0 \end{cases} \tag{3.15}$$

which can be rephrased as $y = mx + q$:

$$\begin{cases} y = \ln\left\{\frac{I}{\left[1-\exp\left(-\frac{q(V_{DS}-IR_S)}{k_B T}\right)\right]}\right\} \quad x = (V_{DS} - IR_S) \quad m = \frac{q}{n_1 k_B T} \quad q = \ln(I_{S1}) \quad \text{for} \quad V_{DS} < 0 \\ y = \ln\left\{\frac{I}{\left[\exp\left(\frac{q(V_{DS}-IR_S)}{k_B T}\right)-1\right]}\right\} \quad x = (V_{DS} - IR_S) \quad m = -\frac{q}{n_2 k_B T} \quad q = \ln(I_{S2}) \quad \text{for} \quad V_{DS} > 0 \end{cases}$$

From the slope and the intercept of this linear graph it is possible to extract n and I_S, respectively. In particular, according to Eq. 3.13, we can evaluate the Schottky barrier for a given value of gate voltage as:

$$\phi_B = \frac{k_B T}{q} \ln\left(\frac{W A^*_{2D} T^{3/2}}{I_S}\right) \tag{3.16}$$

In the case of ambipolar transport, to define which barrier is coming into play for a given source-drain and gate voltage polarization, we can simulate the band bending following the exponential barriers model proposed by Taur et al. [239]. According to the model, the potential variation along the channel is by:

$$V(x) = \frac{(E_S - \phi_{S(e)})\sinh(\pi(L-x)/\lambda) + (E_D - \phi_{D(e)})\sinh(\pi x/\lambda))}{\sinh(\pi L/\lambda)} \tag{3.17}$$

where E_S and E_D are the Fermi levels at the source and at the drain, $\phi_{S(e)}$ and $\phi_{D(e)}$ are the electron Schottky barriers at the source and at the drain, L is the channel length and λ is the

length scale defined in Eq. 3.8. Figure 3.9 shows the simulated bands bending in four possible configurations of polarization: $V_{DS} > 0$ and $V_G > 0$ or $V_G < 0$ and, $V_{DS} < 0$ and $V_G > 0$ or $V_G < 0$.

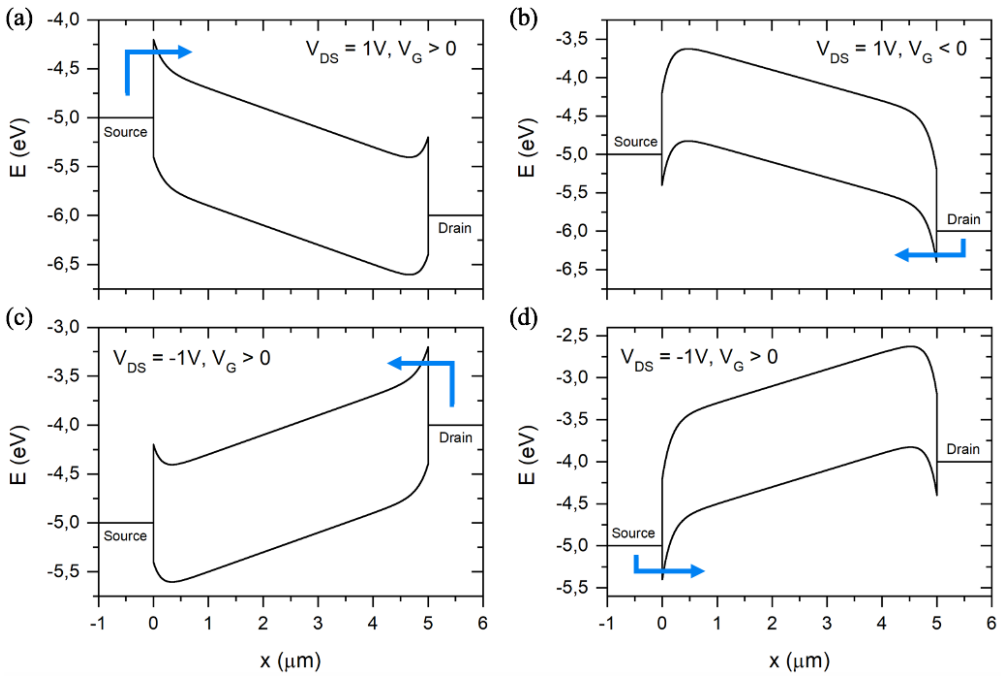

Figure 3.9 – Band bending simulation based on an analytical model [239] of the channel potential based on exponential barriers at the source/channel and channel/drain interfaces.

For a positive source-drain bias (Figures 3.9a and 3.9b), the current that we measure for positive gate voltages is the reverse current of electrons flowing from source to drain which is limited by the electrons Schottky barrier at the source ($\phi_{S(e)}$). When the semiconductor bands are bend upwards for negative gate voltages, the saturation current is due to holes flowing from the drain to the source and it is limited by the hole Schottky barrier at the drain ($\phi_{D(h)}$). The same reasoning can be done for negative source-drain bias, as illustrated in Figures 3.9c and 3.9d. In this case, positive gate voltages will allow us to explore the electron Schottky barrier at the drain ($\phi_{D(e)}$) and negative gate voltages will allow us to explore the hole Schottky barrier at the source ($\phi_{S(h)}$). This approach relies in the measurement of the I_{DS} vs V_{DS} characteristics on a large range of gate voltages at a fixed temperature. This has been the method of choice for my devices that have been studied at room temperature.

3.3 Charge transport measurements

To investigate the charge transport and to extract the Schottky barrier height created at the metal-semiconductor interfaces, I have fabricated several hBN-supported WSe_2-based field effect transistors with different metallic contacts and local gate. In the adopted configuration, the hBN flake plays the role of dielectric material.

In literature, various materials such as oxides (e.g., SiO_2, HfO_2, and Al_2O_3), nitrides (e.g., hexagonal BN and Si_3N_4), and organic polymers (e.g., poly(methyl methacrylate) (PMMA)) [240] are usually selected as dielectric layer to electrically isolate the semiconducting channel from the gate. Among them, the most common is SiO_2 since it can be easily prepared by thermal oxidation on the top of a Si substrate. In general, the specific gate capacitance of a dielectric can be written as

$$C = \frac{\varepsilon_0 \varepsilon_r}{t_{ox}} \tag{3.18}$$

where $\varepsilon_0 = 8.85 \times 10^{-12}$ F/m and ε_r are the vacuum permittivity and the relative dielectric constant, respectively, and t_{ox} is the thickness of the dielectric layer. Given the relative dielectric constant of silicon dioxide ($\varepsilon_{SiO_2} \sim 3.8$), for 280 nm-thick SiO_2 $C_{SiO_2} \approx 12$ nF/cm^2. Reducing the thickness of SiO_2 leads to larger capacitance. However, the formation of leakage currents by direct tunneling does not allow an excessive reduction. Using thin dielectric layered crystals, such as hBN, opens to the possibility to have a much thinner dielectric layer. For example, for a thickness of 10 nm and considering 3.76 as the static out-of-plane dielectric constant for a multi-layers hBN [241], $C_{hBN} \approx 330$ nF/cm^2, which is an order of magnitude greater than C_{SiO_2}. To further increase the gate capacitance, it is possible to employ the electric double-layer transistor (EDLT) configuration by using ionic liquids as gate dielectrics. In this case, it is possible to achieve dielectric capacitance on the order of ~5 μF/cm^2 [79, 232]. However, due to their liquid nature, ionic liquids dielectrics can be employed in a quite narrow range of temperature and they are unsuitable for applications.

In my work, hexagonal boron nitride is the material of choice used as dielectric layer because of its atomic flat surface and its strong gate modulation capability. Moreover, by decoupling the semiconducting material from the substrate, hBN prevents any possible doping due to the interaction with the substrate. The breakdown electric field was estimated in my devices as ~ 0.7 V/nm, in agreement with the values reported in literature ranging between 0.2 V/nm [242] and 1.2 V/nm [243] depending on the hBN thickness. Knowing the dielectric capacitance, it is possible to determine the sheet carrier density of the channel material, defined as

$$n_{2D} = \frac{C_{hBN}(V_G - V_{th})}{q} \tag{3.19}$$

where V_G is the gate voltage, V_{th} is the threshold voltage (or the gate voltage corresponding to the Dirac point for graphene) and q is the elementary charge. Thanks to the thin hBN dielectric layer, it is possible to achieve values of carrier density exceeding 10^{13} cm^{-2}, corresponding to $n_{3D} \sim 10^{22}$ cm^{-3} ($n_{3D} = n_{2D}/t$, with t the thickness of the conductive channel). Finally, the transfer characteristic $I_{DS} - V_G$ of a FET-like device allows to extract the "effective" mobility of the device, intended as the mobility of the whole device including the metal contact interfaces and not the intrinsic mobility of the 2D material. The device mobility can be evaluated as

$$\mu = \frac{L}{W}\frac{dI_{DS}}{dV_G}\frac{1}{C_{\text{hBN}} \cdot V_{DS}} \tag{3.20}$$

where L and W are the length and width of the semiconducting channel and dI_{DS}/dV_G is the trans-conductance.

3.3.1 Charge transport measurements in WSe_2 with different metal contacts

WSe_2-based transistors have been fabricated with Ag, Pd, Co and Ti metal contacts. Figure 3.10a shows the optical image of a representative sample. Given the electrons and holes affinities for WSe_2, 4 eV and 5.3 eV, respectively [244], high work function metals (as Pd and Co) are expected to achieve good hole injection [245] while low work function ones (as Ag and Ti) to achieve good electron injection. All the fabricated devices have been characterized by atomic force microscopy (AFM) to evaluate the hBN and WSe_2 thickness by averaging step heights of profiles taken in ~ 50 different sample zones. The obtained values are summarized in Table 3.1. For each employed metal contact, only one representative sample (highlighted in gray in the table) will be discussed in detail in the following.

	Metal	t_{hBN} [nm]	t_{WSe_2} [nm]	# of layers
s175	Ag	–	–	–
s180	Ag	57 ± 3	3.8 ± 0.4	6
s204	Ag	41 ± 2	4.9 ± 0.4	8
s182	Pd	45 ± 3	3.6 ± 0.5	6
s183	Pd	45 ± 1	3.0 ± 0.5	4
s187	Co	51 ± 3	2.7 ± 0.4	4
s189	Co	50 ± 3	2.8 ± 0.4	4
s190	Co	48 ± 2	3.1 ± 0.4	5
s209	Ti	41 ± 2	2.9 ± 0.3	4
s212	Ti	35 ± 3	5.4 ± 0.4	8

Table 3.1 – Discussed samples with their relative metal connection, hBN and WSe_2 thicknesses. For s175 the AFM was not possible because the sample was broken during the measurements.

All the electrical measurements have been performed in a Nextron micro probe station (shown in Figure 3.10b) in high-vacuum ($p \sim 10^{-7}$ mbar) and controlled temperature ($T = 25$°C). Since semiconducting devices may reach very large resistances in their OFF-state, a voltage-biasing technique has been used to measure the two-probe electrical current of WSe_2-based devices both in their ON and OFF operation regimes. The schematic circuit is illustrated in Figure 3.10c. A source-drain voltage V_{DS} is applied at the drain electrode while the source electrode is connected to a low noise current-voltage amplifier providing a 10^6 gain to the current which is measured by a voltmeter (Agilent 34401A). The amplifier also ensures the source reference to the ground. The gate voltage V_G is applied to the local Au gate electrode underneath the hBN. V_{DS} and V_G are provided by two DC source-meter (Yokogawa 7651). The WSe_2 conductive channel size is considered to be the portion of WSe_2 in which the doping can be modulated

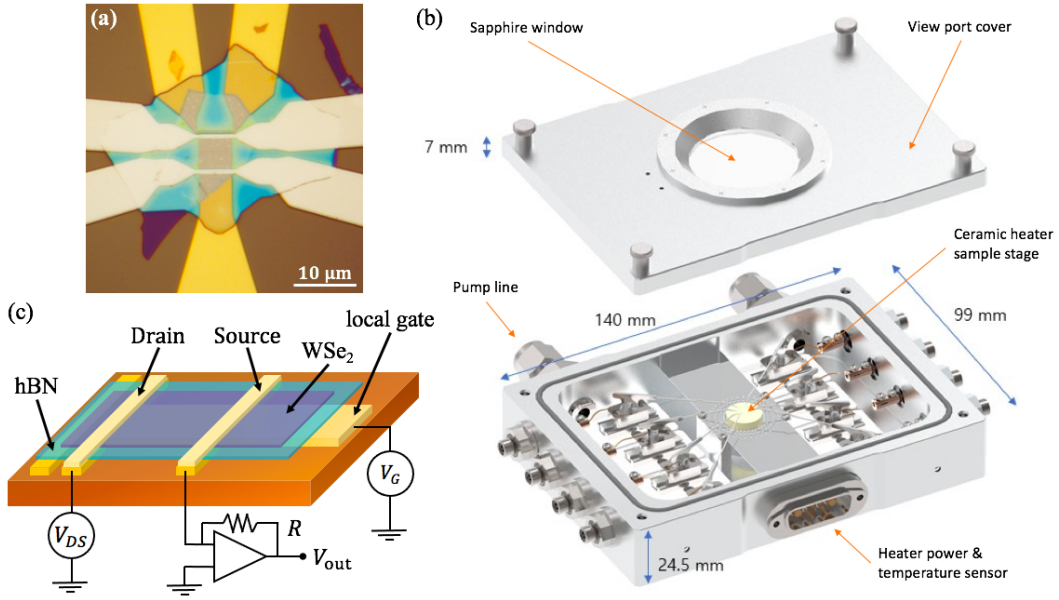

Figure 3.10 – (a) Optical image of a representative hBN/WSe_2 sample. (b) 8-probes Nextron micro-probe station employed for the electrical measurements. (c) Schematic circuit employed for the electrical characterization.

by the applied local gate (V_G). This defines a nominal channel width of W = 5 μm for all the fabricated devices. The channel length is defined as the internal edge-to-edge distance between the source and drain electrodes and, the nominal channel length is designed for all the devices as L = 5 μm. Figure 3.11 shows the example of a 3D electrical map showing the source-drain current I_{DS} variation as a function of V_{DS} and V_G, obtained for the Ag- and Co-connected WSe_2 samples, respectively. For each value of V_G in the range ± 25 V, V_{DS} is swept between ± 2 V. In the case of Ag-WSe_2 (Figure 3.11a), the current is flowing just for positive gate voltages, meaning that the device is able to support only electron injection. On the other hand (Figure 3.11b), the Co-WSe_2 sample shows a clear ambipolar behavior, being the device conductive both for positive and negative gate voltages.

To evaluate the threshold voltage, the ON/OFF ratio, the device mobility and the inverse subthreshold slope, the plot of I_{DS} versus V_G has been extracted from the 3D electric map for V_{DS} = 2 V. This configuration allows to minimize the influence of the Schottky barriers, even though it is always present. Figure 3.12 shows the transfer characteristic of the highlighted samples in linear (red points) and logarithmic (blue points) scale. We can clearly distinguish the different operation regimes: the devices are in their OFF-state approximately for -20 V < V_G < 10 V and they switch to the ON-state approximately for V_G < -20/-25 V and V_G > 10/15 V, depending on the samples. In the subthreshold regime, the current increases exponentially as a function of V_G until the threshold voltage (V_{th}), when the device turns in the ON-state. The threshold voltage is extracted from the linear scale plots as the gate voltage at which the extrapolation of the linearly rising region of the $I_{DS}(V_G)$ curve reaches the zero current, as shown in Figure 3.12 by the dashed black lines. Typical threshold voltage for electrons (hole) for all the fabricated samples are in the range 10 V < V_{th-e} < 20 V (V_{th-h} < -20 V). We find

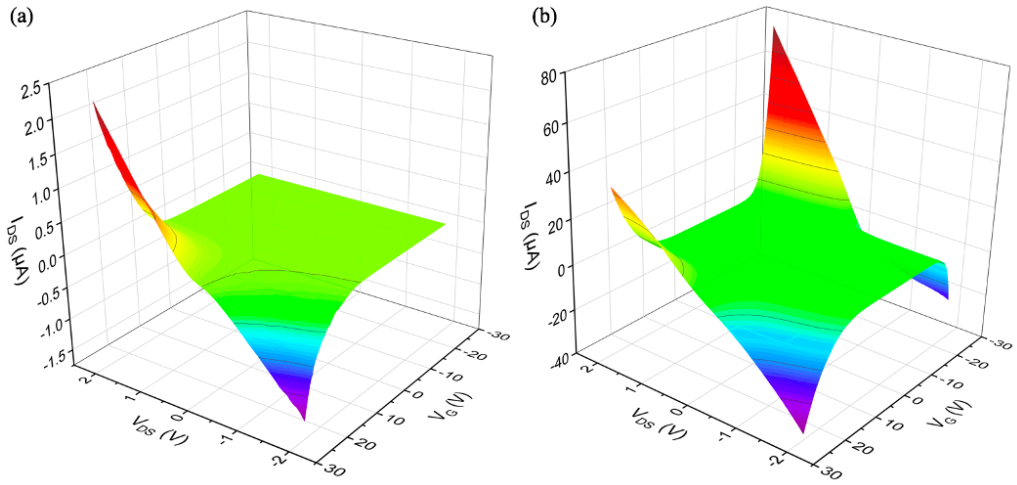

Figure 3.11 – 3D electrical maps obtained for (a) the Ag- and (b) Co-connected WSe_2 samples.

out the highest electron (hole) mobility equal to ~ 0.8, ~ 100 (10), ~ 42 (300) and ~ 274 (125), $cm^2/V\,s$ for Ag, Pd, Co and Ti respectively, in agreement with values reported in literature [233, 225, 246, 247, 245]. Note that, this is what we have defined as the "effective" mobility, which includes the contribution of the interface contact resistance and it has to be interpreted as a lower limit of the actual mobility in the WSe_2 layer. The highest mobility, as high as 300 $cm^2/V\,s$, is observed for the Co-contacted sample in the hole transport regime. The density of charge carriers, n_{3D}, can be evaluated at the highest gate voltage of the order of 10^{19} cm^{-3} for both charge carriers (corresponding to a sheet carrier density n_{2D} of ~ 10^{10} cm^{-2}). All fabricated devices have quite large ON/OFF ratio (~ 10^5), but they also show high inverse subthreshold slopes for both bands injections with typical values ranging in the interval 2000 mV/dec < SS < 4500 mV/dec. Detailed values for the extracted quantities are reported in Table 3.2. In some cases, indicated with a dash in the table, the estimation of some quantities was not possible since the device has not reach the ON-state for electron or hole transport.

	s175	s180	s204	s182	s183	s187	s189	s190	s209	s212
Metal	Ag	Ag	Ag	Pd	Pd	Co	Co	Co	Ti	Ti
V_{th_h} [V]	–	–	–	-19	-20.5	-15	-21.5	-21.5	-12	-9.5
V_{th_e} [V]	21.6	12	21	8.5	12.5	–	17.5	21.5	14.6	15.5
ON/OFF_h	–	–	–	10^4	10^4	10^6	10^6	10^5	10^4	10^3
ON/OFF_e	10^6	10^6	10^4	10^6	10^6	–	10^6	10^5	10^3	10^3
μ_h [$cm^2/V\,s$]	–	–	0.2	10	10	300	200	55	125	19
μ_e [$cm^2/V\,s$]	??	0.8	0.6	100	100	14	42	0.5	20	274
SS_h [mV/dec]	–	–	–	4000	3000	4000	1000	3000	2770	2600
SS_e [mV/dec]	3600	4320	5000	2500	2500	–	3500	3000	4980	8000

Table 3.2 – Synthesis of the main electrical parameters of the discussed samples: metal used for the contact, threshold voltages (V_{th_h}, V_{th_e}), ON/OFF ratios, electron and hole mobilities (μ_h, μ_e) and subthreshold swings (SS_h, SS_e).

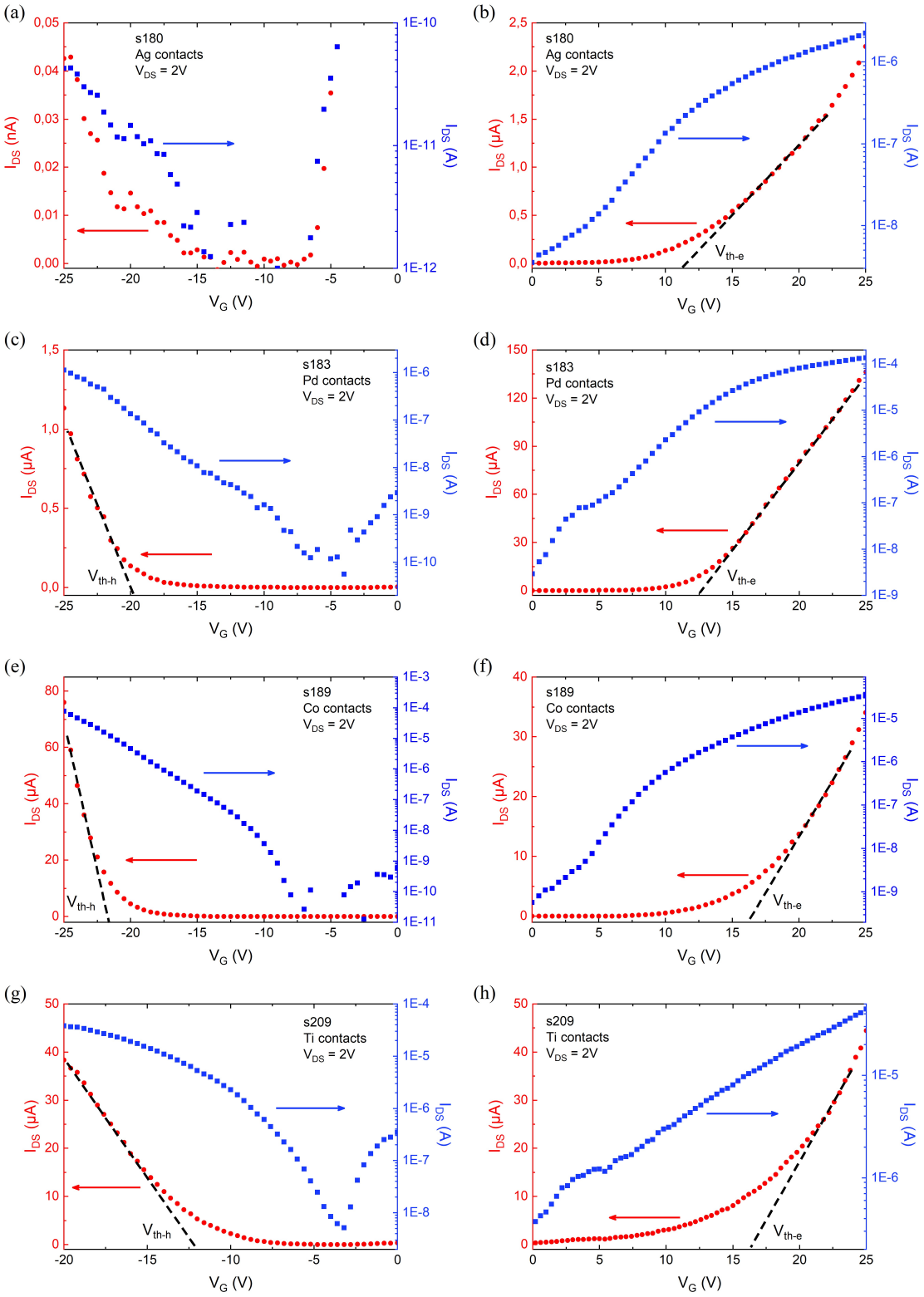

Figure 3.12 – Transfer characteristics for $V_G < 0$ (left panel) and $V_G > 0$ (right panel) for the highlighted samples in linear (red, left) and logarithmic (blue, right) scale.

3.4 Modified bandgap and Fermi level pinning origins

The electrical characterization of the WSe_2-based transistors reveals very high values of subthreshold swing, indicating a slow ON/OFF switch. This slow and gradual transition, which reduces the electrical performances of our devices, can be related to the presence of localized energy states in the energy gap of the 2D semiconductor. These states can originate from the presence of defects and impurities in the 2D material. However, band structure calculations for WSe_2-based transistors have shown that the metallic electrodes used to contact the semiconducting channel can induce gap states close to the conduction and valence bands due to orbital hybridization. These gap states can strongly modify the energy gap and the transport properties of the 2D material [248]. To better understand the orbital hybridization at the metal contact interface, we can refer to the DFT band structure computation performed by Wang et al. [248] for monolayer WSe_2 at the interface with several metal contacts. Figure 3.13 illustrates the band structures of a pristine monolayer (ML) of WSe_2 and Al-, Ag-, Au- Pd- Pt-contacted WSe_2, respectively. The gray lines represent the metal surface bands, while the red lines represent the bands of WSe_2 without considering the SOC effects. As shown in the figure, weak metal-WSe_2 bonding results in a quite preserved band structure if compared to the pristine material. This is the case of aluminum (Al) or silver (Ag) metal contacts. On the other hand, a stronger metal-WSe_2 coupling leads to an important band structure modification with a highly reduced bandgap and ambipolar expected transfer characteristics, as in the case of palladium (Pd) or platinum (Pt) contacts.

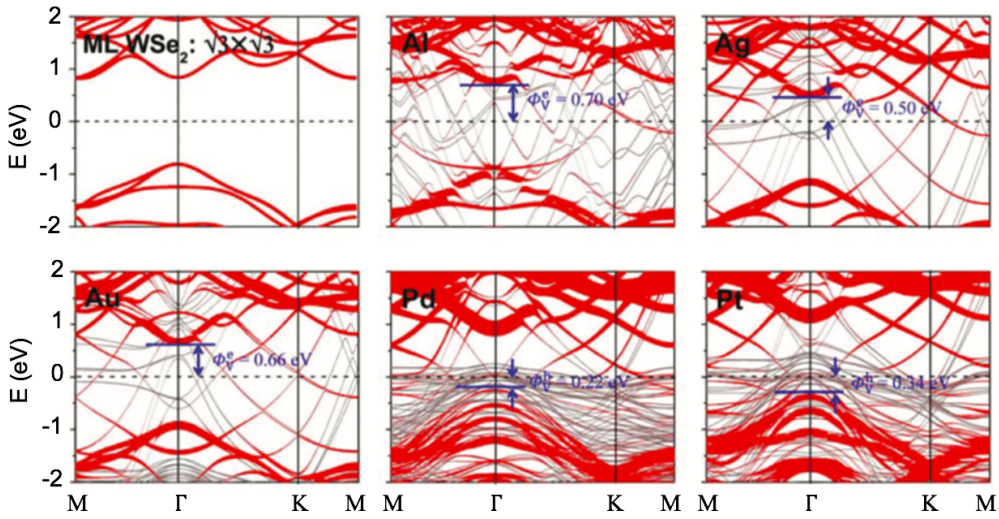

Figure 3.13 – Band structures of pristine monolayer (ML) WSe_2 and Al-, Ag-, Au- Pd- Pt-contacted WSe_2, respectively. The gray lines represent the metal surface bands, while the red lines represent the bands of WSe_2 without considering the SOC effects. The line width is proportional to the weight. Extracted from [248].

Indeed, when dealing with 2D materials, the properties of the interface, such as the chemical interaction between the metal and the semiconductor, can dominate the entire device properties [249]. In general, the pristine surface (free from dangling bonds) of a 2D material is expected to form weak interface bonds with a metal, thereby increasing the contact resistance.

Figure 3.14 illustrates the possible interfaces that can be created when a semiconducting material is contacted with a metal electrode. Contrary to the case of bulk (3D) semiconductors, the pristine surfaces of 2D materials do not tend to form covalent bonds. In most cases, the interfaces between metals and 2D materials are, in fact, characterized by a van der Waals gap (Figure 3.14a), which acts as a tunnel barrier for carriers. The tunnel barrier greatly reduces the charge injection resulting in higher contact resistance. However, as predicted by DFT studies [248, 250], orbital overlap between the metal and the semiconductor can lead to the formation of orbital states in the 2D material bandgap. In this case, the charge carrier injection is modified by the presence of such states, making more difficult to predict the relative contributions from thermionic emission and tunneling. On the other hand, a strong metal-semiconductor coupling results in a more important decay of the metallic wave-function into the nanometric thickness of the 2D semiconductor which can be considered as "metallized". In this case (Figure 3.14b), the tunnel barrier can be neglected and the Schottky barrier is generated between the hybridized 2D material (region B) and the 2D channel (region B') [248, 250, 251]. DFT simulations show that specific metals are more suitable to form covalent bonds with 2D

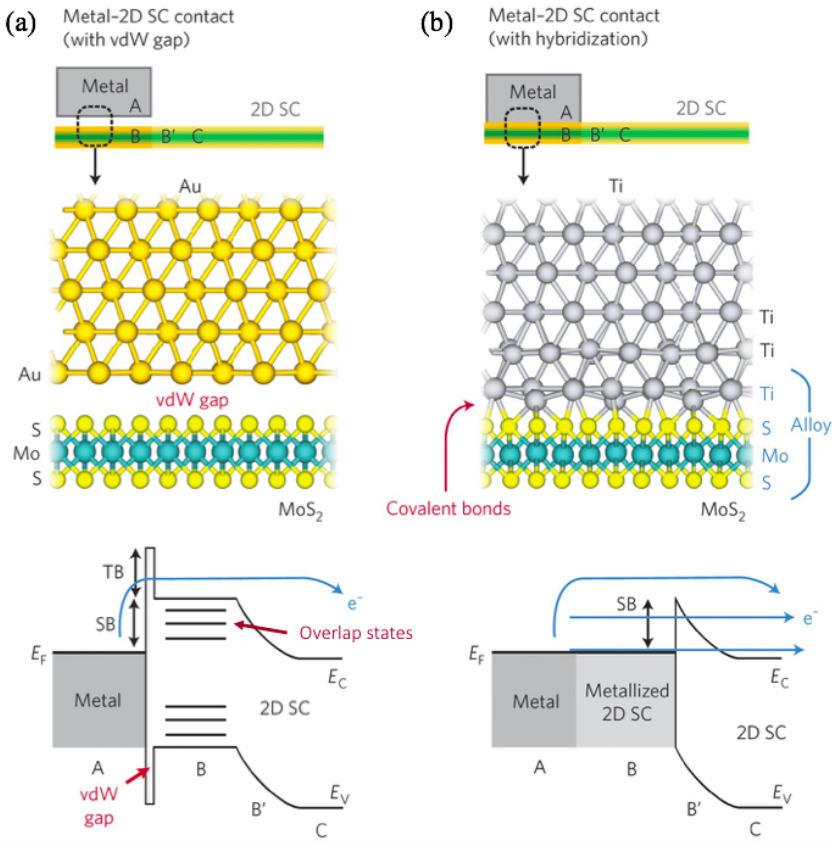

Figure 3.14 – Schematic and corresponding band diagrams of (a) a metal/2D semiconductor interface with van der Waals gap and (b) a metal/2D semiconductor interface with hybridization. A, B, B' and C represent different regions in the current path from the metal to the semiconductor. E_F, E_C and E_V represent the Fermi level of the metal, and the conduction and valence bands of the 2D SC, respectively. TB and SB indicate the tunnel and Schottky barrier heights, respectively. Figure extracted from [249].

semiconducting material surfaces and, thus, eliminate the van der Waals gap. In particular, Ni contacts for graphene [252], Ti and Mo for MoS_2 [253, 254, 255], Pd and W for WSe_2 [255, 256] create orbital overlapping interfaces.

In general, WSe_2-based FETs are expected to form quite transparent contacts with the valence band when contacted with high work-function metals promoting efficient hole transport, while lower work-function metals induce high Schottky barrier heights to both the valence and the conduction bands. However, due to the strong Fermi level pinning which modifies the metal Fermi level alignment to the semiconductor bands, this is not always the case. Moreover, the modified interlayer bonding strength at the metal contact interface due to the metal-semiconductor orbital hybridization, leads to the creation of gap states in the TMD layer [257] which play also a fundamental role in Fermi level pinning [226] and affects the charge injection from the metal to the semiconductor. Such effects can significantly impact the Schottky barrier height (SBH).

3.5 Schottky barrier height evaluation

The Schottky barrier heights have been extracted according to the back-to-back Schottky diode (BBSD) model previously introduced, by fitting the device output characteristics to the thermionic transport equation of a reversed diode (Eq. 3.12). Figure 3.15a shows two representative output characteristics in the case of a Co-contacted sample for V_G = 6.5 V (black data) and V_G = -6.5 V (red data), corresponding to the subthreshold electron and hole injection regimes, respectively. The continuous lines are the corresponding fits from the BBSD model. The 2D equivalent Richardson constant was evaluated as A^*_{2D} = 0.0566 A m^{-1} K$^{-3/2}$ with an effective mass approximated to $0.4m_0$ both for electrons and holes [258, 259, 260].

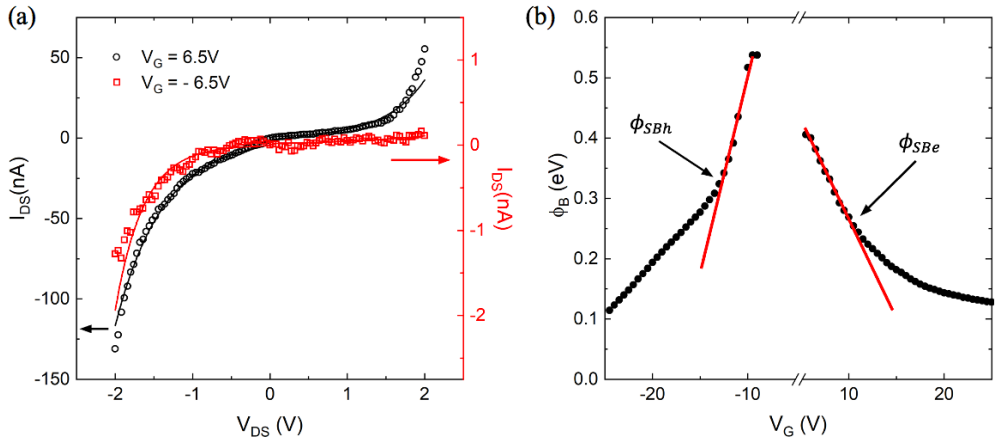

Figure 3.15 – (a) Representative output characteristics for a Co-contacted sample at V_G = 6.5 V (black data, left axis) and V_G = -6.5 V (red data, right axis). (b) Schottky barriers extraction following the BBSD model.

Figure 3.15b shows an example of extracted values of the Schottky barrier, ϕ_B, in the gate voltage range $|V_G| \leq 25$ V. The actual electron (hole) Schottky barrier height, $\phi_{SBe(h)}$, is defined

at the flat band condition, identified as the gate voltage for which the barrier height diverges from the linear trend as indicated by the solid red lines. The plots of the extracted Schottky barriers as a function of the gate voltage for the highlighted samples are reported in Figure 3.16. In the left side of the panel are reported the values for negative source-drain bias, while in the right side the ones for positive bias. In the inset, schematic band diagrams illustrate which is the dominant barrier according to the source-drain and gate polarization. All the extracted values are summarized in Table 3.3.

	s175	s180	s204	s182	s183	s187	s189	s190	s209	s212
Metal	Ag	Ag	Ag	Pd	Pd	Co	Co	Co	Ti	Ti
ϕ_{SBe}	0.33	0.46	< 0.28	0.26	0.19	–	0.22	0.39	0.24	0.13
	0.45	0.46	0.32	0.29	0.21	–	0.21	0.41	< 0.18	0.16
ϕ_{SBh}	0.46	–	0.36	0.26	0.27	0.37	< 0.11	< 0.22	0.25	0.23
	–	–	0.33	< 0.22	0.27	0.38	< 0.11	0.27	0.21	0.22
E_g	0.91	> 0.46	0.68	0.55	0.48	> 0.38	0.33	0.68	0.49	0.39

Table 3.3 – Extracted values of electron and hole Schottky barriers (ϕ_{SBe}, ϕ_{SBh}) and, approximation of the energy gap E_g given by the sum of the two injection barriers. All the values are given in eV.

We find out similar values of ϕ_{SBe} and ϕ_{SBh} on the order of ~ 0.2 - 0.3 eV for Pd, Co and Ti, for which ambipolar behavior is observed, in agreement with what can be found in literature [255, 249, 261]. Ag-contacted samples, which are mainly dominated by n-type transport, shows slightly higher Schottky barriers values for electron injection on the order of 0.4 eV. For all the samples, the sum of the electron and hole barriers defines a reduced energy gap, of the order of ~ 0.4 - 0.7 eV, well below the predicted value for few layers WSe_2 of ~ 1.1 - 1.2 eV [232, 16]. Such a strong reduction can be attributed to the presence of interfacial gap states in the WSe_2 bandgap for strong hybridization at the metal/2D material interface in agreement with theoretical predictions [248]. Electronic transport is likely to be dominated by the local modified DOS of the source and drain interfaces of the WSe_2-based transistors rather than by the channel electronic structure. The ambipolar behavior observed with Pd, Co and Ti is coherent with calculations of Schulman et al. [262] where pinning for Pd and Ni is predicted almost in the middle of the gap.

Given the similarity in hBN thickness, we can reasonably assume similar capacitive coupling for all samples and compare all the devices in the same gate voltage range, as illustrated in Figure 3.12. In the case of Ag-based transistor, the device is always in the OFF-state for hole injection, while it switches to the ON-state for electron injection (Figures 3.12a and 3.12b), with an extracted barrier on the order of 0.46 eV, higher than the values estimated for the other samples, indicating a larger bandgap and preferred injection in the conduction band with higher Schottky barriers. This is in agreement with the expected weak coupling nature of the Ag-WSe_2 interface. On the other hand, due to the stronger coupling, Pd-, Co- and Ti-WSe_2 samples show the smallest Schottky barriers and highly reduced bandgap down to ~ 0.35 eV.

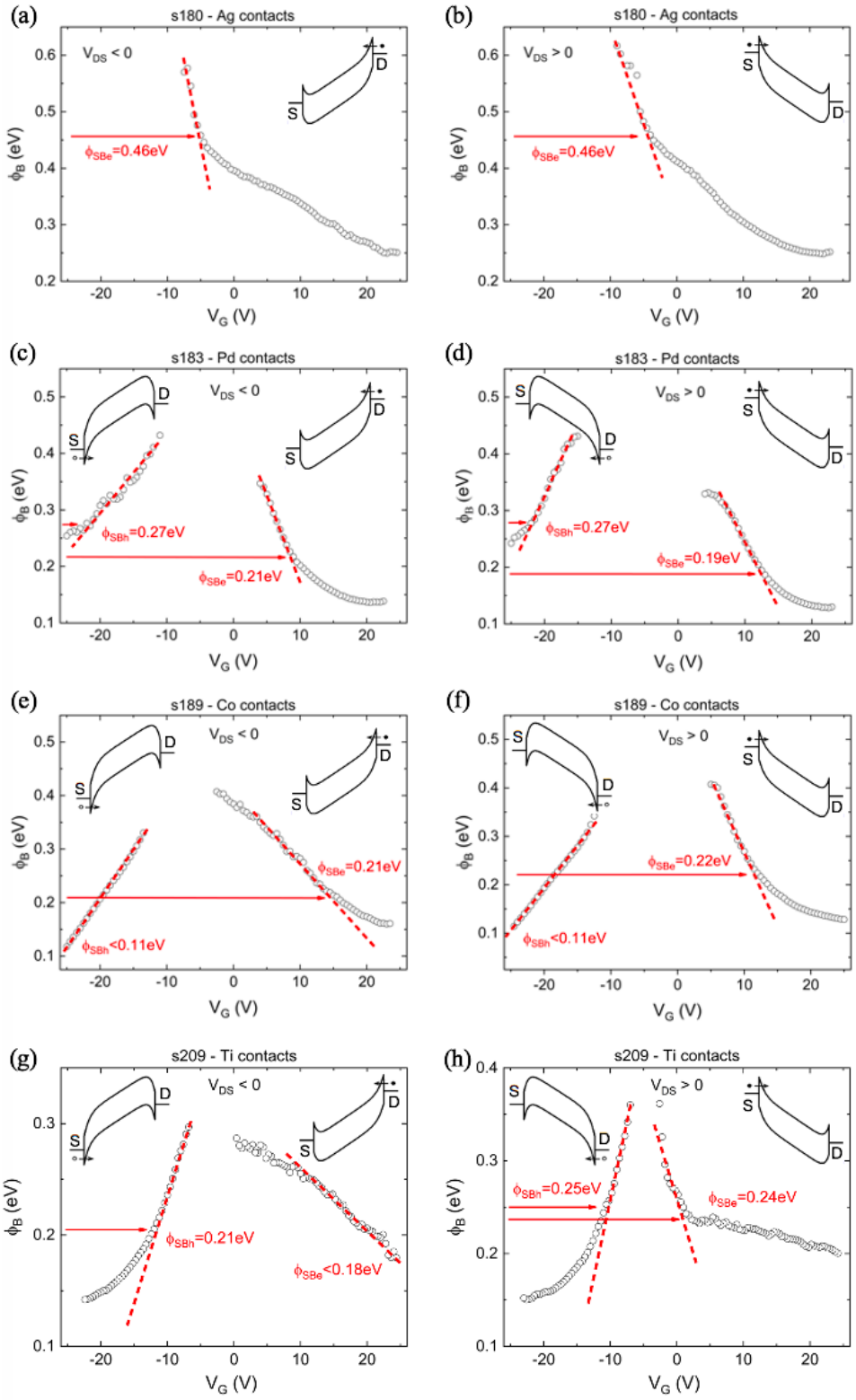

Figure 3.16 – Schottky barriers extracted from the BBSD model for negative and positive applied source-drain voltages in the case of the Pd-contacted sample (a-b), Co-contacted sample (c-b), Ag-contacted sample (e-f) and Ti-contacted sample (g-h). The energy band diagrams for the different applied source-drain and gate voltages are reported in the insets.

Finally, we can plot the extracted values of Schottky barrier heights as a function of the metal work-function as illustrated in Figures 3.17a and 3.17b for electrons and holes, respectively. According to Eq. 3.3, the slope of the $\Phi_{SBe/h}$ vs. Φ_m plots gives an evaluation of the Fermi level pinning factor s. Just to recall, $s \rightarrow +1$ for electrons SBH and $s \rightarrow -1$ for holes SBH would indicate the absence of pinning. In our case, data are quite dispersed, especially in the case of Ag and Co samples. An attempt of linear fit produces as a result $s \rightarrow 0$ both for the electron and hole SBHs, meaning that the Fermi level pinning is strongly dominating the charge injection. Moreover, we record a negative trend for the electron SBH which is counter-intuitive. In fact, one would expect that higher work-function metals create higher Schottky barriers with the conduction band. However, due to the metal-semiconductor interface hybridization, the actual barriers turn out to be reduced. As a matter of fact, the smallest barriers are recorded for Ti, Pd and Co contacts which are also the ones which induce higher orbital hybridization.

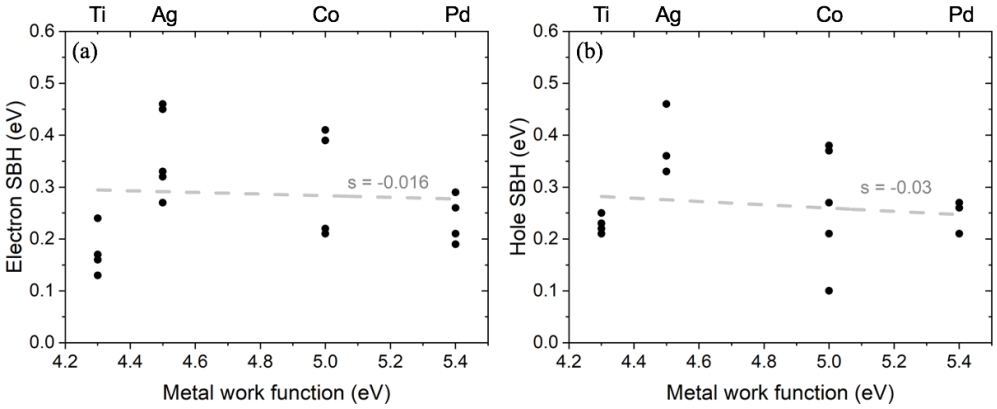

Figure 3.17 – (a) Electron and (b) hole Schottky barriers as a function of the metal work function. The extracted slope is a measure of the Fermi level pinning.

3.6 Conclusion

In this chapter, I have discussed the charge injection in hBN-supported WSe_2-based field effect transistors. After a brief overview on the physics of the subthreshold regime, which is mainly dominated by thermally activated injection, I have introduced two of the most used models for the evaluation of the Schottky barrier height: the temperature-dependent thermionic injection model and the back-to-back Schottky diode model. Afterwards, I have characterized the transfer characteristic of the fabricated devices and, by applying the back-to-back Schottky diode model, I have evaluated the injection barriers for both electrons and holes with different metal contacts. I recorded a strong Fermi level pinning fixing the metal Fermi level inside the semiconductor bandgap. Moreover, the energy gap turns out to be reduced with respect to the theoretical expectations. Indeed, a detailed analysis reveals that metals (such as Pd, Co and Ti), for which a strong hybridization is expected, lead to an important energy gap reduction in the semiconducting material. Metal-2D material interface hybridization can be a possible origin of energy states inside the bandgap which create a smooth transition from the insulating state to the conducting state. The high values of inverse subthreshold slope confirm this statement.

4 Seebeck coefficient in WSe_2 on hBN

Thermoelectric effects result from the charge and heat transport interaction when a material is subjected to an applied electric field or a temperature gradient. For such effects to be remarkable, an appropriate charge density is needed in the material. Naively, if a material owns too many free charges, like metals, a more efficient thermalization will occur, preventing an unbalanced heat gradient. On the other hand, a too low amount of charges would result in a too low electrical signal. The Seebeck coefficient S (or thermoelectric power, TEP), already introduced in Chapter 1, is a measure of the electric potential due to charge diffusion produced by a temperature gradient. Typical values for metals are on the order of few μV/K, while they increase up to few mV/K in semiconductors. This is due to the fact that the Seebeck coefficient is inversely proportional to the density of charge carriers. According to its definition, S is the open-circuit voltage V_{TE} generated in a material when a temperature gradient ΔT is applied:

$$S = -\frac{V_{TE}}{\Delta T} \tag{4.1}$$

In this chapter, I will focus on the in-plane thermoelectric characterization of WSe_2 as a representative 2D material of the transition metal dichalcogenides family. As seen in Chapter 1, the thermoelectric properties of WSe_2 are still poorly studied in literature with respect to other TMDs, even if this material clearly represents an intriguing thermoelectric platform because of its very low in-plane thermal conductivity, on the order of few W/m K, lower than other TMDs. I will start with a detailed description of the measurement approach that I have used in my PhD to investigate the Seebeck coefficient, i.e., the local DC Joule heating method, which was already briefly introduced in Chapter 1. Later on, I will present the results that I have obtained in hBN-supported WSe_2 devices, of which structural and electrical characterization has already been discussed, and I will try to qualitatively discuss them on the basis of the most used theoretical approaches. The Seebeck coefficient is a powerful tool to investigate the semiconductors density of state and, our measurements are in agreement with the electronic transport investigation presented in Chapter 3, revealing a strong influence of the metal-semiconductor interface on the semiconductor density of states. Finally, I will

discuss the power factor PF and figure of merit ZT of hBN-supported WSe_2, which are the main parameters used to quantify the performances of a material for energy conversion and energy recovery applications.

4.1 Seebeck coefficient by local DC heating

In Chapter 1, I gave an overview of the most common approaches used to study the Seebeck coefficient in 2D materials. Here, I will focus on the DC heating method employed in my work. Figure 4.1 shows the schematic representation of the device with the electrical circuit for the thermoelectric measurements. The electric contacts, used for the electrical characterization as source and drain contacts, are now employed as local thermometers (Th_1 and Th_2). An extra metallic nanowire, electrically disconnected from the device, is used as a micro-heater to locally increase the temperature by Joule effect and create a temperature gradient in the longitudinal direction of the device.

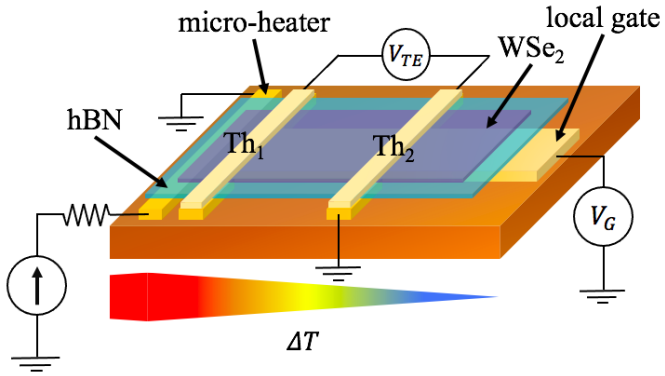

Figure 4.1 – Schematic representation of the device with electrical circuit for the thermoelectric measurements.

The principle of the experimental approach is simple: the two thermometer, Th_1 and Th_2, are first finely calibrated as function of the temperature of the environment, then they are used to monitor the local temperature increase due to Joule heating of the micro-heater. The open-circuit voltage is finally measured as a function of the known temperature gradient, ΔT, established in the device longitudinal direction. Because of experimental set-up limitations (only 8 probes available in the micro probe station), we cannot measure the local temperature of Th_1 and Th_2 nanowires by a local 4-point resistance measurement by simultaneously contacting all the device parts (Th_1, Th_2, gate and micro-heater), which represent the most accurate probe for the local temperature change in the device. Consequently, the temperature gradient evaluation has been performed in a 2-point configuration. This implies that the temperature measured by each thermometer (Th_1, Th_2) is the average temperature of the whole metallic line and not only of the metallic nanowire over the sample area. We refer to this temperature estimation as the "equivalent" 2-point temperature, T_{eq}. Following this approach, in a first step, the temperature of the entire sample is controlled by the temperature regulation of the molybdenum plate of the Nextron micro probe station (as already illustrated in Chapter

3, Figure 3.10b) which is in isothermic contact with the sample. A small DC current (± 20 μA) is fed using a source-meter (Yokogawa 7651) into the metallic nanowires (Th_1 and Th_2) to measure the induced voltage drop by a nanovoltmeter (Keithley 2182A). The two metallic nanowires are 6 μm-long, 400 nm-wide, 80 nm-thick and they are 5 μm-apart from each other. The resistance R of each metallic nanowire is measured as a function of the environment temperature T as illustrated in a representative example in Figure 4.2a. The linear dependence of $R(T)$ is described as

$$R(T) = R_0[1 + \alpha(T - T_0)] \tag{4.2}$$

where the temperature coefficient of resistance α can be extracted as

$$\alpha = \frac{1}{R_0}\frac{dR}{dT} \tag{4.3}$$

The temperature coefficient of resistance for the two thermometers is the main result of this first calibration. In the second step, the temperature of the molybdenum plate is fixed at the operating temperature for all the measurements, T_0 = 25°C. A DC current ramp (from 0 to 5 mA, with steps of 1 mA) is applied into the micro-heater inducing Joule heating and thus a temperature gradient along the sample. For each value of the heater current I_{heater}, the metallic nanowires resistances R_1 and R_2, are simultaneously measured. Thanks to the first calibration step, it is possible to evaluate the average "equivalent" temperature of Th_1 and Th_2 for a given value of I_{heater}. The curves follow a quadratic trend ($T_{eq} = aI^2_{heater} + b$) due to the relation $R \propto T_{eq} \propto I^2_{heater}$. A representative graph of this calibration step is given in Figure 4.2b where the black and red dots indicate the "equivalent" temperature of Th_1 and

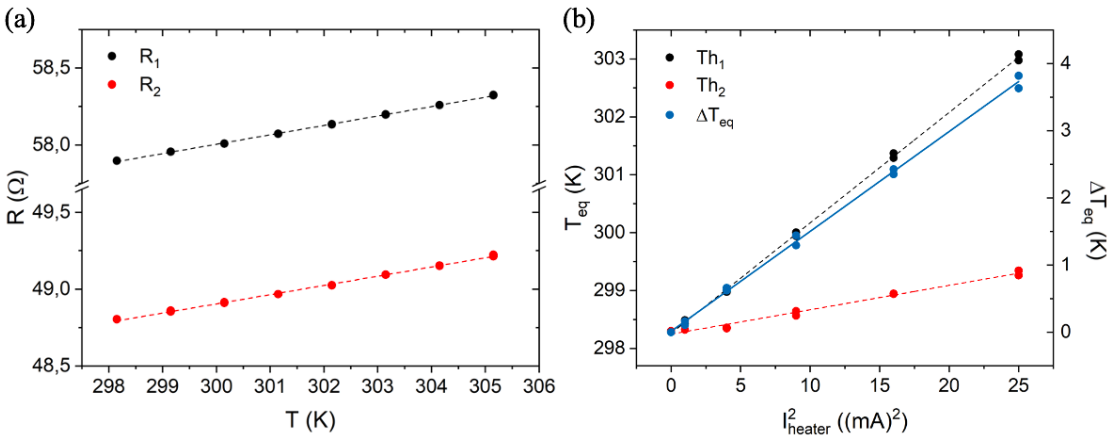

Figure 4.2 – (a) Resistance R of each metallic nanowire used as thermometers (Th_1, Th_2) measured as a function of the environment temperature T in a 2-point configuration. The dashed lines are the linear fits used to extract the temperature coefficient of resistance for each thermometer. (b) Local temperature increase measured by the thermometers Th_1 (black dots) and Th_2 (red dots) when Joule heating occurs in the micro-heater. Dashed lines represent the linear fit to the data. The temperature difference ΔT_{eq} is indicated by the blue dots and line.

Th_2, respectively, as a function of I^2_{heater}. Being the nearest thermometer to the micro-heater, Th_1 is the thermometer that mainly detects a local temperature increase, while the second thermometer (Th_2) does not record a significant temperature rise. The temperature difference between the two thermometers, ΔT_{eq}, evaluated following this "equivalent" 2-point approach, is equal to $[T_{eq}]_{Th_1} - [T_{eq}]_{Th_2}$ and it is illustrated by the blue dots and line in the plot.

To better understand and correct the error introduced by adopting this "equivalent" 2-point measurement configuration, the temperature gradient in the device has been simulated by finite element modeling (FEM) using COMSOL multiphysics. The device geometry reproduces the details of the fabricated samples, as illustrated in Figure 4.3. In particular, I have considered a thickness of the hBN and WSe_2 layers of 40 nm and 3 nm, respectively, and all electrical, thermal and other physical parameters, such as the electrical conductivity σ, the thermal conductivity κ, the mass density ρ, the electrical permittivity ε have been extracted from the literature or, when possible, from the electrical characterization presented on Chapter 3.

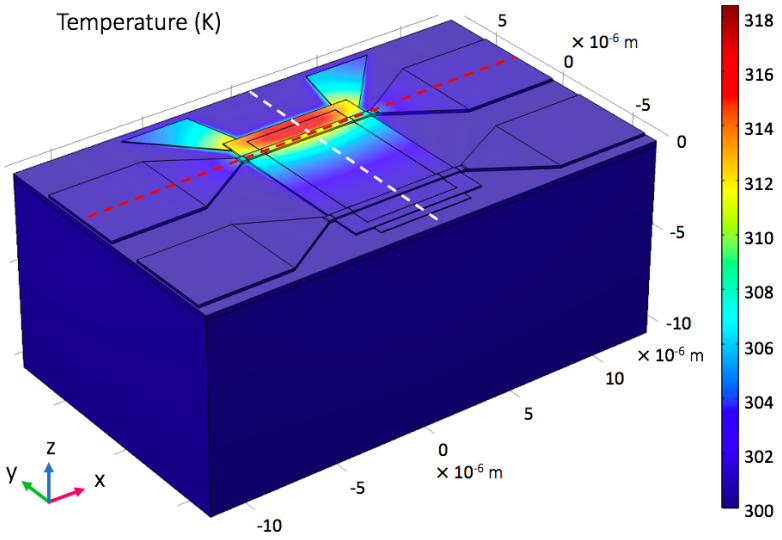

Figure 4.3 – Device geometry simulated using COMSOL multiphysics. The color legend indicates the temperature at the outermost surface of the device.

Joule heating is achieved by applying an electric current (I_{heater}) at one extremity of the micro-heater while grounding the other extremity. The current is varied between 1 and 5 mA, which is the range of current and the configuration used in the experiments. Figure 4.4a shows, for each value of the heating current, the temperature profile in the longitudinal (y) direction of the device in the middle of the structure ($x = 0$), on the WSe_2 surface, following the white dashed line in Figure 4.3. The simulation confirms that only the closer thermometer to the heater (Th_1) is subjected to a significant temperature variation while the second thermometer (Th_2), 5 μm-far from Th_1, is not affected by a significant temperature rise and it is almost thermalized at the environment temperature. Figure 4.4b shows the temperature profile developed along thermometer Th_1 in the x direction at the metal-WSe_2 interface, following the red dashed line in Figure 4.3, as a function of current injected in the micro-heater. In this

case, the profiles clearly show that the main temperature increase occurs, as expected, over the sample region ($|x| < 2.5\ \mu$m). However, the temperature rise in the external region to the sample is not negligible. For each current value, I have evaluated the average temperature increase T^* affecting the portion of nanowire Th_1 on the WSe_2 by integrating the temperature profile in the region $|x| < 3\ \mu$m, which corresponds to the temperature that would be measured in a 4-point configuration. I have also evaluated the average temperature increase of the whole metallic line T_{eq}, by integrating the temperature profile over the whole length of the metallic line (25 μm in the simulation), which better describes the "equivalent" 2-point approach experimentally used. The obtained temperature values are plotted in the inset of Figure 4.4b as a a function of the current injected in the micro-heater. It turns out that the ratio of the temperature variation due to the heating current evaluated on the basis of these two estimations, dT^*/dT_{eq}, is equal to a constant value of 2.76, independently of the current injected in the micro-heater.

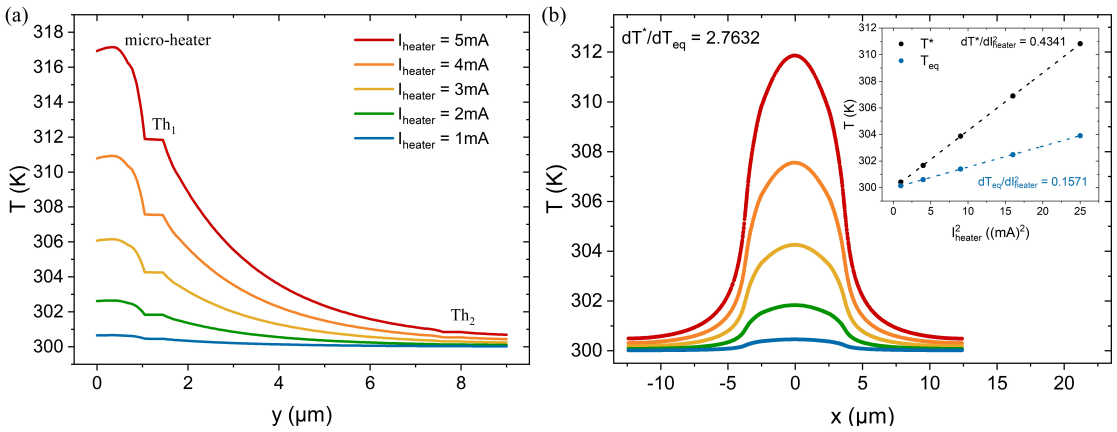

Figure 4.4 – (a) Temperature profile in the longitudinal direction of the device at $x = 0$ and z corresponding to the WSe_2 surface when the current in the micro-heater is varied from 1 mA (blue line) to 5 mA (red line). (b) Temperature profile developed in the thermometer Th_1 as a function of injected current in the micro-heater. The inset shows the simulated T^* and T_{eq} as a function of I^2_{heater}. Dashed lines are the linear fit to the data.

To confirm the COMSOL simulations and to prove that the ratio dT^*/dT_{eq} is sample independent, control measurements have been carried out on three samples equivalent to the ones used for the complete electric and thermoelectric characterization (which have been introduced in Chapter 3). These test samples are designed with 4-leads thermometers (as shown in the inset of Figure 4.5b). Separately for each thermometer, I have first evaluated the temperature coefficient of resistance in a 4-point and 2-point configuration as a function of the temperature of the environment, as illustrated in Figure 4.5a for a representative sample. Subsequently, I have measured the temperature increase of each thermometer as a function of the applied current in the micro-heater on the basis of the two calibration configurations. Figure 4.5b illustrates a representative example of such a temperature increase for the two thermometers, Th_1 and Th_2, on the basis of the 4-point (black and green data) and 2-point (blue and red data) calibration configuration, respectively. Dashed lines represent the linear fit to the data ($T = aI^2_{heater} + b$). These test measurements need the opening of the vacuum

chamber to change the electrical connections from one thermometer to the other, which exposes the whole device to atmosphere, adsorption of gas or water molecules, not beneficial to preserve its properties. For these reasons, we cannot adopt the 4-point calibration procedure for a complete in-situ electric and thermoelectric characterization.

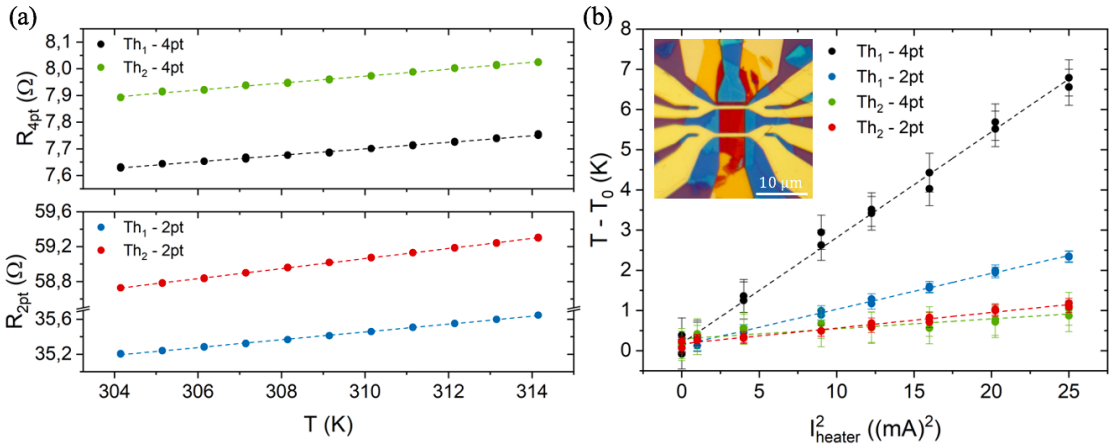

Figure 4.5 – (a) Resistance R of each metallic nanowire used as thermometers (Th_1, Th_2) measured as a function of the environment temperature T at 4-point and 2-point configuration. The dashed lines are the linear fits used to extract the temperature coefficient of resistance for each thermometer. (b) Local temperature increase measured by the thermometers Th_1 (black and blue dots for the 4-point and 2-point configuration, respectively) and Th_2 (red and green dots for the 4-point and 2-point configuration, respectively) when Joule heating occurs in the micro-heater. Dashed lines represent the linear fit to the data. The inset shows an optical image of a representative sample with 4-leads thermometers used to validate the "equivalent" temperature gradient evaluation.

We can note that for thermometer Th_2, the detected temperature increase is lower than 1 K, in both measurement configuration (red and green data in Figure 4.5b). This confirms that Th_2 is nearly in thermal equilibrium with the environment, in agreement with the COMSOL simulation (Figure 4.4a). By considering the estimated error bars of ~ 0.5 K, we have chosen to assume $dT^*/dT_{eq} \sim 1$ for Th_2. On the other hand, the temperature rise in Th_1 is larger when measured in 4-point configuration and the ratio $dT^*/dT_{eq} > 1$, experimentally. The analysis has been carried out for three samples having the same electrodes geometry and similar hBN and WSe_2 flakes dimensions and thicknesses. For the three samples, we have found experimentally that the ratio dT^*/dT_{eq} for Th_1 is constant and equal to $\gamma = 2.93 \pm 0.06$, which is in agreement with the FEM simulations.

Supported by these experimental tests, I have empirically corrected the measured 2-point "equivalent" temperature increase dT_{eq} in the longitudinal direction of the sample by the experimentally evaluated γ factor as follow:

$$\Delta T_{corr} = \gamma \left[T_{Th_1}\right]_{eq} - \left[T_{Th_2}\right]_{eq} = \left(\gamma a_{Th_1} - a_{Th_2}\right) I^2_{heater} \tag{4.4}$$

where a_{Th_1} and a_{Th_2} are the results of the fitting procedure of the current dependence temperature increase ($T_{eq} = aI^2_{heater} + b$) for the thermometer Th_1 and Th_2, respectively.

4.1.1 Thermoelectric voltage measurement

Having clarified the procedure to estimate the temperature gradient along the device by local heating of the micro-heater, I present here how we measure the thermoelectric voltage V_{TE} generated accordingly. For each value of gate voltage V_G, the current in the heater is swept from 0 to 5 mA (with a current step of 50 μA and a sweeping rate of 50 μA/s) and, for each point of current, the open-circuit thermoelectric voltage V_{TE} is measured. The gate voltage is applied by adopting the same electrical connection employed for the electrical measurements, by referring the thermometer Th_2 to the ground and leaving the Th_1 floating. Due to the relationship $V_{TE} \propto \Delta T \propto I^2_{\text{heater}}$, the recorded $V(I_{\text{heater}})$ exhibits a parabolic behavior. Figure 4.6 shows a representative example of the measured open-circuit voltage as a function of the current flowing into the heater line (a) for V_G = -25 V and (b) for V_G = 25 V in the case of a Co-WSe_2 sample (s189).

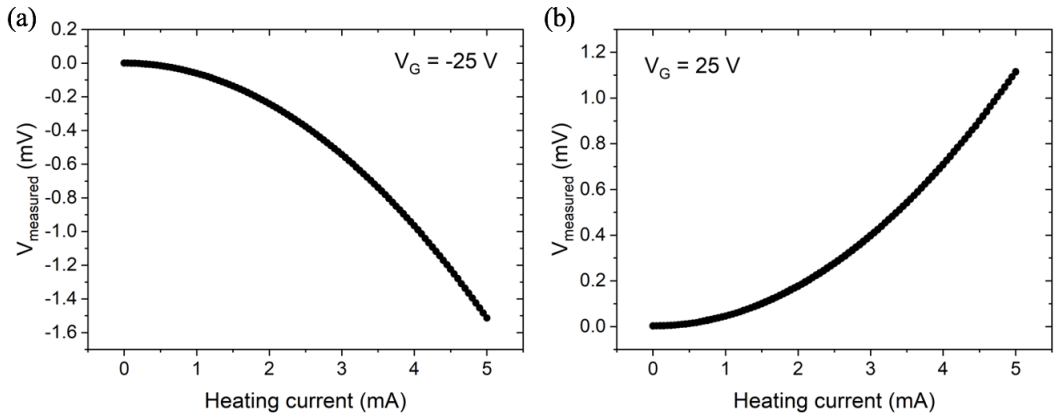

Figure 4.6 – Measured open-circuit voltage as a function of the current flowing into the micro-heater line for (a) V_G = -25 V and (b) for V_G = 25 V in the case of a Co-WSe_2 sample (s189).

To correctly extract the thermoelectric part of the measured signal, we follow the approach proposed by Kayyajha et al. [136]. The measured open-circuit voltage as a function of the heating current is of the form $\hat{a}I^2 + \hat{b}I + \hat{c}$, meaning that its nature is not purely thermoelectric. The constant term ($\hat{c}$) corresponds to the contribution of the voltmeter offset and the resistive coupling between the semiconducting channel and the back-gate. The linear term ($\hat{b}I$) indicates contributions of coupling from the heater pads to the channel. Finally, the second order term ($\hat{a}I^2$) is the pure thermoelectric contribution to the measured signal. Thus, the Seebeck coefficient is obtained as $S = -\hat{a}I^2/\Delta T_{\text{corr}}$ for the each value of gate voltage V_G. Figure 4.7 illustrates the quadratic, linear and constant components dependence of a representative sample (s189) as a function of the gate voltage for a given heating current of 2.5 mA. We can note that the linear component (orange data) is always negligible in the explored V_G range, meaning that the semiconducting channel is well isolated from the metallic line used to generate the temperature gradient. The constant component (green data) becomes the dominant one when the WSe_2 channel is in the OFF-state, while it vanishes in the ON-state. On the contrary, the thermoelectric component (blue data) becomes the dominant component

when the device enters its subthreshold regime and reaches a maximum value around the electrons and holes threshold voltage. It is important to note that the Seebeck coefficient measured in the gap region has to be considered with caution: in this region, S could be affected by a high incertitude since the device has a very high impedance which reduces the signal measured by the meter. Globally, the behavior presented in Figure 4.7 is well representative of what is observed for all the samples measured during my PhD.

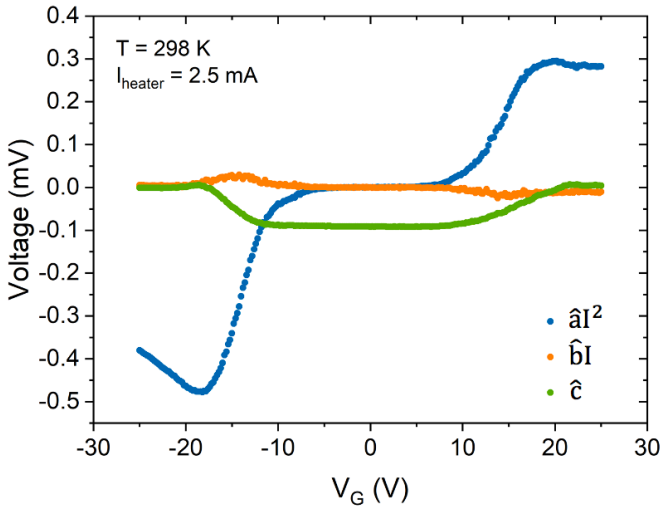

Figure 4.7 – Quadratic, linear and constant components dependence of the measured open-circuit voltage as a function of the gate voltage for a given heating current.

4.2 Seebeck coefficient in hBN-supported WSe_2

We can now move our attention to the results of the thermoelectric characterization of the devices introduced in Chapter 3, focusing on the Seebeck coefficient analysis. Just to recall, several hBN-supported WSe_2 samples have been fabricated with different metal contacts (Table 3.1). Here, I will present a representative sample for each one of them. For each choice of metal contact, at least a second sample has been electrically and thermoelectrically characterized. The obtained results for these samples are reported in Appendix B.

The gate voltage dependence of the Seebeck coefficient for the four discussed samples is illustrated in the top panel of Figure 4.8 for both direction of gate voltage sweep. As expected, the sign of S reveals the nature of the majority carriers: a positive (negative) sign corresponds to hole- (electron-) dominating transport. No signal can be revealed in the gap region, where the density of charge carriers goes to zero, while S increases suddenly as we move the Fermi level towards the conduction or valence bands edges. When further increasing the density of charge carriers, the Seebeck coefficient starts to decrease, being S roughly $\propto 1/n_{3D}$ (beyond threshold) in accordance with the Mott formula for degenerately doped semiconductors. In all cases, we reveal values of Seebeck coefficient in agreement with what previously reported in literature for WSe_2-based transistors [79, 80]. The maximum S values, $|S_{max}|$, are of the

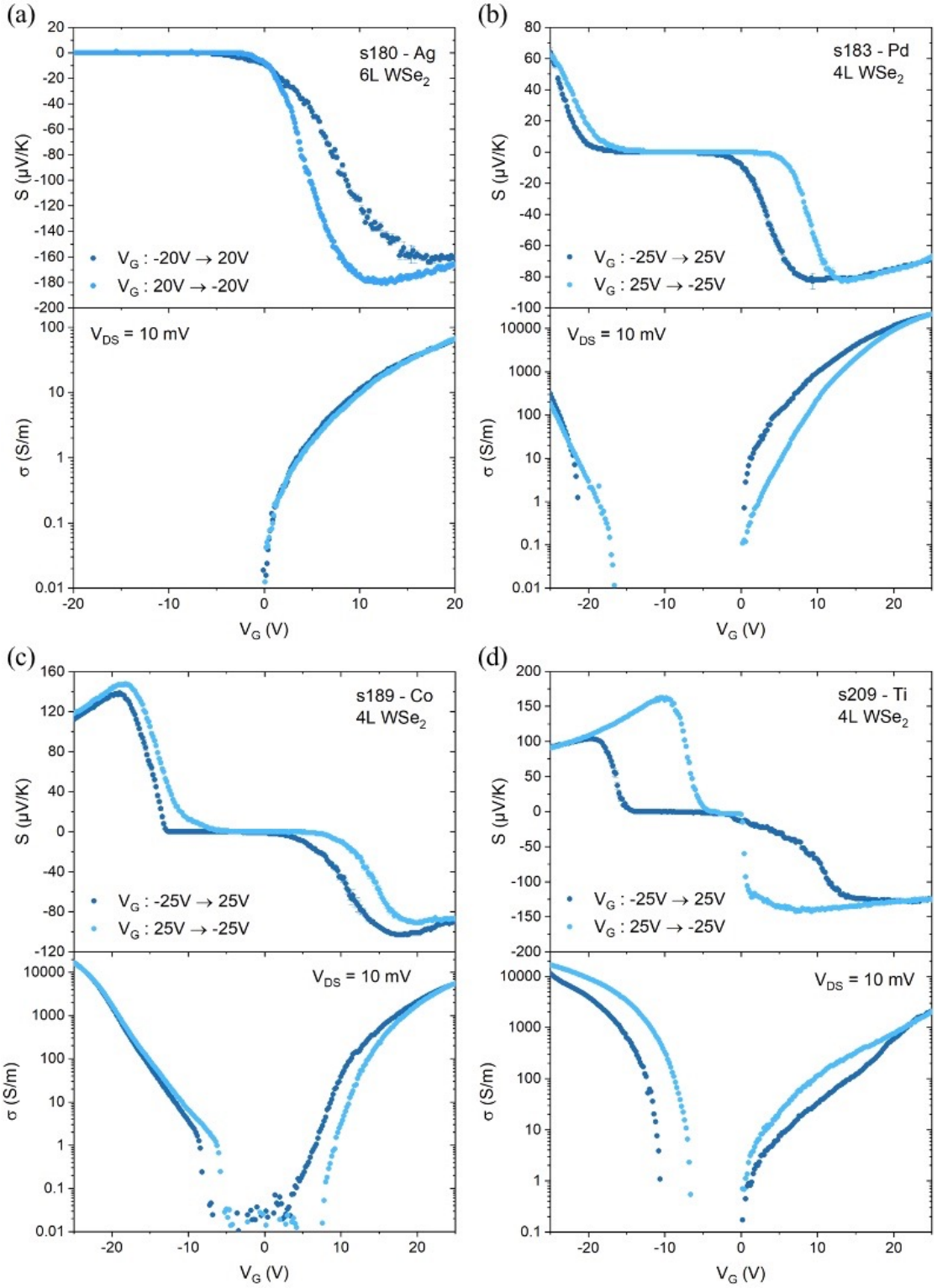

Figure 4.8 – Gate voltage dependence of the Seebeck coefficient (top panel) and the electrical conductivity (bottom panel) for the highlighted samples in Table 3.1, for increasing and decreasing gate voltage sweep.

order of 180 μV/K for Ag, 90 μV/K for Pd and 160 μV/K for Co and Ti. The thermoelectric measurements confirm the ambipolar behavior in Pd-, Co- and Ti-contacted devices, as well as their reduced bandgaps, as already inferred by the electrical characterization (Chapter 3). This is also illustrated by the 2-point electrical conductivity measurements reported in the bottom panels of Figure 4.8 in semi-log scale for each sample. Furthermore, both the S and σ measurements also show that electron injection is favored in all samples, indicative of Fermi level pinning towards the conduction bands independently of the nature of the metal contacts.

4.2.1 Metal-induced orbital hybridization

By comparing the four samples presented in Figure 4.8, it appears that the nature of the metallic contact has a strong influence on both the electric and thermoelectric response of the studied WSe_2-based devices. For instance, we can note that charge injection in the conduction and valence bands occurs with different slopes. This is particularly evident in the Co- and Ti-WSe_2 samples for electron and hole injection or if comparing the electron injection region of all the samples. The slopes of S and σ at the band edges are typically related to the presence of gap states close to the valence band maximum or the conduction band minimum, inducing an exponential tail of the DOS in the bandgap region. Commonly, gap states can be induced by the presence of impurities and defects in the structure. In our case, given the evident metallic contact dependence, they could be related to metal-induced orbital hybridization as already introduced in Chapter 3. Indeed, our results reveal a metal dependent modulation of the transport gap which is evident from both the electric and thermoelectric analysis. This behavior can be explained by the modified band structure of WSe_2 due to orbital hybridization at the contacts interfaces.

Several theoretical works have investigated the effect of different metal/2D material interface on the local density of state, including the case of WSe_2 as well as other TMDs. However, to my knowledge, no experimental study exists in literature exploring such interface effect simultaneously on the electric and thermoelectric properties of 2D materials. Figure 4.9

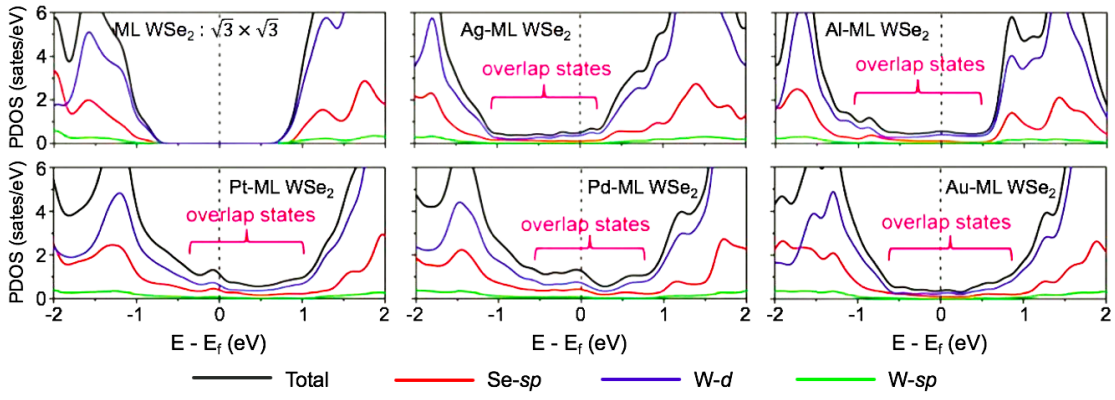

Figure 4.9 – Total and partial density of states of W and Se electron orbitals, for pristine ML WSe_2 and Ag-, Al-, Pt-, Pd-, Au-ML WSe_2 systems, respectively, in the absence of the SOC. Figures extracted from [248].

shows a representative theoretical work by Wang et al. [248] calculating by DFT the partial density of states (PDOS) of W and Se electron orbitals for a pristine WSe_2 monolayer and several metal-WSe_2 systems. The contact with a metal leads to the appearance of electronic states in the band gap of the pristine WSe_2, due to the metallic wave function decaying into the semiconducting 2D material. In particular, it is mainly the W d- and Se sp-states that arise in the pristine band gap, while W sp-states are generally unmodified after the metal absorption. In the weak hybridization case (Ag- or Al-WSe_2 interfaces), only a small portion of states redistribute in the pristine band gap of the TMD and valence and conduction bands can still be identified. Thus, WSe_2 preserves its semiconducting nature. On the other hand, in moderate and strong hybridization (Pt-, Pd- and Au-WSe_2 interfaces), a large portion of states arise in the original band gap of the semiconductor. This leads to a metallization for the 2D material at these surfaces. A similar study has been carried out also for $MoSe_2$ in contact with several metals in the theoretical work of Pan et al. [250] by applying ab initio energy band calculations. Similar results, such as the ones for WSe_2, are illustrated in Figure 4.10.

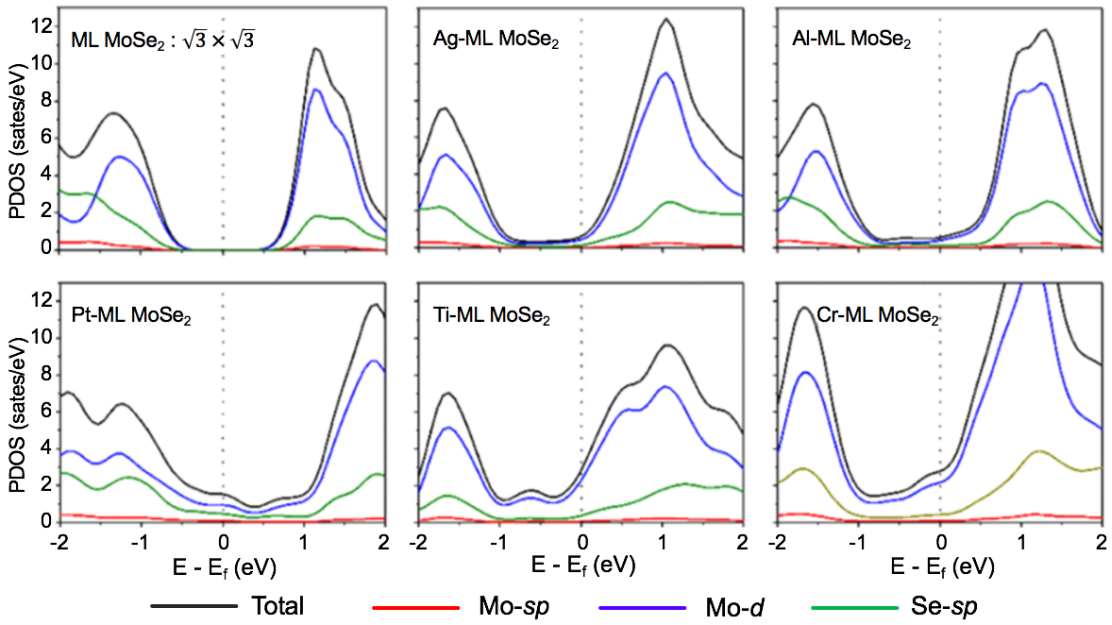

Figure 4.10 – Total and partial density of states of pristine $MoSe_2$ and $MoSe_2$ on the Ag, Al, Pt, Ti, and Cr surfaces computed by DFT calculations. The Fermi level is at zero energy. Extracted from [250].

According to the reported theoretical works, bonding strength at the metal/2D material interface can be understood in terms of d-band hybridization. Al has no d-orbitals and Ag and Au have full d-shells, all resulting in a weak bonding with WSe_2 or $MoSe_2$. The relative position of the d-band also plays an important role. Even though Pd and Ag both have full d-shell, the d-band of Pd is located closer to the Fermi level than that of Ag, thus Pd strongly hybridizes with the valence band of WSe_2. On the contrary, Co and Ti have partially filled d-shells and thus, they are prone to a strong hybridization. As shown in Figure 4.10, the interaction with Ti generate a large portion of Mo and Se states in the original band gap of $MoSe_2$. Moreover, the Fermi level in the Ti-$MoSe_2$ system is shifted towards the conduction band. As a result, not

only overlap states modify the effective energy gap of the semiconductor, but they can also contribute to the electron or hole injections from the metal to the semiconductor.

From our results, as illustrated in Figure 4.8, we can see that Co and Ti interfaces lead to the strongest reduction of the energy gap resulting in a clear ambipolar behavior. The Seebeck coefficient for these two devices shows a peak in both the electrons and holes branches, meaning that the Fermi level is starting to explore more delocalized band states rather than localized states at the conduction and valence band edges. The sample based on Pd contacts also shows a bandgap reduction but less important with respect to the two previous cases. Due to Fermi level pinning, Pd-WSe_2 samples show a favored n-type injection and the peak for the Seebeck coefficient is only visible in the electron branch. Ag-WSe_2 samples only show a n-type transport behavior in the explored gate voltage range. This could indicate that the band structure of the semiconductor is less modified, and the energy gap is better preserved. However, the Fermi level of the semiconductor seems to be very close to the conduction band as visible from Figure 4.8a. This is in agreement with the theoretical prediction illustrated in the PDOS in Figure 4.9 for the case of Ag-WSe_2 interface.

As expected, the measured low-voltage electrical conductivities strongly depend on the nature of the metallic contact as well, and Ag-based samples show the lowest conductivity. Weak coupling, predicted at the Ag-WSe_2 interfaces, allows to consider that the thermoelectric response is mostly related to the WSe_2 electronic structure in the channel rather than under the contacts. In agreement with this picture, one can note that this is the only particular case for which we measure the highest Seebeck coefficient. Strong coupling, expected at the Pd-WSe_2, Co-WSe_2 and Ti-WSe_2 interfaces, seems to favor a thermoelectric response more related to the interfacial electronic structure. Even if all this analysis is purely qualitative, the general trend seems to confirm that a careful engineering of electrical contacts in 2D material-based devices can be a possible tool to control the thermoelectric properties for energy conversion applications.

4.2.2 Gate-dependent hysteresis

Here, I would like to spend few comments on the gate-dependent hysteresis visible in electric and thermoelectric measurements, which I have not discussed until now. Hysteresis is a recurrent phenomenon in TMDs-based field effect transistors, and it has already been studied in previews works in relation to charge transport [235, 232, 263, 264]. Current hysteresis in TMDs is often associated to substrate charge trapping or to possible surface adsorbates related to the fabrication process and it can be reduced by performing temperature annealing [235]. In our case, these hypotheses can be very likely excluded since WSe_2 is electrically decoupled from the substrate by the atomically thin and dangling bond-free hBN layer and the measurements are performed in high-vacuum conditions after in-situ annealing up to 400°C. However, these are not the only reasons for such behavior. Shu et al. [264] studied the current hysteresis in suspended MoS_2 under vacuum conditions in order to exclude the

influence of the substrate or the atmosphere. In agreement with our results, they found that the hysteresis is strongly related to the gate voltage stress and that the gate voltage sweep range, sweep direction, sweep time and loading history all affect the hysteresis observed in the transfer-curves. In particular, they remarked that negative gate voltages have a stronger effect on the hysteresis. Moreover, they observed a thickness dependence of the hysteresis meaning that, not only the hysteresis is intrinsically related to the material, but also the surface plays an important role.

In all the devices studied in this work, depending on the gate voltage direction sweep, the Seebeck coefficient shows a hysteretic behavior when the device is crossing its electrical sub-threshold regime, both in the electron and hole branches (top panels of Figure 4.8). Moreover, the Seebeck hysteresis is more evident with respect to the one appearing in the electrical conductivity measurements. In agreement with the experimental observation reported in literature, Figure 4.11 illustrates the example of different measurements of Seebeck for a Ag-WSe_2 sample in two different cases. On one side, Figure 4.11a shows the Seebeck coefficient response when changing the sweep direction while keeping the same gate voltage range. On the other side, Figure 4.11b shows the case in which the gate voltage range has been gradually increased from a measurement to the other, without changing the sweep direction. In both cases, the curves are sensible to the different application of V_G. However, if the measurement is repeated in the same gate voltage range and sweep conditions, the curve is completely reproducible.

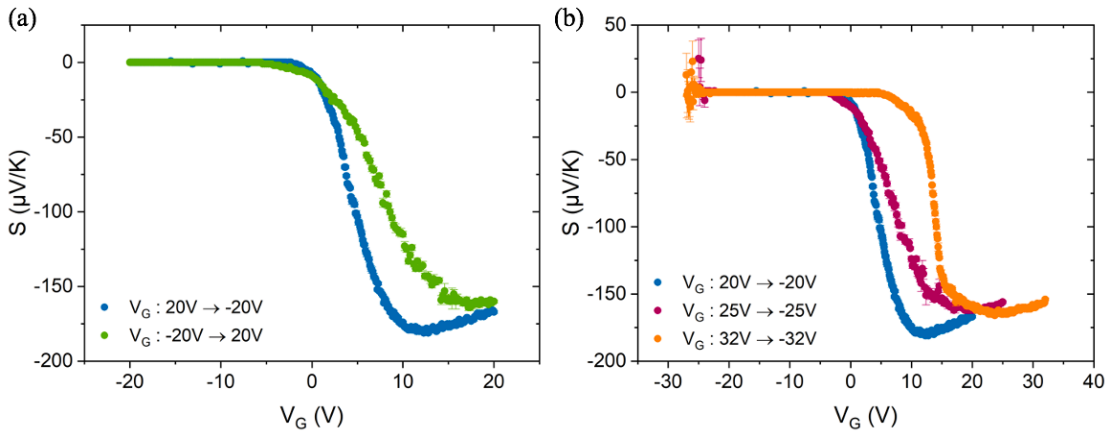

Figure 4.11 – Hysteretic response of the Seebeck coefficient in a Ag-WSe_2 sample in the case of (a) same gate voltage range but different sweep direction and (b) same sweep direction but different gate voltage range.

Quite particular is also the case of Ti-WSe_2 samples (see Figure 4.8d). While for all the devices an inversion of the gate voltage sweep direction results in a slight shift of the Seebeck coefficient plot, in the case of Ti the effect is more surprising. Not only the Seebeck coefficient peak is strongly modified (from 162 μV/K to 104 μV/K), but also the bandgap is different, and it is extremely reduced when sweeping from positive to negative gate voltage. This experimental evidence can only be the result of a reversible modification of the semiconductor band structure due to the applied transverse electric field. This phenomenon has already

been reported in literature for 2D materials. For example, bi-layer graphene can develop a gap when an out-of-plane electric field is applied to the system acting as a gate [265]. Such a band structure modification has been reported also for bilayer MoS_2, $MoSe_2$, $MoTe_2$ and WS_2 [266, 220], but also for multilayer WSe_2 [267]. According to some DFT computations, the intrinsic inversion symmetry can be broken simply by applying a perpendicular electric field in bilayer or bulk two-dimensional electron systems where the crystal symmetry governs the nature of electronic states. In other words, upon application of an external field, the valence and conduction subband states separately undergo to a mixing, leading to a field-induced splitting of the electronic levels [267].

The hysteretic behavior is also recorded in the electrical measurements. Figure 4.8 (bottom panels) shows the devices conductivities as function of the gate voltage (trans-conductance curves) measured at V_{DS} = 10 mV for the discussed samples in the two gate sweep directions. The weak source-drain polarization is chosen in order to have a negligible band deformation at the metal-semiconductor interfaces and to approach the Seebeck configuration measurements, in which no source-drain voltage is applied. Also in this case, it is possible to record a hysteresis in the same gate voltage regions as for the Seebeck curves. However, the amplitude of the hysteresis is quite reduced and sometimes negligible.

Even though the origin and the mechanisms remain unclear, it is evident that hysteretic behaviors are related to the energy band stress to which the semiconducting material undergoes when a strong electric field is applied. In this context, the Seebeck coefficient measurement appears to be a more powerful tool with respect to the classical charge transport measurements for this investigation.

4.3 Comparison with existing theoretical approaches

4.3.1 Mott relation

In this paragraph, I will try to qualitatively discuss my results on the basis of the most used approaches to evaluate the Seebeck coefficient in 2D materials. A commonly used expression is given by the Mott relation which is derived from the Boltzmann transport equation (BTE) for degenerately doped materials and it gives a simple expression of the Seebeck coefficient as a function of the electrical conductivity. The Mott formula can be derived from Eq. 1.10 and is expressed by:

$$S = -\frac{\pi^2 k_B^2 T}{3e}\frac{1}{\sigma}\frac{d\sigma}{dV_G}\frac{dV_G}{dE}\bigg|_{E=E_F} \tag{4.5}$$

By considering a parabolic band dispersion relation $E = \frac{\hbar^2 k^2}{2m^*}$ and the spin and valley degeneracy, it is possible to write $\frac{dV_G}{dE} = \frac{2em^*}{\pi\hbar^2 C}$ [136]. Here, m^* is the charge effective mass and C is the dielectric capacitance. Eq. 4.5 can be rewritten to directly evaluate the Seebeck coefficient as a

function of the electrical conductivity obtained from the charge transport measurements:

$$S = -\frac{2\pi^2 m^* k_B^2 T}{3\hbar^2 C} \frac{1}{\sigma} \frac{d\sigma}{dV_G} \tag{4.6}$$

For some of the studied WSe_2 samples, I have tried a comparison with the Seebeck coefficient evaluated according to the Mott formula, using the experimentally measured electrical conductivity shown in the bottom panels of Figure 4.8. Figure 4.12 shows two examples for the case of Ag and Co contacts, samples s180 and s189, respectively. The dark and light blue points are the experimentally measured S values for up and down gate sweep direction, respectively, while the solid red and yellow lines are calculated from Eq. 4.6 by numerical derivation of the corresponding electrical conductivity measurement. Since the measured 2-point electrical conductivity is a lower estimation of the actual electrical conductivity of the semiconducting channel, the obtained values of S calculated with Eq. 4.6 are overestimated. In order to compare the computed values with the experimental ones, the calculated curves are re-scaled by a multiplicative factor.

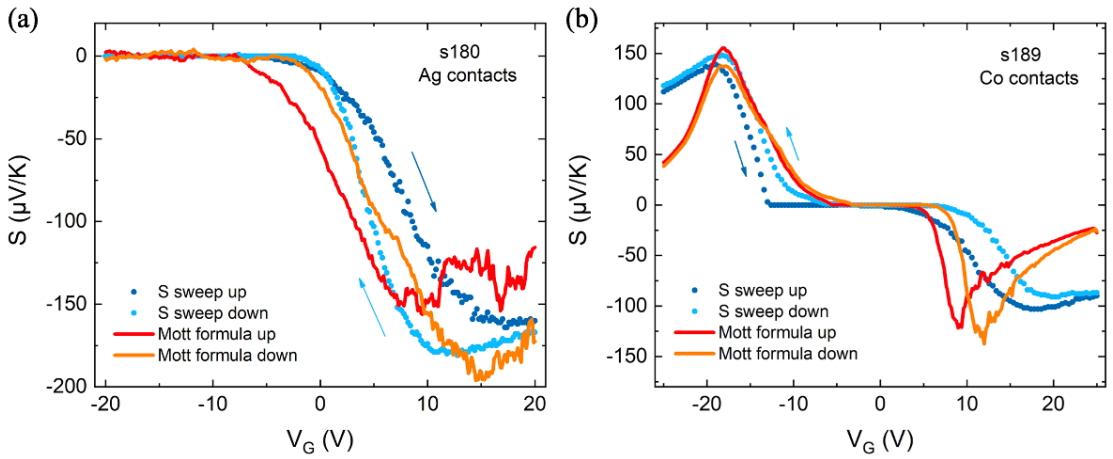

Figure 4.12 – Seebeck coefficient values for two hBN/WSe_2 based-devices with (a) Ag and (b) Co contacts. The dark and light blue points are the experimentally measured Seebeck coefficient values for up and down gate sweep directions (as indicated by the arrows), while the solid red and yellow lines are calculated from Eq. 4.6.

We can note that, while the comparison is quite good for sample s180 (Ag contacts), this is less the case for sample s189 (Co contacts). In this last case, a maximum S value is found around a gate voltage value for which a maximum experimental value of S has been measured. However, the Mott formula forecasts a faster reduction of the Seebeck coefficient when further increasing V_G in absolute value. The main explanation for this lack of agreement is probably related to the fact that a full band transport, necessary for the Mott relation to be valid, is not achieved in the explored gate voltage range. As already pointed out, the devices under investigation are characterized by an electric and thermoelectric response probably mainly dominated by localized energy stated at the conduction and valence bands edges. This suggests a divergence from the delocalized band-like transport. It is worthwhile to note that, as discussed previously,

samples with Ag-based metal/semiconductor interfaces present a reduced hybridization effect with respect to the other metallic contacts (Co, Pd, Ti) and the highest measured Seebeck signal as well as the larger bandgap. For this sample, the Mott relation seems to describe data qualitatively better with respect to the other samples. In the case of samples based on Co contacts (as well as Pd and Ti contacts, not shown), the expected interface hybridization is stronger and we find out that the Mott relation is less effective in describing the experimental Seebeck measurements. In any case, we have to keep in mind that a direct comparison of the Seebeck coefficient extracted from the Mott relation is not allowed in all the explored gate voltage range, being the Mott formula only valid in the degenerate limit. Thus, the comparison can be considered only valid for V_G approaching and exceeding the threshold voltage for both electrons and holes.

I would like to underline that, by comparing the measured Seebeck coefficient with the Mott formula, I have no ambition to theoretically explain my experimental results. Even though the Mott formula is widely used in literature to reproduce the Seebeck coefficient of degenerately doped semiconductors and it is widely used in the analysis of the thermoelectric response of TMD materials, the transport mechanisms taking place in 2D semiconducting materials requires a deeper and more careful modeling. Moreover, in literature, a theoretical study on the metal-semiconductor interface influence on the thermoelectric properties is missing. My discussion has the aim to give some hints on a possible explanation for this phenomenon.

4.3.2 Effect of reduced dimensionality and disorder on the thermoelectric power

A deeper theoretical analysis of the thermopower in TMDs-based devices has to take into account the effect of dimensionality and the dominating scattering mechanism in 2D materials. Hippalgaonkar et al. [137, 268] have considered these aspects in analyzing experimental data of charge transport and thermoelectric effect in MoS_2-based devices. According to the Boltzmann transport equation (BTE) under the relaxation time approximation, the expression of the Seebeck coefficient when considering n-type transport can be written as:

$$S = -\frac{1}{qT}\frac{\int_{E_c}^{\infty}\frac{df_{FD}}{dE}D_{2D}(E)(E-E_F)\tau(E)dE}{\int_{E_c}^{\infty}\frac{df_{FD}}{dE}D_{2D}(E)\tau(E)dE} \tag{4.7}$$

where f_{FD} is the Fermi Dirac distribution, D_{2D} is the 2D DOS, E_F is the Fermi level, E_c is the conduction band minimum (CBM) and $\tau(E) = \tau_0 E^r$ is the energy-dependent relaxation time, where r is the scattering exponent that depends on the dominant scattering mechanism [137]. Using the energy-independent DOS approximation and accounting for the energy-dependent scattering rate, the steady-state solution to the linearized BTE allows to write Eq. 4.7 as follows:

$$S(\eta) = -\frac{k_B}{q}\left[\eta - \frac{\left(r+\frac{D}{2}+1\right)\int_0^{\infty} f_{FD}\varepsilon^{r+\frac{D}{2}}d\varepsilon}{\left(r+\frac{D}{2}\right)\int_0^{\infty} f_{FD}\varepsilon^{r+\frac{D}{2}-1}d\varepsilon}\right] \tag{4.8}$$

where $\eta = (E_F - E_c)/k_B T$, $\varepsilon = (E - E_c)/k_B T$ and D is the dimensionality of the system (in our case $D = 2$). Different scattering mechanisms affect carrier transport in 2D materials. Considering a 2D single parabolic band model, it has been shown that $\tau(E)$ scales with the DOS for acoustic phonons scattering, thus, for acoustic phonon-limited scattering $r = 0$. The same coefficient has been evaluated for intervalley scattering ($r = 0$), which is also phonon-mediated and thus energy independent. For charged impurity scattering, the scattering roughly has the energy dependence $r = 3/2$, and strongly screened Coulomb scattering is characterized by $r = -1/2$ [268]. A detailed analysis of the Seebeck coefficient allows determining the dominating scattering mechanism in the material under study. Comparing their experimentally measured Seebeck coefficient to this theoretical equation, Hippalgaonkar et al. found that, in 2D MoS_2, the dominating scattering mechanism is related to electron-phonon interaction. Moreover, they found a lower mobility than the intrinsic phonon-limited one, as calculated from first principles [269, 270], suggesting that substrate-monolayer coupling may significantly alter the phonon channels [268, 137]. On the other hand, 3D MoS_2 is mainly dominated by charged impurity scattering which is absent in the 2D counterpart. Charged impurity scattering deteriorates the electric and thermoelectric performances of materials and, thus, the reduced dimensionality turns out to be a good strategy to enhance both the electrical conductivity and the Seebeck coefficient.

In light of this approach, I have tried a comparison of my experimental data with this theoretical treatment. In order to calculate the Seebeck coefficient, we need to evaluate the quantity $E_F - E_c$, and to limit the analysis in the degenerate limit, where $|E_F - E_c| \leq 2k_B T$ and transport occurs through the band density of state. In this condition the carrier concentration n_{2D} is given by :

$$n_{2D} = \int_{E_c}^{\infty} D_{2D}(E) f_{FD}(E) dE = N_{c,2D} \int_0^{\infty} f_{FD}(\varepsilon) d\varepsilon \tag{4.9}$$

where $N_{c,2D} = D_{2D} k_B T$ is the effective 2D density of states. The quantity $\int_0^{\infty} f_{FD}(\varepsilon) d\varepsilon = F_0(\eta)$ is the 0^{th} order Fermi integral and it can be analytically evaluated as $F_0(\eta) = \ln(1 + e^{\eta})$. This result, combined with Eq. 4.9, gives:

$$\eta = \ln\left(e^{n_{2D}/N_{c,2D}} - 1\right) \tag{4.10}$$

The carrier concentration, n_{2D}, can be experimentally evaluated as a function of the gate voltage:

$$n_{2D} = \frac{C_{\text{hBN}}}{q}(V_G - V_{th}) \tag{4.11}$$

Where C_{hBN} is the capacitance between the WSe_2 channel and the gate, q is the electron charge and V_G and V_{th} are the gate and threshold voltage, respectively. In Figures 4.13a and

4.13b we can compare the experimental Seebeck coefficient measured for samples s180 (Ag contacts) and s189 (Co contacts), respectively, in the n-type transport regime as a function of η (extracted using Eqs 4.10 and 4.11) to the theoretical expression of $S(\eta)$ given by Eq. 4.8. The theoretical expression of $S(\eta)$ is plotted for the different scattering mechanisms considered (by varying the r exponent). In both cases $N_{c,2D}$, which represents an unknown parameter, has been varied between $10^{16} - 10^{17}$ m^{-2} accordingly to refs [268, 137] without notably affecting the final result. The plot in Figure 4.13 are given for $N_{c,2D}$ fixed at 3×10^{16} m^{-2}.

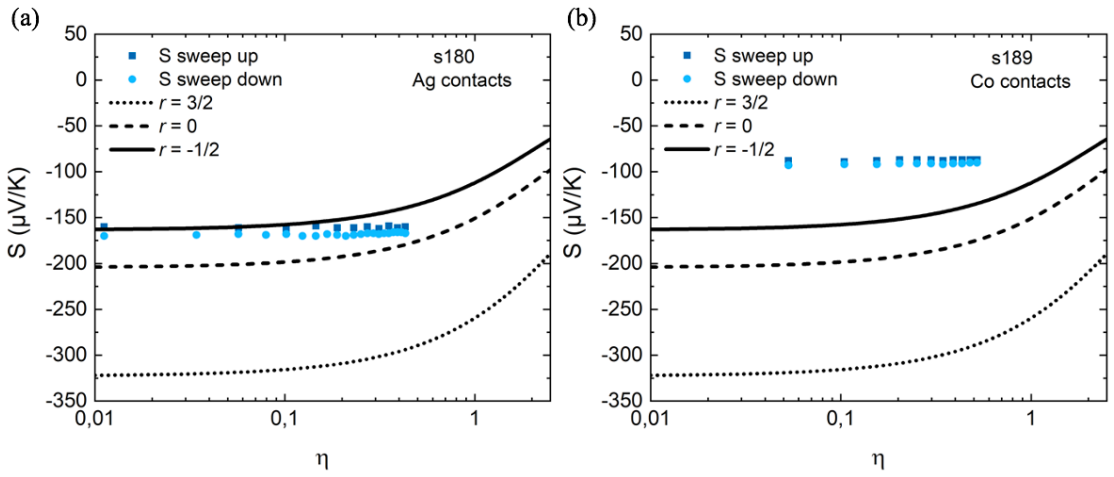

Figure 4.13 – Comparison of the experimental Seebeck coefficient measured for (a) samples s180 (Ag contacts) and (b) sample s189 (Co contacts) as a function of η to the theoretical expression of $S(\eta)$ given in Eq. 4.8 (η is mapped using Eq. 4.10 and 4.11). The theoretical expression of $S(\eta)$ is plotted for the different scattering mechanisms considered (by varying the r exponent according to refs [268, 137]).

In both cases, data are not in agreement with the theoretical treatment proposed by Hippalgaonkar et al.. While for sample s180 (Ag contacts) at least the order of magnitude of the experimental data is coherent with a dominating strongly screened Coulomb scattering, in the case of sample s189 (Co contacts), the experimental data are well lower than the theoretical predictions. Our gate dependent Seebeck measurement are far to satisfy the degenerate condition, where a full band transport with an energy independent DOS is a good approximation. Moreover, the presented theoretical description does not take into account interfacial hybridization modifying the local density of states of the 2D material.

The presence of bandgap localized states, typical in 2D materials, implies that hopping mechanism can represent a dominant contribution to transport and, as a consequence, carrier conduction can occur via Mott's variable range hopping (VRH). Recently, Wang et al. have proposed a statistical model for the computation of the Seebeck coefficient on the basis of percolation theory and hopping mechanisms [271]. The basic idea of their model is schematically illustrated in Figure 4.14a, which shows how structural disorder in 2D systems induces the formation of energy-fluctuating localized sites along the current-carrying path. The presence of localized states results in an exponential tail in the density of states as illustrated in Figure 4.14b, which depends on the total defects density. Carrier hopping process via these localized

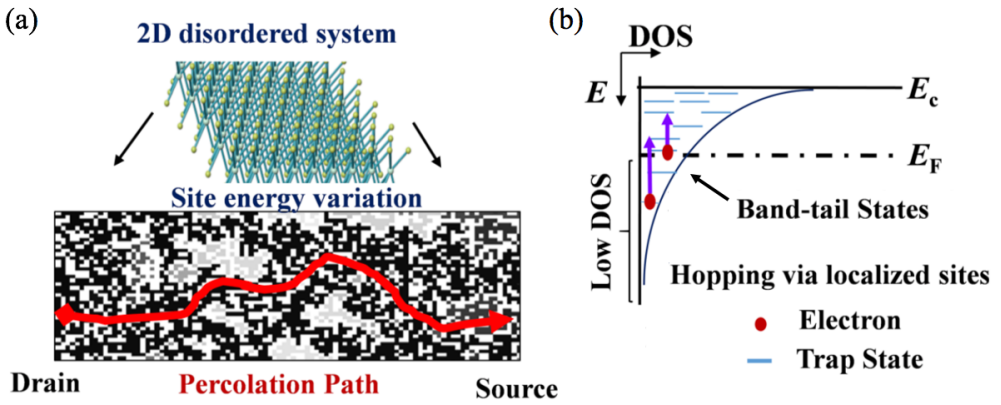

Figure 4.14 – (a) Schematic of percolation transport in 2D disordered materials with energy variations along the current-carrying path. (b) Diagram of variable range hopping (for electrons) via localized states in the exponential band tail. E_F represents the Fermi level and E_c is the conduction band edge. Extracted from [271].

states is considered as the main transport mechanism and, since the site energy fluctuates along the current-carrying path, the Seebeck coefficient is calculated by weighting the number of sites participating to the conduction. This approach has been proved to be successful in describing the experimental measured Seebeck coefficient as a function of the back gate voltage and the temperature of MoS_2- and BP-based devices in the high doping regime. The Seebeck coefficient is predicted to increase with decreasing the carrier density at fixed temperature and to increase with the temperature, following a $T^{1/3}$ dependence, typical of the variable range hopping mechanism, while saturating in the high temperature regime.

A direct comparison of this model with my experimental data is out of my scope. I have cited here this recent study to underline that a similar approach could be considered to take into account the contribution to thermoelectric effect due to localized gap states induced in 2D materials by interfacial hybridization, which is a subject not treated in literature.

4.4 Power factor and figure of merit

The power factor, $PF = S^2\sigma$, is a quantity often used to indicate the performances of a thermoelectric converter. For example, while in passive cooling heat is transported via phonons and the heat flux is set by the thermal conductance of the cooler, active cooling uses the Peltier effect via the electronic channel, and it can be controlled and tuned with an applied current. In this case, the cooling performance is strictly related to the power factor. Moreover, unlike the ZT figure of merit, the power factor does not require low thermal conductivity and thus, it does not have any theoretical limitation [38].

In the family of 2D materials, due to its high electrical conductivity, graphene owns one of the highest recorded power factor values in 2D materials up to 360 μW/cm K^2 when supported on a hBN substrate [38]. For this reason, graphene is an optimum candidate for active cooling applications. However, due to its high thermal conductivity which limits the figure of merit,

graphene is generally not a very popular material for thermoelectric applications. Concerning WSe_2, the PF values estimated by Yoshida et al. [79] are, to my knowledge, the only values reported for mechanically exfoliated WSe_2 using a device geometry similar to the one that I have used, being the main differences the use of a ionic liquid as a gate and the absence of hBN. They reported a maximum PF of ~ 37 μW/cm K^2. Implementing electric double-layer transistors (EDLTs) of large-area TMDC monolayers using the CVD method, Pu et al. [80] reported a maximum PF for WSe_2 of ~ 2.8 μW/cm K^2. Kim et al. [138] studied the thermal properties of a polycrystalline WSe_2 synthesized by thermally assisted conversion. They reported a maximum PF of 1.27 nW/cm K^2 which is considerably smaller than that of mechanically exfoliated or CVD-grown WSe_2 flakes due to the large amount of defects related to the fabrication process.

The gate voltage dependent power factor of eight of the studied samples is shown in Figure 4.15. The highest PF are observed for Pd-, Co- and Ti-based devices with maximum values, PF_{max}, ranging between 1.5 and 3.5 μW/cm K^2. Such values of PF are smaller than what has been reported in literature for WSe_2 by Yoshida et al. using Ti/Au contacts [79], but comparable with the other reported results [80, 138]. However, it is worthy to notice that Yoshida et al. measured $| S_{max} |$ of ~ 300 μV/K and they adopted a 4-point approach to measure the electrical conductivity of few-layers WSe_2 on SiO_2 substrate. In our case, due to our set-up limitation, PF is under-estimated since σ is obtained by a 2-point measurement technique. Thus, it is expected a remarkable enhancement of power factor in our devices if a 4-probe conductivity measurement would be performed. The extracted power factors allow to foresee room temperature figures of merit, ZT_{300K}, of the order of 0.02 - 0.08, as illustrated in the insets of Figure 4.15. To evaluate ZT, a value of in-plane thermal conductivity κ = 1.4 W/mK has been used, extracted from the literature [81, 82].

In literature, most of the studies reporting the power factor for 2D materials have used Ti-based contacts. In my PhD, I have tried to expand the investigation by experimentally exploring the effect of different metal contacts on the thermoelectric response of hBN-supported WSe_2-based devices. Even if we find out quite reduced S and PF values with respect to the best measured result in literature [79], we clearly find out an important and unprecedentedly-measured influence of the nature of the metallic contact. Moreover, theoretical and experimental works exploring thermoelectric effects in WSe2-based device are still limited in number and further investigations are needed to pick out the best strategies to optimize the thermoelectric performances of devices based on this promising TMD.

4.5 Conclusions

To summarize, in this chapter, I have presented the experimental investigation of the effect of different metal contacts (Pd, Co, Ag and Ti) on the electric and thermoelectric properties of hBN-supported few layers WSe_2 transistors by simultaneously measuring the gate voltage dependence of σ and S. In order to achieve an efficient gate voltage modulation, allowing

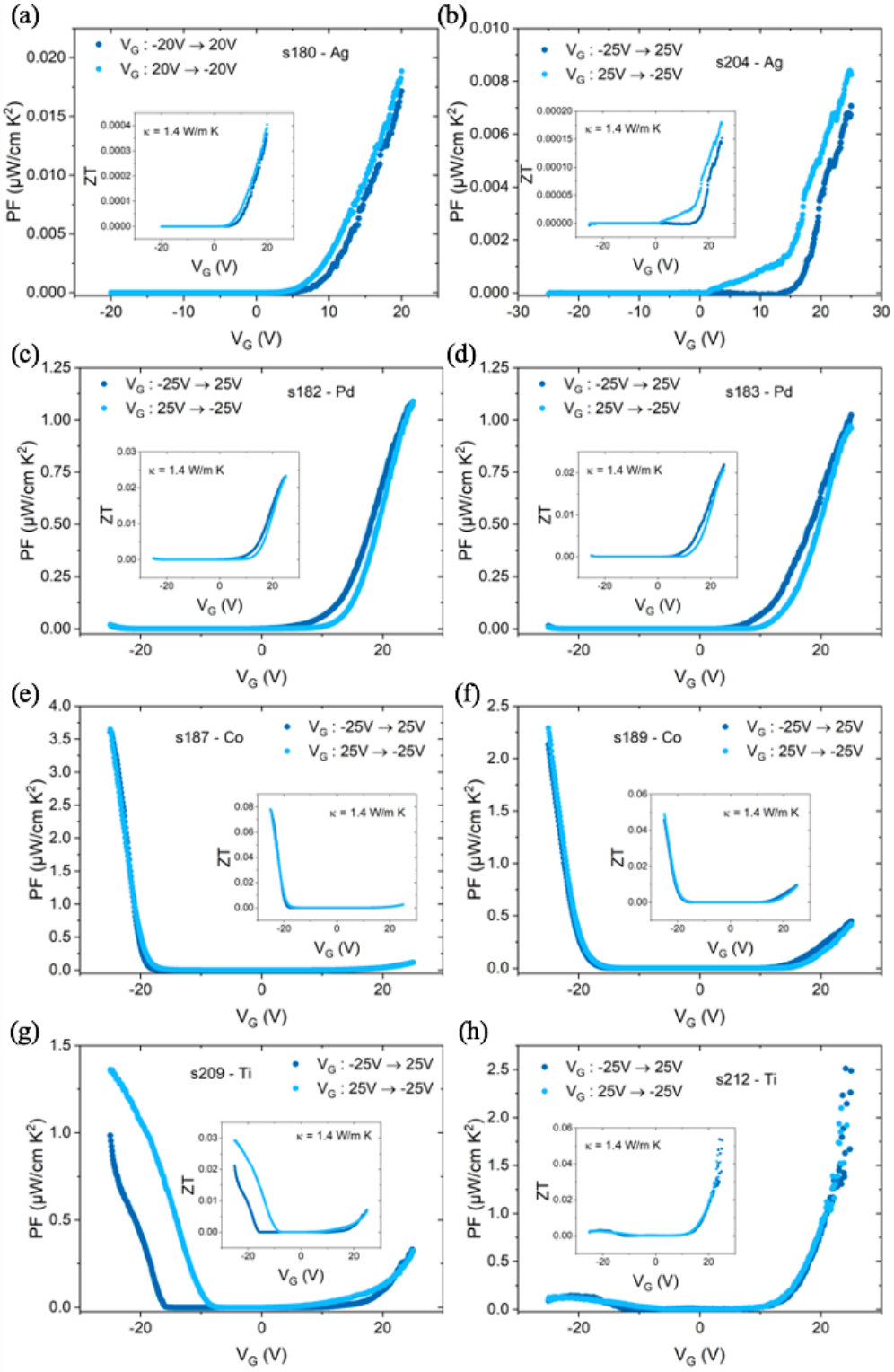

Figure 4.15 – Gate voltage dependence of the power factor PF for the discussed samples, for increasing and decreasing gate voltage sweep. The inset contains the figure of merit ZT extracted for an in-plane thermal conductivity of κ = 1.4 W/mK.

to explore both the hole and electron doping branches in WSe_2, I have fabricated van der Waals heterostructures with WSe_2 on hBN and I have used a local metallic gate to ensure a uniform and stable electric field. Moreover, hBN provides an atomically flat substrate for the semiconductor allowing to isolate it from local charge trapping states. As a result, it was possible to achieve large and reproducible thermoelectric power values, with S_{max} values as large as ~ 200 μV/K. I found out that the electric and thermoelectric response of WSe_2 is strongly influenced by the employed metal contact. Theoretically predicted orbital hybridization at the metal-semiconductor interface is in agreement with the results shown in this work. Induced interface gap states are likely at the origin of the local DOS modification at the contact interfaces and reduce the semiconducting bandgap, strongly affecting charge injection and the thermoelectric power. In contrast with the S-σ anti-correlation, strong hybridization enhances the device electrical conductivity by a factor of 500 with respect to the weak hybridization case, still preserving quite similar values of the Seebeck coefficient.

The Mott relation, generally used to predict the Seebeck coefficient in degenerately doped semiconducting materials, does not appear to be able to describe the experimental results, particularly in the strong hybridized limit. The reason of this mismatch can be explained by the presence of localized energy states which dominate the transport, but also because the scattering process in the studied samples are not accurately taken into account. For instance, the hBN substrate employed in this work is expected to reduce the acoustic phonon scattering which is generally the dominating scattering mechanism in 2D materials.

Finally, the obtained results reveal that contact engineering can be a useful tool to control the thermoelectric performances of actual WSe_2-based devices. Promoting strong interface coupling allows improving the power factor of TMDs-based devices for an optimized thermoelectric response.

5 High temperature thermal conductivity in supported graphene

In the study of low dimensional materials for energy conversion, several aspects come into play. Due to their large surface, 2D materials strongly interact with the environment and their properties change from one particular device configuration to another (e.g., suspended or supported devices, number of layers of the 2D flakes, nature of the substrate, etc.). Among them, the thermal conductivity of a supported 2D material is particularly challenging to determine, since the heat propagation into the device and the surrounding environment can be very complex and heat diffusion through the substrate becomes a dominating factor. For this reason, as illustrated in Chapter 1, the thermal conductivity of a 2D material is generally measured by suspending the 2D material itself. However, this is not really pertinent for actual applications or in the case of heterostructures. In this chapter, the discussion will focus on the measurement of the thermal properties of low dimensional materials in a supported configuration by applying the Joule self-heating method. This approach has the important advantage of laying on a device architecture highly compatible with the measurements of the thermoelectric and electric properties of 2D materials, and thus, particularly suitable for an effective evaluation of the device figure of merit ZT. As a test bed material to prove the validity of the method, I have chosen to investigate graphene nanowires, being graphene one of the most studied among 2D materials and for which many investigations of thermal conductivity already exist in literature.

5.1 Joule self-heating method

The Joule self-heating method has already been briefly introduced in Chapter 1. This approach is based on the resolution of the heat diffusion equation in a nanowire crossed by a current in a steady-state condition [83, 151, 150] and it can be easily generalized for any conductive material. Figure 5.1 illustrates schematically the adopted device configuration. A nanowire, represented by the gray layer, is connected to four metallic contacts for electrical transport measurements allowing to heat the sample by Joule effect and, to monitor the electrical potential across it. The two external contacts, used to inject the current in the nanowire, are much wider and thicker with respect to the nanowire to ensure a good thermalization of the

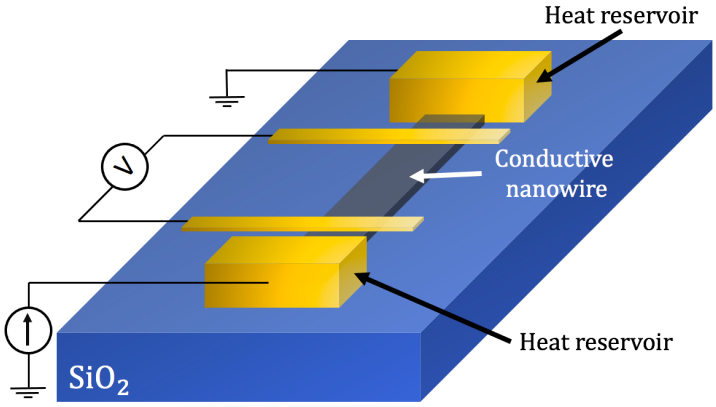

Figure 5.1 – Schematic of nanowire device with electrical connections to measure the thermal conductivity by Joule self-heating method.

nanowire edges with the environment temperature T_0. The nanowire length L is defined as the inside edge-to-edge distance between the closest contacts. In the approximation of one-dimensional heat transport, the temperature evolution along the nanowire can be described as follows:

$$\kappa A \frac{d^2T(x)}{dx^2} + p\,[1+\alpha(T(x)-T_0)] - g(T(x)-T_0) - W\sigma\varepsilon T^4 = 0 \tag{5.1}$$

where κ is the total thermal conductivity of the nanowire (including the electronic and lattice contribution), $A(=Wt)$ is the cross sectional area of the nanowire (with W and t the nanowire width and thickness, respectively), $p(=IV/L)$ is the applied electrical power per unit length, α (or TCR) is the temperature coefficient of resistance and g is the heat loss per unit length to the substrate. The last term in the equation describes the heat lost through radiation per unit length, where σ is the Stefan–Boltzmann constant and ε is the emissivity. In the case of graphene nanowires, the thermal radiated losses from the surface can be neglected, being of the order of 0.15 W/m^{2}K at room temperature [186]. Equation 5.1 can be solved to obtain the temperature profile along the nanowire, given by:

$$T(x) = T_0 + \frac{p}{g-\alpha p}\left(1 - \frac{\cosh(mx)}{\cosh(mL/2)}\right) \tag{5.2}$$

where $m = \sqrt{(g-\alpha p)/\kappa A}$. Integrating Eq. 5.2 over the nanowire length L, we obtain the average temperature $\overline{T}$ of the nanowire.

$$\overline{T} = T_0 + \frac{p}{g-\alpha p}\left[1 - \frac{2}{mL}\tanh\left(\frac{mL}{2}\right)\right] \tag{5.3}$$

It is then possible to combine Eq. 5.3 with the temperature variation of the average resistance $\overline{R}$ given by

$$\overline{R} = R_0 \left[1 + \alpha \left(\overline{T} - T_0 \right) \right] \tag{5.4}$$

Here R_0 is the nanowire resistance at T_0 when no heating occurs. We can finally calculate the relative variation of the electrical resistance as a function of the applied electrical power per unit length:

$$\frac{\Delta R}{R_0} = \frac{\alpha p}{g - \alpha p} \left(1 - \frac{2}{mL} \tanh\left(\frac{mL}{2} \right) \right) \tag{5.5}$$

being m a function of α, g and κ.

The device design illustrated in Figure 5.1 allows to measure the relative variation of the electrical resistance of the nanowire in a 4-probe configuration. The experimental approach consists in measuring $\Delta R/R_0$ as a function of the applied electrical power p in a couple of nanowires in a self-consistent way. The two nanowires composing the couple meet different configurations, that we will call "long" and "short" and that will be discussed in detail later on. To proceed with the evaluation of κ and g, we implement two main steps. First, we measure the resistance as function of the temperature of the environment of both nanowires, in order to evaluate the TCR and calibrate the temperature response of the nanowires resistance. This is done with low enough current to avoid self-heating. Second, the graphene nanowires resistance variation due to self-heating is measured at higher current. The fit of Eq. 5.5 to the experimental data is performed in a self-consistent form: starting from a fixed value of κ, g is extracted by fitting the “long” nanowire $\Delta R/R_0$ experimental data, the obtained g is used to estimate κ by fitting the “short” nanowire $\Delta R/R_0$ experimental data. The iterations are continued until convergence of the κ and g extracted values. This approach has already been successfully applied in the case of metallic nanowires [83], as well as in the case of 2D materials [150], resulting in a quite versatile method to evaluate the thermal conductivity of conductive materials in supported configurations.

5.2 Device engineering: "long" and "short" nanowire configurations

Before entering into the details of the application of the Joule self-heating method on supported 2D material nanowires, some considerations on the device size and on the subsequent ability of carrying the heat are mandatory. When a 2D material-based device is supported on a substrate, the thermal losses are quite relevant. Thermal losses to the substrate are affected by different parameters, such as the interfacial thermal conductance G, the thermal conductivity of the substrate κ_{Si} and of the overlying oxide layer κ_{ox}, as well as the oxide layer thickness t_{ox}. Among the other parameters, the heat spreading profile into the substrate, in fact, is related to the width of the device with respect to the underlying oxide thickness. Figure 5.2 shows a schematic of the different heat spreading profiles in the case $W > t_{ox}$ and $W < t_{ox}$. In the first case (Figure 5.2a), the width of the nanowire is larger than the oxide thickness and the heat

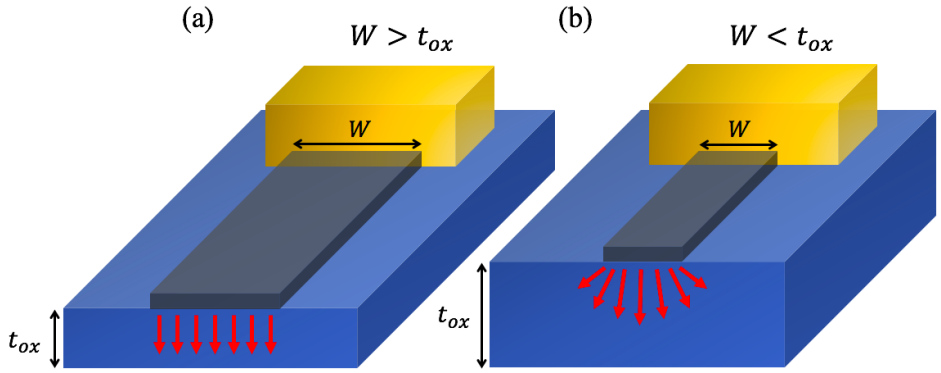

Figure 5.2 – Schematic of heat losses to the substrate in case of a thin substrate (a) and in case of a thick substrate (b) with respect to the device width.

propagates vertically to the substrate. The thermal losses per unit length are described as the inverse of the total thermal resistance which is the series of the interface thermal resistance, the oxide thermal resistance and the Si thermal resistance [272]:

$$g = \frac{1}{L}\left(\frac{1}{GS} + \frac{t_{ox}}{\kappa_{ox}S} + \frac{1}{2\kappa_{\mathrm{Si}}\sqrt{S}}\right)^{-1} \tag{5.6}$$

where L is the device length, G is the interfacial thermal conductance between the nanowire and the underling substrate, which is on the order of 10 MW/m^{2}K for supported single and multi-layers graphene [110, 185, 273], t_{ox} is the oxide thickness, $S(= WL)$ is the interfacial surface, $\kappa_{ox} \sim 1.4$ W/mK [152] and $\kappa_{\mathrm{Si}} \sim 140$ W/mK [182] are the thermal conductivity of the SiO_2 and Si, respectively. The thermal losses are estimated to few units of W/mK depending on the interlayer surface as illustrated in Figure 5.3a. For a given nanowire length, the thermal losses are strongly reduced by decreasing the nanowire width. To further reduce g, the oxide thickness can be increased. However, if the oxide thickness overcomes the nanowire width, Eq. 5.6 is not valid anymore. In this case, as illustrated in Figure 5.2b, due to the considerable thickness of the oxide, the lateral heat spreading needs to be taken into account. FEM simulations proposed by Liao et al. [113] allow to describe the thermal losses per unit length as follow:

$$g^{-1} = \left(\frac{\pi\kappa_{ox}}{\log(6(t_{ox}/W+1))} + \frac{\kappa_{ox}W}{t_{ox}}\right)^{-1} + \frac{1}{GW} \tag{5.7}$$

Figure 5.3b confirms that, even by taking into account the lateral heat spreading, increasing the oxide thickness is a good strategy to reduce the thermal losses to the substrate. In particular, for $W = 300$ nm and $t_{ox} = 5$ μm, which are the values I have experimentally used, and considering $G = 10$ MW/m^{2}K, we find out from Eq. 5.7 an estimated g of ~ 0.76 W/mK. Such a value is reduced of about 22.5% with respect to the value expected in the opposite limit of $W > t_{ox}$, where uniform heat flux through the substrate is dominating. In this case, considering $t_{ox} =$

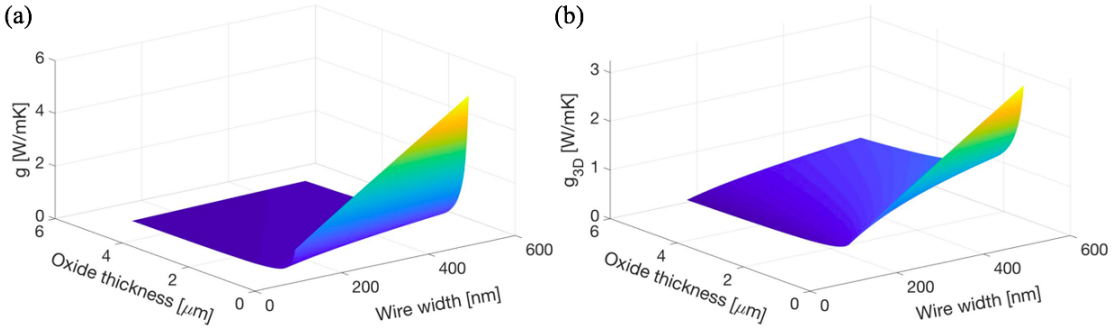

Figure 5.3 – (a) 3D plot of the thermal losses g as a function of the oxide thickness t_{ox} and nanowire width W in the limit $W > t_{ox}$ (eq. 5.6). (b) Same plot in the limit $W < t_{ox}$ (eq. 5.7).

280 nm, we obtain from Eq. 5.6 $g \sim 0.98$ W/mK. The values that one can obtain from those equations (5.6 and 5.7) are referred to an ideal sample where the nanowire is in intimate contact with the substrate and the substrate does not have any roughness. Since this is never the case, Eqs 5.6 and 5.7 always over-estimate the actual losses.

5.2.1 Thermal healing length

The ability of the substrate to efficiently drain the heat generated into the device strongly influences the ability to measure the thermal conductivity of the device itself, making more difficult the effective application of the method. In order to evaluate these limitations, we can refer to the well-known thermal healing length [274]:

$$L_H = \sqrt{\frac{\kappa W t}{g}} \tag{5.8}$$

where κ is the nanowire thermal conductivity, W and t are the width and the thickness of the nanowire and g is the above-discussed thermal losses. This characteristic length, L_H, represents the distance over which the heat dissipation is effectively taking place through the metallic contacts at the nanowire extremities (Figure 5.1). Numerical simulations [85, 150, 274, 275] suggest that for devices longer than $3L_H$, the dissipation occurs almost entirely though the nanowire-substrate interface, while devices shorter than $3L_H$ benefit of an efficient cooling through the metal contacts. For this reason, thermal losses through the substrate are better evaluated in a device longer than $3L_H$ and the thermal conductivity in a device shorter than $3L_H$. Thus, the choice of the nanowire length is fundamental to assure the validity of the applied method. The evaluation of thermal conductivity in nanowires shorter than $3L_H$ and thermal losses in nanowires longer than $3L_H$ can be done in a self-consistent way until convergence to the optimal values occurs.

In the particular case of graphene nanowires tested in this work, the thermal healing length can be calculated by using a value of κ equal to 600 W/mK, as extracted from the literature for

supported graphene at 300 K [110], and a value of g estimated by Eq. 5.7 using the geometrical parameters (W, t_{ox}) corresponding to our devices (where W = 300 nm, and t_{ox} = 5 μm). We find out $L_H \sim 0.9$ μm, implying that the threshold length separating the short/long limit is equal to $3L_H \sim 2.7$ μm. Thus, long nanowires are conceived with a length L higher than 3 μm and short nanowires with a length shorter than 3 μm.

5.2.2 Temperature profile simulations

To support and to better understand the difference between the "long" and "short" nanowire configurations, we can simulate the temperature profile in the two cases (according to Eq. 5.2). For this simulation, we will imagine to have two SLG nanowires 300 nm-wide. We choose 1 μm as length of the short nanowire and 10 μm for the long one. The resistance of the two nanowires is approximated to 1 kΩ and 10 kΩ, respectively. The temperature coefficient of resistance is set to 1.5×10^{-4} K^{-1}. The values chosen here for the resistance and for the temperature coefficient are suggested by my experimental measurements, since they are recurrent values. The temperature of the environment, and thus of the metallic contacts, is set to 300 K and a current of 100 μA is injected in the nanowires to heat them up. By fixing the value of thermal conductivity to κ = 600 W/mK, we can see how the temperature profile changes by varying the thermal losses to the substrate in the two nanowire configurations (Figures 5.4a and 5.4b). Subsequently, we can fix the value of thermal losses to g = 1 W/mK and observe the temperature profile as function of the thermal conductivity (Figures 5.4c and 5.4d).

For a fix value of κ, Figure 5.4a reveals a bell-shape temperature profile for the short nanowire. The profile is weakly influenced by the value of thermal losses, which is varied over two order of magnitude, from 0.05 to 1 W/mK. This is due to the reduced surface of interaction with the substrate. For this reason, this configuration is not suited for a precise evaluation of the thermal losses. In the long nanowire limit (Figure 5.4b), the profile dependents on the losses and, for sufficiently high values of g, it is mainly flat along the device length. This means that the temperature gradient is negligible along the nanowire ($d^2T(x)/dx^2 \sim 0$) and the shape of the temperature profile is not influenced by the value of the nanowire thermal conductivity (see Eq. 5.1). On the other hand, the thermal losses are significantly affecting the temperature profile. This configuration turns out to be the optimal for a more accurate evaluation of g.

We can now fix the value of the losses g and observe the temperature profile as function of the thermal conductivity. We can see that the long nanowire (Figure 5.4d) prevents us to evaluate κ due to the flat temperature profile, again confirming that the thermal losses to the substrate are the dominating factor. On the contrary, the smooth thermalization to the metallic contacts, which takes place in the short nanowire (Figure 5.4c), is influenced by the thermal conductivity of the material. In this case, heat flow through the nanowire towards the lateral metal contacts according to the in-plane thermal properties of the nanowire plays a non-negligible role. The short nanowire is then the best configuration to evaluate the thermal

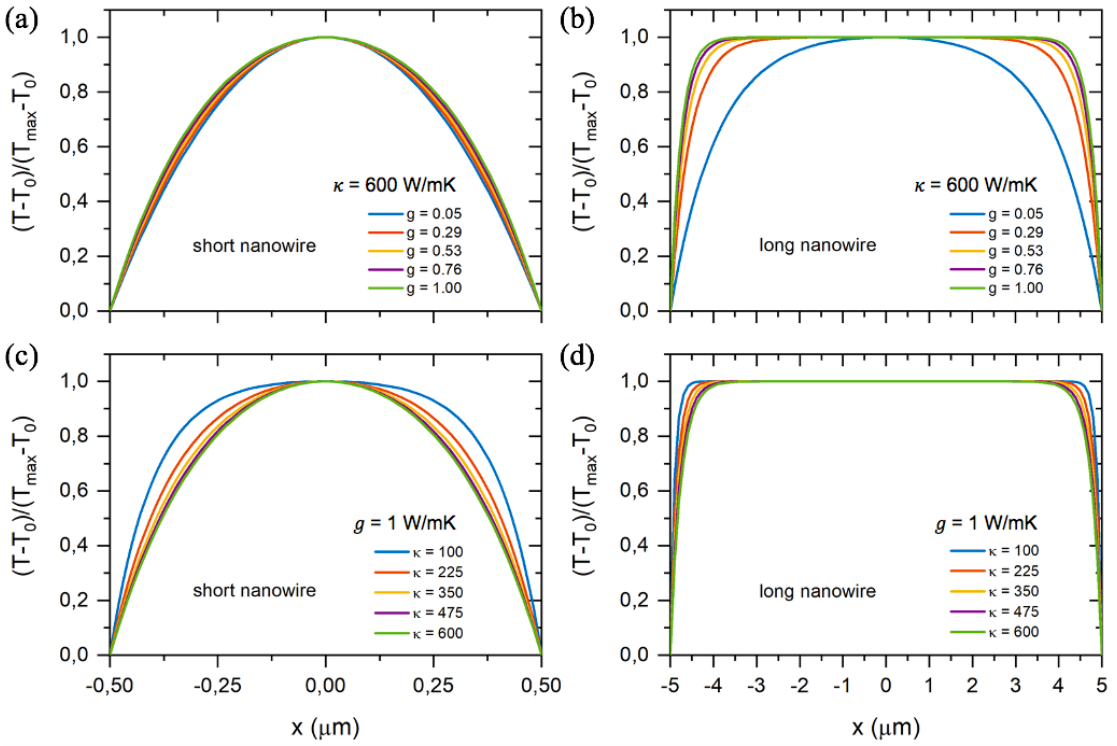

Figure 5.4 – (a,b) Normalized temperate profile as a function of the thermal losses to the substrate for a given value of thermal conductivity for a short (a) and long (b) nanowire. (c,d) Normalized temperate profile as a function of the thermal conductivity to the substrate for a given value of thermal losses for a short (c) and long (d) nanowire.

conductivity of our sample.

These considerations justify the choice of sample dimensions and allow us to affirm that in the two nanowires the heat propagation evolves in two different ways:

- in the "short" nanowire the thermal losses to the substrate have a reduced influence on the temperature profile (still remaining non-negligible) due to the smaller surface of interaction with the substrate; the heat generated in the device rises up the temperature in the center of the nanowire and the heat propagates through the nanowire to the metal contacts to ensure the thermalization with the environment.
- in the "long" nanowire the thermal losses dominate the heat transport; the temperature profile is flat and the thermalization is abrupt on the extremities of the nanowire.

5.3 Sample fabrication and characterization

The arguments presented in the previous paragraphs illustrate that, to correctly evaluate the thermal conductivity and the thermal losses through the substrate of a supported graphene nanowire, we need to exploit two different configurations. In one case, we need to maximize the length of the device, while in the other case, the length needs to be minimized with respect

to the healing length. However, this is not straightforward to achieve in reality. The graphene that is used in our experiments is mechanically exfoliated from bulk graphite. Thus, the size of the flakes is random. An accurate work of research of the thinnest, larger and more uniform flakes is carried out. The desired flakes are subsequently transferred with the hot pick-up transfer technique [199], discussed in detail in Chapter 2, over a Si substrate covered by a 5 μm-thick SiO_2 layer fabricated by plasma enhanced chemical vapor deposition (PECVD). The growth of SiO_2 is performed at 280°C in a chamber with 40 sccm of SiH_4, 1000 sccm of N_2O and 500 sccm of Ar as precursor gases. The plasma is activated with a power of 120 W. Electrodes are obtained by mean of electron beam lithography and Ti/Au (5/100 nm) deposition. Finally, the graphene flakes are etched by reactive ion etching (RIE) with oxygen plasma to shape the intended nanowire geometries. All the fabrication processes are equivalent to what described for the van der Waals heterostructure in Chapter 2.

Based on the estimated value of $3L_H$ previously discussed, I have fabricated a couple of nanowires with a "short" nanowire 1.8 μm-long and a "long" nanowire 9 μm-long. Both nanowires are 300 nm-wide. This couple defines the sample A. A second sample, sample B, is composed by a single nanowire of width $W = 300$ nm and length $L = 0.9$ μm and it is considered to be a "short" nanowire. Figure 5.5 shows optical images of the two supported graphene devices under investigation before etching. In particular, in the case of sample A, the short and long nanowires composing the couple are fabricated intentionally as close as possible to each other on the same graphene flake, in order to assure similar material properties. Etching is obtained by oxygen plasma through a resist mask of MaN-2401 defined by the red stripes in the figure. Samples are cleaned in acetone and isopropanol.

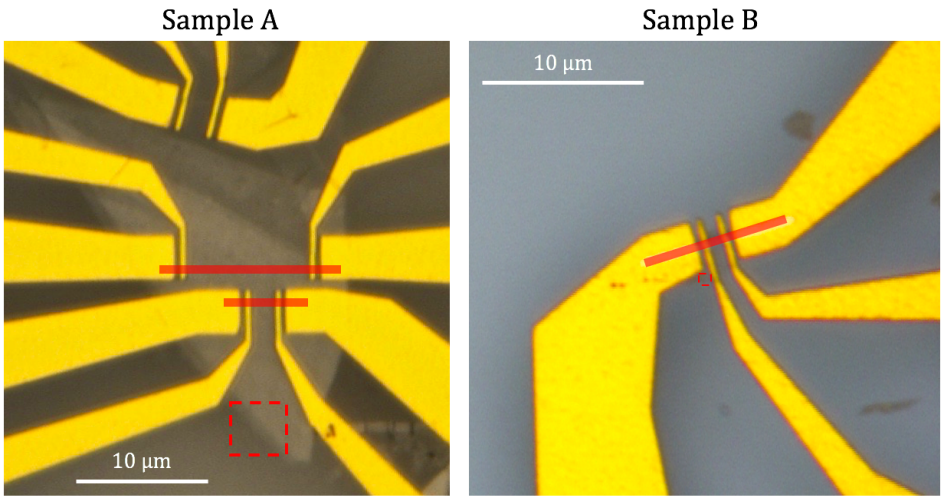

Figure 5.5 – Optical image of the graphene flake for sample A and B after the metal deposition and before the etching. The red stripes represent the etching masks and the dotted squares are the regions in which AFM images are reported in Figure 5.7.

The number of layers in the graphene samples is estimated by Raman spectroscopy in air at room temperature and atmospheric pressure with a laser excitation wavelength of 514 nm, addressing in-plane vibrational modes. By comparing peak intensity, shape and position of the

2D-mode at ~ 2700 cm^{-1} to Raman spectra extracted from the literature for 2, 5 and 10 layers [276], as illustrated in Figure 5.6, we conclude that the graphene flakes under investigation have a number of layers of ~ 10 for sample A, corresponding to a thickness of ~ 3.5 nm, and a number of layers equal to 2, corresponding to a thickness of ~ 0.7 nm for the nanowire of sample B. Given these thicknesses, we will also refer to the nanowires of sample A as supported multilayer graphene (sMLG) and to sample B as supported bilayer graphene (sBLG).

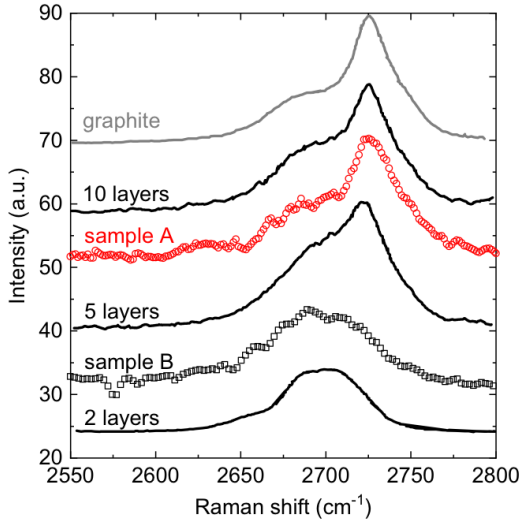

Figure 5.6 – Raman spectra of sample A (red circles) and B (black squares) compared to Raman spectra extracted from the literature for a 2, 5 and 10 layers graphene [276].

Atomic force microscopy (AFM) has been employed to investigate the surface morphology and roughness of the graphene flakes and of the underlying SiO_2 oxide layer in the proximity of the samples. The analyzed areas are indicated with dotted red squares in Figure 5.5. Figure 5.7(a,b) and Figure 5.7(d,e) show 2D and 3D AFM images for sample A and B respectively, obtained at ambient conditions. For sample A, the SiO_2 surface presents a root mean square roughness of 8 ± 2 nm and maximum peak-to-valley roughness up to 20 nm. These parameters are calculated over average areas of ~ 1 × 1 μm^2. The roughness reduces to 5 ± 2 nm when measured on the graphene flake. In the case of sample B, while the SiO_2 roughness remains unchanged, we measure a slightly increased roughness on the graphene flake, equal to 6 ± 1 nm over average areas of ~ 0.5 × 0.5 μm^2. Note that, the different resolutions of the AFM images for sample A and B are related to the different sizes of the two samples, being sample B much smaller than sample A. Representative line profiles are reported in Figures 5.7c and 5.7f for the sMLG and sBLG nanowires, respectively. In both graphs, the solid gray line is a profile extracted over the SiO_2 surface while the solid red (black) line is extracted over the the graphene flake for sample A (B). The measured surface roughness hampers the estimation of the graphene flakes thickness by AFM. It is important to notice that the AFM images highlight suspended zones of the graphene flakes, revealing the non-conformal character at the interface.

All the electrical measurements have been performed in the Nextron micro probe station (already presented in Chapter 3) under high vacuum (~ 10^{-7} mbar). The nanowires and their metallic contacts are in thermal equilibrium with the underlying Si/SiO_2 substrate with large heat capacity. The substrate is anchored to an isothermal ceramic plate, whose temperature

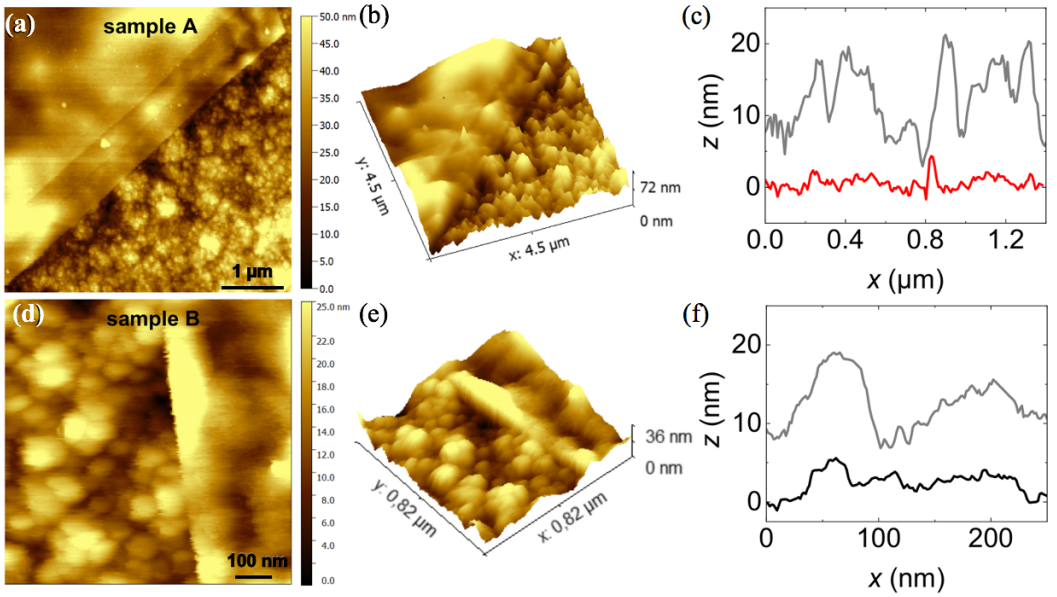

Figure 5.7 – (a) AFM image of multilayer graphene on 5 μm-thick SiO_2 (sample A). (b) 3D AFM image of sample A. (c) AFM line profiles from sample A: the gray line is measured over the SiO_2 surface while the red line over the the graphene flake. (d) AFM image of bilayer graphene over a 5 μm-thick SiO_2 (sample B). (e) 3D AFM image of sample B. (f) AFM line profiles from sample B: the gray line is measured over the SiO_2 surface while the black line over the graphene flake.

can be regulated with 0.1 K precision from 300 K up to 750 K. Since residuals of resist could be present on the surface [277], an electrical current annealing is performed before measurements. The current is continuously swept between -2 mA and 2 mA under vacuum conditions at room temperature overnight. The maximum annealing current corresponds to an increase in temperature up to $\sim$ 600 K. Note that the thermal conductivity of supported graphene on rough SiO_2 substrates showing suspended zones has been measured close to that of suspended graphene. This value is found to drastically decrease by repeated in-vacuum thermal annealing, that removes intercalated impurities, increasing graphene-substrate conformity and interfacial scattering [188]. In our case, the AFM characterization is performed before the annealing procedure. As a consequence, the graphene-substrate conformity during the transport experiments could be quite different from what revealed by AFM.

The graphene-based nanowires current voltage characteristics $I(V)$ are measured in a 4 contacts configuration, by current polarizing the nanowires while measuring the induced voltage drop. The nanowires resistances are evaluated by the slopes of the $I(V)$ curves. The nanowires resistance calibration measurements have been done by fixing the temperature of the sample holder in the micro probe station and by measuring the $I(V)$ curve at low bias ($|I| \leq 20$ μA). In this condition the $I(V)$ curves have a clear linear behavior, indicating that no detectable heating is induced. The procedure is repeated in a large range of temperatures (up to 575 K). The calibration procedure allows to determine the TCR entering Eq. 5.1. After calibration, the sample holder is mantained at a fixed temperature T_0, and the sample is self-heated by sweeping the injected current I form $-I_{heat}$ to $+I_{heat}$, where I_{heat} is in the range of 300-400 μA

depending on the nanowire. Typically a maximum dissipated power on the sMLG and sBLG nanowires lower than 300 μW is allowed in order to guarantee that the maximum temperature variation ΔT occurring in the nanowire is below 30 K. Self-heating is revealed by a slightly non-linear behavior in the $I(V)$ characteristics as the current increases. The resistance is computed as the derivative of the $I(V)$ curves and the applied power p per unit length is defined as $p = I^2 R_0 / L_{\text{short/long}}$. By repeating this measurement at different temperatures of the environment, the resistance relative variation $\Delta R/R_0$ of the nanowires can be experimentally estimated. Electrical transport measurements are performed in the temperature range above room temperature. This limit is weakly investigated in literature but extremely important by considering that commercial electronic devices work typically above room temperature.

5.4 Temperature coefficient of resistance in graphene

In order to apply the model discussed in this chapter and to fit Eq. 5.5 with the experimental data, it is of primary importance to investigate first the behavior of the nanowires resistance as a function of the temperature. This variation can be described by the general formula:

$$R(T) = R_0(T_0) + \beta(T - T_0) \tag{5.9}$$

where β is the slope of the $R(T)$ plot. In metallic objects, β is a positive constant because the resistivity $\rho(T)$ has a linear temperature dependence above the Debye temperature. The $\rho \propto T$ behavior can be derived by noticing that at high temperatures, the phonon concentration n_{ph} increases as T and, the mean electron-phonon scattering time τ is inversely proportional to n_{ph}. $1/\rho \propto \sigma \propto \tau \propto 1/n_{ph} \propto 1/T$, thus $\rho \propto T$. Below the Debey temperature, the $\rho \propto T$ behavior fails and $\rho \propto T^5$. In fact, as the temperature is lowered, electron-phonon scattering becomes less efficient and more collisions are required to fully randomize the initial electron velocity. At even lower temperatures, the scattering of electrons is dominated by impurities, dislocations, interstitial atoms, vacancies, grain boundaries and so on. In this regime, the resistivity saturates to the residual resistivity ρ_R which shows very little temperature dependence [278]. Thus, in metallic materials, the $\rho \propto T$ trend at high temperature is related to the increasing electron-phonon scattering, even though the number of carriers does not change. On the other hand, in semiconductors, the resistance decreases with increasing the temperature because of the growing concentration of thermally generated electron-hole pairs.

Reported behavior of temperature dependent resistance in graphene

Graphene is a zero bandgap material. For this reason, one can expect graphene to behave as a classical metallic material, with an electrical resistance linearly increasing with the temperature. However, the measurements of $R(T)$ reported in literature for graphene samples show a decreasing trend of the electrical resistance as a function of the temperature and a deep understanding of this phenomenon is still missing. Figure 5.8 shows some examples.

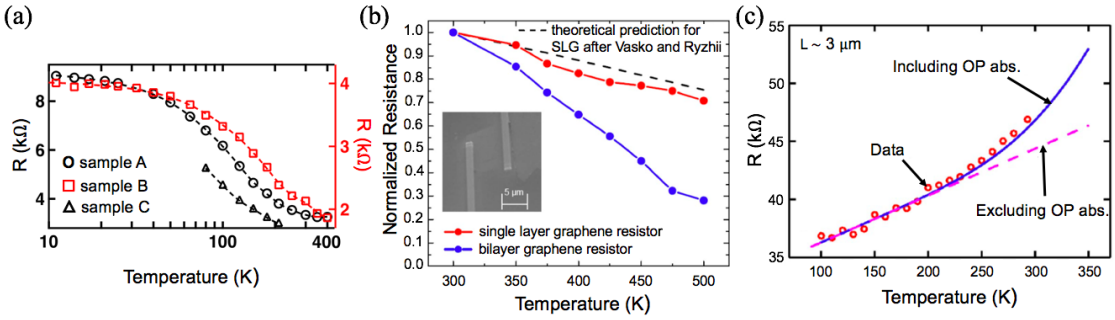

Figure 5.8 – (a) Temperature dependent resistance in three SLG samples near charge degeneracy $n = 5.7$, 2.9 and -1.5 × 10^9 cm^{-2}: sample A (650 nm-long, 675 nm-wide, circles, left axis), sample B (400 nm-long, 1.05 μm-wide, squares, right axis), and sample C (400 nm-long, 970 nm-wide, triangles, left axis). Extracted from [160]. (b) Normalized electrical resistance of SLG and BLG interconnects as a function of temperature. The theoretical prediction for SLG from Ref. [279] is shown for comparison. Extracted from [280]. (c) Temperature dependent resistance of a 3 μm-long metallic SWCNT. Symbols are experimental data, while lines represent an electro-thermal transport model with (solid line) and without (dashed line) optical phonon contribution. Extracted from [151].

In their study of the electronic component of the thermal conductivity in graphene, Yiğen et al. reported the behavior of the electrical resistance of three suspended single layer graphene samples from 10 K up to 400 K [160]. As illustrated in Figure 5.8a, they show a reduction of resistance which seems to saturate when reaching 400 K. Since this was not the topic of their study, they only commented that the temperature dependence of the data shows an insulating behavior up to ~ 200 K for samples A and C, and up to 300 K for sample B. Focusing on the high-temperature quenching of electrical resistance, Shao et al. studied a single and double layer supported graphene [280]. Figure 5.8b shows their results compared with the theoretical prediction from Vasko et al. [279] (black dashed line). According to their explanation, the decrease in resistance at room temperature and above comes from the thermal generation of carriers. The values and shape of the resistance curve are determined by electron and hole scattering by long- and short-range disorder and acoustic phonons. Following the theoretical predictions, the onset of optical phonon contribution to the scattering would suggest the existence of a minimum of resistance taking place above ~ 500 K. However, to our knowledge, such an effect has never been experimentally reported up to date for graphene. On the other hand, the same effect has been reported for single wall carbon nanotubes (SWCNTs). Pop et al. reported the electrical resistance characterization up to 350 K, as illustrated in Figure 5.8c [151]. By fitting the experimental data with an electrothermal transport model including and excluding the optical phonon (OP) absorption mechanism, they find that the OP absorption plays a non-negligible role on the resistance increase for temperature exceeding 250 K.

Measured TCR in the fabricated graphene nanowires

In this work, I have studied the temperature dependence of three graphene samples in the temperature range 300 K < T < 575 K. For a given temperature of the sample holder in the Nextron micro probe station, the resistance has been extracted from the linear fit of low-bias $I(V)$ plots ($|I| \leq 20$ μA). Figure 5.9 illustrates the result of the measured temperature dependent

resistance for the short (a) and long (b) nanowire in the case of sample A. In both cases, we can extract high values of electrical conductivity σ on the order of 1-2 $\times$ 10^7 S/m, revealing good electronic transport properties. Starting from room temperature, the experimental data show a different trend in the two cases. For the short nanowire, the resistance decreases until a minimum is reached around 550 K and subsequently it starts to rise. For the long nanowire, a resistance minimum is first revealed around 350 K, followed by an increasing behavior at higher temperature. The two temperature dependencies of the nanowires resistances can be well described by cubic curves of the form $R(T) = aT^3 + bT^2 + cT + d$, where the quadratic term strongly dominates over the cubic one ($b \sim 10^3$ - 10^4 a). Solid lines in Figures 5.9a and 5.9b represent the best fit of the experimental data, dotted lines define the level of accuracy of the measurements obtained by repeated calibrations. Our experimental observations clearly show the existence of a minimum which, to our knowledge, has only been predicted theoretically, and the subsequent increasing of the sMLG nanowire resistance in the explored temperature range.

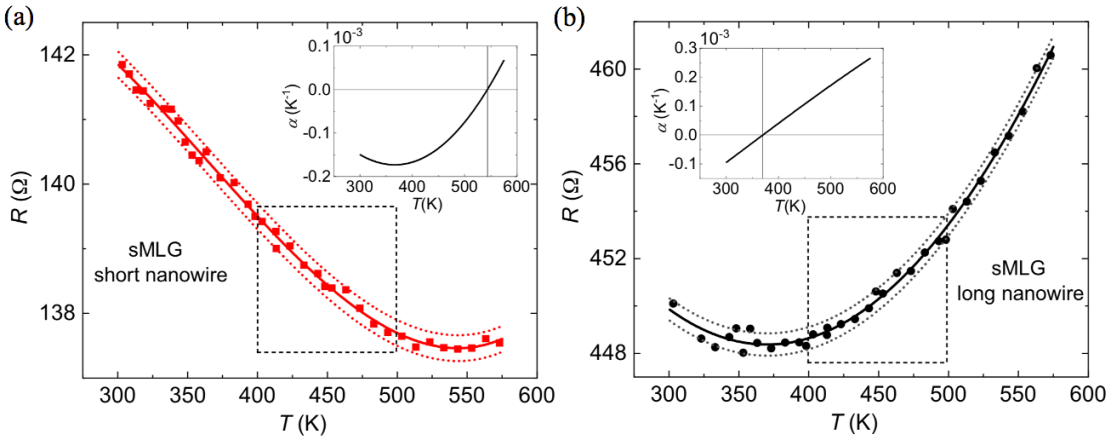

Figure 5.9 – Electrical resistance as a function of temperature for the long (a) and short (b) graphene nanowires (points) in sample A. The solid line represents the best experimental fit of the data. Dotted lines define the data dispersion over repeated measurements. Insets: temperature coefficients of the resistances α for the two nanowires as a function of the temperature.

The $R(T)$ calibration curve of the sBLG nanowire in sample B is reported in Figure 5.10. Similarly to sample A, we find out good electronic transport properties with σ on the order of 1 $\times$ 10^7 S/m. The resistance shows also a decreasing behavior with the temperature with no revealed minimum. In this case, a linear fit for the resistance has been employed. The monotonically decreasing behavior seems to indicate a length-dependence of the resistance minimum position, with a shift towards lower temperatures as the length of the nanowire is increased. However, further investigations are necessary for a better understanding. In particular, it would be necessary to carry out a study of the temperature dependency of the graphene samples as a function of their geometrical shape, namely length and width, but also as a function of the substrate roughness, since this also plays a fundamental role in electron-phonon scattering mechanisms.

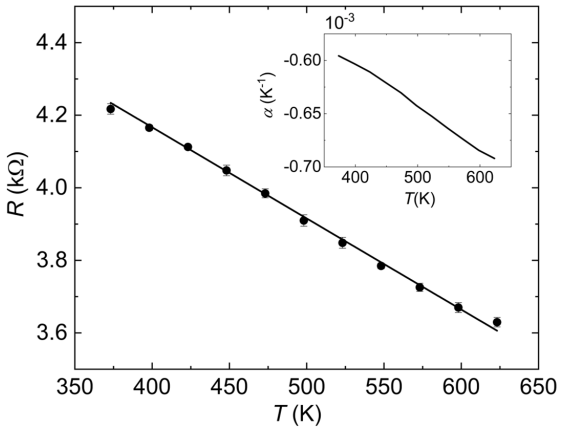

Figure 5.10 – Electrical resistance as a function of temperature for the short sBLG nanowire (points) in sample B. The solid line represents the linear fit of the data. Inset: temperature coefficient of the resistances α for the nanowire as a function of the temperature.

The insets in Figures 5.9 and 5.10 show the temperature coefficient of resistance extracted by curves fitting procedure for the short and long nanowire of sample A and for sample B. The TCR is defined as

$$\alpha(T) = \frac{1}{R(T)} \frac{dR(T)}{dT} \tag{5.10}$$

For sample A, the TCR temperature dependencies reveal that close to the temperature at which each sMLG nanowire presents the resistance minimum, α approaches zero. As a consequence, to use Eq. 5.2 for self-heating data analysis, we need to restrict our experimental investigation in the temperature region 400 K $< T <$ 500 K, where both long and short nanowires are not affected by extremely low value of the α (dotted boxes in Figures 5.9a and 5.9b). For each measured temperature point, T^*, we can consider $\alpha = \alpha(T^*)$ to apply the fitting procedure. Given its temperature dependency, in order to guarantee that using $\alpha(T^*)$ is a correct approximation for data analysis, we need to limit the nanowires local temperature increase, as already discussed in Section 5.3.

5.5 Thermal conductivity and losses

Owing the knowledge of the TCR of each single nanowire, we can evaluate the resistance variation produced by a flowing current in the nanowire, and we can apply the Joule self-heating method to extract the thermal conductivity and the thermal losses, in accordance with Eq. 5.5.

Sample A

Figures 5.11a and 5.11b show the example of the measured nanowire resistance as a function of the heating current for the short and long nanowire, respectively, for a current sweeping in the range $|I_{\text{heating}}| \leq 2$ mA at $T = 403$ K in sample A. In the case of short nanowire, for which the minimum of resistance has not been reached at this temperature (as visible in

Figure 5.9a), the the $R(I)$ shows a downward bending parabola up to $I \sim \pm 1.5$ mA and then it starts to increase, meaning that at this current the nanowire has reached the temperature corresponding to the minimum of resistance. On the contrary, the long nanowire records a very weak resistance variation for $|I_{\text{heating}}| < 0.5$ mA since at this temperature the $R(T)$ curve is close to its minimum (Figure 5.9b), corresponding to a TCR approaching to zero. The inset of Figure 5.11b shows a magnification of the plot for $|I_{\text{heating}}| < 0.4$ mA. From this plot, it is possible to see that the behavior of the $R(I)$ corresponds to an upward bending parabola. Given that the thermal conductivity and losses, as well as the TCR, are temperature dependent, we will limit the adopted method to a sufficiently small current range ($\sim \pm 0.4$ mA) to avoid an excessive heating of the nanowires.

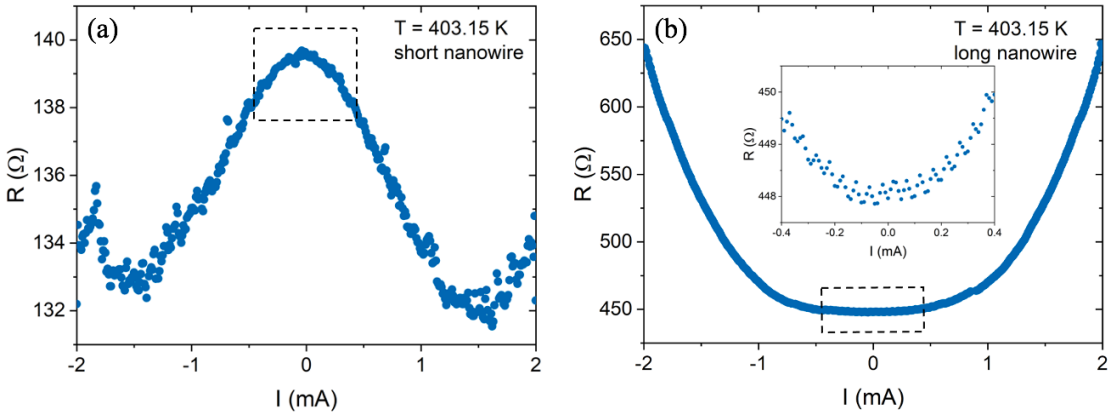

Figure 5.11 – (a) Short and (b) long nanowire resistance variation as a function of the heating current flowing in the nanowires. The inset shows a magnification of the curve in the range $|I_{\text{heating}}| < 0.4$ mA. The dotted rectangles represent the section of the data actually used to fit Eq. 5.5.

Finally, we can measure the relative variation $\Delta R/R_0$ of the sMLG nanowires of sample A as a function of the applied electrical power p at different temperatures for a heating current ramping up to maximum values of $\sim \pm 400$ μA. Figure 5.12 shows two examples of data analysis at $T = 393$ K and $T = 453$ K for the (a) long and (b) short nanowire, respectively. The points are the measured experimental data, while the solid black and dotted red lines are plots of Eq. 5.5 resulting from the self-consistent fitting procedure for the two temperatures, respectively. Convergence on the extracted κ and g values is typically reached after 10 iterations.

Figure 5.13a shows the complete set of κ values extracted in the temperature range 400 K - 500 K. The results show an extremely reduced values of the thermal conductivity in the explored temperature range. The extracted κ values are of the order of ~ 40 W/mK. The quite large error bars result from the fitting procedure and reflect the dispersion of the $\Delta R/R_0$ data points. The obtained results do not allow to define a trend in the $\kappa(T)$ behavior, but a clear reduction with respect to what expected is evident in the whole explored temperature range. Even if we cannot discriminate the main physical mechanism inducing the κ reduction, some arguments can be discussed. Such low κ values are comparable to what has been measured in the case of encased trilayer graphene [112]. In this particular example, the κ reduction is due to induced defects and interactions between the outermost graphene layers

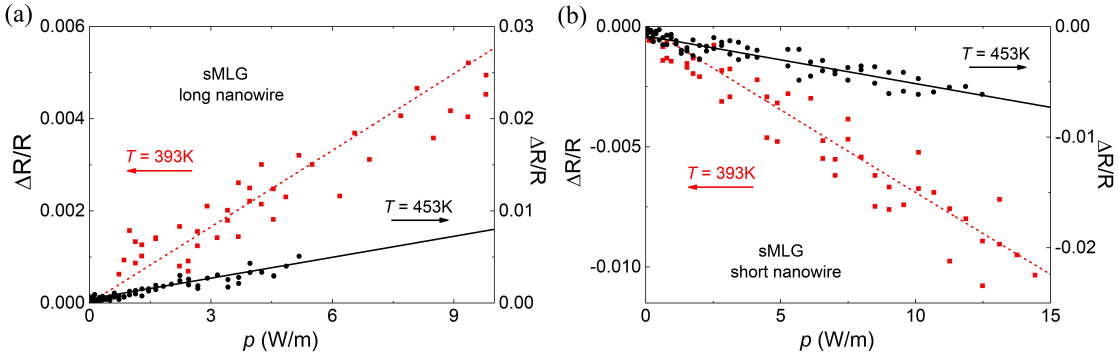

Figure 5.12 – (a) Relative variation of resistance for the long wire in sample A at T = 393 K (red squares) and T = 463 K (black circles) with the theoretical fit obtained from eq. 5.2 (solid and dot lines). (b) Same plot for the short nanowires in sample A.

and the encapsulating oxide layers. Two mechanisms are cited to explain the κ reduction: phonon leakage into the low-sound-velocity oxide and additional phonon scattering by the non-homogeneous graphene-oxide interface. Similar κ reduction has been also reported in supported graphene nanoribbons (below RT) [143], where scattering with boundaries and with the substrate are dominant and limit the phonon diffusion. In addition, it has been also experimentally demonstrated the control of the in-plane thermal conductivity of supported graphene by varying the thermo-mechanical affiliation at graphene/substrate interface [188]. Indeed, repeated annealing enhances graphene-substrate conformity and interfacial scattering. Our experimental approach cannot distinguish between the scattering mechanisms inducing the thermal conductivity reduction. However, all the experimental evidences reported in literature can also apply to our graphene nanowires and can be invoked as possible origin of κ reduction.

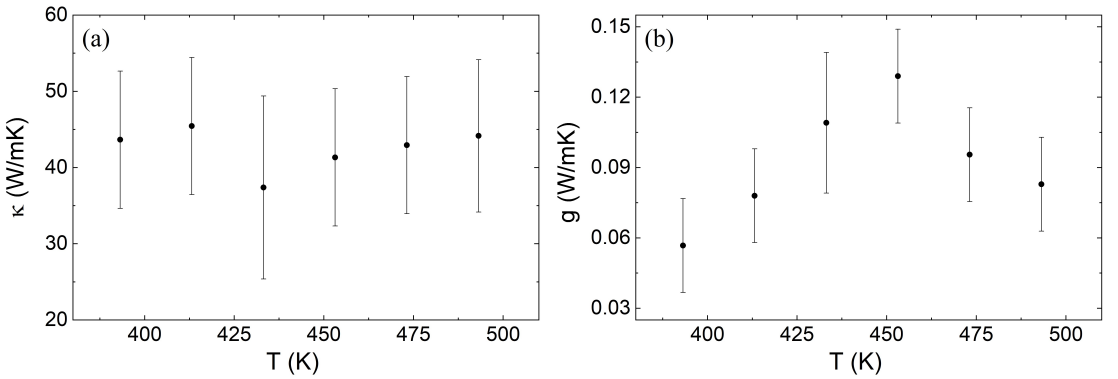

Figure 5.13 – (a) Thermal conductivity of sMLG nanowires in sample A as a function of the temperature. Error bars are derived from the fitting procedure. (b) Thermal losses through the substrate per unit length of sMLG nanowires in sample A as a function of the temperature.

Figure 5.13b shows the values of the thermal losses per unit length through the substrate, g, extracted simultaneously to κ. The values are dispersed between 0.05 and 0.13 W/mK, in the explored temperature range. The obtained values are in the same order of magnitude with

what estimated in Section 5.2, even if slightly smaller. This is not really surprising since it has been demonstrated that interfacial corrugation at the graphene/SiO_2 interface can drastically reduce the interfacial thermal conductance over more than one order of magnitude [185, 186].

Sample B

Sample B is composed only by a sBLG nanowire that, with a length equal to 0.9 μm, matches even with more accuracy than sample A the "short" limit condition. The experimental g, output of sample A, can be used as a good approximation for the analysis of the self-heating response of the sBLG nanowire in sample B even if the sample thickness is different. It has been revealed, in fact, that the thermal conductance at the graphene/substrate interface does not change significantly across few-layer graphene (from 1 to ~ 10 layers) [85, 112]. This is due to the fact that the thermal resistance between graphene and its environment dominates over the one between individual graphene sheets. Thus, the self-heating response of the sBLG nanowire in sample B is computed by using a g value equal to 0.09 W/mK, corresponding to the average value extracted for sample A and by leaving only κ as free fit parameter in Eq. 5.2. The result of the fitted κ values as a function of the temperature is shown in Figure 5.14. The thermal conductivity follows a trend equivalent to sample A, but with slightly higher values ranging between 80 and 120 W/mK. This result seems to indicate that the value of κ can slightly vary depending on the local morphology and coupling to the underlying substrate.

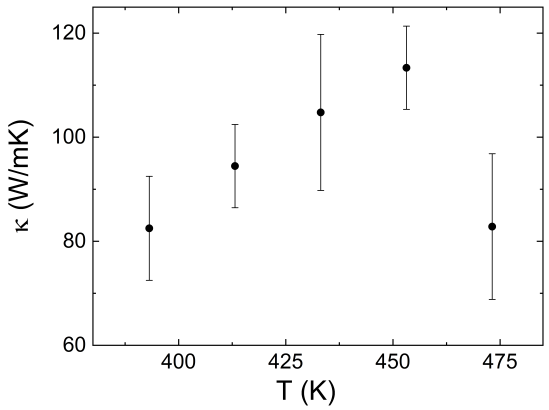

Figure 5.14 – Thermal conductivity of sBLG nanowire in sample B as a function of the temperature. Error bars are derived from the fitting procedure.

Thermal healing length

Having extracted the κ and g values, we can estimate the effective thermal healing length L_H of the fabricated sMLG nanowires to verify "a posteriori" if they meet the "short" and "long" limits. To this aim, we can use Eq. 5.8 with the actual values of thermal conductivity and thermal losses. Figure 5.15a shows the extracted L_H as a function of the temperature in the explored range for sample A. The value of L_H slightly varies between 0.5 and 1 μm. Being

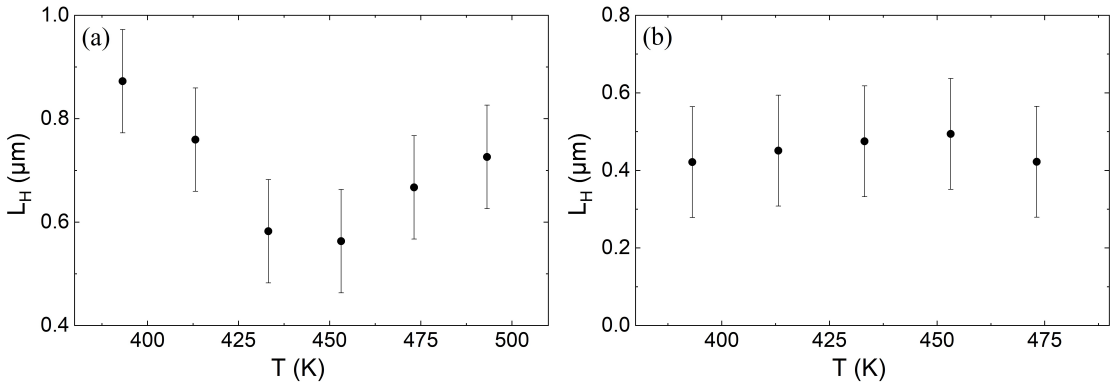

Figure 5.15 – Thermal healing length estimated by the extracted κ and g values as a function of the temperature (a) for sample A and (b) for sample B.

9 μm-long, we can conclude that the long nanowire fully matches the required conditions ($L > 3L_H$), providing a reliable evaluation of g. The 1.8 μm-long short nanowire partially meets the required conditions ($L < 3L_H$), giving a slightly higher uncertainty on the measurement of κ in the temperature range in which L_H approaches 0.5 μm. On the other hand, the 0.9 μm-long nanowire which constitutes sample B fully answers to the healing length condition more tightly than sample A, being $L_H \sim 0.45$ μm as illustrated in Figure 5.15b. This justifies the used data analysis and giving more reliability to the results.

5.5.1 Callaway model

As we have seen from the analysis carried out in this work, it is not possible to determine a temperature trend of the thermal conductivity in the studied graphene nanowires. Theoretically, the thermal conductivity temperature dependence is predicted to reach a maximum value slightly around room temperature. At higher temperature, significant Umklapp phonon scattering takes place, inducing a decreasing behavior [112, 161, 162, 281]. Figure 5.16 shows the prediction of the $\kappa(T)$ behavior based on the Callaway model [282]. Within this description, the expression of the thermal conductivity is given by:

$$\kappa(T) = \frac{k_B}{2\pi^2 v}\left(\frac{k_B T}{\hbar}\right)^3 \int_0^{\theta_D/T} \tau \frac{x^4 e^x}{(e^x-1)^2} dx \tag{5.11}$$

where k_B is the Boltzmann constant, v is the sound velocity, $\hbar$ is the Planck constant, θ_D is the Debye temperature and x is a dimensionless variable defined as $\hbar\omega/k_B T$. Here τ is the overall scattering time given by the Matthiessen's rule:

$$\tau = \left(vL_0^{-1} + A\omega^4 + BT^3\omega^2\right)^{-1} \tag{5.12}$$

where the different terms in the parenthesis are, in the order, the boundary scattering term,

the scattering by local impurities such as point defects and the phonon-phonon scattering term, including the Umklapp scattering. L_0 is the characteristic length of the sample and the A and B coefficients are constants [283]. Figure 5.16 illustrates the influence on $\kappa(T)$ of increasing impurity and phonon scattering contributions, starting from a common curve of thermal conductivity (red curve in the figure). By increasing the impurity scattering term A and keeping B constant (Figure 5.16a), the thermal conductivity is reduced and the peak position shows a slightly shift towards higher temperatures. On the other hand, for a given value of the A term and by varying the the phonon-phonon scattering term B (Figure 5.16b), the thermal conductivity curve is again reduced and a more evident shift of the peak position towards lower temperatures takes place. In general, a strong suppression of $\kappa(T)$ can be predicted by increasing both scattering terms. Since in our experimental results a clear temperature trend is not defined, it is not possible to determine which scattering mechanism is dominant in our samples. Impurities can be most likely related to the fabrication procedure, while phonon scattering is probably determined by the enhanced substrate roughness. Nevertheless, the widely used Callaway model captures quite well the strong κ reduction experimentally observed.

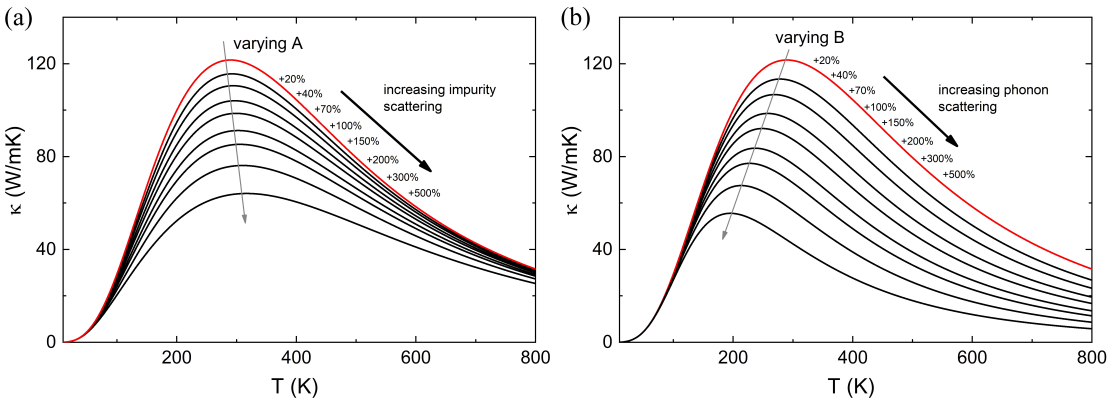

Figure 5.16 – Thermal conductivity reduction due to increasing (a) scattering with impurities and (b) phonon-phonon scattering according to the Callaway model [282].

5.6 Conclusions

In this Chapter, I have demonstrated how the Joule self-heating method can be a reliable approach to evaluate the thermal conductivity and the thermal losses to the substrate in graphene nanowires. To correctly implement this approach for supported devices, it is necessary to understand how the heat generated in the sample is dissipated in the environment and distinguish between the case in which the dissipation through the substrate is fully dominating or the case in which the heat flowing laterally through the sample plays also a role. This is possible thanks to the characteristic healing length which allows to distinguish between the two regimes. In the studied samples, the extracted values of thermal conductivity are lower than what has been previously observed in literature by different approaches for supported few layers graphene. Regardless the relatively large error bars in the obtained results, a decisive

κ suppression is evident. This suppression can be qualitatively related to several scattering mechanisms which are playing an important role, especially at high temperature and, which are difficult to discern one from the other. Scattering at the interface and the presence of residues related to the pick-up transfer method or to the device nanofabrication contribute to increase impurities in the system, further reducing the thermal conductivity. Moreover, lateral edge roughness and boundary effects can also contribute to the suppressed κ behavior. Annealing treatments can further contribute to decrease the graphene thermal conductivity since the interfacial phonon scattering rate increases with increasing graphene-substrate contact strength and conformity. Finally, the high surface roughness of the substrate is likely to increase the thermal resistance at the interface, implying reduced thermal losses through the substrate too, which is an advantageous point to make the Joule self-heating method more reliable.

The results extracted from this analysis also suggest that graphene can still be a good candidate for thermoelectric applications, since its thermal conductivity can be tuned thanks to an accurate sample design. In particular, phonon-boundary and phonon-substrate scattering, which appear among the dominant factors for κ reduction, weakly affect the electronic properties. Moreover, the method implemented in this chapter is very versatile concerning the device design and can be easily applied when 2D materials are combined in van der Waals heterostructures. However, its main limitation is related to the possibility of being applied only to conductive materials. In principle, the thermal conductivity of TMDs can be evaluated using this approach when they are in high doped regimes. This would allow to estimate κ in-situ, taking into consideration the possible phonon scattering enhancement which is strongly sample dependent. The main drawback is the need to apply a transverse local electric field for the gate modulation which could complicate the device operations.

6 Conclusions and perspectives

Overcoming the S-σ anti-correlation limit and reducing the thermal conductivity are among the main concerns in the optimization of high-performing thermoelectric energy converters. 2D materials offer new platforms of investigation since the intrinsic carrier confinement in these materials shows unprecedented electric and thermoelectric properties. Moreover, being extremely sensitive to the environment, 2D materials are highly prone to several device engineering for enhanced performances. During my PhD, I investigated the electric and thermoelectric properties of 2D tungsten diselenide (WSe_2), as a representative member of the transition metals dichalcogenides (TMDs) family. This 2D material, poorly investigated in literature, is highly attractive for thermoelectric applications due to its particularly low thermal conductivity ($\sim$ 1 - 2 W/mK). To explore its properties, I implemented a van der Waals heterostructure set-up, in which a local gate allowed me to modulate the semiconductor charge density by field effect doping. Furthermore, I have applied a simple approach, the Joule self-heating, to measure the thermal conductivity of supported 2D materials, allowing to open new routes for the complete thermoelectric characterization on the same supported device.

The main results and achievements of my work can be summarized as follows:

- I developed the experimental set-up and the practical expertise for dry transfer of mechanically exfoliated 2D materials, allowing to fabricate quite complex van der Waals heterostructures with a good alignment accuracy, wide surfaces and high yield of sample production.
- I studied the structural properties of the fabricated heterostructure and I investigated possible ways to reduce the interface contamination between the 2D materials layers. Moreover, I also developed a recipe for the etching of van der Waals heterostructures.
- I investigated the electrical and thermoelectrical properties of hBN-supported WSe_2 with a local metallic gate. I found out that the different choice of metallic electrodes used to connect the WSe_2 results in a different electric and thermoelectric response which can be understood in terms of metal-semiconductor interface hybridization effects. The

interaction with the metal generates localized band gap states at the bandgap edges which affect the charge carrier injection, as shown from the evaluation of the Schottky barrier heights. A highly metal-WSe_2 hybridized interface, creating a textured band structure as theoretically predicted, enhances the charge injection and reduces the Seebeck coefficient.

- I examined the thermal conductivity of SiO_2-supported graphene in a configuration highly compatible to the one used for electric and thermoelectric characterizations and I proved that the thermal conductivity of graphene can be strongly reduced by the enhanced contribution of impurity and phonon scattering related to the device engineering. Indeed, to fully characterize the figure of merit for energy conversion in real devices, the knowledge of the material thermal conductivity is a striking point since the properties of 2D materials are strongly influenced by the device configuration.

Perspectives

The ability to modify the 2D material properties by device engineering opens the way to plenty of possibilities. Some of them will be explored in the future in my team at MPQ lab within new PhD projects and collaborations with other labs (ITODYS and C2N).

Short term perspectives:

- For a more reliable and precise electric and thermoelectric characterization, my team is soon going to upgrade the measurement setup with a 14-probe Nextron micro probe station. This system will allow us, without breaking the vacuum in the chamber, to perform a simultaneous 4-point calibration of the local thermometers to precisely measure the temperature gradient developed by local Joule heating, but also to perform a 4-point electrical measurement on the 2D semiconducting material.

- Given the strong influence of the metal-semiconductor interface hybridization on the electrical and thermoelectrical properties, we plan to push the interface engineering in order to achieve a better control of their properties. A possible way can be to intentionally reduce the hybridization effect by inserting a thin tunnel barrier at the metal-semiconductor contact, for example by introducing a monolayer hBN or a thin oxide layer. This strategy could be a possible way to enhance the Seebeck coefficient while preserving the charge carrier injection.

- Other metal contacts can be further tested. For example, theoretical band structures calculations [248] predict Scandium (Sc) to be the metal allowing for the strongest hybridization with WSe_2. To my knowledge, this element has never been used for the fabrication of electrical contacts on TDMs-based devices. Since strong hybridization seems to reduce the Seebeck coefficient less than the expected gain in charge injection, this approach could lead to interesting and promising results.

Long term perspectives:

- To achieve the optimized value of power factor or ZT, a constant gate voltage needs to be applied to modulate the doping of the conductive channel material. However, if electric-gating methods are powerful for evaluating the intrinsic material properties, stable chemical doping methods are inevitable for device applications. This could be achieved, for example, by molecular absorption or surface functionalization of the 2D material surface.
- To fully characterize the thermoelectric figure of merit, a measurement of the thermal conductivity needs to be carried out also for WSe_2 in the same configuration used for the Seebeck measurement. Moreover, substrate engineering or material nano-structuring (such as nano-patterning, etc) could be implemented to reduce the thermal conductivity by enhanced phonon scattering, without compromising the electrical transport properties.
- 2D materials in van der Waals heterostructures have the ability of "transfer" some of their properties to the adjacent layers by proximity effects. Thus, it would be interesting to combine several 2D materials to explore the combined response to thermoelectricity.

A Atomic force microscopy

Atomic force microscopy (AFM) is used to determine the thicknesses of the hBN and WSe_2 layers for the discussed samples in Chapters 3 and 4. Figure A.1 shows AFM images for (a) Ag-contacted sample, (b) Pd-contacted sample, (c) Co-contacted sample and (d) Ti-contacted sample. The figure shows a large area (~ 50×50 μm^2) image of the whole device, a zoom on a smaller area of few μm^2 (red rectangles) where an example of line profile of the WSe_2 step is reported. The hBN and WSe_2 thicknesses are listed in Table 3.1 of Chapter 3 and they have been evaluated by averaging 50 step heights of line profiles taken in different samples zones.

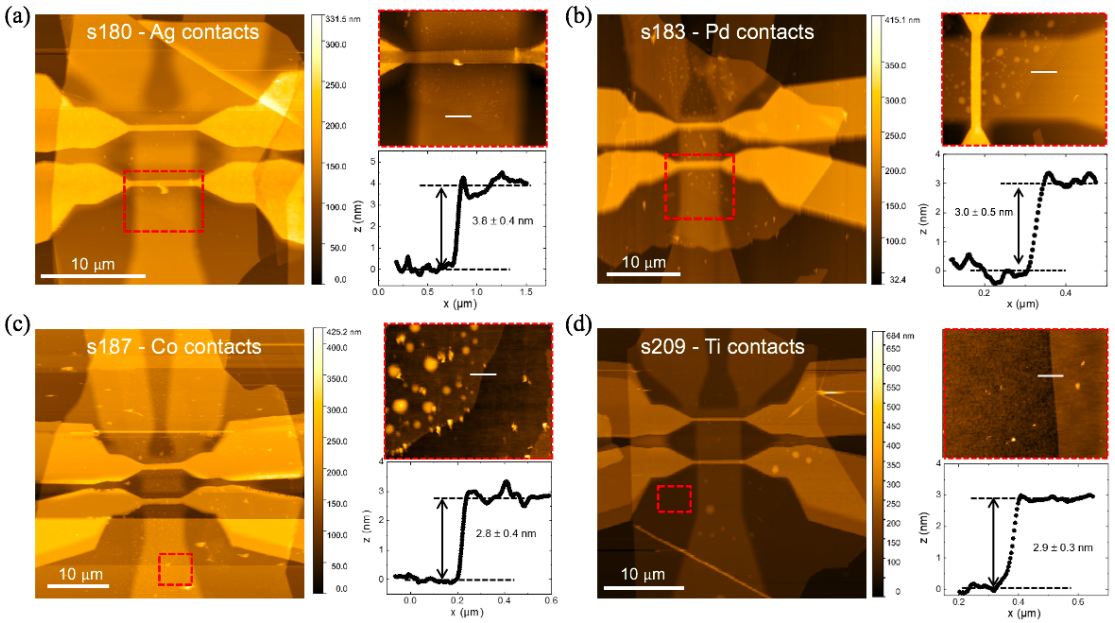

Figure A.1 – AFM images of the samples discussed in Chapters 3 and 4.

B Seebeck

To prove the reproducibility of the results obtained in the thermoelectic characterization of the samples, for each choice of metal contact, at least a couple of samples has been studied. In Chapter 4, I have reported only one representative sample for each metal. Here, I will report the results obtained for the other samples. The following figures show the Seebeck coefficient as a function of the applied gate voltage and the corresponding electrical conductivity evaluated in the same V_G range for a source-drain polarization of 10 mV.

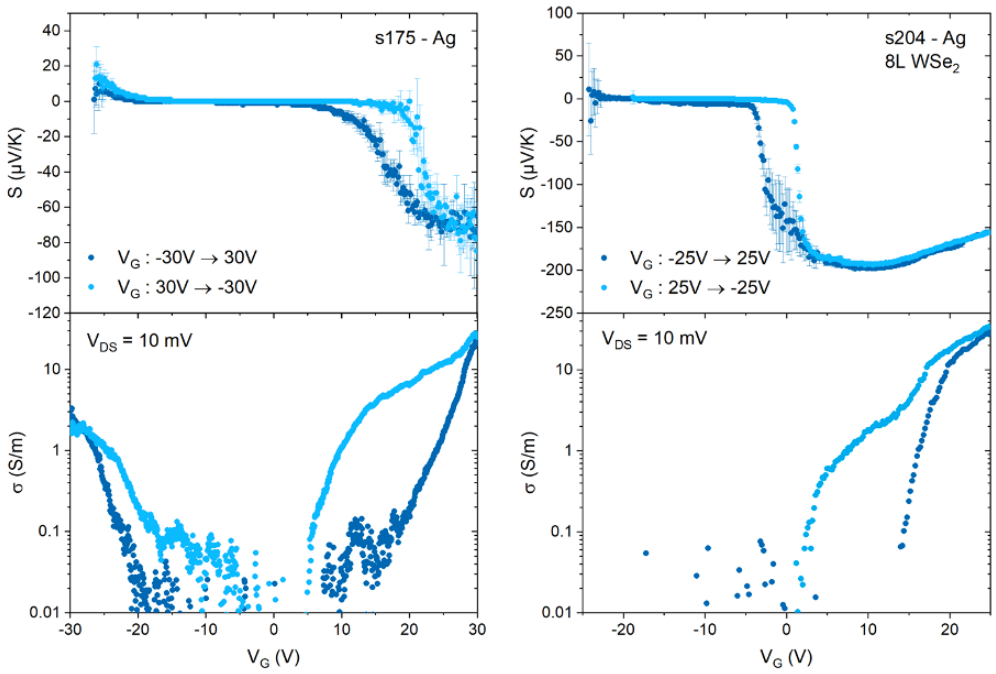

Figure B.1 – Gate voltage dependence of the Seebeck coefficient (top panel) and the electrical conductivity (bottom panel) for the samples 175 and 204 (Silver contact), for increasing and decreasing gate voltage sweep.

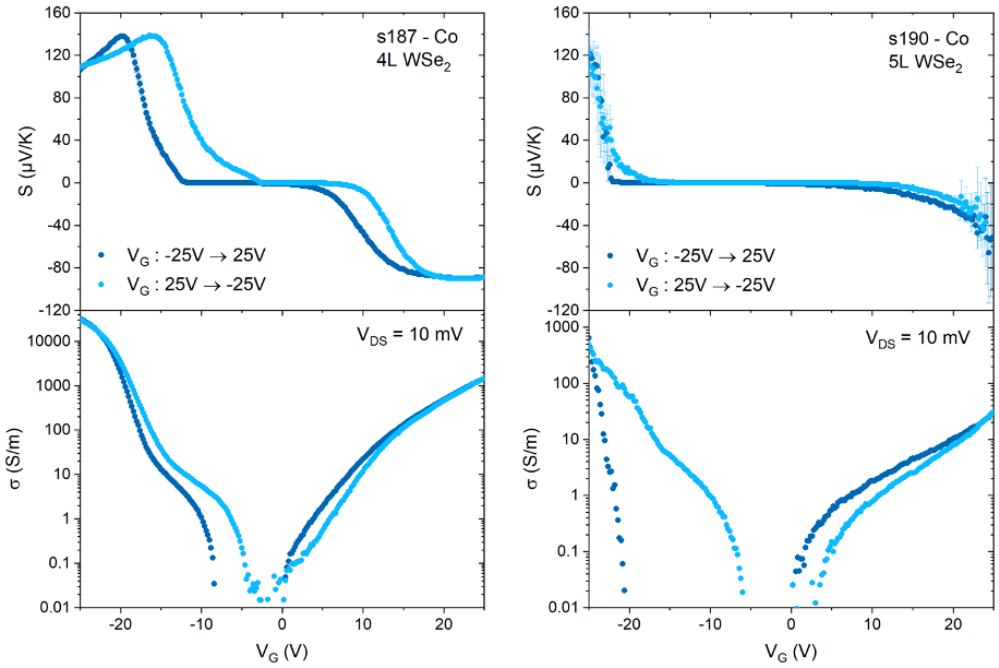

Figure B.2 – Gate voltage dependence of the Seebeck coefficient (top panel) and the electrical conductivity (bottom panel) for the samples 187 and 190 (Cobalt contact), for increasing and decreasing gate voltage sweep.

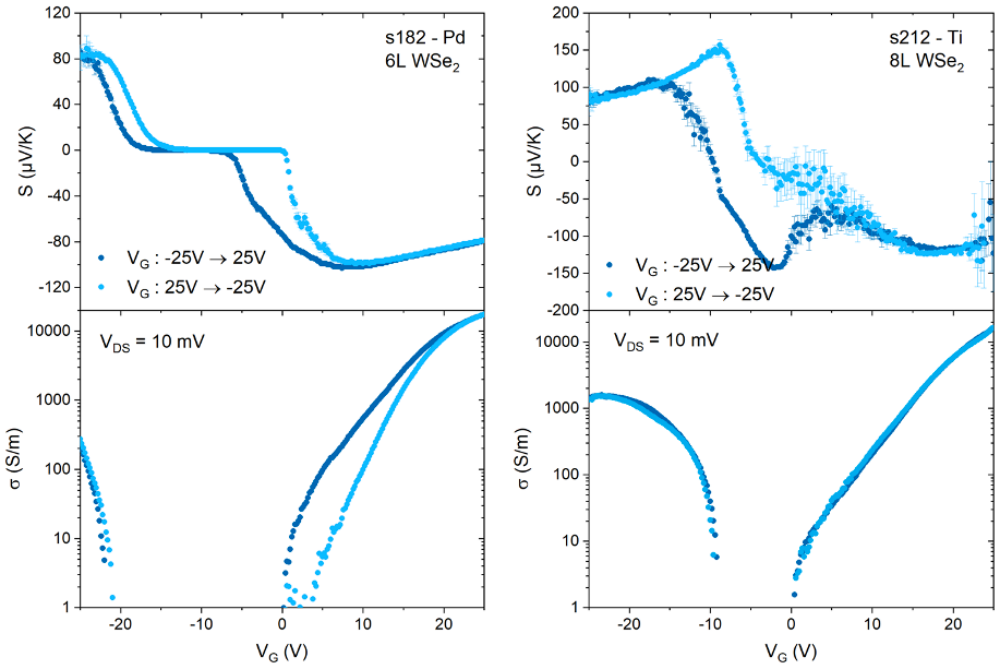

Figure B.3 – Gate voltage dependence of the Seebeck coefficient (top panel) and the electrical conductivity (bottom panel) for sample 182 (Palladium contact) and sample 212 (Titanium contact), for increasing and decreasing gate voltage sweep.

C Photoluminescence in single layer $MoSe_2$

During my PhD, I have been part of a collaboration with the group PMTeQ (Photons, Magnons et Technologies Quantiques) from INSP (Institut des NanoScieces de Paris). The aim of this collaboration was to fabricate van der Waals heterostructures to study the photoluminescence (PL) response in fully-encapsulated single layer (SL) TMDs in relation to excitonic states as a function of the charge density modulation achieved with a local metallic gate. My contribution was related to the fabrication of the samples while the measurements were performed by the PMTeQ team.

Monolayer transition metal dichalcogenide semiconductors offer an interesting platform to investigate the interaction between excitons and a Fermi sea of charges [284]. As illustrated in Figure C.1a, the innate broken inversion symmetry in TMD monolayers, together with the spin-orbit interaction, lifts the spin degeneracy at ±K valleys, giving rise to two species of excitons, A and B, involving electrons and holes of opposite spin in each valley, as represented in the figure by filled and open circles, respectively. In particular, the impact of charge doping on the A exciton has been extensively studied and widely interpreted with the formation of trions: tightly bound composite particles composed of either two electrons and

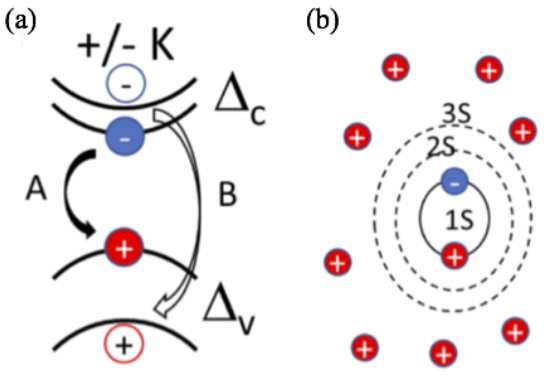

Figure C.1 – (a) Schematic of the TMD band structure at the K point. Filled/open circles denote charges in A and B excitons. (b) Illustration of an exciton surrounded by a charged Fermi sea of holes. The state 1s denotes the exciton ground state while 2s, 3s, etc are the excited states. Extracted from [284].

one hole or two holes and one electron [285, 286]. However, there still exists the question of whether this interpretation is the most correct or whether the system is better described by exciton–polarons, that is, as illustrated in Figure C.1b, the interaction between an exciton and a Fermi sea of charges [287, 288].

High-quality hBN-encapsulated samples clearly produce optical features including the ground state and excited states of both A and B excitons, allowing for a comprehensive examination of interaction effects arising from different exciton species and coupling to a Fermi sea of charges. Photoluminescence is a powerful tool to study this charge interaction. To this aim, I have fabricated fully hBN-encapsulated $MoSe_2$ van der Waals heterostructures with a local metallic gate and electrical connection to modulate the charge density in the semiconductor. Figure C.2a shows the schematic of the fabricated device, while Figure C.2b shows an optical image of a representative sample.

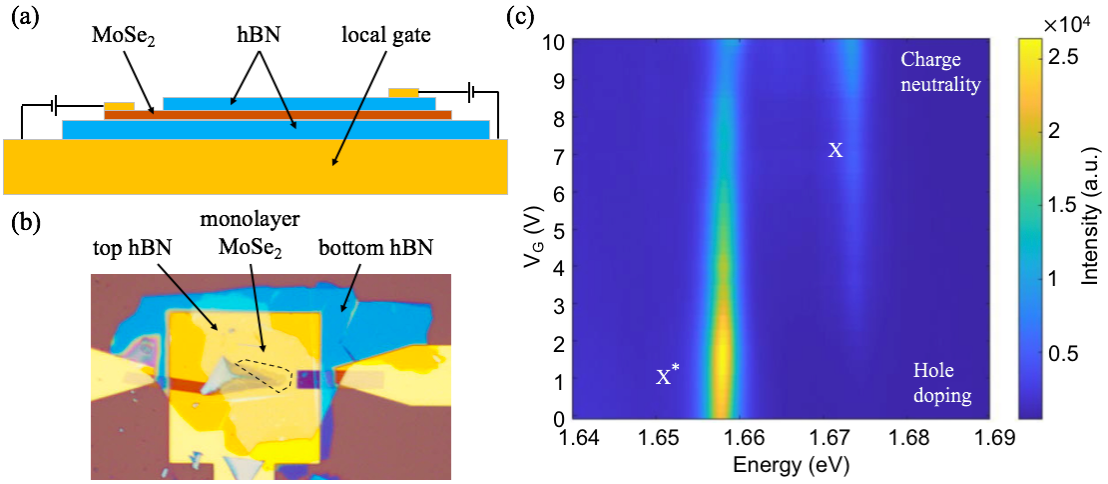

Figure C.2 – (a) Schematic image of a hBN/$MoSe_2$/hBN van der Waals heterostructure with local gate. (b) Optical image of a representative sample. (c) Photoluminescence spectrum as a function of the gate voltage V_G.

For optical measurements, the sample is cooled down to 5 K, and the charge density is tuned by the local metallic gate. Figure C.2c shows the gate voltage dependent photoluminescence of the presented sample, obtained with a 660 nm excitation laser. Two strong features are visible at ~ 1.66 eV (labeled X*) and at ~ 1.67 eV (labeled X), both attributable to the ground state of the A exciton. (The B exciton is expected to be recorded at higher energies (~ 1.85 eV)). For high gate voltages, both X and X* modes are visible. Reducing V_G the X branch vanishes, while the X* peak becomes more intense. This allows to correlate the X* mode to the interaction of excitons with charge doping (p-type, in this case), while the X mode to neutral exciton emission. Thus, the gate voltage dependent photoluminescence spectrum can be divided into two ranges, roughly for $V_G > 7$ V and $V_G < 7$ V. For $V_G < 7$ V, holes are filling the valence band and the X* mode is dominant. We can call this range "hole doping" region. For $V_G > 7$ V, the Fermi level is pushed towards the energy gap and we can call this range "charge neutrality" region. The X* feature visible in this nominally charge neutral range can be attributed to states formed by the binding of neutral excitons with residual holes that have not yet formed

a well-defined Fermi sea. A more detailed investigation, including the study of the X and X^* linewidth broadening and their peak position as a function of the charge doping modulation, can allows to confirm the nature of these optical features.

This measurement, which represents a preliminary study for the PMTeQ team, is in agreement with the state-of-the-art of exciton-polarons interaction in 2D TMDs. Given the promising results and the reliable fabrication procedure, a step forward can be done by combining different single layer TMDs to create Moiré patterns and to study the optical response in more complex van der Waals heterostructures as a function of the relative orientation of the layers and the charge doping.

Bibliography

[1] K. S. Novoselov, A. K. Geim, S. V. Morozov, D. Jiang, Y. Zhang, S. V. Dubonos, I. V. Grigorieva, and A. A. Firsov, "Electric field effect in atomically thin carbon films," Science, vol. 306, no. 5696, pp. 666–669, 2004.

[2] P. R. Wallace, "The band theory of graphite," Phys. Rev., vol. 71, pp. 622–634, 1947.

[3] K. S. Novoselov, D. Jiang, F. Schedin, T. J. Booth, V. V. Khotkevich, S. V. Morozov, and A. K. Geim, "Two-dimensional atomic crystals," Proceedings of the National Academy of Sciences, vol. 102, no. 30, pp. 10451–10453, 2005.

[4] F. Xia, H. Wang, D. Xiao, M. Dubey, and A. Ramasubramaniam, "Two-dimensional material nanophotonics," Nature Photonics, vol. 8, no. 12, pp. 899–907, 2014.

[5] M. Xu, T. Liang, M. Shi, and H. Chen, "Graphene-like two-dimensional materials," Chemical Reviews, vol. 113, no. 5, pp. 3766–3798, 2013.

[6] S. V. Morozov, K. S. Novoselov, M. I. Katsnelson, F. Schedin, D. C. Elias, J. A. Jaszczak, and A. K. Geim, "Giant intrinsic carrier mobilities in graphene and its bilayer," Phys. Rev. Lett., vol. 100, p. 016602, 2008.

[7] W. Choi, N. Choudhary, G. H. Han, J. Park, D. Akinwande, and Y. H. Lee, "Recent development of two-dimensional transition metal dichalcogenides and their applications," Materials Today, vol. 20, no. 3, pp. 116 – 130, 2017.

[8] S. Das, H.-Y. Chen, A. V. Penumatcha, and J. Appenzeller, "High performance multilayer MoS_2 transistors with scandium contacts," Nano Letters, vol. 13, no. 1, pp. 100–105, 2013.

[9] C. R. Dean, A. F. Young, I. Meric, C. Lee, L. Wang, S. Sorgenfrei, K. Watanabe, T. Taniguchi, P. Kim, K. L. Shepard, and J. Hone, "Boron nitride substrates for high-quality graphene electronics," Nature Nanotechnology, vol. 5, no. 10, pp. 722–726, 2010.

[10] A. K. Geim and I. V. Grigorieva, "Van der Waals heterostructures," Nature, vol. 499, no. 7459, pp. 419–425, 2013.

[11] H. Terrones, F. López-Urías, and M. Terrones, "Novel hetero-layered materials with tunable direct band gaps by sandwiching different metal disulfides and diselenides," Scientific Reports, vol. 3, no. 1, p. 1549, 2013.

[12] Coogan and Y. K. Gun'ko, "Solution-based "bottom-up" synthesis of group VI transition metal dichalcogenides and their applications," Mater. Adv., vol. 2, pp. 146–164, 2021.

[13] S. Wang, A. Robertson, and J. H. Warner, "Atomic structure of defects and dopants in 2D layered transition metal dichalcogenides," Chem. Soc. Rev., vol. 47, pp. 6764–6794, 2018.

[14] A. Splendiani, L. Sun, Y. Zhang, T. Li, J. Kim, C.-Y. Chim, G. Galli, and F. Wang, "Emerging photoluminescence in monolayer MoS_2," Nano Letters, vol. 10, no. 4, pp. 1271–1275, 2010.

[15] A. Kuc, N. Zibouche, and T. Heine, "Influence of quantum confinement on the electronic structure of the transition metal sulfide TS_2," Phys. Rev. B, vol. 83, p. 245213, 2011.

[16] W. S. Yun, S. W. Han, S. C. Hong, I. G. Kim, and J. D. Lee, "Thickness and strain effects on electronic structures of transition metal dichalcogenides: 2H-MX_2 semiconductors (M = Mo, W; X = S, Se, Te)," Phys. Rev. B, vol. 85, p. 033305, 2012.

[17] R. Roldán, J. A. Silva-Guillén, M. P. López-Sancho, F. Guinea, E. Cappelluti, and P. Ordejón, "Electronic properties of single-layer and multilayer transition metal dichalcogenides MX_2 (M = Mo, W and X = S, Se)," Annalen der Physik, vol. 526, no. 9-10, pp. 347–357, 2014.

[18] W. Zhao, R. M. Ribeiro, M. Toh, A. Carvalho, C. Kloc, A. H. Castro Neto, and G. Eda, "Origin of indirect optical transitions in few-layer MoS_2, WS_2, and WSe_2," Nano Letters, vol. 13, no. 11, pp. 5627–5634, 2013.

[19] L. Britnell, R. M. Ribeiro, A. Eckmann, R. Jalil, B. D. Belle, A. Mishchenko, Y.-J. Kim, R. V. Gorbachev, T. Georgiou, S. V. Morozov, A. N. Grigorenko, A. K. Geim, C. Casiraghi, A. H. C. Neto, and K. S. Novoselov, "Strong light-matter interactions in heterostructures of atomically thin films," Science, vol. 340, no. 6138, pp. 1311–1314, 2013.

[20] Y. Sun, D. Wang, and Z. Shuai, "Indirect-to-direct band gap crossover in few-layer transition metal dichalcogenides: A theoretical prediction," The Journal of Physical Chemistry C, vol. 120, no. 38, pp. 21866–21870, 2016.

[21] H. Yuan, M. S. Bahramy, K. Morimoto, S. Wu, K. Nomura, B.-J. Yang, H. Shimotani, R. Suzuki, M. Toh, C. Kloc, X. Xu, R. Arita, N. Nagaosa, and Y. Iwasa, "Zeeman-type spin splitting controlled by an electric field," Nature Physics, vol. 9, no. 9, pp. 563–569, 2013.

[22] O. Lopez-Sanchez, D. Lembke, M. Kayci, A. Radenovic, and A. Kis, "Ultrasensitive photodetectors based on monolayer MoS_2," Nature Nanotechnology, vol. 8, no. 7, pp. 497–501, 2013.

[23] Z. Yin, H. Li, H. Li, L. Jiang, Y. Shi, Y. Sun, G. Lu, Q. Zhang, X. Chen, and H. Zhang, "Single-layer MoS_2 phototransistors," ACS Nano, vol. 6, no. 1, pp. 74–80, 2012.

[24] X. Wang, P. Wang, J. Wang, W. Hu, X. Zhou, N. Guo, H. Huang, S. Sun, H. Shen, T. Lin, M. Tang, L. Liao, A. Jiang, J. Sun, X. Meng, X. Chen, W. Lu, and J. Chu, "Ultrasensitive and broadband MoS_2 photodetector driven by ferroelectrics," Advanced Materials, vol. 27, no. 42, pp. 6575–6581, 2015.

[25] K. F. Mak, C. Lee, J. Hone, J. Shan, and T. F. Heinz, "Atomically thin MoS_2: A new direct-gap semiconductor," Phys. Rev. Lett., vol. 105, p. 136805, 2010.

[26] L. Bawden, S. P. Cooil, F. Mazzola, J. M. Riley, L. J. Collins-McIntyre, V. Sunko, K. W. B. Hunvik, M. Leandersson, C. M. Polley, T. Balasubramanian, T. K. Kim, M. Hoesch, J. W. Wells, G. Balakrishnan, M. S. Bahramy, and P. D. C. King, "Spin-valley locking in the normal state of a transition-metal dichalcogenide superconductor," Nature Communications, vol. 7, no. 1, p. 11711, 2016.

[27] H. Yu and W. Yao, "Magnetization without polarization," Nature Materials, vol. 16, no. 9, pp. 876–877, 2017.

[28] H. Zhu, Y. Wang, J. Xiao, M. Liu, S. Xiong, Z. J. Wong, Z. Ye, Y. Ye, X. Yin, and X. Zhang, "Observation of piezoelectricity in free-standing monolayer MoS_2," Nature Nanotechnology, vol. 10, no. 2, pp. 151–155, 2015.

[29] B. Radisavljevic and A. Kis, "Mobility engineering and a metal-insulator transition in monolayer MoS_2," Nature Materials, vol. 12, no. 9, pp. 815–820, 2013.

[30] X.-L. Yu, D.-Y. Liu, Y.-M. Quan, J. Wu, H.-Q. Lin, K. Chang, and L.-J. Zou, "Electronic correlation effects and orbital density wave in the layered compound 1T-TaS_2," Phys. Rev. B, vol. 96, p. 125138, 2017.

[31] F. Withers, O. Del Pozo-Zamudio, A. Mishchenko, A. P. Rooney, A. Gholinia, K. Watanabe, T. Taniguchi, S. J. Haigh, A. K. Geim, A. I. Tartakovskii, and K. S. Novoselov, "Light-emitting diodes by band-structure engineering in van der Waals heterostructures," Nature Materials, vol. 14, no. 3, pp. 301–306, 2015.

[32] A. Favron, E. Gaufrès, F. Fossard, A.-L. Phaneuf-L'Heureux, N. Y.-W. Tang, P. L. Lévesque, A. Loiseau, R. Leonelli, S. Francoeur, and R. Martel, "Photooxidation and quantum confinement effects in exfoliated black phosphorus," Nature Materials, vol. 14, no. 8, pp. 826–832, 2015.

[33] M. Ishigami, J. H. Chen, W. G. Cullen, M. S. Fuhrer, and E. D. Williams, "Atomic structure of graphene on SiO_2," Nano Letters, vol. 7, no. 6, pp. 1643–1648, 2007.

[34] T. Ando, "Screening effect and impurity scattering in monolayer graphene," Journal of the Physical Society of Japan, vol. 75, no. 7, p. 074716, 2006.

[35] J.-H. Chen, C. Jang, S. Xiao, M. Ishigami, and M. S. Fuhrer, "Intrinsic and extrinsic performance limits of graphene devices on SiO_2," Nature Nanotechnology, vol. 3, no. 4, pp. 206–209, 2008.

[36] K. Bolotin, K. Sikes, Z. Jiang, M. Klima, G. Fudenberg, J. Hone, P. Kim, and H. Stormer, "Ultrahigh electron mobility in suspended graphene," Solid State Communications, vol. 146, no. 9, pp. 351 – 355, 2008.

[37] P. J. Zomer, S. P. Dash, N. Tombros, and B. J. van Wees, "A transfer technique for high mobility graphene devices on commercially available hexagonal boron nitride," Applied Physics Letters, vol. 99, no. 23, p. 232104, 2011.

[38] J. Duan, X. Wang, X. Lai, G. Li, K. Watanabe, T. Taniguchi, M. Zebarjadi, and E. Y. Andrei, "High thermoelectricpower factor in graphene/hBN devices," Proceedings of the National Academy of Sciences, vol. 113, no. 50, pp. 14272–14276, 2016.

[39] X. Cui, G.-H. Lee, Y. D. Kim, G. Arefe, P. Y. Huang, C.-H. Lee, D. A. Chenet, X. Zhang, L. Wang, F. Ye, F. Pizzocchero, B. S. Jessen, K. Watanabe, T. Taniguchi, D. A. Muller, T. Low, P. Kim, and J. Hone, "Multi-terminal transport measurements of MoS_2 using a van der Waals heterostructure device platform," Nature Nanotechnology, vol. 10, no. 6, pp. 534–540, 2015.

[40] Y. Uchiyama, A. Kutana, K. Watanabe, T. Taniguchi, K. Kojima, T. Endo, Y. Miyata, H. Shinohara, and R. Kitaura, "Momentum-forbidden dark excitons in hBN-encapsulated monolayer MoS_2," npj 2D Materials and Applications, vol. 3, no. 1, p. 26, 2019.

[41] X. Zhao, L. Li, and M. Zhao, "Lattice match and lattice mismatch models of graphene on hexagonal boron nitride from first principles," Journal of Physics: Condensed Matter, vol. 26, no. 9, p. 095002, 2014.

[42] A. S. Mayorov, R. V. Gorbachev, S. V. Morozov, L. Britnell, R. Jalil, L. A. Ponomarenko, P. Blake, K. S. Novoselov, K. Watanabe, T. Taniguchi, and A. K. Geim, "Micrometer-scale ballistic transport in encapsulated graphene at room temperature," Nano Letters, vol. 11, no. 6, pp. 2396–2399, 2011.

[43] L. Banszerus, T. Sohier, A. Epping, F. Winkler, F. Libisch, F. Haupt, K. Watanabe, T. Taniguchi, K. Müller-Caspary, N. Marzari, F. Mauri, B. Beschoten, and C. Stampfer, "Extraordinary high room-temperature carrier mobility in graphene-WSe_2 heterostructures," arXiv:1909.09523, 2019.

[44] F. Cadiz, E. Courtade, C. Robert, G. Wang, Y. Shen, H. Cai, T. Taniguchi, K. Watanabe, H. Carrere, D. Lagarde, M. Manca, T. Amand, P. Renucci, S. Tongay, X. Marie, and B. Urbaszek, "Excitonic linewidth approaching the homogeneous limit in MoS_2-based van der Waals heterostructures," Phys. Rev. X, vol. 7, p. 021026, 2017.

[45] L. A. Ponomarenko, R. V. Gorbachev, G. L. Yu, D. C. Elias, R. Jalil, A. A. Patel, A. Mishchenko, A. S. Mayorov, C. R. Woods, J. R. Wallbank, M. Mucha-Kruczynski,

B. A. Piot, M. Potemski, I. V. Grigorieva, K. S. Novoselov, F. Guinea, V. I. Fal'ko, and A. K. Geim, "Cloning of Dirac fermions in graphene superlattices," Nature, vol. 497, no. 7451, pp. 594–597, 2013.

[46] C. R. Dean, L. Wang, P. Maher, C. Forsythe, F. Ghahari, Y. Gao, J. Katoch, M. Ishigami, P. Moon, M. Koshino, T. Taniguchi, K. Watanabe, K. L. Shepard, J. Hone, and P. Kim, "Hofstadter's butterfly and the fractal quantum Hall effect in moiré superlattices," Nature, vol. 497, no. 7451, pp. 598–602, 2013.

[47] M. Yankowitz, J. Xue, D. Cormode, J. D. Sanchez-Yamagishi, K. Watanabe, T. Taniguchi, P. Jarillo-Herrero, P. Jacquod, and B. J. LeRoy, "Emergence of superlattice Dirac points in graphene on hexagonal boron nitride," Nature Physics, vol. 8, no. 5, pp. 382–386, 2012.

[48] J. Jung, A. M. DaSilva, A. H. MacDonald, and S. Adam, "Origin of band gaps in graphene on hexagonal boron nitride," Nature Communications, vol. 6, no. 1, p. 6308, 2015.

[49] B. Hunt, J. D. Sanchez-Yamagishi, A. F. Young, M. Yankowitz, B. J. LeRoy, K. Watanabe, T. Taniguchi, P. Moon, M. Koshino, P. Jarillo-Herrero, and R. C. Ashoori, "Massive dirac fermions and hofstadter butterfly in a van der Waals heterostructure," Science, vol. 340, no. 6139, pp. 1427–1430, 2013.

[50] Y. Cao, V. Fatemi, S. Fang, K. Watanabe, T. Taniguchi, E. Kaxiras, and P. Jarillo-Herrero, "Unconventional superconductivity in magic-angle graphene superlattices," Nature, vol. 556, no. 7699, pp. 43–50, 2018.

[51] A. L. Sharpe, E. J. Fox, A. W. Barnard, J. Finney, K. Watanabe, T. Taniguchi, M. A. Kastner, and D. Goldhaber-Gordon, "Emergent ferromagnetism near three-quarters filling in twisted bilayer graphene," Science, vol. 365, no. 6453, pp. 605–608, 2019.

[52] A. Avsar, J. Y. Tan, T. Taychatanapat, J. Balakrishnan, G. K. W. Koon, Y. Yeo, J. Lahiri, A. Carvalho, A. S. Rodin, E. C. T. O'Farrell, G. Eda, A. H. Castro Neto, and B. Özyilmaz, "Spin-orbit proximity effect in graphene," Nature Communications, vol. 5, no. 1, p. 4875, 2014.

[53] Z. Wang, D.-K. Ki, H. Chen, H. Berger, A. H. MacDonald, and A. F. Morpurgo, "Strong interface-induced spin-orbit interaction in graphene on WS_2," Nature Communications, vol. 6, no. 1, p. 8339, 2015.

[54] V. Leonov and R. J. M. Vullers, "Wearable thermoelectric generators for body-powered devices," Journal of Electronic Materials, vol. 38, no. 7, pp. 1491–1498, 2009.

[55] F. Suarez, D. P. Parekh, C. Ladd, D. Vashaee, M. D. Dickey, and M. C. Öztürk, "Flexible thermoelectric generator using bulk legs and liquid metal interconnects for wearable electronics," Applied Energy, vol. 202, pp. 736 – 745, 2017.

[56] L. L. Baranowski, G. J. Snyder, and E. S. Toberer, "Concentrated solar thermoelectric generators," Energy Environ. Sci., vol. 5, pp. 9055–9067, 2012.

[57] N. R. Kristiansen, G. J. Snyder, H. K. Nielsen, and L. Rosendahl, "Waste heat recovery from a marine waste incineratorusing a thermoelectric generator," Journal of Electronic Materials, vol. 41, no. 6, pp. 1024–1029, 2012.

[58] W. He, G. Zhang, X. Zhang, J. Ji, G. Li, and X. Zhao, "Recent development and application of thermoelectric generator and cooler," Applied Energy, vol. 143, pp. 1 – 25, 2015.

[59] W. Xie, X. Tang, Y. Yan, Q. Zhang, and T. M. Tritt, "Unique nanostructures and enhanced thermoelectric performance of melt-spun BiSbTe alloys," Applied Physics Letters, vol. 94, no. 10, p. 102111, 2009.

[60] D.-Y. Chung, T. Hogan, P. Brazis, M. Rocci-Lane, C. Kannewurf, M. Bastea, C. Uher, and M. G. Kanatzidis, "$CsBi_4Te_6$: A high-performance thermoelectric material for low-temperature applications," Science, vol. 287, no. 5455, pp. 1024–1027, 2000.

[61] B. Poudel, Q. Hao, Y. Ma, Y. Lan, A. Minnich, B. Yu, X. Yan, D. Wang, A. Muto, D. Vashaee, X. Chen, J. Liu, M. S. Dresselhaus, G. Chen, and Z. Ren, "High-thermoelectric performance of nanostructured bismuth antimony telluride bulk alloys," Science, vol. 320, no. 5876, pp. 634–638, 2008.

[62] G. Joshi, H. Lee, Y. Lan, X. Wang, G. Zhu, D. Wang, R. W. Gould, D. C. Cuff, M. Y. Tang, M. S. Dresselhaus, G. Chen, and Z. Ren, "Enhanced thermoelectric figure-of-merit in nanostructured p-type silicon germanium bulk alloys," Nano Letters, vol. 8, no. 12, pp. 4670–4674, 2008.

[63] A. J. Minnich, H. Lee, X. W. Wang, G. Joshi, M. S. Dresselhaus, Z. F. Ren, G. Chen, and D. Vashaee, "Modeling study of thermoelectric SiGe nanocomposites," Phys. Rev. B, vol. 80, p. 155327, 2009.

[64] Y. Pei, J. Lensch-Falk, E. S. Toberer, D. L. Medlin, and G. J. Snyder, "High thermoelectric performance in PbTe due to large nanoscale Ag_2Te precipitates and La doping," Advanced Functional Materials, vol. 21, no. 2, pp. 241–249, 2011.

[65] L.-D. Zhao, S.-H. Lo, Y. Zhang, H. Sun, G. Tan, C. Uher, C. Wolverton, V. P. Dravid, and M. G. Kanatzidis, "Ultralow thermal conductivity and high thermoelectric figure of merit in SnSe crystals," Nature, vol. 508, no. 7496, pp. 373–377, 2014.

[66] L.-D. Zhao, G. Tan, S. Hao, J. He, Y. Pei, H. Chi, H. Wang, S. Gong, H. Xu, V. P. Dravid, C. Uher, G. J. Snyder, C. Wolverton, and M. G. Kanatzidis, "Ultrahigh power factor and thermoelectric performance in hole-doped single-crystal SnSe," Science, vol. 351, no. 6269, pp. 141–144, 2016.

[67] P.-C. Wei, S. Bhattacharya, J. He, S. Neeleshwar, R. Podila, Y. Y. Chen, and A. M. Rao, "The intrinsic thermal conductivity of SnSe," Nature, vol. 539, no. 7627, pp. E1–E2, 2016.

[68] J. He and T. M. Tritt, "Advances in thermoelectric materials research: Looking back and moving forward," Science, vol. 357, no. 6358, 2017.

[69] D. Champier, "Thermoelectric generators: A review of applications," Energy Conversion and Management, vol. 140, pp. 167 – 181, 2017.

[70] L. D. Hicks and M. S. Dresselhaus, "Effect of quantum-well structures on the thermoelectric figure of merit," Phys. Rev. B, vol. 47, pp. 12727–12731, 1993.

[71] L. D. Hicks and M. S. Dresselhaus, "Thermoelectric figure of merit of a one-dimensional conductor," Phys. Rev. B, vol. 47, pp. 16631–16634, 1993.

[72] T. Feng and X. Ruan, "Ultra-low thermal conductivity in graphene nanomesh," Carbon, vol. 101, pp. 107–113, 2016.

[73] S. Timpa, J. Rastikian, S. Suffit, P. Lafarge, C. Barraud, and M. Della Rocca, "Strongly reduced thermal conductivity of supported multilayer-graphene nanowires," Phys. Rev. Applied, vol. 14, p. 014056, 2020.

[74] H. Schmidt, F. Giustiniano, and G. Eda, "Electronic transport properties of transition metal dichalcogenide field-effect devices: Surface and interface effects," Chemical Society Reviews, vol. 44, no. 21, pp. 7715–7736, 2015.

[75] M. Buscema, M. Barkelid, V. Zwiller, H. S. J. van der Zant, G. A. Steele, and A. Castellanos-Gomez, "Large and tunable photothermoelectric effect in single-layer MoS_2," Nano Letters, vol. 13, no. 2, pp. 358–363, 2013.

[76] S. Sahoo, A. P. S. Gaur, M. Ahmadi, M. J.-F. Guinel, and R. S. Katiyar, "Temperature-dependent Raman studies and thermal conductivity of few-layer MoS_2," The Journal of Physical Chemistry C, vol. 117, no. 17, pp. 9042–9047, 2013.

[77] R. Yan, J. R. Simpson, S. Bertolazzi, J. Brivio, M. Watson, X. Wu, A. Kis, T. Luo, A. R. Hight Walker, and H. G. Xing, "Thermal conductivity of monolayer molybdenum disulfide obtained from temperature-dependent Raman spectroscopy," ACS Nano, vol. 8, no. 1, pp. 986–993, 2014.

[78] I. Jo, M. T. Pettes, E. Ou, W. Wu, and L. Shi, "Basal-plane thermal conductivity of few-layer molybdenum disulfide," Applied Physics Letters, vol. 104, no. 20, p. 201902, 2014.

[79] M. Yoshida, T. Iizuka, Y. Saito, M. Onga, R. Suzuki, Y. Zhang, Y. Iwasa, and S. Shimizu, "Gate-optimized thermoelectric power factor in ultrathin WSe_2 single crystals," Nano Letters, vol. 16, no. 3, pp. 2061–2065, 2016.

[80] J. Pu, K. Kanahashi, N. T. Cuong, C.-H. Chen, L.-J. Li, S. Okada, H. Ohta, and T. Takenobu, "Enhanced thermoelectric power in two-dimensional transition metal dichalcogenide monolayers," Phys. Rev. B, vol. 94, p. 014312, 2016.

[81] C. Chiritescu, D. G. Cahill, N. Nguyen, D. Johnson, A. Bodapati, P. Keblinski, and P. Zschack, "Ultralow thermal conductivity in disordered, layered WSe_2 crystals," Science, vol. 315, no. 5810, pp. 351–353, 2007.

[82] P. Norouzzadeh and D. J. Singh, "Thermal conductivity of single-layer WSe_2 by a Stillinger-Weber potential," Nanotechnology, vol. 28, no. 7, p. 075708, 2017.

[83] T. Kodama, Woosung Park, A. Marconnet, J. Lee, M. Asheghi, and K. E. Goodson, "In-plane thermal conductivity measurement on nanoscale conductive materials with on-substrate device configuration," 13^{th} InterSociety Conference on Thermal and Thermomechanical Phenomena in Electronic Systems, pp. 250–255, 2012.

[84] Y. Xu, Z. Li, and W. Duan, "Thermal and thermoelectric properties of graphene," Small, vol. 10, no. 11, pp. 2182–2199, 2014.

[85] E. Pop, V. Varshney, and A. K. Roy, "Thermal properties of graphene: Fundamentals and applications," MRS Bulletin, vol. 37, no. 12, p. 1273–1281, 2012.

[86] J. Wu, Y. Chen, J. Wu, and K. Hippalgaonkar, "Perspectives on thermoelectricity in layered and 2D materials," Advanced Electronic Materials, vol. 4, no. 12, p. 1800248, 2018.

[87] V.-T. Tran, J. Saint-Martin, P. Dollfus, and S. Volz, "Optimizing the thermoelectric performance of graphene nano-ribbons without degrading the electronic properties," Scientific Reports, vol. 7, no. 1, p. 2313, 2017.

[88] Z. G. Fthenakis and D. Tománek, "Computational study of the thermal conductivity in defective carbon nanostructures," Phys. Rev. B, vol. 86, p. 125418, 2012.

[89] F. Hao, D. Fang, and Z. Xu, "Mechanical and thermal transport properties of graphene with defects," Applied Physics Letters, vol. 99, no. 4, p. 041901, 2011.

[90] C. Wang, Y. Liu, L. Li, and H. Tan, "Anisotropic thermal conductivity of graphene wrinkles," Nanoscale, vol. 6, pp. 5703–5707, 2014.

[91] Y. Anno, Y. Imakita, K. Takei, S. Akita, and T. Arie, "Enhancement of graphene thermoelectric performance through defect engineering," 2D Materials, vol. 4, no. 2, p. 025019, 2017.

[92] S. Chen, Q. Wu, C. Mishra, J. Kang, H. Zhang, K. Cho, W. Cai, A. A. Balandin, and R. S. Ruoff, "Thermal conductivity of isotopically modified graphene," Nature Materials, vol. 11, no. 3, pp. 203–207, 2012.

[93] J. J. Urban, A. K. Menon, Z. Tian, A. Jain, and K. Hippalgaonkar, "New horizons in thermoelectric materials: Correlated electrons, organic transport, machine learning, and more," Journal of Applied Physics, vol. 125, no. 18, p. 180902, 2019.

[94] L. Wang, Z. Zhang, Y. Liu, B. Wang, L. Fang, J. Qiu, K. Zhang, and S. Wang, "Exceptional thermoelectric properties of flexible organicinorganic hybrids with monodispersed and periodic nanophase," Nature Communications, vol. 9, no. 1, p. 3817, 2018.

[95] A. J. Minnich, M. S. Dresselhaus, Z. F. Ren, and G. Chen, "Bulk nanostructured thermoelectric materials: Current research and future prospects," Energy Environ. Sci., vol. 2, pp. 466–479, 2009.

[96] M. Cutler and N. F. Mott, "Observation of anderson localization in an electron gas," Phys. Rev., vol. 181, pp. 1336–1340, 1969.

[97] J. Wu, Y. Liu, Y. Liu, Y. Cai, Y. Zhao, H. K. Ng, K. Watanabe, T. Taniguchi, G. Zhang, C.-W. Qiu, D. Chi, A. H. C. Neto, J. T. L. Thong, K. P. Loh, and K. Hippalgaonkar, "Large enhancement of thermoelectric performance in MoS_2/hBN heterostructure due to vacancy-induced band hybridization," Proceedings of the National Academy of Sciences, vol. 117, no. 25, pp. 13929–13936, 2020.

[98] C. Wood, "Materials for thermoelectric energy conversion," Reports on Progress in Physics, vol. 51, no. 4, pp. 459–539, 1988.

[99] C. B. Satterthwaite and R. W. Ure, "Electrical and thermal properties of Bi_2Te_3," Phys. Rev., vol. 108, pp. 1164–1170, 1957.

[100] S. Lee, J. A. Bock, S. Trolier-McKinstry, and C. A. Randall, "Ferroelectric-thermoelectricity and Mott transition of ferroelectric oxides with high electronic conductivity," Journal of the European Ceramic Society, vol. 32, no. 16, pp. 3971 – 3988, 2012.

[101] D. Li, Y. Gong, Y. Chen, J. Lin, Q. Khan, Y. Zhang, Y. Li, H. Zhang, and H. Xie, "Recent progress of two-dimensional thermoelectric materials," Nano-Micro Letters, vol. 12, no. 1, p. 36, 2020.

[102] G. Zhang and Y.-W. Zhang, "Thermoelectric properties of two-dimensional transition metal dichalcogenides," J. Mater. Chem. C, vol. 5, pp. 7684–7698, 2017.

[103] W. Huang, X. Luo, C. K. Gan, S. Y. Quek, and G. Liang, "Theoretical study of thermoelectric properties of few-layer MoS_2 and WSe_2," Phys. Chem. Chem. Phys., vol. 16, pp. 10866–10874, 2014.

[104] D. Wickramaratne, F. Zahid, and R. K. Lake, "Electronic and thermoelectric properties of few-layer transition metal dichalcogenides," The Journal of Chemical Physics, vol. 140, no. 12, p. 124710, 2014.

[105] A. Harzheim, C. Evangeli, O. V. Kolosov, and P. Gehring, "Direct mapping of local Seebeck coefficient in 2D material nanostructures via scanning thermal gate microscopy," 2D Materials, vol. 7, no. 4, p. 041004, 2020.

[106] J. Wu, H. Schmidt, K. K. Amara, X. Xu, G. Eda, and B. Özyilmaz, "Large thermoelectricity via variable range hopping in chemical vapor deposition grown single-layer MoS_2," Nano Letters, vol. 14, no. 5, pp. 2730–2734, 2014.

[107] T. Mueller, F. Xia, M. Freitag, J. Tsang, and P. Avouris, "Role of contacts in graphene transistors: A scanning photocurrent study," Phys. Rev. B, vol. 79, p. 245430, 2009.

[108] C. Lee, X. Wei, J. W. Kysar, and J. Hone, "Measurement of the elastic properties and intrinsic strength of monolayer graphene," Science, vol. 321, no. 5887, pp. 385–388, 2008.

[109] D. L. Nika, S. Ghosh, E. P. Pokatilov, and A. A. Balandin, "Lattice thermal conductivity of graphene flakes: Comparison with bulk graphite," Applied Physics Letters, vol. 94, no. 20, p. 203103, 2009.

[110] J. H. Seol, I. Jo, A. L. Moore, L. Lindsay, Z. H. Aitken, M. T. Pettes, X. Li, Z. Yao, R. Huang, D. Broido, N. Mingo, R. S. Ruoff, and L. Shi, "Two-dimensional phonon transport in supported graphene," Science, vol. 328, no. 5975, pp. 213–216, 2010.

[111] E. Muñoz, J. Lu, and B. I. Yakobson, "Ballistic thermal conductance of graphene ribbons," Nano Letters, vol. 10, no. 5, pp. 1652–1656, 2010.

[112] W. Jang, Z. Chen, W. Bao, C. N. Lau, and C. Dames, "Thickness-dependent thermal conductivity of encased graphene and ultrathin graphite," Nano Letters, vol. 10, no. 10, pp. 3909–3913, 2010.

[113] A. D. Liao, J. Z. Wu, X. Wang, K. Tahy, D. Jena, H. Dai, and E. Pop, "Thermally limited current carrying ability of graphene nanoribbons," Phys. Rev. Lett., vol. 106, p. 256801, 2011.

[114] Y. M. Zuev, W. Chang, and P. Kim, "Thermoelectric and magnetothermoelectric transport measurements of graphene," Phys. Rev. Lett., vol. 102, p. 096807, 2009.

[115] J. Martin, N. Akerman, G. Ulbricht, T. Lohmann, J. H. Smet, K. von Klitzing, and A. Yacoby, "Observation of electron-hole puddles in graphene using a scanning single-electron transistor," Nature Physics, vol. 4, no. 2, pp. 144–148, 2008.

[116] E. Y. Andrei, G. Li, and X. Du, "Electronic properties of graphene: A perspective from scanning tunneling microscopy and magnetotransport," Reports on Progress in Physics, vol. 75, no. 5, p. 056501, 2012.

[117] X. Li, J. Yin, J. Zhou, Q. Wang, and W. Guo, "Exceptional high Seebeck coefficient and gas-flow-induced voltage in multilayer graphene," Applied Physics Letters, vol. 100, no. 18, p. 183108, 2012.

[118] S. Ryu, L. Liu, S. Berciaud, Y.-J. Yu, H. Liu, P. Kim, G. W. Flynn, and L. E. Brus, "Atmospheric oxygen binding and hole doping in deformed graphene on a SiO_2 substrate," Nano Letters, vol. 10, no. 12, pp. 4944–4951, 2010.

[119] Y. Yang and R. Murali, "Binding mechanisms of molecular oxygen and moisture to graphene," Applied Physics Letters, vol. 98, no. 9, p. 093116, 2011.

[120] J. C. Slater, G. F. Koster, and J. H. Wood, "Symmetry and free electron properties of the gallium energy bands," Phys. Rev., vol. 126, pp. 1307–1317, 1962.

[121] L. Cartz, S. R. Srinivasa, R. J. Riedner, J. D. Jorgensen, and T. G. Worlton, "Effect of pressure on bonding in black phosphorus," The Journal of Chemical Physics, vol. 71, no. 4, pp. 1718–1721, 1979.

[122] Z.-Y. Ong, Y. Cai, G. Zhang, and Y.-W. Zhang, "Strong thermal transport anisotropy and strain modulation in single-layer phosphorene," The Journal of Physical Chemistry C, vol. 118, no. 43, pp. 25272–25277, 2014.

[123] L. Li, Y. Yu, G. J. Ye, Q. Ge, X. Ou, H. Wu, D. Feng, X. H. Chen, and Y. Zhang, "Black phosphorus field-effect transistors," Nature Nanotechnology, vol. 9, no. 5, pp. 372–377, 2014.

[124] H. Liu, A. T. Neal, Z. Zhu, Z. Luo, X. Xu, D. Tománek, and P. D. Ye, "Phosphorene: an unexplored 2D semiconductor with a high hole mobility," ACS Nano, vol. 8, no. 4, pp. 4033–4041, 2014.

[125] S. P. Koenig, R. A. Doganov, H. Schmidt, A. H. Castro Neto, and B. Özyilmaz, "Electric field effect in ultrathin black phosphorus," Applied Physics Letters, vol. 104, no. 10, p. 103106, 2014.

[126] M. Buscema, D. J. Groenendijk, G. A. Steele, H. S. J. van der Zant, and A. Castellanos-Gomez, "Photovoltaic effect in few-layer black phosphorus PN junctions defined by local electrostatic gating," Nature Communications, vol. 5, no. 1, p. 4651, 2014.

[127] S. Das, M. Demarteau, and A. Roelofs, "Ambipolar phosphorene field effect transistor," ACS Nano, vol. 8, no. 11, pp. 11730–11738, 2014.

[128] R. Fei, A. Faghaninia, R. Soklaski, J.-A. Yan, C. Lo, and L. Yang, "Enhanced thermoelectric efficiency via orthogonal electrical and thermal conductances in phosphorene," Nano Letters, vol. 14, no. 11, pp. 6393–6399, 2014.

[129] A. Jain and A. J. H. McGaughey, "Strongly anisotropic in-plane thermal transport in single-layer black phosphorene," Scientific Reports, vol. 5, no. 1, p. 8501, 2015.

[130] Z. Luo, J. Maassen, Y. Deng, Y. Du, R. P. Garrelts, M. S. Lundstrom, P. D. Ye, and X. Xu, "Anisotropic in-plane thermal conductivity observed in few-layer black phosphorus," Nature Communications, vol. 6, no. 1, p. 8572, 2015.

[131] Y. Saito, T. Iizuka, T. Koretsune, R. Arita, S. Shimizu, and Y. Iwasa, "Gate-tuned thermoelectric power in black phosphorus," Nano Letters, vol. 16, no. 8, pp. 4819–4824, 2016.

[132] H. T. Yuan, M. Toh, K. Morimoto, W. Tan, F. Wei, H. Shimotani, C. Kloc, and Y. Iwasa, "Liquid-gated electric-double-layer transistor on layered metal dichalcogenide, SnS_2," Applied Physics Letters, vol. 98, no. 1, p. 012102, 2011.

[133] E. Flores, J. R. Ares, A. Castellanos-Gomez, M. Barawi, I. J. Ferrer, and C. Sánchez, "Thermoelectric power of bulk black-phosphorus," Applied Physics Letters, vol. 106, no. 2, p. 022102, 2015.

[134] S. J. Choi, B.-K. Kim, T.-H. Lee, Y. H. Kim, Z. Li, E. Pop, J.-J. Kim, J. H. Song, and M.-H. Bae, "Electrical and thermoelectric transport by variable range hopping in thin black phosphorus devices," Nano Letters, vol. 16, no. 7, pp. 3969–3975, 2016.

[135] J. Xue, S. Huang, J.-Y. Wang, and H. Q. Xu, "Mott variable-range hopping transport in a MoS_2 nanoflake," RSC Adv., vol. 9, pp. 17885–17890, 2019.

[136] M. Kayyalha, J. Maassen, M. Lundstrom, L. Shi, and Y. P. Chen, "Gate-tunable and thickness-dependent electronic and thermoelectric transport in few-layer MoS_2," Journal of Applied Physics, vol. 120, no. 13, p. 134305, 2016.

[137] K. Hippalgaonkar, Y. Wang, Y. Ye, D. Y. Qiu, H. Zhu, Y. Wang, J. Moore, S. G. Louie, and X. Zhang, "High thermoelectric power factor in two-dimensional crystals of MoS_2," Phys. Rev. B, vol. 95, p. 115407, 2017.

[138] W. Kim, H. Kim, T. Hallam, N. McEvoy, R. Gatensby, H. C. Nerl, K. O'Neill, R. Siris, G.-T. Kim, and G. S. Duesberg, "Field-dependent electrical and thermal transport in polycrystalline WSe_2," Advanced Materials Interfaces, vol. 5, no. 11, p. 1701161, 2018.

[139] X. Gu and R. Yang, "First-principles prediction of phononic thermal conductivity of silicene: A comparison with graphene," Journal of Applied Physics, vol. 117, no. 2, p. 025102, 2015.

[140] Y. Cai, J. Lan, G. Zhang, and Y.-W. Zhang, "Lattice vibrational modes and phonon thermal conductivity of monolayer MoS_2," Phys. Rev. B, vol. 89, p. 035438, 2014.

[141] S. Ghosh, I. Calizo, D. Teweldebrhan, E. P. Pokatilov, D. L. Nika, A. A. Balandin, W. Bao, F. Miao, and C. N. Lau, "Extremely high thermal conductivity of graphene: Prospects for thermal management applications in nanoelectronic circuits," Applied Physics Letters, vol. 92, no. 15, p. 151911, 2008.

[142] A. A. Balandin, "Thermal properties of graphene and nanostructured carbon materials," Nature Materials, vol. 10, no. 8, pp. 569–581, 2011.

[143] M.-H. Bae, Z. Li, Z. Aksamija, P. N. Martin, F. Xiong, Z.-Y. Ong, I. Knezevic, and E. Pop, "Ballistic to diffusive crossover of heat flow in graphene ribbons," Nature Communications, vol. 4, no. 1, p. 1734, 2013.

[144] P. N. Martin, Z. Aksamija, E. Pop, and U. Ravaioli, "Reduced thermal conductivity in nanoengineered rough Ge and GaAs nanowires," Nano Letters, vol. 10, no. 4, pp. 1120–1124, 2010.

[145] J. Sadhu and S. Sinha, "Room-temperature phonon boundary scattering below the Casimir limit," Phys. Rev. B, vol. 84, p. 115450, 2011.

[146] A. A. Balandin, S. Ghosh, W. Bao, I. Calizo, D. Teweldebrhan, F. Miao, and C. N. Lau, "Superior thermal conductivity of single-layer graphene," Nano Letters, vol. 8, no. 3, pp. 902–907, 2008.

[147] W. Cai, A. L. Moore, Y. Zhu, X. Li, S. Chen, L. Shi, and R. S. Ruoff, "Thermal transport in suspended and supported monolayer graphene grown by chemical vapor deposition," Nano Letters, vol. 10, no. 5, pp. 1645–1651, 2010.

[148] Z. L. Wang, D. W. Tang, X. B. Li, X. H. Zheng, W. G. Zhang, L. X. Zheng, Y. T. Zhu, A. Z. Jin, H. F. Yang, and C. Z. Gu, "Length-dependent thermal conductivity of an individual single-wall carbon nanotube," Applied Physics Letters, vol. 91, no. 12, p. 123119, 2007.

[149] J. L. Braun, D. H. Olson, J. T. Gaskins, and P. E. Hopkins, "A steady-state thermoreflectance method to measure thermal conductivity," Review of Scientific Instruments, vol. 90, no. 2, p. 024905, 2019.

[150] H. R. Barnard, E. Zossimova, N. H. Mahlmeister, L. M. Lawton, I. J. Luxmoore, and G. R. Nash, "Boron nitride encapsulated graphene infrared emitters," Applied Physics Letters, vol. 108, no. 13, p. 131110, 2016.

[151] E. Pop, D. A. Mann, K. E. Goodson, and H. Dai, "Electrical and thermal transport in metallic single-wall carbon nanotubes on insulating substrates," Journal of Applied Physics, vol. 101, no. 9, p. 093710, 2007.

[152] D. G. Cahill, "Thermal conductivity measurement from 30 to 750K: the 3ω method," Review of Scientific Instruments, vol. 61, no. 2, pp. 802–808, 1990.

[153] D. Zhao, X. Qian, X. Gu, S. A. Jajja, and R. Yang, "Measurement techniques for thermal conductivity and interfacial thermal conductance of bulk and thin film materials," Journal of Electronic Packaging, vol. 138, no. 4, 2016.

[154] M. D. Losego, M. E. Grady, N. R. Sottos, D. G. Cahill, and P. V. Braun, "Effects of chemical bonding on heat transport across interfaces," Nature Materials, vol. 11, no. 6, pp. 502–506, 2012.

[155] H.-K. Lyeo and D. G. Cahill, "Thermal conductance of interfaces between highly dissimilar materials," Phys. Rev. B, vol. 73, p. 144301, 2006.

[156] P. Jiang, X. Qian, and R. Yang, "Tutorial: Time-domain thermoreflectance (TDTR) for thermal property characterization of bulk and thin film materials," Journal of Applied Physics, vol. 124, no. 16, p. 161103, 2018.

[157] Z. Wang, R. Xie, C. T. Bui, D. Liu, X. Ni, B. Li, and J. T. L. Thong, "Thermal transport in suspended and supported few-layer graphene," Nano Letters, vol. 11, no. 1, pp. 113–118, 2011.

[158] V. E. Dorgan, A. Behnam, H. J. Conley, K. I. Bolotin, and E. Pop, "High-field electrical and thermal transport in suspended graphene," Nano Letters, vol. 13, no. 10, pp. 4581–4586, 2013.

[159] L. Lindsay, D. A. Broido, and N. Mingo, "Flexural phonons and thermal transport in multilayer graphene and graphite," Phys. Rev. B, vol. 83, p. 235428, 2011.

[160] S. Yiğen, V. Tayari, J. O. Island, J. M. Porter, and A. R. Champagne, "Electronic thermal conductivity measurements in intrinsic graphene," Phys. Rev. B, vol. 87, p. 241411, 2013.

[161] S. Chen, A. L. Moore, W. Cai, J. W. Suk, J. An, C. Mishra, C. Amos, C. W. Magnuson, J. Kang, L. Shi, and R. S. Ruoff, "Raman measurements of thermal transport in suspended monolayer graphene of variable sizes in vacuum and gaseous environments," ACS Nano, vol. 5, no. 1, pp. 321–328, 2011.

[162] J.-U. Lee, D. Yoon, H. Kim, S. W. Lee, and H. Cheong, "Thermal conductivity of suspended pristine graphene measured by Raman spectroscopy," Phys. Rev. B, vol. 83, p. 081419, 2011.

[163] C. Faugeras, B. Faugeras, M. Orlita, M. Potemski, R. R. Nair, and A. K. Geim, "Thermal conductivity of graphene in corbino membrane geometry," ACS Nano, vol. 4, no. 4, pp. 1889–1892, 2010.

[164] M. T. Pettes, I. Jo, Z. Yao, and L. Shi, "Influence of polymeric residue on the thermal conductivity of suspended bilayer graphene," Nano Letters, vol. 11, no. 3, pp. 1195–1200, 2011.

[165] C. Y. Ho, R. W. Powell, and P. E. Liley, "Thermal conductivity of the elements," Journal of Physical and Chemical Reference Data, vol. 1, no. 2, pp. 279–421, 1972.

[166] E. Pop, D. Mann, Q. Wang, K. Goodson, and H. Dai, "Thermal conductance of an individual single-wall carbon nanotube above room temperature," Nano Letters, vol. 6, no. 1, pp. 96–100, 2006.

[167] P. Kim, L. Shi, A. Majumdar, and P. L. McEuen, "Thermal transport measurements of individual multiwalled nanotubes," Phys. Rev. Lett., vol. 87, p. 215502, 2001.

[168] L. Lindsay and D. A. Broido, "Enhanced thermal conductivity and isotope effect in single-layer hexagonal boron nitride," Phys. Rev. B, vol. 84, p. 155421, 2011.

[169] C. Wang, J. Guo, L. Dong, A. Aiyiti, X. Xu, and B. Li, "Superior thermal conductivity in suspended bilayer hexagonal boron nitride," Scientific Reports, vol. 6, no. 1, p. 25334, 2016.

[170] I. Jo, M. T. Pettes, J. Kim, K. Watanabe, T. Taniguchi, Z. Yao, and L. Shi, "Thermal conductivity and phonon transport in suspended few-layer hexagonal boron nitride," Nano Letters, vol. 13, no. 2, pp. 550–554, 2013.

[171] H. Zhou, J. Zhu, Z. Liu, Z. Yan, X. Fan, J. Lin, G. Wang, Q. Yan, T. Yu, P. M. Ajayan, and J. M. Tour, "High thermal conductivity of suspended few-layer hexagonal boron nitride sheets," Nano Research, vol. 7, no. 8, pp. 1232–1240, 2014.

[172] E. K. Sichel, R. E. Miller, M. S. Abrahams, and C. J. Buiocchi, "Heat capacity and thermal conductivity of hexagonal pyrolytic boron nitride," Phys. Rev. B, vol. 13, pp. 4607–4611, 1976.

[173] C. W. Chang, A. M. Fennimore, A. Afanasiev, D. Okawa, T. Ikuno, H. Garcia, D. Li, A. Majumdar, and A. Zettl, "Isotope effect on the thermal conductivity of boron nitride nanotubes," Phys. Rev. Lett., vol. 97, p. 085901, 2006.

[174] S. Lee, F. Yang, J. Suh, S. Yang, Y. Lee, G. Li, H. Sung Choe, A. Suslu, Y. Chen, C. Ko, J. Park, K. Liu, J. Li, K. Hippalgaonkar, J. J. Urban, S. Tongay, and J. Wu, "Anisotropic in-plane thermal conductivity of black phosphorus nanoribbons at temperatures higher than 100 K," Nature Communications, vol. 6, no. 1, p. 8573, 2015.

[175] Y. Wang, N. Xu, D. Li, and J. Zhu, "Thermal properties of two dimensional layered materials," Advanced Functional Materials, vol. 27, no. 19, p. 1604134, 2017.

[176] J. Liu, G.-M. Choi, and D. G. Cahill, "Measurement of the anisotropic thermal conductivity of molybdenum disulfide by the time-resolved magneto-optic Kerr effect," Journal of Applied Physics, vol. 116, no. 23, p. 233107, 2014.

[177] A. Mavrokefalos, N. T. Nguyen, M. T. Pettes, D. C. Johnson, and L. Shi, "In-plane thermal conductivity of disordered layered WSe_2 and $(W)_x(WSe_2)_y$ superlattice films," Applied Physics Letters, vol. 91, no. 17, p. 171912, 2007.

[178] W.-X. Zhou and K.-Q. Chen, "First-principles determination of ultralow thermal conductivity of monolayer WSe_2," Scientific Reports, vol. 5, no. 1, p. 15070, 2015.

[179] N. Peimyoo, J. Shang, W. Yang, Y. Wang, C. Cong, and T. Yu, "Thermal conductivity determination of suspended mono- and bilayer WS_2 by Raman spectroscopy," Nano Research, vol. 8, no. 4, pp. 1210–1221, 2015.

[180] Z. Yan, C. Jiang, T. R. Pope, C. F. Tsang, J. L. Stickney, P. Goli, J. Renteria, T. T. Salguero, and A. A. Balandin, "Phonon and thermal properties of exfoliated $TaSe_2$ thin films," Journal of Applied Physics, vol. 114, no. 20, p. 204301, 2013.

[181] C. J. Glassbrenner and G. A. Slack, "Thermal conductivity of silicon and germanium from 3K to the melting point," Phys. Rev., vol. 134, pp. A1058–A1069, 1964.

[182] H. R. Shanks, P. D. Maycock, P. H. Sidles, and G. C. Danielson, "Thermal conductivity of silicon from 300 to 1400 K," Phys. Rev., vol. 130, pp. 1743–1748, 1963.

[183] J. Kimling, A. Philippi-Kobs, J. Jacobsohn, H. P. Oepen, and D. G. Cahill, "Thermal conductance of interfaces with amorphous SiO_2 measured by time-resolved magneto-optic Kerr-effect thermometry," Phys. Rev. B, vol. 95, p. 184305, 2017.

[184] Z. Chen, W. Jang, W. Bao, C. N. Lau, and C. Dames, "Thermal contact resistance between graphene and silicon dioxide," Applied Physics Letters, vol. 95, no. 16, p. 161910, 2009.

[185] S. Vaziri, E. Yalon, M. Muñoz Rojo, S. V. Suryavanshi, H. Zhang, C. J. McClellan, C. S. Bailey, K. K. H. Smithe, A. J. Gabourie, V. Chen, S. Deshmukh, L. Bendersky, A. V. Davydov, and E. Pop, "Ultrahigh thermal isolation across heterogeneously layered two-dimensional materials," Science Advances, vol. 5, no. 8, 2019.

[186] X. Tang, S. Xu, J. Zhang, and X. Wang, "Five orders of magnitude reduction in energy coupling across corrugated graphene/substrate interfaces," ACS Applied Materials & Interfaces, vol. 6, no. 4, pp. 2809–2818, 2014.

[187] V. Geringer, M. Liebmann, T. Echtermeyer, S. Runte, M. Schmidt, R. Rückamp, M. C. Lemme, and M. Morgenstern, "Intrinsic and extrinsic corrugation of monolayer graphene deposited on SiO_2," Phys. Rev. Lett., vol. 102, p. 076102, 2009.

[188] H. G. Kim, K. D. Kihm, W. Lee, G. Lim, S. Cheon, W. Lee, K. R. Pyun, S. H. Ko, and S. Shin, "Effect of graphene-substrate conformity on the in-plane thermal conductivity of supported graphene," Carbon, vol. 125, pp. 39 – 48, 2017.

[189] Y. Huang, E. Sutter, N. N. Shi, J. Zheng, T. Yang, D. Englund, H.-J. Gao, and P. Sutter, "Reliable exfoliation of large-area high-quality flakes of graphene and other two-dimensional materials," ACS Nano, vol. 9, no. 11, pp. 10612–10620, 2015.

[190] Y. Yu, T. Minhaj, L. Huang, Y. Yu, and L. Cao, "In-plane and interfacial thermal conduction of two-dimensional transition-metal dichalcogenides," Phys. Rev. Applied, vol. 13, p. 034059, 2020.

[191] C. Huo, Z. Yan, X. Song, and H. Zeng, "2D materials via liquid exfoliation: a review on fabrication and applications," Science Bulletin, vol. 60, no. 23, pp. 1994–2008, 2015.

[192] G. Li, Y.-Y. Zhang, H. Guo, L. Huang, H. Lu, X. Lin, Y.-L. Wang, S. Du, and H.-J. Gao, "Epitaxial growth and physical properties of 2D materials beyond graphene: From monatomic materials to binary compounds," Chem. Soc. Rev., vol. 47, pp. 6073–6100, 2018.

[193] H. Li, Y. Li, A. Aljarb, Y. Shi, and L.-J. Li, "Epitaxial growth of two-dimensional layered transition-metal dichalcogenides: Growth mechanism, controllability, and scalability," Chemical Reviews, vol. 118, no. 13, pp. 6134–6150, 2018.

[194] Y. Huang, Y.-H. Pan, R. Yang, L.-H. Bao, L. Meng, H.-L. Luo, Y.-Q. Cai, G.-D. Liu, W.-J. Zhao, Z. Zhou, L.-M. Wu, Z.-L. Zhu, M. Huang, L.-W. Liu, L. Liu, P. Cheng, K.-H. Wu, S.-B. Tian, C.-Z. Gu, Y.-G. Shi, Y.-F. Guo, Z. G. Cheng, J.-P. Hu, L. Zhao, G.-H. Yang, E. Sutter, P. Sutter, Y.-L. Wang, W. Ji, X.-J. Zhou, and H.-J. Gao, "Universal mechanical exfoliation of large-area 2D crystals," Nature Communications, vol. 11, no. 1, p. 2453, 2020.

[195] P. Y. Huang, C. S. Ruiz-Vargas, A. M. van der Zande, W. S. Whitney, M. P. Levendorf, J. W. Kevek, S. Garg, J. S. Alden, C. J. Hustedt, Y. Zhu, J. Park, P. L. McEuen, and D. A. Muller, "Grains and grain boundaries in single-layer graphene atomic patchwork quilts," Nature, vol. 469, no. 7330, pp. 389–392, 2011.

[196] M. M. Benameur, B. Radisavljevic, J. S. Héron, S. Sahoo, H. Berger, and A. Kis, "Visibility of dichalcogenide nanolayers," Nanotechnology, vol. 22, no. 12, p. 125706, 2011.

[197] T.-H. Le, Y. Oh, H. Kim, and H. Yoon, "Exfoliation of 2D materials for energy and environmental applications," Chemistry – A European Journal, vol. 26, no. 29, pp. 6360–6401, 2020.

[198] N. Petrone, C. R. Dean, I. Meric, A. M. van der Zande, P. Y. Huang, L. Wang, D. Muller, K. L. Shepard, and J. Hone, "Chemical vapor deposition-derived graphene with electrical performance of exfoliated graphene," Nano Letters, vol. 12, no. 6, pp. 2751–2756, 2012.

[199] F. Pizzocchero, L. Gammelgaard, B. S. Jessen, J. M. Caridad, L. Wang, J. Hone, P. Bøggild, and T. J. Booth, "The hot pick-up technique for batch assembly of van der Waals heterostructures," Nature Communications, vol. 7, no. 1, p. 11894, 2016.

[200] W. Pan, J. Xiao, J. Zhu, C. Yu, G. Zhang, Z. Ni, K. Watanabe, T. Taniguchi, Y. Shi, and X. Wang, "Biaxial compressive strain engineering in graphene/boron nitride heterostructures," Scientific Reports, vol. 2, no. 1, p. 893, 2012.

[201] A. V. Kretinin, Y. Cao, J. S. Tu, G. L. Yu, R. Jalil, K. S. Novoselov, S. J. Haigh, A. Gholinia, A. Mishchenko, M. Lozada, T. Georgiou, C. R. Woods, F. Withers, P. Blake, G. Eda, A. Wirsig, C. Hucho, K. Watanabe, T. Taniguchi, A. K. Geim, and R. V. Gorbachev, "Electronic properties of graphene encapsulated with different two-dimensional atomic crystals," Nano Letters, vol. 14, no. 6, pp. 3270–3276, 2014.

[202] S. J. Haigh, A. Gholinia, R. Jalil, S. Romani, L. Britnell, D. C. Elias, K. S. Novoselov, L. A. Ponomarenko, A. K. Geim, and R. Gorbachev, "Cross-sectional imaging of individual layers and buried interfaces of graphene-based heterostructures and superlattices," Nature Materials, vol. 11, no. 9, pp. 764–767, 2012.

[203] A. Castellanos-Gomez, M. Buscema, R. Molenaar, V. Singh, L. Janssen, H. S. J. van der Zant, and G. A. Steele, "Deterministic transfer of two-dimensional materials by all-dry viscoelastic stamping," 2D Materials, vol. 1, no. 1, p. 011002, 2014.

[204] G. F. Schneider, V. E. Calado, H. Zandbergen, L. M. K. Vandersypen, and C. Dekker, "Wedging transfer of nanostructures," Nano Letters, vol. 10, no. 5, pp. 1912–1916, 2010.

[205] G. A. Luinstra and E. Borchardt, Material Properties of Poly(Propylene Carbonates). Berlin, Heidelberg: Springer Berlin Heidelberg, 2012.

[206] R. C. Cooper, C. Lee, C. A. Marianetti, X. Wei, J. Hone, and J. W. Kysar, "Nonlinear elastic behavior of two-dimensional molybdenum disulfide," Phys. Rev. B, vol. 87, p. 035423, 2013.

[207] D. Akinwande, C. J. Brennan, J. S. Bunch, P. Egberts, J. R. Felts, H. Gao, R. Huang, J.-S. Kim, T. Li, Y. Li, K. M. Liechti, N. Lu, H. S. Park, E. J. Reed, P. Wang, B. I. Yakobson, T. Zhang, Y.-W. Zhang, Y. Zhou, and Y. Zhu, "A review on mechanics and mechanical properties of 2D materials - graphene and beyond," Extreme Mechanics Letters, vol. 13, pp. 42–77, 2017.

[208] J. J. Schwartz, H.-J. Chuang, M. R. Rosenberger, S. V. Sivaram, K. M. McCreary, B. T. Jonker, and A. Centrone, "Chemical identification of interlayer contaminants within van der Waals heterostructures," ACS Applied Materials & Interfaces, vol. 11, no. 28, pp. 25578–25585, 2019.

[209] D. Rhodes, S. H. Chae, R. Ribeiro-Palau, and J. Hone, "Disorder in van der Waals heterostructures of 2D materials," Nature Materials, vol. 18, no. 6, pp. 541–549, 2019.

[210] A. G. F. Garcia, M. Neumann, F. Amet, J. R. Williams, K. Watanabe, T. Taniguchi, and D. Goldhaber-Gordon, "Effective cleaning of hexagonal boron nitride for graphene devices," Nano Letters, vol. 12, no. 9, pp. 4449–4454, 2012.

[211] N. Lindvall, A. Kalabukhov, and A. Yurgens, "Cleaning graphene using atomic force microscope," Journal of Applied Physics, vol. 111, no. 6, p. 064904, 2012.

[212] M. R. Rosenberger, H.-J. Chuang, K. M. McCreary, A. T. Hanbicki, S. V. Sivaram, and B. T. Jonker, "Nano-"squeegee" for the creation of clean 2D material interfaces," ACS Applied Materials & Interfaces, vol. 10, no. 12, pp. 10379–10387, 2018.

[213] L. A. Ponomarenko, A. K. Geim, A. A. Zhukov, R. Jalil, S. V. Morozov, K. S. Novoselov, I. V. Grigorieva, E. H. Hill, V. V. Cheianov, V. I. Fal'ko, K. Watanabe, T. Taniguchi, and R. V. Gorbachev, "Tunable metal-insulator transition in double-layer graphene heterostructures," Nature Physics, vol. 7, no. 12, pp. 958–961, 2011.

[214] L. Wang, I. Meric, P. Y. Huang, Q. Gao, Y. Gao, H. Tran, T. Taniguchi, K. Watanabe, L. M. Campos, D. A. Muller, J. Guo, P. Kim, J. Hone, K. L. Shepard, and C. R. Dean, "One-dimensional electrical contact to a two-dimensional material," Science, vol. 342, no. 6158, pp. 614–617, 2013.

[215] S. Goler, V. Piazza, S. Roddaro, V. Pellegrini, F. Beltram, and P. Pingue, "Self-assembly and electron-beam-induced direct etching of suspended graphene nanostructures," Journal of Applied Physics, vol. 110, no. 6, p. 064308, 2011.

[216] A. Jain, P. Bharadwaj, S. Heeg, M. Parzefall, T. Taniguchi, K. Watanabe, and L. Novotny, "Minimizing residues and strain in 2D materials transferred from PDMS," Nanotechnology, vol. 29, no. 26, p. 265203, 2018.

[217] W. Ma, P. Alonso-González, S. Li, A. Y. Nikitin, J. Yuan, J. Martín-Sánchez, J. Taboada-Gutiérrez, I. Amenabar, P. Li, S. Vélez, C. Tollan, Z. Dai, Y. Zhang, S. Sriram, K. Kalantar-Zadeh, S. T. Lee, R. Hillenbrand, and Q. Bao, "In-plane anisotropic and ultra-low-loss

polaritons in a natural van der Waals crystal," Nature, vol. 562, no. 7728, pp. 557–562, 2018.

[218] M. G. Stanford, P. R. Pudasaini, N. Cross, K. Mahady, A. N. Hoffman, D. G. Mandrus, G. Duscher, M. F. Chisholm, and P. D. Rack, "Tungsten diselenide patterning and nanoribbon formation by gas-assisted focused-helium-ion-beam-induced etching," Small Methods, vol. 1, no. 4, p. 1600060, 2017.

[219] L. F. Voss, C. E. Reinhardt, R. T. Graff, A. M. Conway, R. J. Nikolić, N. Deo, and C. L. Cheung, "Etching of ^{10}boron with SF_6-based electron cyclotron resonance plasmas for pillar-structured thermal neutron detectors," Journal of Electronic Materials, vol. 39, no. 3, pp. 263–267, 2010.

[220] A. Ramasubramaniam, D. Naveh, and E. Towe, "Tunable band gaps in bilayer transition-metal dichalcogenides," Phys. Rev. B, vol. 84, p. 205325, 2011.

[221] M. Kang, B. Kim, S. H. Ryu, S. W. Jung, J. Kim, L. Moreschini, C. Jozwiak, E. Rotenberg, A. Bostwick, and K. S. Kim, "Universal mechanism of band-gap engineering in transition-metal dichalcogenides," Nano Letters, vol. 17, no. 3, pp. 1610–1615, 2017.

[222] S. Sucharitakul, N. J. Goble, U. R. Kumar, R. Sankar, Z. A. Bogorad, F.-C. Chou, Y.-T. Chen, and X. P. A. Gao, "Intrinsic electron mobility exceeding 10^3 cm^2/(V s) in multilayer InSe FETs," Nano Letters, vol. 15, no. 6, pp. 3815–3819, 2015.

[223] Z. Jin, X. Li, J. T. Mullen, and K. W. Kim, "Intrinsic transport properties of electrons and holes in monolayer transition-metal dichalcogenides," Phys. Rev. B, vol. 90, p. 045422, 2014.

[224] L. Cheng and Y. Liu, "What limits the intrinsic mobility of electrons and holes in two dimensional metal dichalcogenides?," Journal of the American Chemical Society, vol. 140, no. 51, pp. 17895–17900, 2018.

[225] I. Lee, S. Rathi, L. Li, D. Lim, M. A. Khan, E. S. Kannan, and G.-H. Kim, "Non-degenerate n-type doping by hydrazine treatment in metal work function engineered WSe_2 field-effect transistor," Nanotechnology, vol. 26, no. 45, p. 455203, 2015.

[226] C. Kim, I. Moon, D. Lee, M. S. Choi, F. Ahmed, S. Nam, Y. Cho, H.-J. Shin, S. Park, and W. J. Yoo, "Fermi level pinning at electrical metal contacts of monolayer molybdenum dichalcogenides," ACS Nano, vol. 11, no. 2, pp. 1588–1596, 2017.

[227] S. Ghatak, A. N. Pal, and A. Ghosh, "Nature of electronic states in atomically thin MoS_2 field-effect transistors," ACS Nano, vol. 5, no. 10, pp. 7707–7712, 2011.

[228] S. Das and J. Appenzeller, "WSe_2 field effect transistors with enhanced ambipolar characteristics," Applied Physics Letters, vol. 103, no. 10, p. 103501, 2013.

[229] S. M. Sze and K. K. Ng, Physics of Semiconductor Devices. Wiley, 2007.

[230] D. J. Frank, Y. Taur, and H. . P. Wong, "Generalized scale length for two-dimensional effects in MOSFETs," IEEE Electron Device Letters, vol. 19, no. 10, pp. 385–387, 1998.

[231] M. Houssa, A. Dimoulas, and A. Molle, 2D Materials for Nanoelectronics. 500 Tips, CRC Press, Taylor & Francis Group, 2016.

[232] A. Prakash and J. Appenzeller, "Bandgap extraction and device analysis of ionic liquid gated WSe_2 Schottky barrier transistors," ACS Nano, vol. 11, no. 2, pp. 1626–1632, 2017.

[233] A. Allain and A. Kis, "Electron and hole mobilities in single-layer WSe_2," ACS Nano, vol. 8, no. 7, pp. 7180–7185, 2014.

[234] Z. Wang, Q. Li, Y. Chen, B. Cui, Y. Li, F. Besenbacher, and M. Dong, "The ambipolar transport behavior of WSe_2 transistors and its analogue circuits," NPG Asia Materials, vol. 10, no. 8, pp. 703–712, 2018.

[235] W. L. Chow, P. Yu, F. Liu, J. Hong, X. Wang, Q. Zeng, C.-H. Hsu, C. Zhu, J. Zhou, X. Wang, J. Xia, J. Yan, Y. Chen, D. Wu, T. Yu, Z. Shen, H. Lin, C. Jin, B. K. Tay, and Z. Liu, "High mobility 2D palladium diselenide field-effect transistors with tunable ambipolar characteristics," Advanced Materials, vol. 29, no. 21, p. 1602969, 2017.

[236] J. Kwon, J.-Y. Lee, Y.-J. Yu, C.-H. Lee, X. Cui, J. Hone, and G.-H. Lee, "Thickness-dependent Schottky barrier height of MoS_2 field-effect transistors," Nanoscale, vol. 9, pp. 6151–6157, 2017.

[237] J. R. Durán Retamal, D. Periyanagounder, J.-J. Ke, M.-L. Tsai, and J.-H. He, "Charge carrier injection and transport engineering in two-dimensional transition metal dichalcogenides," Chem. Sci., vol. 9, pp. 7727–7745, 2018.

[238] S. N. C. Azmi, S. F. A. Rahman, A. Nawabjan, and A. M. Hashim, "Junction properties analysis of silicon back-to-back Schottky diode with reduced graphene oxide Schottky electrodes," Microelectronic Engineering, vol. 196, pp. 32 – 37, 2018.

[239] Y. Taur, J. Wu, and J. Min, "An analytic model for heterojunction tunnel FETs with exponential barrier," IEEE Transactions on Electron Devices, vol. 62, no. 5, pp. 1399–1404, 2015.

[240] K. Kanahashi, J. Pu, and T. Takenobu, "2D materials for large-area flexible thermoelectric devices," Advanced Energy Materials, vol. 10, no. 11, p. 1902842, 2020.

[241] A. Laturia, M. L. Van de Put, and W. G. Vandenberghe, "Dielectric properties of hexagonal boron nitride and transition metal dichalcogenides: From monolayer to bulk," npj 2D Materials and Applications, vol. 2, no. 1, p. 6, 2018.

[242] S. K. Jang, J. Youn, Y. J. Song, and S. Lee, "Synthesis and characterization of hexagonal boron nitride as a gate dielectric," Scientific Reports, vol. 6, no. 1, p. 30449, 2016.

[243] Y. Hattori, T. Taniguchi, K. Watanabe, and K. Nagashio, "Layer-by-layer dielectric breakdown of hexagonal boron nitride," ACS Nano, vol. 9, no. 1, pp. 916–921, 2015.

[244] W.-M. Kang, S. Lee, I.-T. Cho, T. H. Park, H. Shin, C. S. Hwang, C. Lee, B.-G. Park, and J.-H. Lee, "Multi-layer WSe_2 field effect transistor with improved carrier-injection contact by using oxygen plasma treatment," Solid-State Electronics, vol. 140, pp. 2 – 7, 2018.

[245] J. Rastikian, S. Suffit, S. Timpa, P. Martin, P. Lafarge, O. Bezencenet, M. L. Della Rocca, and C. Barraud, "High performance room temperature p-type injection in few-layered tungsten diselenide films from cobalt and palladium contacts," Materials Research Express, vol. 6, no. 12, p. 126307, 2019.

[246] H. C. P. Movva, A. Rai, S. Kang, K. Kim, B. Fallahazad, T. Taniguchi, K. Watanabe, E. Tutuc, and S. K. Banerjee, "High-mobility holes in dual-gated WSe_2 field-effect transistors," ACS Nano, vol. 9, no. 10, pp. 10402–10410, 2015.

[247] N. R. Pradhan, D. Rhodes, S. Memaran, J. M. Poumirol, D. Smirnov, S. Talapatra, S. Feng, N. Perea-Lopez, A. L. Elias, M. Terrones, P. M. Ajayan, and L. Balicas, "Hall and field-effect mobilities in few layered p-WSe_2 field-effect transistors," Scientific Reports, vol. 5, no. 1, pp. 2045–2322, 2015.

[248] Y. Wang, R. X. Yang, R. Quhe, H. Zhong, L. Cong, M. Ye, Z. Ni, Z. Song, J. Yang, J. Shi, J. Li, and J. Lu, "Does p-type ohmic contact exist in WSe_2–metal interfaces?," Nanoscale, vol. 8, pp. 1179–1191, 2016.

[249] A. Allain, J. Kang, K. Banerjee, and A. Kis, "Electrical contacts to two-dimensional semiconductors," Nature Materials, vol. 14, no. 12, pp. 1195–1205, 2015.

[250] Y. Pan, S. Li, M. Ye, R. Quhe, Z. Song, Y. Wang, J. Zheng, F. Pan, W. Guo, J. Yang, and J. Lu, "Interfacial properties of monolayer $MoSe_2$–metal contacts," The Journal of Physical Chemistry C, vol. 120, no. 24, pp. 13063–13070, 2016.

[251] F. Xia, V. Perebeinos, Y.-m. Lin, Y. Wu, and P. Avouris, "The origins and limits of metal-graphene junction resistance," Nature Nanotechnology, vol. 6, no. 3, pp. 179–184, 2011.

[252] K. Stokbro, M. Engelund, and A. Blom, "Atomic-scale model for the contact resistance of the nickel-graphene interface," Phys. Rev. B, vol. 85, p. 165442, 2012.

[253] I. Popov, G. Seifert, and D. Tománek, "Designing electrical contacts to MoS_2 monolayers: A computational study," Phys. Rev. Lett., vol. 108, p. 156802, 2012.

[254] J. Kang, W. Liu, and K. Banerjee, "High-performance MoS_2 transistors with low-resistance molybdenum contacts," Applied Physics Letters, vol. 104, no. 9, p. 093106, 2014.

[255] J. Kang, W. Liu, D. Sarkar, D. Jena, and K. Banerjee, "Computational study of metal contacts to monolayer transition-metal dichalcogenide semiconductors," Phys. Rev. X, vol. 4, p. 031005, 2014.

[256] J. Kang, D. Sarkar, W. Liu, D. Jena, and K. Banerjee, "A computational study of metal-contacts to beyond-graphene 2D semiconductor materials," 2012 International Electron Devices Meeting, pp. 17.4.1–17.4.4, 2012.

[257] C. Gong, L. Colombo, R. M. Wallace, and K. Cho, "The unusual mechanism of partial fermi level pinning at metal-MoS_2 interfaces," Nano Letters, vol. 14, no. 4, pp. 1714–1720, 2014.

[258] F. A. Rasmussen and K. S. Thygesen, "Computational 2D materials database: Electronic structure of transition-metal dichalcogenides and oxides," The Journal of Physical Chemistry C, vol. 119, no. 23, pp. 13169–13183, 2015.

[259] P.-C. Yeh, W. Jin, N. Zaki, D. Zhang, J. T. Liou, J. T. Sadowski, A. Al-Mahboob, J. I. Dadap, I. P. Herman, P. Sutter, and R. M. Osgood, "Layer-dependent electronic structure of an atomically heavy two-dimensional dichalcogenide," Phys. Rev. B, vol. 91, p. 041407, 2015.

[260] B. Fallahazad, H. C. P. Movva, K. Kim, S. Larentis, T. Taniguchi, K. Watanabe, S. K. Banerjee, and E. Tutuc, "Shubnikov-de haas oscillations of high-mobility holes in monolayer and bilayer WSe_2: Landau level degeneracy, effective mass, and negative compressibility," Phys. Rev. Lett., vol. 116, p. 086601, 2016.

[261] C. M. Smyth, L. A. Walsh, P. Bolshakov, M. Catalano, R. Addou, L. Wang, J. Kim, M. J. Kim, C. D. Young, C. L. Hinkle, and R. M. Wallace, "Engineering the palladium–WSe_2 interface chemistry for field effect transistors with high-performance hole contacts," ACS Appl. Nano Mater., vol. 2, pp. 75–88, 2019.

[262] D. S. Schulman, A. J. Arnold, and S. Das, "Contact engineering for 2D materials and devices," Chem. Soc. Rev., vol. 47, pp. 3037–3058, 2018.

[263] F. Urban, F. Giubileo, A. Grillo, L. Iemmo, G. Luongo, M. Passacantando, T. Foller, L. Madauß, E. Pollmann, M. P. Geller, D. Oing, M. Schleberger, and A. D. Bartolomeo, "Gas dependent hysteresis in MoS_2 field effect transistors," 2D Materials, vol. 6, no. 4, p. 045049, 2019.

[264] J. Shu, G. Wu, Y. Guo, B. Liu, X. Wei, and Q. Chen, "The intrinsic origin of hysteresis in MoS_2 field effect transistors," Nanoscale, vol. 8, pp. 3049–3056, 2016.

[265] E. McCann, D. S. Abergel, and V. I. Fal'ko, "Electrons in bilayer graphene," Solid State Communications, vol. 143, no. 1, pp. 110–115, 2007.

[266] T. Chu, H. Ilatikhameneh, G. Klimeck, R. Rahman, and Z. Chen, "Electrically tunable bandgaps in bilayer MoS_2," Nano Letters, vol. 15, no. 12, pp. 8000–8007, 2015.

[267] X. Dai, W. Li, T. Wang, X. Wang, and C. Zhai, "Bandstructure modulation of two-dimensional WSe_2 by electric field," Journal of Applied Physics, vol. 117, no. 8, p. 084310, 2015.

[268] H. K. Ng, D. Chi, and K. Hippalgaonkar, "Effect of dimensionality on thermoelectric powerfactor of molybdenum disulfide," Journal of Applied Physics, vol. 121, no. 20, p. 204303, 2017.

[269] X. Li, J. T. Mullen, Z. Jin, K. M. Borysenko, M. Buongiorno Nardelli, and K. W. Kim, "Intrinsic electrical transport properties of monolayer silicene and MoS_2 from first principles," Phys. Rev. B, vol. 87, p. 115418, 2013.

[270] K. Kaasbjerg, K. S. Thygesen, and K. W. Jacobsen, "Phonon-limited mobility in n-type single-layer MoS_2 from first principles," Phys. Rev. B, vol. 85, p. 115317, 2012.

[271] L. Wang, A. V.-Y. Thean, and G. Liang, "A statistical Seebeck coefficient model based on percolation theory in two-dimensional disordered systems," Journal of Applied Physics, vol. 125, no. 22, p. 224302, 2019.

[272] V. E. Dorgan, M.-H. Bae, and E. Pop, "Mobility and saturation velocity in graphene on SiO_2," Applied Physics Letters, vol. 97, no. 8, p. 082112, 2010.

[273] Y. K. Koh, M.-H. Bae, D. G. Cahill, and E. Pop, "Heat conduction across monolayer and few-layer graphenes," Nano Letters, vol. 10, no. 11, pp. 4363–4368, 2010.

[274] E. Pop, "The role of electrical and thermal contact resistance for Joule breakdown of single-wall carbon nanotubes," Nanotechnology, vol. 19, no. 29, p. 295202, 2008.

[275] A. Behnam, A. S. Lyons, M.-H. Bae, E. K. Chow, S. Islam, C. M. Neumann, and E. Pop, "Transport in nanoribbon interconnects obtained from graphene grown by chemical vapor deposition," Nano Letters, vol. 12, no. 9, pp. 4424–4430, 2012.

[276] A. C. Ferrari, J. C. Meyer, V. Scardaci, C. Casiraghi, M. Lazzeri, F. Mauri, S. Piscanec, D. Jiang, K. S. Novoselov, S. Roth, and A. K. Geim, "Raman spectrum of graphene and graphene layers," Phys. Rev. Lett., vol. 97, p. 187401, 2006.

[277] W. Jang, W. Bao, L. Jing, C. N. Lau, and C. Dames, "Thermal conductivity of suspended few-layer graphene by a modified T-bridge method," Applied Physics Letters, vol. 103, no. 13, p. 133102, 2013.

[278] S. Kasap, C. Koughia, and H. E. Ruda, Electrical Conduction in Metals and Semiconductors. Cham: Springer International Publishing, 2017.

[279] F. T. Vasko and V. Ryzhii, "Voltage and temperature dependencies of conductivity in gated graphene," Phys. Rev. B, vol. 76, p. 233404, 2007.

[280] Q. Shao, G. Liu, D. Teweldebrhan, and A. A. Balandin, "High-temperature quenching of electrical resistance in graphene interconnects," Applied Physics Letters, vol. 92, no. 20, p. 202108, 2008.

[281] L. Lindsay, W. Li, J. Carrete, N. Mingo, D. A. Broido, and T. L. Reinecke, "Phonon thermal transport in strained and unstrained graphene from first principles," Phys. Rev. B, vol. 89, p. 155426, 2014.

[282] J. Callaway, "Model for lattice thermal conductivity at low temperatures," Phys. Rev., vol. 113, pp. 1046–1051, 1959.

[283] M. G. Holland, "Analysis of lattice thermal conductivity," Phys. Rev., vol. 132, pp. 2461–2471, 1963.

[284] T. Goldstein, Y.-C. Wu, S.-Y. Chen, T. Taniguchi, K. Watanabe, K. Varga, and J. Yan, "Ground and excited state exciton polarons in monolayer $MoSe_2$," The Journal of Chemical Physics, vol. 153, no. 7, p. 071101, 2020.

[285] K. F. Mak, K. He, C. Lee, G. H. Lee, J. Hone, T. F. Heinz, and J. Shan, "Tightly bound trions in monolayer MoS_2," Nature Materials, vol. 12, no. 3, pp. 207–211, 2013.

[286] A. Arora, T. Deilmann, T. Reichenauer, J. Kern, S. Michaelis de Vasconcellos, M. Rohlfing, and R. Bratschitsch, "Excited-state trions in monolayer WS_2," Phys. Rev. Lett., vol. 123, p. 167401, 2019.

[287] D. K. Efimkin and A. H. MacDonald, "Many-body theory of trion absorption features in two-dimensional semiconductors," Phys. Rev. B, vol. 95, p. 035417, 2017.

[288] D. K. Efimkin and A. H. MacDonald, "Exciton-polarons in doped semiconductors in a strong magnetic field," Phys. Rev. B, vol. 97, p. 235432, 2018.